Numerical methods to estimate brain micro-structure from diffusion MRI data

Zheyi Yang

INSTITUT POLYTECHNIQUE DE PARIS

NNT : 2023IPPAE016

Thèse de doctorat

Numerical methods to estimate brain micro-structure from diffusion MRI data

Thèse de doctorat de l'Institut Polytechnique de Paris
préparée à École nationale supérieure de techniques avancées

École doctorale n°574 École doctorale de mathématiques Hadamard (EDMH)
Spécialité de doctorat: Mathématiques appliquées

Thèse présentée et soutenue à Palaiseau, le 19-12-2023, par

Zheyi Yang

Composition du Jury :

Gary Zhang Professeur, University College London	Président
Clair Poignard Directeur de recherche, Inria Bordeaux Sud-Ouest (MONC)	Rapporteur
Emmanuel Caruyer Chargé de recherche, Université de Rennes (Empenn)	Rapporteur
Lisl Weynans Maître de conférence, Inria Bordeaux Sud-Ouest (Carmen)	Examinatrice
Dirk Drasdo Directeur de recherche, Inria Saclay Île-de-France (Simbiotx)	Examinateur
Laure Giovangigli Maître de conférence, Ensta Paris (Poems)	Examinatrice
Jing-Rebecca Li Directrice de recherche, Inria Saclay Île-de-France (Idefix)	Directrice de thèse

Acknowledgments

First, I would like to express my sincere gratitude to my Ph.D. advisor, Jing-Rebecca Li, for her patience and continuous support during three years of Ph.D. and for guiding me into the diffusion MRI world. She set an example for me on how to become a scientific researcher.

I would like to express my special gratitude to Chengran Fang for the valuable discussions we had and for the *NeuronSet* he built, which makes the inflection point-based estimation possible. He is always very willing to share his knowledge in diffusion MRI. In addition, I want to thank to Syver Døving Agdestein, for refactorizing the SpinDoctor codes.

I am thankful to all my friends at UMA and CMAP, especially Tuan Anh Vu, Dorian Lereverend, and Fabien Pourre, who share the same office with me, for creating a good working environment.

I would like to thank all my friends in France, especially Rui Li, Yilun Li, Fanwen Sun, Silin Fu, Yang Ye, Heng Zhang, Yihan Xiong, Shenming Wang, Bowen Liu, Lihao Guan, Wenling Dong and Na Deng. Due to the Covid pandemic, I was unable to return home for three years, and during this time, my friends in France became like family to me.

I would like to thank my parents, for their unconditional support and understanding. This accomplishment would not have been possible without them.

I would like to thank my committee members, Clair Poignard and Emmanuel Caruyer for reviewing the thesis, and Gary Zhang, Lisl Weynans, Dirk Drasdo and Laure Giovangigli for examining it.

Abstract

State-of-the-art microstructural diffusion MRI employs a "compartmentalization" concept, suggesting that an imaging voxel in the human brain can be split into multiple spaces that are isolated with respect to diffusion. The diffusion MRI signal is then the sum of the signal contributions of each of these spaces. The spaces, modeled based on the underlying tissue morphologies, each represents a specific geometrical structure. These compartment signal models have analytical signal expressions, and by matching these to measured signals, one can determine the geometrically related parameters in the models. The accuracy of a diffusion MRI compartment signal model depends on the validity of its assumptions and approximations. Any deviation can affect estimation accuracy. A numerical analysis of these assumptions is essential, guiding experimental design and improving estimation precision.

In diffusion MRI, the Bloch-Torrey partial differential equation (PDE) serves as a gold-standard reference model. Due to the high computational cost of solving the Bloch-Torrey PDE in complicated geometries, simulations involving adjusting geometry-related values are challenging. The objectives of this thesis are (1) to introduce novel numerical simulation techniques based on the Bloch-Torrey PDE, facilitating the numerical studies of geometry-related parameters, (2) to employ these proposed approaches to evaluate existing diffusion MRI compartment signal models and to analyze diffusion MRI signal or apparent diffusion coefficient (ADC) behaviors.

First, we present a novel Matrix Formalism representation, which requires only a single eigendecomposition on the impermeable configuration and re-uses the impermeable Laplace eigenfunctions to compute the signals of permeable configurations. Using this formulation, we illustrate that (1) the diffusion MRI signal shows an exponential rate with respect to permeability; (2) the long-time limit ADC shows different rates of dependence at low and high permeabilities; (3) there is a correlation between permeability and the NEXI model parameters.

Second, we develop a second-order asymptotic expansion for two analytical geometrical deformations arising from the modeling of the brain white matter. Through numerical studies, we illustrate that (1) bending will decrease the signal value in the maximum diffusion direction, (2) twisting will change the maximum diffusion direction.

Third, we evaluate the $1/\sqrt{b}$ power-law scaling and the SANDI model. We identify inflection point (IP) derived biomarkers from the deviation of power-law scaling in the brain gray matter. We perform a numerical analysis on the relationship between the IP-derived biomarkers and compartment volume fractions as well as the soma size, and propose an exhaustive search method based on these biomarkers.

Finally, to address the numerical instability issues in diffusion MRI blood flow imaging simulations, we apply the Streamline Upwind Petrov Galerkin scheme. Numerical validation illustrates that this new method is able to yield a stable solution for quite high blood flow velocities on a coarse mesh.

Keyword: Bloch-Torrey equation, diffusion MRI, microstructural estimation, numerical simulation

Résumé

L'imagerie de microstructure par l'IRM de diffusion utilise un concept de "compartimentation", suggérant qu'un voxel d'imagerie dans le cerveau humain peut être divisé en plusieurs espaces isolés du point de vue de la diffusion. Le signal IRM de diffusion est la somme des contributions du signal de chacun de ces espaces. Chaque espace, modélisé selon des connaissances des morphologies tissulaires biologiques, représente une structure géométrique spécifique. Ces modèles de signaux de compartiments ont des expressions analytiques de signaux sous certaines assumptions, et en minimisant la différence entre ces modèles et les signaux mesurés, on peut déterminer les paramètres liés à la géométrie dans les modèles. La précision d'un modèle de signal de compartiment d'IRM de diffusion dépend de la validité de ses hypothèses et de ses approximations appliquées. Tout déviation peut affecter la précision de l'estimation. Une analyse numérique de ces hypothèses est essentielle, guidant les recherches dans la conception expérimentale et améliorer la précision de l'estimation.

Dans l'IRM de diffusion, l'équation différentielle partielle (EDP) de Bloch-Torrey sert comme modèle de référence standard. En raison du coût de calcul élevé de la résolution de l'EDP de Bloch-Torrey dans des géométries compliquées, les simulations nécessitant des ajustements des paramètres liés à la géométrie sont difficiles. Les objectifs de cette thèse sont (1) de présenter de nouvelles techniques de simulation numérique basées sur l'EDP de Bloch-Torrey, facilitant les études numériques sur les paramètres liés à la géométrie et (2) d'utiliser ces approches proposées pour évaluer les modèles de signal de compartiment IRM de diffusion existants et d'analyser le signal IRM de diffusion ou les comportements du coefficient de diffusion apparent (CDA).

D'abord, nous présentons une nouvelle représentation du Formalisme Matriciel, qui ne nécessite qu'une seule décomposition des fonctions propres sur une configuration imperméable et peut réutiliser ces fonctions propres de l'opérateur Laplacian de la configuration imperméable pour calculer les signaux des configurations perméables. En utilisant cette formulation nouvelle, nous illustrons que (1) le signal IRM de diffusion présente un taux exponentiel par rapport à la perméabilité κ; (2) la limite du CDA à long terme montre différents taux de dépendance à des perméabilités faibles et élevées; (3) il existe une corrélation entre la perméabilité et les paramètres liés à la géométrie du modèle NEXI.

Ensuite, nous développons une expansion asymptotique de second ordre pour deux déformations géométriques analytiques issues de la modélisation de la substance blanche du cerveau. Grâce à des études numériques, nous illustrons que (1) la flexion diminuera la valeur du signal dans la direction de diffusion maximale, (2) la torsion changera la direction de diffusion maximale.

Troisièmement, nous évaluons la loi de puissance $1/\sqrt{b}$ et le modèle SANDI à l'aide des simulations numériques. Nous identifions des biomarqueurs dérivés du point d'inflexion (PI) à partir de la déviation de la loi de puissance dans la substance grise du cerveau. Nous effectuons une analyse numérique de la relation entre les biomarqueurs dérivés du PI et les fractions de volume des compartiments ainsi que la taille du soma, et nous proposons une nouvelle méthode d'estimation en utilisant le moyen de recherche exhaustive basée sur ces biomarqueurs.

Enfin, pour aborder les problèmes d'instabilité numérique dans les simulations d'imagerie du flux sanguin par l'IRM de diffusion, nous appliquons le schéma Streamline Upwind Petrov Galerkin (SUPG). La validation numérique montre que cette nouvelle méthode est capable de produire une solution stable pour des vitesses d'écoulement sanguin assez élevées sur un maillage creux.

Mots-clés : EDP de Bloch-Torrey, IRM de diffusion, estimation micro-structures, simulation numérique

Contributions

List of journal articles

1. **Zheyi Yang**, Imen Mekkaoui, Jan Hesthaven, Jing-Rebecca Li, *Asymptotic models of the diffusion MRI signal accounting for geometrical deformations*, MathematicS In Action, Volume 12 (2023) no. 1, pp. 65-85.
2. **Zheyi Yang**, Chengran Fang, Jing-Rebecca Li, *Incorporating interface permeability into the diffusion MRI signal representation while using impermeable Laplace eigenfunctions*, Physics in Medicine and Biology (2023) 68 175036.
3. Chengran Fang, **Zheyi Yang**, Demian Wassermann, Jing-Rebecca Li, *A simulation-driven supervised learning framework to estimate brain microstructure using diffusion MRI*, Medical Image Analysis (2023) Volume 90, December 2023, 102979.
4. Mojtaba Lashgari, **Zheyi Yang**, Miguel O. Bernabeu, Jing-Rebecca Li, Alejandro F. Frangi, *SpinDoctor-IVIM: An in-silico imaging framework for intravoxel incoherent motion MRI*, submitted.

List of conference abstracts

1. **Zheyi Yang**, Chengran Fang, Jing-Rebecca Li, *Morphological parameters estimation of neurons using a machine learning algorithm on diffusion MRI data*, SIAM Conference on Computational Science and Engineering (CSE23).

Software

1. Maintainer of open-source diffusion MRI simulator SpinDoctor: `https://github.com/SpinDoctorMRI/SpinDoctor`.

Contents

Thesis Overview

The prevalent state-of-the-art microstructural diffusion magnetic resonance imaging (diffusion MRI) methods rely on the concept of "compartmentalization" and depend on diffusion MRI compartment signal models. The idea is that an imaging voxel in the human brain can be divided into several spaces that are disconnected with respect to diffusion. The diffusion MRI signal is represented as the sum of their signal contributions. Each space can be considered as a parameterized compartment characterized by a simplified shape, based on the underlying tissue morphology. These geometrical parameters are the metrics of the model and correlate to specific geometrical structures. For instance, axons in the brain white matter are commonly modeled as a collection of infinitely long cylinders, with the axon radii represented as the cylindrical radii. Additionally, these simplified shapes have analytical signal expressions. Thus, by fitting the measured signals to their analytical signal expressions, one can retrieve the geometrical parameters. Compared to more traditional diffusion MRI imaging methods, such as diffusion tensor imaging (DTI) or kurtosis tensor imaging (KTI), the diffusion MRI compartment signal models link more explicitly the diffusion MRI signals to the histological parameters, providing more interpretable metrics. Some clinical studies have indicated the potential medical values of these models.

The validity of a diffusion MRI compartment signal model depends on the approximations it employs. For example, the signal expressions are often derived from the Gaussian phase approximation and the cell membrane permeability is often assumed to be negligible. Deviation from these approximations may deteriorate the estimation performance of a diffusion MRI compartment signal model. Conducting a numerical analysis on the applicable range of these assumptions would be beneficial. Such analysis would guide researchers in designing suitable experimental sequences, understanding the impact of the deviations from idealized assumptions, and thereby enhancing the estimation accuracy.

In diffusion MRI, the Bloch-Torrey partial differential equation (PDE) serves as a gold-standard reference model. It describes the time evolution of the complex transverse water proton magnetization subject to diffusion-encoding magnetic field gradient pulses. The spatial integral of its solution provides a reference value for the diffusion MRI signal arising from the geometry of interest. Due to the high computational cost of solving the Bloch-Torrey PDE in complicated geometries, simulations involving adjusting geometry-related values are challenging. Solving Bloch-Torrey PDE in such complex domains relies on advanced numerical simulation methods. SpinDoctor is a recent Matlab Toolbox designed for this purpose, applying either (1) a direct finite elements discretization of the Bloch-Torrey PDE or (2) the Numerical Matrix Formalism method which computes the Laplace eigendecomposition using a finite elements discretization.

This thesis aims to (1) introduce novel numerical simulation techniques based on the Bloch-Torrey PDE that aid in the study of geometry-related parameters, (2) employ these proposed approaches to evaluate existing diffusion MRI compartment signal models and analyze diffusion MRI signal or apparent diffusion coefficient (ADC) behaviors. The thesis is organized as follows:

1. In Chapter 1, we introduce the basics of diffusion MRI physics and human brain structures. Then we describe in detail the Bloch-Torrey PDE, diffusion MRI signal behaviors, especially the $1/\sqrt{b}$ power-law scaling at high b-values in the brain white matter, approximation models and two numerical simulation methods, the finite elements method and the Numerical Matrix Formalism method. We also present some diffusion MRI compartment signal models, including the NEXI model and the SANDI model.

2. In Chapter 2, we present a novel Matrix Formalism representation using impermeable Laplace eigenfunctions, to facilitate simulations of a large number of membranes permeability values.

Using the proposed formulation, we evaluate (1) the relationship between the diffusion MRI signals/long-time limit ADC and permeability values on a porous medium, (2) the relationship between the NEXI model parameters and permeability values. We observe that (1) the diffusion MRI signal shows an exponential rate with respect to permeability, (2) the long-time limit ADC shows different rates of dependence at low and high permeabilities, (3) there is a correlation between permeability and the NEXI model parameters. The proposed formulation has been published in the paper[1] and integrated into the developer version of SpinDoctor.

3. In Chapter 3, we develop a second-order asymptotic expansion for two analytical geometrical deformations. Using the asymptotic expansion of the Bloch Torrey PDE, we evaluate the impact of deformations on the ADC and diffusion MRI signals from axons. It is observed that (1) the deformations have the same effects on the ADC and signals, (2) bending will decrease the signal value in the maximum diffusion direction, (3) twisting will change the maximum diffusion direction. The asymptotic models have been implemented using SpinDoctor and published in the paper[2].

4. In Chapter 4, using the Numerical Matrix Formalism method, we evaluate the $1/\sqrt{b}$ power-law scaling on individual realistic neurons and simple shapes. Based on the numerical analysis, we identify inflection point-derived biomarkers coming from the deviation of the power-law scaling for use in the brain gray matter. We derive the mathematical expressions of the proposed biomarkers using the Numerical Matrix Formalism method and conduct a numerical analysis of the biomarkers. We propose an exhaustive search estimation method based on these proposed biomarkers. We validate the novel biomarker-based estimation method and compare it to alternative signal-based estimations as well as the SANDI model on a Synthetic Voxels Set and an *in vivo* dataset. This work extends upon the PhD thesis of Chengran Fang [3] and has been published in the paper[4].

5. In Chapter 5, to study diffusion MRI accounting for the blood flow via numerical simulations, we adopt a stabilized finite elements scheme using the Streamline Upwind Petrov-Galerkin scheme and the theta method. This work is a collaboration with the computational medicine team at the University of Leeds, aiming to extend the existing Bloch-Torrey PDE finite elements solver of SpinDoctor for diffusion MRI blood flow simulations. By numerical analysis, we show that this new scheme is able to yield a stable solution for quite high blood flow velocities on a coarse mesh, whereas the standard Galerkin method encounters instability issues and numerical explosion. This approach has been implemented as a new module of SpinDoctor and has been detailed in a pre-print article.

6. In Chapter 6, we conclude the thesis and discuss possible future works.

Aperçu de la thèse

Les méthodes d'imagerie par résonance magnétique de diffusion (IRM de diffusion) pour estimer les microstructures du cerveau les plus répandues reposent sur le concept de "compartimentation" et dépendent des modèles de signaux de compartiments de l'IRM de diffusion. L'idée est qu'un voxel d'imagerie dans le cerveau humain peut être divisé en plusieurs espaces qui sont déconnectés du point de vue de la diffusion. Le signal IRM de diffusion est représenté par la somme de leurs contributions. Chaque espace peut être considéré comme un compartiment paramétré caractérisé par une forme simplifiée, basée sur la morphologie du tissu sous-jacent. Ces paramètres géométriques sont les métriques du modèle et correspondent à des informations géométriques spécifiques. Par exemple, les axones de la substance blanche du cerveau sont généralement modélisés comme une collection de cylindres infiniment longs, et les rayons des axones étant représentés par les rayons cylindriques. En outre, ces formes simplifiées ont des expressions analytiques du signal sous certaines assumptions. Ainsi, en adaptant les signaux mesurés à les expressions analytiques du modèle, il est possible de récupérer les paramètres géométriques et faire l'estimation. Par rapport aux méthodes d'imagerie IRM de diffusion plus traditionnelles, telles que l'imagerie du tenseur de diffusion (ITD) ou l'imagerie du tenseur de kurtosis (ITK), les modèles de signal du compartiment IRM de diffusion relient plus explicitement les signaux IRM de diffusion aux paramètres histologiques, ce qui permet d'obtenir des mesures plus faciles à interpréter. Certaines études cliniques ont montré les valeurs médicales potentielles de ces modèles.

La validité d'un modèle de signal de compartiment d'IRM de diffusion dépend des approximations qu'il utilise. Par exemple, les expressions du signal sont souvent dérivées de l'approximation de la phase gaussienne (APG) et la perméabilité de la membrane cellulaire est souvent supposée négligeable. Toute déviation par rapport à ces approximations peut détériorer les performances d'estimation d'un modèle de signal de compartiment d'IRM de diffusion. Il serait utile de procéder à une analyse numérique de la gamme applicable de ces hypothèses. Une telle analyse aiderait les chercheurs à concevoir des séquences expérimentales appropriées, à comprendre l'impact des écarts par rapport aux hypothèses idéalisées et, par conséquent, à améliorer la précision de l'estimation.

Dans l'IRM de diffusion, l'équation différentielle partielle (EDP) de Bloch-Torrey sert comme modèle de référence standard. Elle décrit l'évolution temporelle de la magnétisation transversale complexe des protons de l'eau soumise à des impulsions de gradient de champ magnétique codant pour la diffusion. L'intégrale spatiale de la solution fournit une valeur de référence pour le signal IRM de diffusion provenant de la géométrie d'intérêt. En raison du coût de calcul élevé de la résolution de l'EDP de Bloch-Torrey dans des géométries compliquées, les simulations impliquant l'ajustement des valeurs liées à la géométrie sont difficiles et intensif en calcul. La résolution de l'EDP de Bloch-Torrey dans des domaines aussi complexes repose sur des méthodes de simulation numérique avancées. SpinDoctor est une boîte à outils Matlab récente conçue, appliquant soit (1) une discrétisation directe par éléments finis de l'EDP de Bloch-Torrey, soit (2) la méthode du Formalisme Matriciel Numérique qui calcule la décomposition des fonctions propres de l'opérateur Laplacian en utilisant une discrétisation par éléments finis.

L'objectif ultime de cette thèse est d'offrir des outils numériques robustes pour étudier les signaux IRM de diffusion et les comportements ADC dans un contexte plus complexe et réaliste, en évaluant les techniques existantes d'estimation de la microstructure, telles que les modèles de signaux de compartiment d'IRM de diffusion, en concevant des configurations expérimentales d'IRM de diffusion appropriées et en développant de nouveaux modèles d'estimation de la microstructure. Concrètement, dans cette thèse, nous (1) introduisons de nouvelles techniques de simulation

numérique basées sur l'EDP de Bloch-Torrey qui facilitent l'étude des paramètres liés à la géométrie, (2) utilisons ces approches proposées pour évaluer les modèles de signal de compartiment d'IRM de diffusion existants et analyser les comportements du signal IRM de diffusion ou du coefficient de diffusion apparent (CDA).

La thèse est organisée comme suit :

Chapitre 1 : Introduction Dans ce permier chapitre, nous présentons le contexte physique et mathématique de l'estimation microstrucutrale du cerveau à l'aide de l'IRM de diffusion. Ce chapitre est divisé en trois parties.

La première partie du chapitre aborde les aspects de la physique concernant l'IRM de diffusion. Nous présentons d'abord les bases de la physique de l'IRM, et son équation gouvernante, l'équation de Bloch. Ensuite, on présente le processus de la diffusion puis l'EDP de Bloch-Torrey en tenant compte de la diffusion. Par ailleurs, comme la thèse se concentre sur la microstructure du cerveau, nous introduisons les structures du cerveau humain du point de vue des types de cellules neuronales, de l'anatomie et des fonctionnalités.

Dans la deuxième partie, nous décrivons les modèles mathématiques de l'IRM de diffusion. Nous donnons en détail l'expression de l'EDP de Bloch-Torrey avec les conditions aux limites de Neumann homogène, la définition du coefficient de diffusion apparent, et les comportements du signal IRM de diffusion, en particulier la loi de puissance de $1/\sqrt{\mathrm{b}}$ à des valeurs b élevées dans la substance blanche du cerveau. Même pour certaines géométries simples, comme les sphères ou les cylindres, il est difficile de résoudre analytiquement l'EDP de Bloch-Torrey. Pour pouvoir relier les signaux IRM de diffusion et la microstructure du cerveau, le calcul du signal IRM de diffusion est effectué par (1) des simulations numériques ou (2) des modèles d'approximation. Dans la section 1.3.5, nous présentons trois modèles d'approximation : l'approximation de l'impulsion étroite, l'approximation gaussienne et le modèle de Kärger. À l'exception de certains cas limités, il n'existe pas de solutions analytiques de l'EDP de Bloch-Torrey. Les méthodes numériques prédominantes pour résoudre l'EDP de Bloch-Torrey sont : (1) les simulations de Monte Carlo, (2) la méthode des éléments finis/différence finis et (3) Représentation du Formalisme Matriciel (FM). Dans la section 1.3.6, nous présentons en détail les expressions des deux dernière méthodes, qui sont implémenté dans SpinDoctor.

Dans la dernière partie du chapitre, nous décrivons quatre modèles de signaux de compartiments d'IRM de diffusion avancés utilisés pour estimer la microsturcture de la substance blanche et de la substance grise du cerveau : l'Imagerie de la dispersion et de la densité de l'orientation des neurites (NODDI en anglais), l'Estimation du diamètre et de la densité des axones (ActiveAx en anglais), l'Imagerie de la densité des somas et des neurites (SANDI en anglais) et l'Imagerie de l'échange de neurites (NEXI en anglais). NODDI et ActiveAx sont conçus pour l'imagerie de la substance blanche du cerveau. SANDI et NEXI sont conçus pour l'imagerie de la substance grise du cerveau.

Chapitre 2 : Représentation du Formalisme Matriciel perméables en utilisant des fonctions propres de l'opérateur Laplacian imperméables Dans ce chapitre, nous présentons une nouvelle représentation du Formalisme Matriciel utilisant des fonctions propres de l'opérateur Laplacian imperméables, afin de faciliter les simulations des signaux IRM de diffusion pour un grand nombre de valeurs de perméabilité des membranes.

L'estimation de la perméabilité de la membrane cellulaire à l'aide de l'IRM de diffusion présente un grand intérêt pour la recherche et la clinique. En outre, la perméabilité de la membrane cellulaire peut influencer l'interprétation de l'imagerie de la microstructure du cerveau. De nombreux modèles de signal de compartiment d'IRM de diffusion actuellement utilisés sont basés sur une assumption d'un échange d'eau négligeable entre les compartiments, dont leur validité reste inconnue. Ignorer les effets de la perméabilité pourrait rendre l'estimation de la microstructure difficile à interpréter. Par exemple, un travail récent par Jelescu *et al.* en 2022 a souligné que le fait d'ignorer la perméabilité peut sous-estimer la fraction de volume des neurites, même pour les experiments des temps de diffusion courts. Il est donc essentiel de comprendre ce mécanisme pour améliorer l'estimation de la microstructure. Certains travaux récents dans la littérature sur l'IRM de diffusion concernant l'estimation de la microstructure du cerveau ont commencé à prendre en compte la perméabilité des membranes cellulaires, et ont tenté de déterminer la valeur de la perméabilité à l'aide de données réelles d'IRM de diffusion.

Afin d'estimer le coefficient de perméabilité à partir des données d'IRM de diffusion et de valider les modèles de signaux IRM de diffusion par le moyen numérique, il est souhaitable que l'EDP

de Bloch-Torrey puisse être calculée efficacement pour de nombreuses valeurs de perméabilité membranaire. Pour des géométries simples telles que des cercles, des sphères, des plaques ou des segments unidimensionnels, il existe des expressions analytiques du signal IRM de diffusion. L'effet de la perméabilité est pris en compte par une matrice de transition ou le modèle de Kärger, qui est un modèle d'approximation d'échange à deux compartiments. Ces expressions analytiques ont été utilisées pour estimer la microstructure des tissus et la perméabilité de l'interface. Cependant, pour des géométries cellulaires plus complexes et réalistes, il n'existe pas d'expressions analytiques explicites et des simulations numériques sont nécessaires.

L'objectif de ce chapitre est de développer une nouvelle approche qui facilite les simulations lors de l'ajustement de la valeur de perméabilité de la membrane.

Si seul un petit nombre de simulations est nécessaire, les trois principaux groupes d'approches sont les suivants (1) les simulations de Monte Carlo, (2) la résolution de l'EDP de Bloch-Torrey discrétisée par les éléments finis et (3) la méthode spectrale, appelée représentation du Formalisme Matriciel, comme détaillé dans dans la section 1.3.6 du chapitre 1.

La simulation de Monte Carlo utilise des particules aléatoires pour imiter le processus de diffusion au cours d'une expérience d'IRM de diffusion. Elle place aléatoirement un grand nombre de particules à l'intérieur de la géométrie complexe et les laisse se déplacer en fonction de la dynamique de diffusion. Pour intégrer les membranes perméables dans la simulation, l'échange d'eau à travers les interfaces est modélisé par une probabilité de transit P_{trans}, qui est la probabilité que les particules traversent ou se reflètent lorsqu'ils arrivent à une interface perméable. Cependant, lorsque la perméabilité augmente, les pas de temps doit devenir plus petit, afin de maintenir la condition $P_{\text{trans}} \ll 1$. ce qui entraîne une forte demande en ressources de calcul et en mémoire de serveur.

La discrétisation de l'EDP de Bloch-Torrey peut être utilisée pour résoudre directement la magnétisation dans une configuration géométrique complexe. Le domaine de calcul est discrétisé soit par éléments finis soit par différences finies. Comme il s'agit d'une équation déterministe, l'incorporation de la perméabilité est simple. Les détails de la mise en œuvre de la méthode des éléments finis avec la condition des interfaces de perméabilité se trouvent dans la section 1.3.6.1.

Dans un travail récent, Agdestein *et al.* a présenté une mise en œuvre numérique du Formalisme Matriciel pour les interfaces perméables, appelée méthode du Formalisme Matriciel Numérique (FMN), où les conditions de perméabilité de l'interface sont incorporées dans l'étape de décomposition des fonctions propres de l'opérateur Laplacian.

Dans ce chapitre, nous visons à étendre ce travail et à présenter une nouvelle formulation. Le signal IRM de diffusion dans un milieu perméable est calculé en utilisant uniquement des fonctions propres de l'opérateur Laplacian imperméables. Nous donnons d'abord l'expression de la nouvelle méthode. Nous définissons une nouvelle matrice $\boldsymbol{Q}_{proj}$, qui représente la projection de la matrice des flux sur les fonctions propres de l'opérateur Laplacian avec des conditions d'interface imperméables. L'effet de perméabilité est considéré comme une perturbation et traité dans l'étape de calcul du signal, au lieu de l'étape de décomposition des fonctions propres. La nouvelle formulation ne nécessite donc qu'une seule décomposition sur la configuration imperméable et réutilise les mêmes fonctions propres de l'opérateur Laplacian pour calculer les signaux perméables, alors que la méthode FMN nécessite de ré-calculer les fonctions propres pour chaque valeur de perméabilité.

Ensuite, nous prouvons que la nouvelle méthode produit le même signal IRM de diffusion que la méthode originale du Formalisme Matriciel Numérique, à condition que toutes les fonctions propres discretes soit utilisées pour les deux méthodes.

Nous montrons la convergence numérique de la nouvelle méthode lorsque le nombre de fonctions propres utilisées est beaucoup plus petit que l'ensemble complet. Aux valeurs de perméabilité les plus faibles ($\kappa = 10^{-5}$ m/s), les erreurs relatives de notre nouvelle méthode sont au même niveau que celles de la méthode du Formalisme Matriciel Numérique. Lorsque la perméabilité augmente, les erreurs relatives de la nouvelle méthode augmentent, mais restent dans une gamme raisonnable (moins de 1%). Nous évaluons l'efficacité de calcul de notre nouvelle méthode par rapport au FMN losqu'il s'agit des simulations utilisant de nombreux valeurs de perméabilité. Dans l'étape de calcul du signal, le temps de calcul par la nouvelle méthode est proche de celui de la méthode du Formalisme Matriciel Numérique, mais la nouvelle méthode offre des gains de temps significatifs lors de l'étape de décomposition ne doit être exécuté qu'une seule fois, ce qui réduit considérablement le temps de calcul, permettant l'étude des effets de la perméabilité sur le signal IRM de diffusion à l'avenir.

Afin de démontrer les capacités potentielles de notre nouvelle méthode pour l'étude des effets de la perméabilité, nous effectuons une analyse numérique sur l'impact de la perméabilité sur (1) les signaux IRM de diffusion et (2) le CDA. L'analyse suggère que :

1. Le signal IRM de diffusion a une relation mono-exponentielle avec la perméabilité dans une large gamme de valeurs ($10^{-6}\,\mathrm{m/s} \leq \kappa \leq 10^{-4}\,\mathrm{m/s}$), couvrant les valeurs de perméabilité typiques trouvées dans les cellules biologiques ;

2. Aux faibles valeurs b, l'impact de la perméabilité est négligeable. Cependant, à des valeurs b élevées, même une petite valeur de perméabilité modifierait beaucoup les signaux IRM de diffusion ;

3. Avec une perméabilité élevée, le terme dominant du CDA est $t^{-0,5}$, où t est le temps de diffusion ;

4. A des perméabilités faibles et élevées, la limite du temps long du CDA montre des taux différents de dépendance à la perméabilité.

En outre, nous évaluons le modèle NEXI, à l'aide de la nouvelle méthode. Pour éviter de tomber dans un minimum local, nous faisons l'estimation par une recherche exhaustive. Le résultat numérique indique que le temps d'échange d'eau de NEXI est corrélé à la perméabilité dans une large gamme ($10^{-6} \leq \kappa \leq 2 \times 10^{-5}\,\mathrm{m/s}$).

Ce travail contribue (1) à des simulations numériques rapides tenant compte de la perméabilité, (2) à des études numériques sur les effets de la perméabilité dans des géométries complexes, (3) à l'évaluation de modèles d'imagerie microstructurelle.

Cette nouvelle méthode a été publiée dans l'article[1] et intégrée dans la version développeur de SpinDoctor. Par rapport à la version publiée, j'ajoute deux sections supplémentaires :

1. La section 2.4.2 applique la nouvelle méthode pour analyser l'impact de la perméabilité sur le CDA ;

2. La section 2.4.3 utilise des signaux simulés par notre nouvelle méthode, montrant la corrélation entre la perméabilité et le temps d'échange de l'eau du modèle de NEXI.

Chapitre 3 : Expansion asymptotique de l'IRM de diffusion et du CDA tenant compte des déformations géométriques Dans ce chapitre, nous proposons une nouvelle approche pour étudier l'effet de la déformation géométrique en utilisant l'expansion asymptotique.

Dans l'estimation de la microstructure de la substance blanche cérébrale, les axones ou les fibres de la substance blanche cérébrale sont modélisés le plus souvent par un faisceau de bâtonnets, comme le modèle NODDI, soit par une collection de cylindres avec les rayons non nuls, dans la même direction ou avec une dispersion dans l'orientation, comme le modèle ActiveAx$_{\mathrm{ADD}}$. Ces hypothèses négligent l'imperfection géométrique de la forme réaliste des fibres, y compris les variations de diamètre, les formes de section irrégulières, l'ondulation, le pliage, etc., ce qui peut entraîner des imprécisions dans certains estimations. Dans un travail récent par Lee *et al.* en 2020, une surestimation du diamètre des axones a été constatée à de faibles valeurs b en raison de l'ondulation des axones.

L'objectif de ce chapitre est de proposer un modèle réduit pour faciliter les études sur la déformation géométrique et de révéler davantage la relation entre la structure cellulaire du tissu biologique et le signal IRM de diffusion dans la substance blanche du cerveau par les simulations numériques. Nous analysons l'EDP de Bloch-Torrey et le modèle de coefficient de diffusion apparent homogène (CDAH) dans le contexte des mappings de déformation paramétrés, à partir d'une configuration canonique. La configuration canonique que nous concevons est un ensemble d'axones parallèles droits contenus dans l'espace extracellulaire. Notre idée est de modéliser des axones réalistes comme des déformations spatiales de configurations canoniques d'axones parallèles.

Pour être plus concret, nous nous concentrons sur deux déformations analytiquement définies : la flexion et la torsion. Nous déduirons des modèles asymptotiques du signal IRM de diffusion et du CDA où le paramètre asymptotique indique le degré de la déformation géométrique. Grâce à ce travail, nous pouvons relier plus directement le signal IRM de diffusion aux paramètres géométriques des tissus.

Une application potentielle de ce modèle asymptotique est de servir à étudier la robustesse des méthodes d'estimation de la substance blanche du cerveau, comme l'estimation de la fraction de volume ou les rayons des axones, à face des imperfections de la forme. En outre, on peut utiliser ces modèles asymptotiques pour établir la relation entre les déformations et les signaux IRM de diffusion.

Dans la section 3.2, nous présentons d'abord le modèle de CDAH et donnons les expressions analytiques des déformations de flexion et de torsion. Nous dérivons l'EDP de Bloch-Torrey transformée et le modèle de CDAH transformé en tenant compte de ces deux déformations, et développons les solutions de ces EDP transformées sous la forme d'un développement asymptotique du second ordre dans les deux paramètres de déformation. Nous effectuons des simulations numériques dans la section 3.4, pour valider nos expansions asymptotiques et illustrer les effets des déformations géométriques. Les simulations suggèrent que :

1. Pour le modèle de CDAH et l'EDP de Bloch-Torrey, des développements au moins second ordre sont nécessaires pour améliorer la précision ;
2. Par les imageries de diffusion à haute résolution angulaire (HARDI en anglais), nous observons que la flexion rend le CDA et les signaux moins directionnels, tandis que la torsion fait tourner leur direction maximale ;
3. L'analyse du temps de calcul démontre l'efficacité des expansions asymptotiques lors de l'ajustement des paramètres de déformation.

Ce travail contribue à lier explicitement le signal IRM de diffusion aux structures cellulaires et à fournir un outil numérique pour étudier l'impact des imperfections de forme sur le signal IRM de diffusion et le CDA.

Les modèles asymptotiques ont été implémentés dans SpinDoctor et publiés dans l'article [2]. Par rapport à la version publiée, j'apporte les modifications suivantes :

1. J'étend l'expansion asymptotique de l'EDP de Bloch-Torrey en incluant le cas perméable. Je fournis les résultats numériques de l'expansion asymptotique de l'EDP de Bloch-Torrey en utilisant $\kappa = 10^{-5}\,\mathrm{m/s}$;
2. J'étend les expansions asymptotiques au cas où les deux déformations sont appliquées, et j'ajoute ce cas dans les résultats numériques ;
3. J'ajoute une section 3.4.4 qui compare le temps de calcul pour montrer l'efficacité des expansions asymptotiques ;
4. J'utilise une formulation alternative du modèle de CDAH, qui nécessite un pas de temps plus grand que la formulation originale pour maintenir la même précision pendant les simulations numériques.

Chapitre 4 : Estimation de la taille du soma et des fractions de volume à l'aide de biomarqueurs dérivés du point d'inflexion Dans ce chapitre, nous étudions la cause de la rupture de la loi de puissance de $1/\sqrt{\mathrm{b}}$ dans la sustance grise du cerveau. À la suite de cette étude, nous proposons une nouvelle approche d'estimation de la taille du soma et des fractions de volume des compartiments dans la sustance grise en utilisant les signaux IRM de diffusion.

Dans la substance blanche du cerveau, une étude récente de Veraart *et al.* en 2019 a montré que les signaux moyennés dans la direction du gradient

$$\overline{S} \equiv \int_{\|\boldsymbol{u_g}\|=1} S d\boldsymbol{u_g}$$

diminuent linéairement par rapport à l'inverse de la racine carrée des valeurs b, $1/\sqrt{\mathrm{b}}$, dans la régions d'intensité de gradient élevée. Ce comportement, appelé la loi de puissance de $1/\sqrt{\mathrm{b}}$, est prévalent dans les zones différentes de la substance blanche du cerveau. Les simulations numériques sur des bâtons, des cylindres et des fantômes réalistes de neurites permettent d'expliquer cette observation. Toutefois, dans la substance grise du cerveau, on observe un déviation par rapport

à cette loi de puissance de 1 $/\sqrt{\mathrm{b}}$. Plusieurs explications ont été proposées pour cette déviation. Les trois principales sont : (1) la courbure des neurites, (2) la présence de soma, et (3) l'important échange d'eau entre les neurites et l'espace extracellulaire.

Dans un travail récent, Fang *et al.* a mené une étude numérique sur le comportement du signal des neurones individuels réalistes et leurs branches neuritiques à des valeurs b élevées, en utilisant des séquences PGSE. En fixant l'intensité du gradient et en faisant varier le temps de diffusion (à l'aide de PGSE avec $\delta = \Delta$), il a été révélé que :

1. Pour les branches du neurite, la loi de puissance de $1/\sqrt{\mathrm{b}}$ se vérifie et la pente de cet ligne présente une corrélation avec l'inverse de la racine carrée du coefficient de diffusion intrinsèque $1/\sqrt{\mathcal{D}_0}$;

2. En revanche, $\overline{S}$ des neurones présente un changement de concavité dans la région où la loi de puissance de $1/\sqrt{\mathrm{b}}$ est attendu.

À partir de cette observation, des biomarqueurs potentiels ont donc été proposés autour le point d'inflexion (IP) de la courbe du signal moyenné en fonction de la direction du gradient.

Dans un travail de suivi, la thèse de doctorat de Chengran Fang[3], il a présenté un cadre d'apprentissage supervisé basé sur la simulation numérique pour estimer la microstructure, qui utilise les biomarqueurs dérivés du point d'inflexion ou un grand nombre de valeurs de signal comme entrées en utilisant les perceptrons multicouches, montrant les applications potentielles des biomarqueurs dérivés du PI. Afin de s'adapter à l'ensemble de données *in vivo*, les biomarqueurs dérivés du point d'inflexion sont définis sur la courbe du signal en utilisant une séquence PGSE fixe et l'intensité de gradient variable, ce qui est différent de l'article original[5]. Il a construit un ensemble de voxels synthétiques à partir de neurones réalistes et a utilisé des perceptrons multicouches pour approximer les correspondances sous-jacentes entre les inforations géometriques et (1) un grand nombre de signaux ou (2) des biomarqueurs dérivés du PI et le CDA.

L'objectif de ce chapitre est d'étudier la relation entre les biomarqueurs dérivés du PI et les fractions de volume/la taille du soma, puis d'adapter les résultats pour l'estimation. Différentes configurations de séquences peuvent donner lieu à des relations différentes. Étant donné que les expériments pratiques utilisent généralement des séquences PGSE avec des δ et Δ fixes, en ajustant uniquement l'intensité du gradient, nous adoptons cette définition des biomarqueurs dérivés du PI.

Quatre biomarqueurs dérivés du point d'inflexion sont :

- x_0 : la coordonnée x du point d'inflexion;
- y_0 : la coordonnée y du point d'inflexion;
- c_0 : l'ordonnée de la ligne d'ajustement de la loi de puissance au point d'inflexion;
- c_1 : la pente de la ligne d'ajustement.

Dans ce chapitre, nous présentons d'abord dans la section 4.1 les paramètres expérimentaux, la construction du *NeuronSet*, l'ensemble de voxels synthétiques et la méthode d'interpolation spline, qui sont fait dans la thèse de doctorat de Fang.

Ensuite, nous examinons le comportement des signaux de différentes formes géométriques en utilisant des séquences PGSE avec des δ et Δ fixes ($\delta < \Delta$) et en ajustant l'intensité du gradient. Nous montrons que les neurones individuels présentent toujours le même comportement de signal. Nous pouvons donc également identifier les biomarqueurs dérivés du PI dans la configuration avec δ et Δ fixés. En outre, nous trouvons que les sphères individuelles présentent un comportement de signal similaire à celui des neurones individuels, qui peut lier cette déviation de la loi de puissance de $1/\sqrt{\mathrm{b}}$ dans la substance grise à la présence de structures sphériques.

Pour pouvoir calculer precisément les biomarqueurs dérivés du PI, nous dérivons leurs expressions mathématiques à l'aide de la méthode du Formalisme Matriciel Numérique. Ensuite, en analysant la relation entre ces biomarqueurs dérivés du PI, et les fractions de volume/la taille du soma, nous démontrons que :

1. Dans le cas d'une sphère individuelle, la valeur de x_0 est déterminée de manière unique par le rayon du soma R_{soma}, avec une relation monotone;

2. Dans le cas d'une sphère combinée à un faisceau de bâtons, la valeur de c_0 est liée à la fraction de volume du soma f_{soma} ;

3. Dans le cas d'une sphère, combinée aux bâtonnets et à un compartiment de diffusion libre, la valeur de y_0 est en corrélation avec la fraction de volume du compartiment de diffusion libre f_{free}.

Ces recherches suggèrent que nous pouvons extraire les informations relatives à la taille du soma et aux fractions de volume à partir des biomarqueurs dérivés du PI.

Pour démontrer la possibilité d'utiliser les biomarqueurs dérivés du PI dans l'estimation pratique, nous proposons une méthode de recherche exhaustive au lieu des algorithmes d'optimisation ou des algorithmes d'apprentissage. La raison de ce choix est que l'approche de recherche exhaustive élimine le besoin d'ajuster une fonction non convexe.

Sur l'ensemble de données d'un neurone individuel, nous utilisons une méthode itérative basée sur les biomarqueurs dérivés du PI et comparons avec le modèle SANDI. Les résultats numériques montrent que la performance de la nouvelle méthode d'estimation dépasse celle du modèle SANDI sur cet emsemble.

Nous évaluons cette méthode de recherche exhaustive sur un ensemble de tests synthétiques et sur un ensemble de données *in vivo*. Il est démontré que les valeurs estimées sont similaires à celles du modèle SANDI et de la méthode de recherche exhaustive basée sur l'utilisation d'un grand nombre de valeurs de signaux moyennées en fonction de la direction.

Par rapport à l'estimation basée sur les valeurs de signal, les erreurs d'estimation par l'estimation basée sur les biomarqueurs sont au même niveau. L'estimation prend moins de temps parce qu'elle ne nécessite que trois biomarqueurs comme données d'entrée au lieu de tous les valeurs de signal.

Ce travail contribue à l'interprétation de la déviation par rapport à la loi de puissance de $1/\sqrt{\text{b}}$ à des valeurs b élevées dans la substance grise du cerveau, avec des biomarqueurs dérivés du PI, et à l'exploitation de cette compréhension pour l'estimation de la microstructure.

Certaines sections de ce chapitre ont été publiées dans l'article [4]. Il s'agit des éléments suivants :

1. Les paramètres expérimentaux, les constructions du *NeuronSet*, le Synthetic Voxels Set, et la méthode d'interpolation spline, décrits dans la section 4.1 (qui provient de la thèse de doctorat de Chengran Fang[3]) ;

2. La méthode de recherche exhaustive dans la section 4.3.2 ;

3. Les résultats de l'estimation sur l'ensemble de voxels synthétiques dans la section 4.4.2 ;

4. L'estimation sur les données réelles dans la section 4.4.3.

Le reste du chapitre est nouveau pour cette thèse et n'a pas été publié ailleurs.

Chapitre 5 : Simulation d'IRM de diffusion avec Streamline Upwind Petrov-Galerkin Une autre application de l'IRM de diffusion au-delà de l'imagerie du tissu cérébral est l'évaluation de la perfusion sanguine (connue sous le nom d'IRM à mouvement incohérent intravoxel) et l'imagerie du flux sanguin cardiaque. Dans ce chapitre, nous présentons un nouveau schéma spatial d'éléments finis pour les applications d'imagerie du flux sanguin par l'IRM de diffusion.

Ce travail est une collaboration avec l'équipe de médecine computationnelle de l'Université de Leeds, visant à étendre le solveur d'éléments finis de l'EDP de Bloch-Torrey existant du SpinDoctor pour les simulations d'écoulement sanguin par IRM de diffusion.

La simulation de l'IRM de diffusion implique le traitement d'un terme d'écoulement. La vitesse sanguine est généralement déterminée par l'équation de Navier-Stokes au moyen de simulations numériques. Elle est ensuite souvent fournie comme variable prédéfinie pour les simulations d'IRM de diffusion.

À faible valeur b, les signaux de l'IRM de diffusion sont sensibles à la microcirculation du sang dans le réseau capillaire cérébral, ce qui fait que le CDA s'écarte de la valeur attendue. Cet écart a été largement utilisé pour mesurer l'indice de perfusion dans les cliniques. Ces dernières années, l'imagerie du tenseur de diffusion (ITD) a devenu un domaine populaire dans l'imagerie cardiaque, mettant en évidence sa polyvalence en imagerie médicale.

Lorsque l'on considère le flux sanguin, l'EDP de Bloch-Torrey devient une EDP de convection-diffusion-réaction, avec un terme de réaction imaginaire. Cette EDP présente différents comportements en fonction du rapport entre la vitesse et le coefficient de diffusion. Lorsque la vitesse est comparativement faible, comme dans les capillaires, le mouvement des molécules est principalement déterminé par le processus de diffusion et un signal similaire à l'IRM de diffusion classique sera produit. Au contraire, lorsque la vitesse est comparativement élevée, par exemple dans les artères ou les veines, les molécules sont principalement transposées par l'écoulement et, dans ce cas, la simulation numérique pourrait rencontrer des problèmes d'instabilité.

Le raffinement du maillage peut améliorer la stabilité, mais il ne garantit pas toujours, en particulier lors de l'utilisation de la méthode standard des éléments finis de Galerkin. Cela dépend de la vitesse maximale et du maillage des éléments finis. Dans certains cas, un maillage extrêmement fin peut être nécessaire, ce qui peut être impossible dans la simulation numérique en raison de contraintes de ressources informatiques. Dans d'autres cas, le maillage est prédéfini et il n'est pas possible de le modifier. Certaines études suggèrent une stratégie de raffinement local pour améliorer la stabilité et maintenir une taille raisonnable. Un autre problème est qu'avec la méthode standard des éléments finis de Galerkin, des oscillations artificielles peuvent être produites, conduisant à des résultats non-physiques.

L'objectif de ce chapitre est d'appliquer un schéma de simulation stabilisé pour l'IRM de diffusion en tenant compte du flux sanguin. De nombreuses approches de stabilisation ont été proposées pour résoudre la simulation de l'équation de diffusion-convection dépendante du temps dans la communauté de la dynamique des fluides numérique, comme la méthode Streamline Upwind Petrov-Galerkin (SUPG), la méthode de stabilisation symétrique et la méthode des moindres carrés de Galerkin.

Dans ce travail, nous présentons un nouveau schéma d'éléments finis pour les simulations d'IRM de diffusion qui combine la méthode Streamline Upwind Petrov-Galerkin et la méthode de discrétisation temporelle thêta. La technique proposée aborde le problème de l'instabilité de la simulation du signal de l'IRM de perfusion à une vitesse élevée du flux sanguin, en particulier dans les artérioles et les veinules. L'idée de la méthode SUPG est d'ajouter un terme de diffusion artificiel uniquement dans la direction de l'écoulement, afin d'atténuer les oscillations artificielles survenant près des zones présentant des gradients prononcés. L'amplitude de ce terme de régularisation est contrôlée par les paramètres de stabilisation τ_k. Cette nouvelle schéma sert d'outil de simulation puissant, ouvrant la voie à l'étude numérique des comportements des signaux et à la conception de nouveaux modèles d'estimation de la microstructure pour les futures études sur la perfusion sanguine.

Nous présentons tout d'abord la forme généralisée de l'EDP de Bloch-Torrey, qui intègre le terme de convection et le nombre de Péclet, une mesure indiquant le potentiel d'instabilité. Nous donnons ensuite l'expression complète du schéma proposé. Nous comparons la méthode Galerkin standard et la méthode Streamline Upwind Petrov-Galerkin, démontrant ainsi son efficacité. Les résultats des simulations numériques démontrent que la méthode Galerkin standard conduit à des oscillations artificielles à des vitesses d'écoulement sanguin élevées, alors que le nouveau schéma peut fournir une solution stable même sur un maillage d'éléments finis creux. Afin de guider le choix des paramètres de stabilisation et du diamètre des éléments, nous effectuons une analyse de l'effet du choix des paramètres de stabilisation et des diamètres des éléments. D'après cette étude, deux combinaison des paramètres sont choisis pour un maillage creuse et fine.

Cette approche a été implémentée en tant que nouveau module de SpinDoctor et a été détaillée dans un article préimprimé.

Chapitre 6 : Conclusions et perspectives Ce chapitre donne un résumé des résultats obtenus et discute des perspectives de recherche au future dans ce domaine.

Annexe A : Annexe du chapitre 3 Dans cette annexe, nous donnons d'abord la formulation altervative du modèle de CDAH utilisé dans le chapitre 3. Afin d'accélérer les simulations, nous implémentons les développements asymptotiques à l'aide de la méthode de Formalisme Matriciel Numérique. Nous présentons en détail les expressions des développements asymptotiques pour l'EDP de Bloch-Torrey et le modèle de CDAH.

Chapter 1

Introduction

Contents

1.1 Physics of diffusion MRI

1.1.1 Magnetic Resonance Imaging

Magnetic Resonance Imaging (MRI) has been a widely used non-invasive medical imaging technique since the first full-body MRI scanner in 1971[6]. Compared to other radiology modalities, such as computed tomography (CT) or Positron emission tomography (PET), MRI has several benefits, including not involving exposure to ionizing radiation and providing better soft-tissue image contrast[7].

To understand the principles of MRI, in this subsection, we present the underlying physics, nuclear magnetic resonance (NMR), and the prototypical MRI experiment.

For a more comprehensive understanding of the historical evolution, physical phenomena, and experimental configurations of MRI, we refer readers to the works[8–11] and also an educational website, mriquestions.com.

1.1.1.1 Nuclear magnetic resonance

About 63% of an adult's body weight is made up of water, and for the human brain, this value reaches approximately 73%[12, 13]. Each water molecule generally contains two hydrogen atoms, whose nucleus is composed of a single proton. According to quantum physics, protons have a property called spin (around an axis), and hence possess angular momentum, which produces magnetism. In a regular environment, the directions of spins are randomly oriented, as shown in fig. 1.1. Hence, the net magnetization (the sum of all quantum spins) is zero.

In the presence of a strong static external magnetic field $\mathbf{B}_0$, the protons will (macroscopically) precess along the same direction as $\mathbf{B}_0$ at equilibrium, which is called Larmor precession. The angular frequency of Larmor precession is given by[14]

$$\omega_0 = \gamma \mathbf{B}_0, \tag{1.1}$$

where γ is called the gyro-magnetic ratio. For the proton, $\gamma = 2.67513 \times 10^8\,\mathrm{rad/(s \cdot T)}$[15].

For ease of illustration, we set the direction of $\mathbf{B}_0 = B_0 \mathbf{e}_z$ along the z-axis (longitudinal direction), and the transverse plane on x-y plane. Figure 1.1 shows the Larmor precession of spins. As we can see, after adding the external magnetic field, a net magnetization is generated.

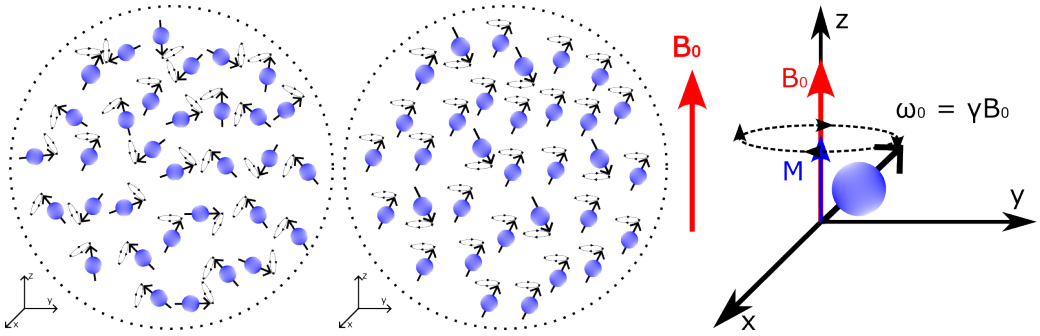

Figure 1.1: Left: In the absence of external magnetic field. The directions of protons precession are randomly distributed and the net magnetization is zero. Middle: In the presence of an external magnetic field $\mathbf{B}_0$. The directions of protons precession are aligned with the external magnetic field, or in the opposite direction. Right: The equivalent scheme. The net magnetization precesses in the direction of external magnetic field.

Macroscopically, the net spin magnetization vector $\mathbf{M}$ precesses around the external magnetic field $\boldsymbol{B}$ satisfies the differential equation below[16]:

$$\frac{d\mathbf{M}}{dt} = \gamma \mathbf{M} \times \mathbf{B}. \tag{1.2}$$

In the static magnetic field case ($\mathbf{B} = \mathbf{B}_0$), eq. (1.2) reduces to,

$$\frac{d\mathbf{M}}{dt} = \omega_0 \begin{bmatrix} M_y \\ -M_x \\ 0 \end{bmatrix}, \tag{1.3}$$

where ω_0 is Larmor frequency, M_x and M_y are the x and y component of the magnetization $\mathbf{M}$. Here, we align the direction of $\mathbf{B}_0$ with the longitudinal direction.

The net magnetization always has a constant component aligned with the direction of the external magnetic field, and a component rotating in the transverse plane. The net magnetization contains statistical information, such as protons density, which can be used to infer properties of biological tissues. However, due to the very low amplitude M_0 compared to external magnetic field B_0, people usually do not directly measure this net magnetization.

To overcome this difficulty, the idea is to perturb the spin orientation from equilibrium to the transverse plane (or a plane quasi-perpendicular to $\mathbf{B}_0$), by applying an additional periodically oscillating magnetic field $\mathbf{B}_{RF}(t)$ for a short time, called a Radio Frequency (RF) pulse[15]:

$$\mathbf{B}_{RF}(t) = B_{RF} \begin{bmatrix} \cos(\omega_0 t) \\ -\sin(\omega_0 t) \\ 0 \end{bmatrix}. \tag{1.4}$$

The RF pulse has a constant amplitude and a direction that periodically rotates in the transverse plane. In order to better show the effect of the RF pulse, here we change the coordinate system from the global coordinate system to a rotating coordinate system, that rotates counterclockwise in

the transverse plane, at an angular frequency of ω_0:

$$\begin{bmatrix} \boldsymbol{e}_{x'} \\ \boldsymbol{e}_{y'} \\ \boldsymbol{e}_{z'} \end{bmatrix} = \begin{bmatrix} \cos(\omega_0 t) & -\sin(\omega_0 t) & 0 \\ \sin(\omega_0 t) & \cos(\omega_0 t) & 0 \\ 0 & 0 & 1 \end{bmatrix} \begin{bmatrix} \mathbf{e}_x \\ \mathbf{e}_y \\ \mathbf{e}_z \end{bmatrix}. \tag{1.5}$$

In this rotating coordinate system, the direction of the RF pulse is fixed in x'-axis.

By replacing $\mathbf{B}$ by $\mathbf{B}_0 + \mathbf{B}_{RF}(t)$ in eq. (1.2) and changing to the rotating coordinate system, the magnetization satisfies

$$\frac{d\mathbf{M}}{dt} = \gamma \begin{bmatrix} 0 & 0 & 0 \\ 0 & 0 & B_{RF} \\ 0 & -B_{RF} & 0 \end{bmatrix} \mathbf{M}. \tag{1.6}$$

Combining with the initial condition $\mathbf{M} = M_0 \boldsymbol{e}_{z'}$, $\mathbf{M}$ becomes

$$\mathbf{M} = M_0(\sin(\gamma B_{RF} t)\boldsymbol{e}_{y'} + \cos(\gamma B_{RF} t)\boldsymbol{e}_{z'}). \tag{1.7}$$

After applying an RF pulse of a duration t, the protons will gain energy and change the precession direction, as shown in fig. 1.2, forming a flip angle α_{flip} with $\mathbf{B}_0$:

$$\alpha_{\text{flip}} = \gamma B_{RF} t. \tag{1.8}$$

By controlling the amplitude of the RF pulse B_{RF} or the duration t, one can achieve a 90 degrees flip angle[17, 18].

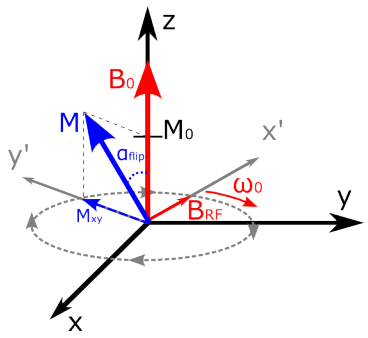

Figure 1.2: The precession when applying RF pulse. The net magnetization will flip into the transverse plane. $\mathbf{B}_0$ is the static external magnetic field, $\mathbf{B}_{RF}$ is the RF pulse, it rotates in the clockwise direction at a rate of ω_0. The blue arrow represents the net magnetization, which forms an angle α_{flip} with $\mathbf{B}_0$.

Once the RF pulse is switched off, the protons tend to come back to the previous equilibrium state and align with $\mathbf{B}_0$ again. Macroscopically, one can observe two phenomena. In the longitudinal direction (the direction of $\mathbf{B}_0$), the net magnetization grows exponentially from 0 to its initial value M_0, called T_1 relaxation or longitudinal relaxation. In the meantime, the net magnetization in the transverse plane will decay exponentially from M_0 to zero, called T_2 relaxation or transverse relaxation[17].

The relaxation process can be described by the Bloch equation below[19]:

$$\frac{d\mathbf{M}}{dt} = \gamma \mathbf{M} \times \mathbf{B}_0 - \begin{bmatrix} \frac{1}{T_2} M_x \\ \frac{1}{T_2} M_y \\ \frac{1}{T_1}(M_z - M_0) \end{bmatrix} = \begin{bmatrix} \omega_0 M_y - \frac{1}{T_2} M_x \\ -\omega_0 M_x - \frac{1}{T_2} M_y \\ -\frac{1}{T_1}(M_z - M_0) \end{bmatrix}, \tag{1.9}$$

where M_0 is the net magnetization in equilibrium, M_x, M_y and M_z are the x, y and z components of $\mathbf{M}$, respectively.

Let the transverse magnetization be $M_{xy} = M_x + \imath M_y$, where $\imath$ is the imaginary unit. Equation (1.9) can be rewritten as

$$\frac{dM_{xy}}{dt} = -(\imath\omega_0 + \frac{1}{T_2})M_{xy} \Rightarrow M_{xy} = M_0 e^{-\imath\omega_0 t} e^{-\frac{1}{T_2}t}, \tag{1.10}$$

$$\frac{dM_z}{dt} = -\frac{1}{T_1}(M_z - M_0) \Rightarrow M_z = M_0(1 - e^{-\frac{1}{T_1}t}). \tag{1.11}$$

It is clear that at time T_1, the longitudinal component M_z regains 63% $(1-1/e)$ of the initial value M_0, and at time T_2, the transverse component M_{xy} falls to 37% $(1/e)$ of its maximum value M_0. T_1 and T_2 values vary among different biological tissues. In the human brain, T_1 is typically on the order of 1 second and T_2 is about 100 milliseconds[20].

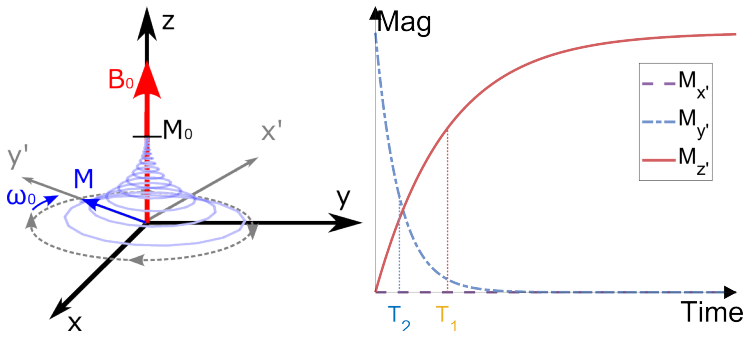

Figure 1.3: Left: Relaxation process; Right: The evolution of the net magnetization during relaxation. The red blue and yellow lines represent the x', y' and z' components of the magnetization, respectively.

The received transverse signal after one single RF pulse is called the free induction decay (FID), as shown in fig. 1.4. It is an oscillating signal that decays at an exponential rate. In actual experiments, due to the inhomogeneity of $\mathbf{B}_0$ caused by instrumental imperfections, protons at different spatial positions precess at different Larmor frequencies, which leads to a faster decay. To eliminate this inhomogeneity effect, in 1950, Hahn proposed the spin echo sequence in his paper[21]. The spin echo sequence is composed of one 180-degree RF pulse after the 90 RF pulse at half of the echo time, as shown in fig. 1.4. This sequence is able to refocus the dephasing spins.

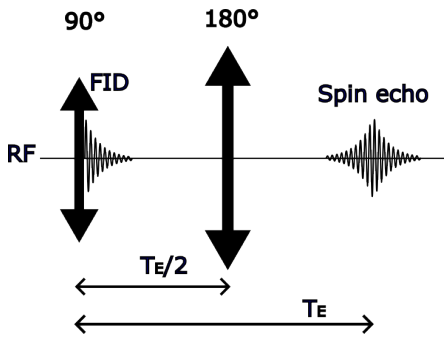

Figure 1.4: Free induction decay (FID) signal and Spin echo signal.

1.1.1.2 Magnetic gradient field

Typical MRI resolution ranges in size from $128\times128\times128\text{mm}^3$ to $512\times512\times512\text{mm}^3$, containing over 1,000,000 voxels (the counterpart of pixels in a three-dimensional image)[22]. To create such images, one need to make the received transverse signal be spatial-sensitive. To achieve that, the principle is adding another external magnetic field $(\mathbf{G}\cdot\mathbf{x})\mathbf{e}_z$, where $\mathbf{G}=[G_x,G_y,G_z]^T$, called a magnetic gradient field. The direction of this magnetic field is the same as the static magnetic field $\mathbf{B}_0$ and its amplitude varies linearly with the spatial variable.

Typically, the MRI spatial encoding is realized in two steps: slice selection and image encoding (including phase and frequency encodings)[20]. In the first step, only the protons located in one specific slice in the z-axis are flipped into the transverse plane. Then, the second step will encode the MRI signal in the Fourier domain. The spatial information on the selected plane can be retrieved after, by applying an inverse Fourier transformation.

Slice selection occurs by simultaneously switching on a longitudinal gradient field (G_z) with the

90-degree RF pulse:

$$\boldsymbol{B}(\mathbf{x}) = (B_0 + G_z z)\mathbf{e}_z, \tag{1.12}$$

where z is the longitudinal position. In this case, the Larmor frequency varies along z-axis:

$$\omega(z) = \omega_0 + \gamma G_z z. \tag{1.13}$$

In order to excite solely the protons in z_0 plane and to suppress interference from neighboring frequencies, an RF pulse with frequencies centered at $\omega(z_0) = \omega_0 + \gamma G_z z_0$ is applied[23]:

$$\mathbf{B}_{RF} = B_{RF}(\Delta F t) \begin{bmatrix} \cos(\omega(z_0)t) \\ -\sin(\omega(z_0)t) \\ 0 \end{bmatrix}, \tag{1.14}$$

where ΔF is the bandwidth, determined the selected slice thickness. $B_{RF}(\Delta F t)$ serves as a low pass filter to avoid interacting with particles precessing at other frequencies. One kind of RF pulse used in practice is the truncated sinc function. With this new RF pulse, in the rotating coordinate system, eq. (1.2) becomes

$$\frac{\partial \mathbf{M}(\mathbf{x},t)}{\partial t} = \gamma \begin{bmatrix} 0 & (z-z_0)G_z & 0 \\ -(z-z_0)G_z & 0 & B_{RF}(\Delta F t) \\ 0 & -B_{RF}(\Delta F t) & 0 \end{bmatrix} \mathbf{M}(\mathbf{x},t). \tag{1.15}$$

Figure 1.5 shows the time profile and frequency profile of the RF pulse, and the relation of the bandwidth and the slice thickness. It is clear that the smaller the bandwidth is, the thinner the selected slice is. Besides, a phase shift depending on the longitudinal position will occur after the RF pulse. To rephase the spins, an extra longitudinal gradient field will be employed after the RF pulse. This gradient field is in the opposite direction and applied for half of the duration of the RF pulse.

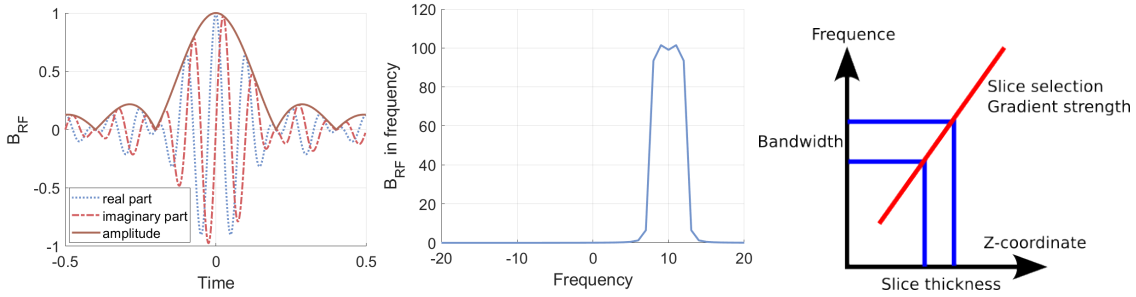

Figure 1.5: Left: RF pulse in the temporal domain. The envelope function is the truncated sinc function; Middle: RF pulse in the frequency domain. It is like a window function, to suppress other frequencies. The center frequency is 10Hz and the bandwidth is 5Hz; Right: the relation between the bandwidth ΔF and the slice thickness.

After slice selection, only the spins on the selected slice are flipped into the transverse plane. Then, image encoding occurs after the 180-degree RF pulse by adding a new magnetic gradient field in the transverse plane, denoted by $\mathbf{G} = [G_x, G_y, 0]^T$, to make the magnetization be spatial sensitive in the plane.

In the presence of the image encoding gradient, the external magnetic field becomes $\mathbf{B}(\mathbf{x}) = (B_0 + G_x x + G_y y)\mathbf{e}_z$ and the Bloch equation eq. (1.9) becomes

$$\frac{\partial \mathbf{M}(\mathbf{x},t)}{\partial t} = \begin{bmatrix} (\omega_0 + \gamma \mathbf{G}\cdot\mathbf{x})M_y - \frac{1}{T_2}M_x \\ -(\omega_0 + \gamma \mathbf{G}\cdot\mathbf{x})M_x - \frac{1}{T_2}M_y \\ -\frac{1}{T_1}(M_z - M_0) \end{bmatrix}. \tag{1.16}$$

The transverse gradient field has no effect on T_1 relaxation. For the transverse magnetization $M_{xy}(\mathbf{x},t)$, eq. (1.10) becomes

$$\frac{\partial M_{xy}(\mathbf{x},t)}{\partial t} = -\left(\imath(\omega_0 + \gamma \mathbf{G}\cdot\mathbf{x}) + \frac{1}{T_2}\right) M_{xy}(\mathbf{x}) \Rightarrow M_{xy}(\mathbf{x},t) = M_0(\mathbf{x}) e^{-\frac{1}{T_2}t} e^{-\imath\omega_0 t} e^{-\imath\gamma \mathbf{G}\cdot\mathbf{x}t}, \tag{1.17}$$

where $M_0(\mathbf{x})$ is the initial transverse magnetization density depending on the position.

The received MRI signal is the spatial integral of the magnetization at the received time t_r:

$$S(t_r) = \int M_{xy}(\mathbf{x}, t_r) d\mathbf{x} = \int M_0(\mathbf{x}) e^{-\frac{1}{T_2} t_r} e^{-\imath \omega_0 t_r} e^{-\imath \gamma \mathbf{G} \cdot \mathbf{x} t_r} d\mathbf{x}. \tag{1.18}$$

Since the Larmor frequency is known, one can factor out the term caused by the static magnetic field by multiplying $\exp(\imath \omega_0 t_r)$ during the post-processing. From eq. (1.18), it is clear that the received signal is the 2D Fourier transform of the initial magnetization density attenuated by T_2 relaxation, at the spatial frequencies vector $\frac{\gamma t_r}{2\pi}[G_x, G_y, 0]^T$. This spatial spectrum is called k-space[24]. In the case of $\frac{1}{T_2} t_r \ll 1$, the T_2 effect is negligible. The initial magnetization density can be retrieved by applying the inverse Fourier transform to the densely sampled received signal in k-space., as shown in eq. (1.18).

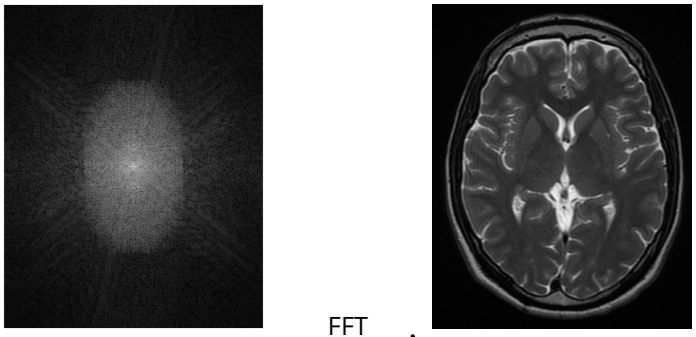

(a) Real part of received signal

(b) Axial slice of brain image after FFT

Figure 1.6: Imaging encoding. Left: Real part of the received MRI signal plotted in k-space; Right: Brain MRI image after Fast Fourier transformation (FFT). The brain MRI picture is distributed under copyright license CC BY-SA 4.0 Deed, from Wikipedia (The link).

There are many different imaging encoding sampling schemes in use, we refer to the works[23] for a further description. Figure 1.7 illustrates the full MRI image acquisition scheme, integrating all the components mentioned above.

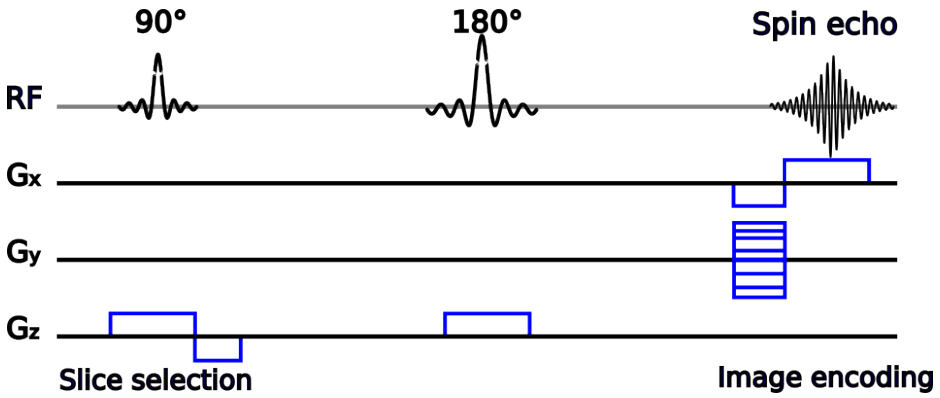

Figure 1.7: MRI experimental prototype.

1.1.2 Diffusion

Self-diffusion is the physical process by which particles of a single type move from one place to another within a homogeneous or heterogeneous phase, driven by Brownian motion[25]. At the microscopic scale, particles are in random motion all the time due to thermal energy. In liquids or gases, particles have more freedom to move and self-diffusion occurs at a faster rate. Under the

same conditions, the extent of particle self-diffusion reflects the nature of a medium, helping study the properties of material.

At the macroscopic scale, the diffusion process can be described from a probabilistic perspective, firstly proposed by Einstein in 1905[26]. The displacement probability of a particle initially positioned at $\mathbf{x}_0$, and located at $\mathbf{x}$ at the moment t is denoted by $P(\mathbf{x}, t; \mathbf{x}_0)$, which satisfies the diffusion equation

$$\begin{aligned} \frac{\partial}{\partial t} P(\mathbf{x}, t; \mathbf{x}_0) &= \mathcal{D}_0 \nabla^2 P(\mathbf{x}, t; \mathbf{x}_0), \\ P(\mathbf{x}, 0; \mathbf{x}_0) &= \delta(\mathbf{x} - \mathbf{x}_0), \end{aligned} \tag{1.19}$$

where $\mathcal{D}_0$ is the diffusion coefficient, which is isotopic and spatially constant, and $\delta(\cdot)$ denotes the Dirac function.

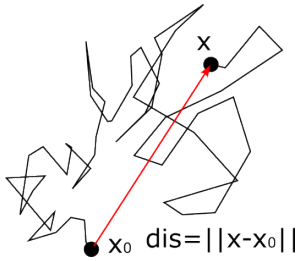

Figure 1.8: Isotropic diffusion process in an unbounded medium. Particles can move freely in the medium.

In the case of isotropic diffusion in a homogeneous free medium (free diffusion), the propagator (or Green's function) of eq. (1.19) is a Gaussian function

$$P(\mathbf{x}, t; \mathbf{x}_0) = \frac{1}{\sqrt{(4\pi \mathcal{D}_0 t)^{\dim}}} \exp\left(-\frac{\|\mathbf{x} - \mathbf{x}_0\|^2}{4\mathcal{D}_0 t}\right) \tag{1.20}$$

where $\dim$ is the spatial dimension. The mean squared displacement of the particles is given by $\langle \|\mathbf{x} - \mathbf{x}_0\|^2 \rangle = 2 \dim \mathcal{D}_0 t$.

In a more complex medium, for instance, a biological tissue, the diffusion process is usually hindered or restricted by geometrical obstacles or boundaries, such as cell membranes and the mean squared displacement will be smaller than in the case of free diffusion. This deviation can serve to infer tissue micro-structural information[27, 28].

In that case, eq. (1.19) needs to be completed with boundary condition accounting for the cell membranes. There are only a few simple shapes, such as spheres, cylinders, etc. for which eq. (1.19) has a closed form solution under the condition that the outer boundary is impermeable and reflective.

Two terms frequently used to describe diffusion are 'isotropic' and 'anisotropic'. Isotropic diffusion refers to diffusion characteristics that are the same in all directions and mainly occurs in free space or the case where the boundary is far away from the particles. In contrast, anisotropic diffusion indicates a directional dependency, where the rate of diffusion will be faster in some specific directions, for example, the case of water diffusion restricted inside axons.

1.1.2.1 Diffusion MRI sequences

Diffusion MRI can be used to indirectly infer information about geometrical microstructure. To make MRI sensitive to diffusion, another magnetic gradient, $\mathbf{G}(t) = [\mathbf{G}_x(t), \mathbf{G}_y(t), \mathbf{G}_z(t)]^T$, needs to be added, called the diffusion encoding gradient, between the slice selection and the image encoding steps, as shown in fig. 1.9. In the presence of the inhomogeneous encoding gradient field, the external magnetic field becomes $\mathbf{B}(\mathbf{x}) = (B_0 + \mathbf{G}_x x + \mathbf{G}_y y + \mathbf{G}_z z)\mathbf{e}_z$, and protons located in different positions would experience different dephasing rates. Through Brownian motion, the protons will travel around in the space, accumulating different phases values when located at different positions. The acquired phases will record the microstructure information.

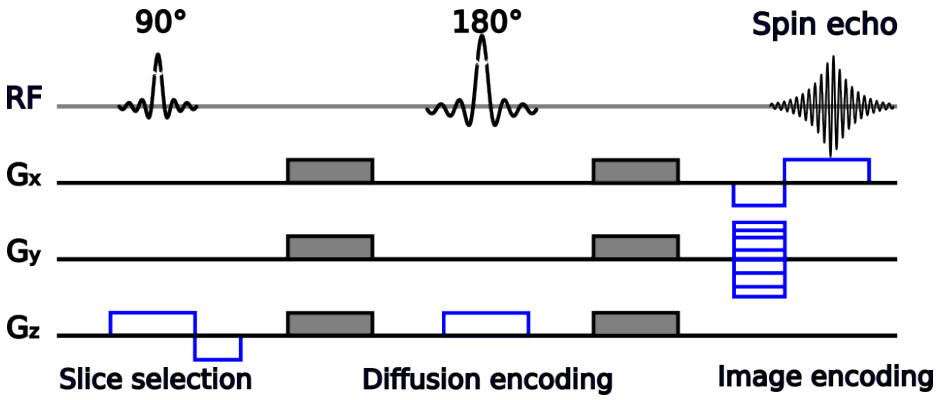

Figure 1.9: In a diffusion MRI scheme, a diffusion encoding gradient is added between the slice selection and the image encoding gradients.

Taking the diffusion effects into account, a modified Bloch equation, called the Bloch-Torrey equation, was proposed by Torrey in 1956[29]:

$$\frac{\partial}{\partial t}M_x = \nabla \cdot \mathcal{D}_0 \nabla M_x + \gamma(\mathbf{B}_0 + \mathbf{G}(t)\cdot\mathbf{x})M_y - \frac{1}{T_2}M_x, \tag{1.21}$$

$$\frac{\partial}{\partial t}M_y = \nabla \cdot \mathcal{D}_0 \nabla M_y - \gamma(\mathbf{B}_0 + \mathbf{G}(t)\cdot\mathbf{x})M_x - \frac{1}{T_2}M_y, \tag{1.22}$$

$$\frac{\partial}{\partial t}M_z = \nabla \cdot \mathcal{D}_0 \nabla M_z + \frac{1}{T_1}(M_z - M_0), \tag{1.23}$$

with initial magnetization in the transverse plane, i.e. $M_z = 0$. Similarly, let the transverse magnetization be $M_{xy} = M_x + \imath M_y$, Bloch-Torrey equation of the transverse magnetization is

$$\frac{\partial}{\partial t}M_{xy} = \nabla \cdot \mathcal{D}_0 \nabla M_{xy} + \imath(\omega_0 + \gamma\mathbf{G}(t)\cdot\mathbf{x})M_{xy} - \frac{1}{T_2}M_{xy}. \tag{1.24}$$

Since ω_0 is independent of spatial position, one can factor out this term and obtain

$$\frac{\partial}{\partial t}M_{xy} = \nabla \cdot \mathcal{D}_0 \nabla M_{xy} + \imath\gamma\mathbf{G}(t)\cdot\mathbf{x}M_{xy} - \frac{1}{T_2}M_{xy}. \tag{1.25}$$

By normalizing the received MRI signal against the MRI signal without any supplementary diffusion encoding gradient, one can retrieve the signal attenuation attributed solely to diffusion.

1.2 Brain structure

As one of the most important and complex organs, the human brain governs a range of essential activities, from fundamental processes, such as respiration, vision, and temperature regulation, to advanced functions, like cognition, memory, and emotion. Understanding the structure and function of the brain has always fascinated the scientific community.

On the cellular level, aside from blood vessels that supply energy and oxygen, the primary constituents of the brain are cells, including neurons and glia. An average adult brain weighs around 1.4 kilograms and hosts nearly 86 billion neurons[30]. These neurons play an important role in information transmission and processing through electrical and chemical signals. Each neuron comprises a cell body, called the soma, dendrites that receive signals, and an extended axon that sends out signals, as depicted in fig. 1.10. Axons exhibit a wide range of lengths, ranging from less than 1mm to up to 1m[31]. Myelinated axons typically have diameters between 1μm and 20μm, while unmyelinated axons often measure less than 1μm in diameter. The diameter of an axon directly influences its conduction velocity, which in turn affects the timing and efficiency of neuronal processing and interactions[32]. Usually, one neuron connects to over 1,000 other neurons via its neurites, leading to

over 100 trillion synapses, where signal exchanges occur. The diameter of the soma varies between 5μm and 100μm, depending on the specific brain regions.

One of the key features of neuron membranes is their permeability. Membrane permeability permits substances, such as liquids or gases, to penetrate or pass through the membranes of cells[33]. This mechanism is essential for living cells as it enables the exchanges of nutrients, ions, chemical information, and oxygen with the environment, and helps to maintain dynamic concentration equilibrium[34–36]. Permeability values differ among different biological tissues. For axonal membranes and myelin sheaths, the typical permeability is 10^{-5} m/s[37, 38].

Alongside the neurons, glia play an important role, helping the intercommunication of the neurons. Glia are of various types including astrocytes, oligodendrocytes, microglia, and ependymal cells, as shown in fig. 1.10. Different shapes serve specific purposes, from providing structural support and nourishment to insulating nerve pathways and engaging in immune responses within the central nervous system[39]. Glia are usually smaller than neurons, depending on the brain regions and their functions.

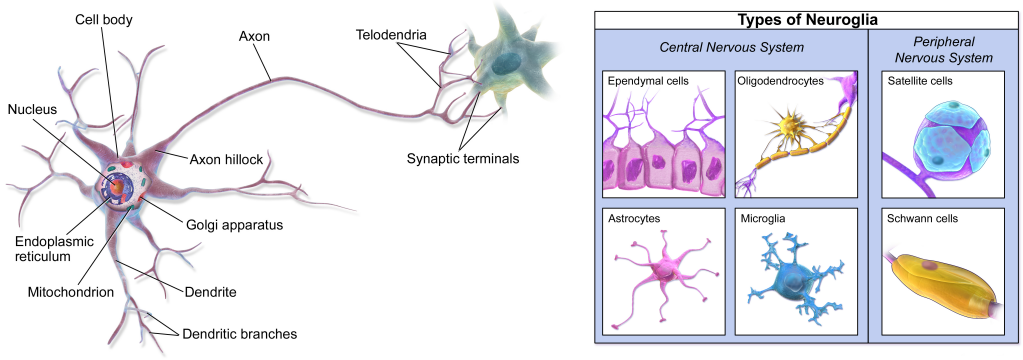

Figure 1.10: Left: A typical neuron, comprising a soma, one long axon, and dendrites. Right: Different types of glia[40]. Both two pictures are from Wikipedia (Link1 and Link2), and distributed under the CC BY 3.0 Deed copyright license.

From an anatomical perspective, the central nervous system (including the brain and the spinal cord) can be divided into two different regions by their colors, the brain gray matter and the brain white matter. The brain ray matter is primarily found in the cerebral cortex (the outermost layer covering the brain) and the nuclei (clusters deep within the cerebral hemispheres and brainstem), whereas the brain white matter is mainly located in the center of the hemispheres, as shown in fig. 1.11. The brain gray matter primarily comprises neuron cell bodies, dendrites, unmyelinated axon terminals, and associated structures, such as glia and capillaries. Information processing occurs in the brain gray matter and it is the most active region in the brain.

On the other hand, the brain white matter consists predominantly of white myelin sheaths axons, which gives its name. The myelin sheaths, produced by oligodendrocytes, act as an insulator that accelerates the transmission of electrical signals. The main function of the brain white matter is to link different the brain gray matter areas and to transmit signals among them.

Figure 1.11: The brain white matter and the brain gray matter. The picture is created by Jones Christiana and licensed under CC BY-SA 4.0 (The link).

From a functional division perspective, the brain can be divided into three parts, the cerebrum,

the brainstem, and the cerebellum[41], as shown in fig. 1.12. Each part has distinct functions and roles.

The cerebrum consists of the brain gray matter located in the cerebral cortex and the brain white matter in its center. It can be divided into two approximately symmetric left and right cerebral hemispheres. As the largest part of the brain, it controls most of our sensory and cognitive processes, including vision, hearing, emotions, and learning ability. The brainstem lies beneath the cerebrum and connects it with the spinal cord. The brainstem is responsible for many involuntary actions, such as breathing and heart rate. The cerebellum is a smaller region located below the cerebrum and behind the brainstem. The main function of the cerebellum is maintaining balance and coordination of movements.

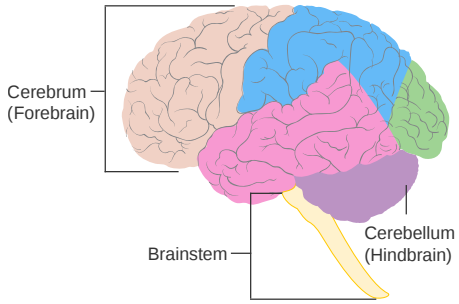

Figure 1.12: Brain functional division. The picture is created by Cancer Research UK and licensed under CC BY-SA 4.0 (The link).

Another component of the brain is the cerebrospinal fluid (CSF), which is a transparent, colorless body fluid that surrounds the brain and spinal cord[42]. This fluid serves to protect the brain from collisions and shock and helps in clearing brain waste products. The CSF occupies a small volume in the brain and its total volume ranges from 100 to 150 ml.

Insights into the microstructural properties of the brain can enhance our understanding of brain processes and help disease diagnosis. Analyzing fiber connectivity provides insights into the collaboration among various brain regions and enables advanced cognitive function studies[43, 44]. Furthermore, certain diseases could be tracked at the microstructural level before they manifest detectable anatomical changes. For example, abnormal changes in permeability could lead to pathology and diseases, such as Alzheimer's disease, Parkinson's Disease, or Multiple Sclerosis[45–48], and a comparatively low volume fraction of neurites is observed in HIV-infected patients within the brain white matter of the frontal lobes[49].

1.3 Mathematical model of diffusion MRI

In the previous section, we made a brief introduction to the governing equation of diffusion MRI, the Bloch-Torrey partial differential equation (PDE), and described how this equation is derived from physical phenomena. In this section, we present its mathematical background. Also, we will discuss the state-of-the-art numerical simulation approaches and some widely-used approximation models.

1.3.1 Geometrical description of brain tissue

Consider a connected domain $\Omega = \bigcup_{i=1}^{N_{cmpt}} \Omega_i \in \mathbb{R}^d$, made up of N_{cmpt} compartments $\{\Omega_i\}_{1\leq i\leq N_{cmpt}}$, without any overlap. The domain Ω represents a sub-domain within a voxel, being as large as computational capacity allows, and containing as many compartments as possible. The interface between two compartments Ω_i and Ω_j is denoted by $\Gamma_{ij} = \Omega_i \cap \Omega_j$ for $i \neq j$, $(i, j) \in \{1, \ldots, N_{cmpt}\}^2$. If two compartments do not touch each other, $\Gamma_{ij} = \emptyset$. Let $\partial\Omega$ be the outer boundary of the domain Ω, and the restriction of the outer boundary in compartment Ω_i is denoted by $\Sigma_i = \partial\Omega \cap \Omega_i$, $i \in \{1, \ldots, N_{cmpt}\}$. If the compartment does not touch the outer boundary, $\Sigma_i = \emptyset$.

Different brain tissue microstructures can be characterized using the aforementioned geometrical framework.

In the brain white matter, each axon is enclosed in the myelin sheath. All these axons are packaged within the extracellular space (ECS). Water exchange between the axons, myelin sheath, and the ECS is quantified by two different permeability coefficients. The geometry has an outer boundary that is impermeable to water. Thus, the number of compartments is twice of the number of axons plus one (the ECS compartment).

For the brain gray matter, the number of compartments is the number of neurons plus one.

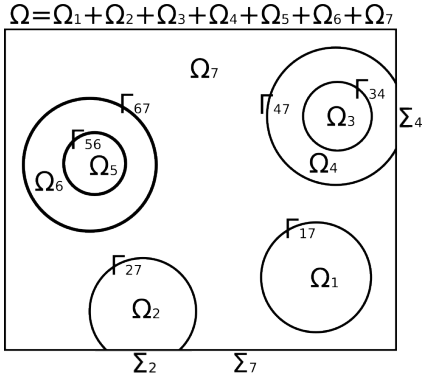

Figure 1.13: Geometrical description of tissue microstructure in 2D.

1.3.2 Bloch-Torrey PDE

In diffusion MRI, a time-varying diffusion-encoding magnetic field gradient is applied to the tissue to probe water diffusion. Denoting the effective time profile of the diffusion-encoding magnetic field gradient by $f(t)$, let the vector $\mathbf{g}$ contain the amplitude and direction information of the diffusion-encoding magnetic field gradient, the restriction of the complex-valued transverse water proton magnetization $M(\mathbf{x}, t)$ in the i-th compartment Ω_i by $M^i(\mathbf{x}, t)$, the diffusion MRI process can be described by the Bloch-Torrey equation[29]:

$$\frac{\partial}{\partial t} M^i(\mathbf{x}, t) = \left(\nabla \cdot \mathcal{D}^i \nabla - \imath\gamma f(t) \mathbf{g} \cdot \mathbf{x} - \frac{1}{T_2} \right) M^i(\mathbf{x}, t), \mathbf{x} \in \Omega_i, \tag{1.26}$$

where

- $\mathcal{D}^i$ is the intrinsic diffusion coefficient in the compartment Ω_i. In this thesis, we assume that $\mathcal{D}^i$ is a constant scalar inside Ω_i;
- $\imath$ is the imaginary unit;
- T_2 is the transverse relaxation coefficient;
- γ is the gyromagnetic ratio. For diffusion MRI of the brain, the gyromagnetic ratio of the water proton is $\gamma = 2.67513 \times 10^8 \, \mathrm{rad}/(\mathrm{s} \cdot \mathrm{T})$.

The magnetization $M(\mathbf{x}, t)$ is a function of position $\mathbf{x}$ and time t, and depends on the diffusion gradient vector $\mathbf{g}$ and the time profile $f(t)$. For simplicity, we consider the case that the gradient direction $\mathbf{u_g}$ is unchanged, i.e. $\mathbf{g} = \|\mathbf{g}\|\mathbf{u_g}$, which is common in many diffusion MRI practical applications.

In this thesis, we consider a simplified case that the T_2 is constant both spatially and temporally, despite evidence suggesting variability in the myelin sheath in white matter, but all the presented results can be extended to the case with varying T_2. Under this assumption, the T_2 relaxation affects all the protons uniformly and its effect on magnetization can be factored out by multiplying a factor of e^{t/T_2}. Consequently, we have

$$\frac{\partial}{\partial t} M^i(\mathbf{x}, t) = \left(\nabla \cdot \mathcal{D}^i \nabla - \imath\gamma f(t) \mathbf{g} \cdot \mathbf{x} \right) M^i(\mathbf{x}, t), \mathbf{x} \in \Omega_i. \tag{1.27}$$

The Bloch-Torrey PDE needs to be supplemented by interface conditions and boundary condition. For the interface between i-th and j-th compartments Γ_{ij}, the two interface conditions are:

$$\mathcal{D}^i \nabla M^i(\mathbf{x},t) \cdot \mathbf{n}^i(\mathbf{x}) \quad = -\mathcal{D}^j \nabla M^j(\mathbf{x},t) \cdot \mathbf{n}^j(\mathbf{x}), \mathbf{x} \in \Gamma_{ij}, \tag{1.28}$$

$$\mathcal{D}^i \nabla M^i(\mathbf{x},t) \cdot \mathbf{n}^i(\mathbf{x}) = \kappa^{ij}(M^j(\mathbf{x},t) - M^i(\mathbf{x},t)), \mathbf{x} \in \Gamma_{ij}, \tag{1.29}$$

where

- $\mathbf{n}^i(\mathbf{x})$ is the unit outward pointing normal vector from i-th compartment;
- κ^{ij} is the permeability coefficient of the interface Γ_{ij}.

These interface conditions suggest the discontinuity of the magnetization at the interfaces. The interface permeability is non negative, i.e. $\kappa^{ij} = \kappa^{ji} \geq 0$. The first boundary condition ensures the flux continuity across the interface Γ_{ij}. The second boundary condition characterizes the flux as a quantity proportional to the magnetization difference across the interface, incorporating the permeability coefficient. When $\kappa^{ij} = 0$ m/s, eq. (1.29) reduces to homogeneous Neumann boundary condition and the interface is impermeable. When $\kappa^{ij} \to +\infty$, it implies that $M^j(\mathbf{x},t) = M^i(\mathbf{x},t)$, then water can diffuse freely across the interface.

Suppose that the outer boundary Σ_i is impermeable, thus the homogeneous Neumann boundary condition:

$$\mathcal{D}^i \nabla M^i(\mathbf{x},t) \cdot \mathbf{n}^i(\mathbf{x}) = 0, \mathbf{x} \in \Sigma_i. \tag{1.30}$$

When the geometry of interest has a periodic structure, another often employed boundary condition is the Bloch periodic boundary condition[50]. Detailed discussion on this topic is out of the scope of this thesis and we refer the readers to the related literature[51].

The Bloch-Torrey PDE also needs initial conditions. When $\mathcal{D}^i$ is the same cross all compartments that are connected by non-zero permeabilities, the initial spin density should be uniform. Thus, unless specified, in this thesis, we assume the initial spin density is the same in all compartments:

$$M^i(\mathbf{x},0) = \rho, \mathbf{x} \in \Omega_i, \tag{1.31}$$

where ρ is the initial spin density in Ω.

The diffusion MRI signal in the domain Ω is the space integral of magnetization, measured at echo time T_E:

$$S(\mathbf{g},f) := \int_{\mathbf{x}\in\Omega} M(\mathbf{x},T_E) d\mathbf{x}. \tag{1.32}$$

It is evident that due to the spatial integral, the diffusion MRI signal would lose some information on the tissue geometrical structures, which poses challenges to microstructure estimation.

The choice of time profiles varies based on the purposes of the experiments. Some commonly used time profiles (diffusion-encoding sequences) include:

- The pulsed gradient sequence (PGSE), proposed by Stejskal and Tanner[52], with two ideal rectangular gradient pulses of duration δ and opposite in amplitude, separated by a time interval $\Delta - \delta$:

$$f(t) = \begin{cases} 1, & 0 \leq t \leq \delta, \\ -1, & \Delta < t \leq \Delta + \delta, \\ 0, & \text{otherwise.} \end{cases} \tag{1.33}$$

- The oscillating gradient spin echo sequence (OGSE), proposed by Callaghan[53, 54], replacing the rectangular pulses in PGSE by either sine or cosine functions with a period τ, during the pulses δ:

$$f(t) = \begin{cases} \sin(\frac{2\pi t}{\tau}), & 0 \leq t \leq \delta, \\ -\sin(\frac{2\pi(t-\Delta)}{\tau}), & \Delta < t \leq \Delta + \delta, \\ 0, & \text{otherwise,} \end{cases} \tag{1.34}$$

or

$$f(t) = \begin{cases} \cos(\frac{2\pi t}{\tau}), & 0 \leq t \leq \delta, \\ -\cos(\frac{2\pi(t-\Delta)}{\tau}), & \Delta < t \leq \Delta + \delta, \\ 0, & \text{otherwise.} \end{cases} \tag{1.35}$$

- The double PGSE, proposed by[55], combining two PGSE, separated by a time interval t_m:

$$f(t) = \begin{cases} 1, & 0 \leq t \leq \delta_1 \\ -1, & \Delta_1 \leq t \leq \Delta_1 + \delta_1 \\ -1, & \Delta_1 + \tau_m \leq t \leq \Delta_1 + \delta_2 + \tau_m \\ 1, & \Delta_1 + \Delta_2 + \tau_m \leq t \leq \Delta_1 + \Delta_2 + \delta_2 + \tau_m \\ 0, & \text{otherwise} \end{cases} \tag{1.36}$$

Figure 1.14 illustrates the time profiles of these sequences. In order to ensure the phase returns to the initial state after diffusion encoding gradient, i.e. the transverse magnetization at echo time $M(\mathbf{x}, T_E)$ is real, the time profile $f(t)$ must satisfy a rephasing condition and an anti-symmetric condition[56]:

$$\int_0^{T_E} f(t) = 0, \tag{1.37}$$

$$f(t) = -f(T_E - t). \tag{1.38}$$

Each time profile has its specificity. The most commonly employed sequence type is the PGSE sequence, proposed by Stejskal and Tanner[52]. This sequence is used in diverse areas such as tractography, pathology detection, and perfusion studies[43, 57, 58]. Double PGSE sequences are often used to assess non-Gaussian diffusion behaviors. For instance, they are adept at separating between intra-axonal and extra-axonal diffusion[59]. OGSE sequences are particularly suited for probing short diffusion time behaviors due to their oscillating gradients[60], enabling to assess information about the tissues with short spatial scales.

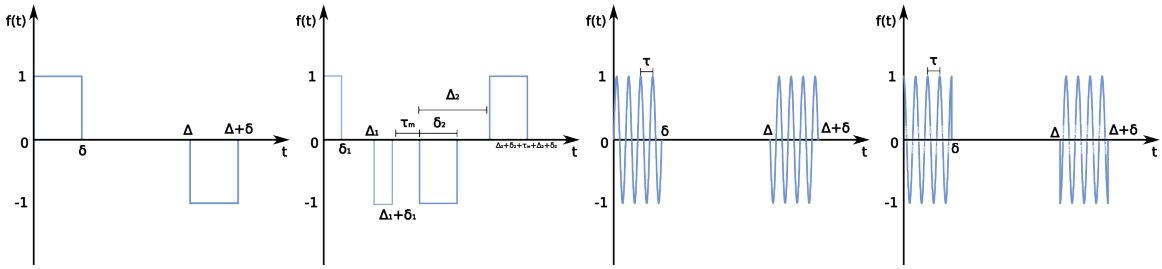

Figure 1.14: From left to right: PGSE, double PGSE, sineOGSE, and coseOGSE.

1.3.3 Diffusion MRI signal behavior

In the homogeneous free space case, assuming that the intrinsic diffusion coefficient is $\mathcal{D}_0$, the Bloch-Torrey PDE has an analytical solution[61], and the diffusion MRI signal is represented as:

$$S = S_0 e^{-\mathcal{D}_0 \mathsf{b}}, \tag{1.39}$$

where S_0 is the diffusion MRI signal at a diffusion encoding gradient strength of zero, and b is defined as

$$\mathsf{b}(\mathbf{g}, f) = \gamma^2 \|\mathbf{g}\|^2 \int_0^{T_E} du \left(\int_0^u f(s) ds \right)^2. \tag{1.40}$$

This quantity is called the b-value, depending on the strength $\|\mathbf{g}\|$ and the time profile $f(t)$, which reflects the diffusion weighting. The higher the b-value, the stronger the diffusion effects on the signal.

For the commonly used diffusion-encoding sequences mentioned in the previous subsection, the expressions of the b-value are:

$$\mathsf{b}(\mathbf{g},\delta,\Delta) = \gamma^2\|\mathbf{g}\|^2\delta^2\,(\Delta-\delta/3) \text{ for PGSE,} \tag{1.41}$$

$$\mathsf{b}(\mathbf{g},\delta,\Delta,\tau) = \gamma^2\|\mathbf{g}\|^2\frac{\delta\tau^2}{4\pi^2} \text{for coseOGSE,} \tag{1.42}$$

$$\mathsf{b}(\mathbf{g},\delta,\Delta,\tau) = \gamma^2\|\mathbf{g}\|^2\frac{3\delta\tau^2}{4\pi^2} \text{for sineOGSE,} \tag{1.43}$$

$$\mathsf{b}(\mathbf{g},\delta,\Delta) = \gamma^2\|\mathbf{g}\|^2\,(\Delta_1-\delta_1/3+\Delta_2-\delta_2/3) \text{ for double PGSE.} \tag{1.44}$$

In order to measure the hindered and restricted effects caused by the tissue microstructure, in a diffusion MRI experiment, the pulse sequence (time profile $f(t)$) is usually fixed, while $\mathbf{g}$ is varied in amplitude, and possibly also in direction[62]. When $\mathbf{g}$ varies only in amplitude (while staying in the same direction), one can fit S against the b-value, to obtain a new quantity, called the apparent diffusion coefficient (ADC)[63]:

$$\mathsf{ADC} := -\frac{\partial}{\partial \mathsf{b}}\log\frac{S(\mathsf{b})}{S(0)}\bigg|_{\mathsf{b}=0}. \tag{1.45}$$

The ADC can be understood as an effective diffusion coefficient, i.e. the diffusion process on the domain Ω is similar to the free diffusion case characterized by a diffusion coefficient equivalent to the ADC.

However, the signal behavior is more complex than this. Figure 1.15 displays the curve of the signal attenuation ($\log(S(\mathsf{b})/S(0))$) against the b-value. In both high and low b-value regimes, the curve is deviated from $e^{-\mathsf{ADCb}}$. At low b-values, the signal decays faster than expected, due to water molecules circulating or perfusing in capillary networks. This phenomenon was firstly found by Denis Le Bihan in the 1980s[57]. It can be used to probe perfusion in capillaries and leads to a new diffusion MRI technique, known as intravoxel incoherent motion (IVIM) imaging. On the other side, at high b-values, the signal attenuation becomes slower than expected due to non-Gaussian diffusion patterns[56].

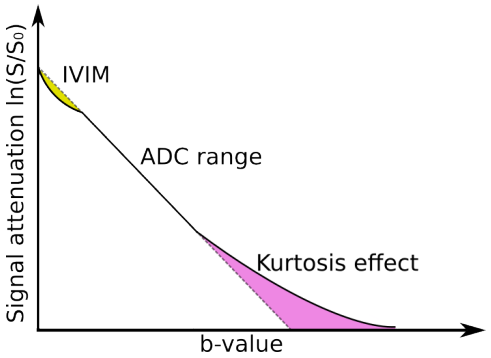

Figure 1.15: Diffusion MRI signals (solid line) as a function of b-values. The dotted line is the ADC approximation. At low b-values, the deviation (yellow area) is caused by the IVIM effect, and at high b-values, the deviation is caused by the non-Gaussian diffusion effect (purple area). This figure is reproduced of the original figure in `https://www.mriquestions.com/ivim.html`.

To illustrate the capability of diffusion MRI sequences in assessing microstructure, there are three critical length scales:

- the size of the cellular geometry L;
- the mean squared diffusion displacement $\sqrt{2\mathsf{ADC}\dim t}$, where $\dim$ is the dimension, which characterizes the average diffusion distance during diffusion time t;
- the gradient length, $1/(\gamma\|\mathbf{g}\|t)$, which characterizes the phase shift degree during time t.

To probe tissue microstructure by restricted diffusion, it is essential to guarantee that spins have enough time to traverse the entire cellular geometries of interest, meaning $L/2 \ll \sqrt{2\text{ADC}\dim t}$ and the phase shift is significant as well.

1.3.3.1 Power-law scaling in the brain white matter

In a recent work of Veraart *el al.*[64, 65], it was shown that the direction-averaged signals of tubular structures such as neurites exhibit a certain high b-value behavior:

$$\overline{S} \equiv \int_{\|\mathbf{u_g}\|=1} S d\mathbf{u_g} \sim c_1 \frac{1}{\sqrt{\text{b}}} + c_0, \tag{1.46}$$

where $\overline{S}$ is the direction-averaged signal. This linear relationship eq. (1.46) is often referred to as the $1/\sqrt{\text{b}}$ power-law scaling of direction-averaged signals. Figure 1.16 depicts $\overline{S}$ for one infinitely long straight cylinder with varying radii. The sticks represent cylinders with zero radius, where diffusion only occurs in the axial direction. It is clear that from $1/\sqrt{\text{b}} \leq 0.03\mu\text{m}\cdot\mu\text{s}^{-1/2}$(or mm $\cdot$ s$^{-1/2}$), $\overline{S}$ is linear to $1/\sqrt{\text{b}}$.

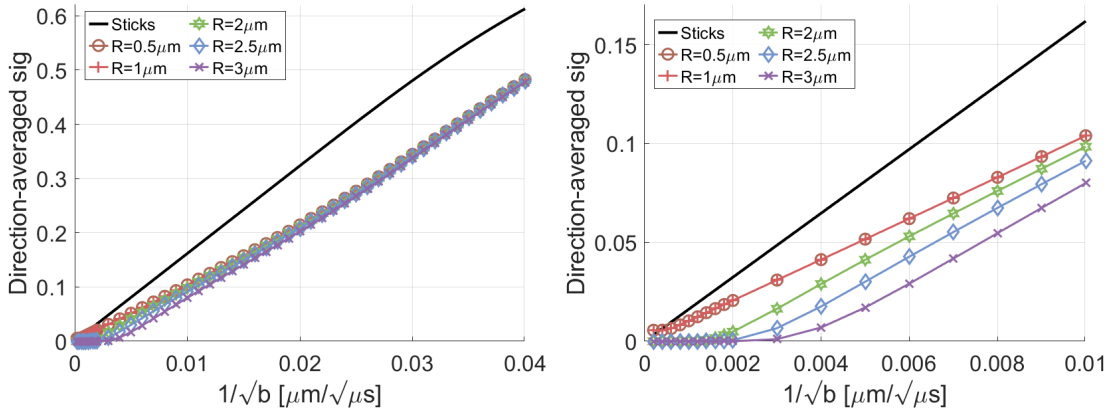

Figure 1.16: Direction-averaged signal for a single infinitely long straight cylinder with varying radii. The simulations are conducted using SpinDoctor. The sequence is PGSE($\delta = 8$ms, $\Delta = 19$ms). Left: $0\mu\text{m}\cdot\mu\text{s}^{-1/2} \leq 1/\sqrt{\text{b}} \leq 0.04\mu\text{m}\cdot\mu\text{s}^{-1/2}$. Power-law scaling for tubular structures. Right: The zoom-in figure, $0\mu\text{m}\cdot\mu\text{s}^{-1/2} \leq 1/\sqrt{\text{b}} \leq 0.01\mu\text{m}\cdot\mu\text{s}^{-1/2}$. We can observe the deviations due to non-zero radius.

This direction-averaged signal behavior in the brain white matter at high b-values indicates that the intra-axonal signal decays at a rate slower than exponential with respect to b, providing the possibility to make MRI specifically sensitive to the intra-axonal signal. Furthermore, it provides theoretical justification for representing neurites (axons, dendrites, cellular process) as a collection of cylinders or sticks in microstructural imaging at high b-values.

However, at ultra-high b-values, deviations from the $1/\sqrt{\text{b}}$ power-law scaling are observed in the brain white matter. This could be attributed to (1) perpendicular diffusion within axons and (2) water exchange between neurites and the extracellular space[66]. Similarly, a breakdown of the $1/\sqrt{\text{b}}$ power-law scaling is observed in the brain gray matter, reported in the literature[5, 28].

1.3.4 Probabilistic perspective of diffusion MRI

Given that a diffusion process is involved, the Bloch-Torrey PDE can also be interpreted from a probabilistic perspective, which provides the theoretical background for Monte-Carlo simulation in diffusion MRI.

Derived from the Bloch equation, during the relaxation process, protons will acquire a phase influenced by the strength of the external magnetic field. When a diffusion-encoding gradient $f(t)\mathbf{g}\cdot\mathbf{x}$ is applied, the phase acquired by the protons becomes dependent on their spatial positions. Due to the Brownian motion, the protons will randomly move around thereby altering their positions.

As a result, the phase they acquire is affected by multiple strength values. Denoting the position of a group of spins as a function of time $\mathbf{x}(t)$, with their initial position as $\mathbf{x}_0$, the acquired phase $\phi(t)$ can be expressed as:

$$\phi(t) = \int_0^t \gamma f(t')\mathbf{g} \cdot \mathbf{x}(t')dt'. \tag{1.47}$$

The phase is a random variable depending on the position $\mathbf{x}(t)$. At the echo time, the diffusion MRI signal is represented as the sum of all spins within the domain Ω, with their respective acquired phases:

$$S(\mathbf{g}, f) = S_0 \int_{-\infty}^{+\infty} P_{T_E}(\phi)e^{\imath\phi}d\phi = S_0\mathbb{E}\{\exp(\imath\phi(T_E))\}, \tag{1.48}$$

where $P_{T_E}(\cdot)$ is the distribution of phase at echo time, $\mathbb{E}\{\cdot\}$ is the expectation and S_0 is the MRI signal without applying the diffusion-encoding gradient. Thus, the diffusion MRI signals can be computed by random walkers' movements inside the simulation domain.

1.3.5 Approximation models

Even for some simple geometries, such as spheres or cylinders, it is difficult to solve analytically the Bloch Torrey PDE. To be able to link diffusion MRI and the tissue microstructure, the computation of the diffusion MRI signal is performed through either numerical simulations or approximation models.

In this subsection, we introduce three approximation models: the narrow pulse approximation, the Gaussian approximation, and the Kärger model.

1.3.5.1 Narrow pulse approximation

The aim of the narrow pulse approximation (NPA) is to solve the Bloch Torrey PDE analytically during the pulses. Considering a PGSE sequence whose pulse duration is negligible compared to the duration of the interval between pulses, i.e. $\delta \ll \Delta$, suppose that the water molecules do not move much during the pulses. Under this assumption, the transverse magnetization is subjected to the Bloch equation, and at time δ, it can be expressed as

$$M(\mathbf{x}, \delta) = \rho e^{-\imath\gamma\delta\mathbf{g}\cdot\mathbf{x}}. \tag{1.49}$$

During the interval between the pulses, the diffusion encoding gradient is turned off and the Bloch Torrey PDE is reduced to pure diffusion equation. The restricted transverse magnetization on Ω_i satisfies:

$$\frac{\partial}{\partial t}M^i(\mathbf{x}, t) = \nabla\mathcal{D}^i\nabla M^i(\mathbf{x}, t),\ \mathbf{x} \in \Omega_i. \tag{1.50}$$

It is supplemented by the same interface conditions eqs. (1.28) to (1.29) and boundary condition eq. (1.30), and uses eq. (1.49) as the initial condition.

After Δ, the second pulse is applied and dephase the magnetization by $e^{-\imath\gamma\delta\mathbf{g}\cdot\mathbf{x}}$ again. Therefore, the magnetization at echo time is

$$M(\mathbf{x}, T_E) = M(\mathbf{x}, \Delta)e^{-\imath\gamma\delta\mathbf{g}\cdot\mathbf{x}}, \tag{1.51}$$

and the received MRI signal becomes

$$S = \int_\Omega M(\mathbf{x}, \Delta)e^{-\imath\gamma\delta\mathbf{g}\cdot\mathbf{x}}d\mathbf{x}. \tag{1.52}$$

From the probabilistic perspective, during the first pulse, the protons remain immobile and acquire a phase given by $e^{\imath\gamma\delta\mathbf{g}\cdot\mathbf{x}_0}$, where $\mathbf{x}_0$ is the initial position. After that, they will diffuse in the domain Ω and maintain this phase until the 180 degrees RF pulse is applied and flip the phase to $e^{-\imath\gamma\delta\mathbf{g}\cdot\mathbf{x}_0}$:

$$S = \int_\Omega\int_\Omega P(\mathbf{x}, \Delta; \mathbf{x}_0)e^{\imath\gamma\delta\mathbf{g}\cdot(\mathbf{x}-\mathbf{x}_0)}d\mathbf{x}d\mathbf{x}_0, \tag{1.53}$$

where $P(\mathbf{x}_0, \mathbf{x}, \Delta)$ is the diffusive propagator at time Δ. The signal can be considered as the spatial Fourier transformation of the average diffusive propagator. one can retrieve the diffusive propagator by dense sampling in the spatial frequency space, as in q-space imaging[67].

Under the narrow pulse assumption, only a pure diffusion equation is needed to be solved. For some simple geometries, such as spheres or cylinders, closed forms of the diffusion MRI signal have been derived under this approximation. This approximation is a popular choice in the diffusion MRI community[68, 69].

A primary limitation of this assumption is that implementing a PGSE sequence with an extremely short pulse duration δ and high amplitude poses significant challenges experimentally. Besides, the assumption that molecular movement during the pulses is negligible might not be accurate.

1.3.5.2 Gaussian phase approximation

The Gaussian phase approximation (GPA) assumes that in the diffusion MRI experiment, the distribution of acquired phases at echo time $P_{T_E}(\phi)$ is a Gaussian distribution, with zero mean and a variance σ^2[70]:

$$P_{T_E}(\phi) = \frac{1}{\sigma\sqrt{2\pi}} e^{-\frac{1}{2}\left(\frac{\phi}{\sigma}\right)^2}. \tag{1.54}$$

Concretely, the variance is proportional to the mean squared displacement. Under this assumption, the diffusion MRI signal can be expressed as:

$$S = S_0 \mathbb{E}\{e^{\imath\phi(T_E)}\} = S_0 e^{-\frac{1}{2}\sigma^2}. \tag{1.55}$$

Replacing it with eq. (1.45), we have ADC $= \frac{1}{2}\sigma^2/\mathrm{b}$, and the ADC is proportional to the mean squared displacement.

The first use of this assumption goes back to the 1960s when Robertson used it to recover the signal for diffusion between two parallel planes[71]. Neumann extended this result to cylinders and spheres[72]. Later on, the GPA has been extensively used in the analysis of the diffusion MRI signal in a variety of structures.

The Gaussian phase approximation typically holds true in either the short-time or long-time limit when b-values are modest, not to accentuate kurtosis effects. In the short time limit, only a small amount of the water molecules in the vicinity of the interfaces or the outer boundaries experience restricted diffusion, and their contribution to the accumulated phase can be neglected, while the majority diffuse as in the free case. In the long time limit, all the particles have fully explored the domain.

1.3.5.3 Kärger model

Kärger model[73] is used to characterize membrane permeability in porous media using narrow pulse approximation with PGSE(δ, Δ), i.e. $\delta \ll \Delta$. It divides the domain into two compartments: (1) the intracellular space, which contains all the biological cells within a voxel, and (2) the extracellular space. The Kärger model incorporates the permeability effect through two coupled ordinary differential equations:

$$\frac{d}{dt}S_i(t) = -\gamma^2\|\mathbf{g}\|^2\delta^2 \mathsf{ADC}_i S_i(t) - \eta_i S_i(t) + \eta_e S_e(t), \tag{1.56}$$

$$\frac{d}{dt}S_e(t) = -\gamma^2\|\mathbf{g}\|^2\delta^2 \mathsf{ADC}_e S_e(t) - \eta_e S_e(t) + \eta_i S_i(t), \tag{1.57}$$

$$S_i(0) = f_i, \tag{1.58}$$

$$S_e(0) = f_e. \tag{1.59}$$

where

- S_i and S_e are intra- and extracellular signals;
- ADC_i and ADC_e are intra- and extracellular effective diffusion coefficient in the diffusion-encoding gradient direction;

- $\eta_i = \kappa|\Gamma_i|/|\Omega_i|$ and $\eta_e = \kappa|\Gamma_i|/|\Omega_e|$, with κ being the permeability, $|\Gamma_i|$ being the surface of biological cells, $|\Omega_i|$ and $|\Omega_e|$ being the intra- and extracellular volumes;
- $f_i = |\Omega_i|/|\Omega|$ and $f_e = |\Omega_e|/|\Omega|$ are intra- and extracellular volume fractions, their sum equals to 1.

The received diffusion MRI signal is the sum of the intra- and extracellular signals at T_E, given by

$$S = S_i(T_E) + S_e(T_E) = f_i' e^{-\mathrm{b}\mathcal{D}_i'} + (1 - f_i') e^{-\mathrm{b}\mathcal{D}_e'}, \tag{1.60}$$

where

$$D_{i/e}' = \frac{1}{2}\left(\mathsf{ADC}_e + \mathsf{ADC}_i + \frac{\eta_e + \eta_i}{(\gamma\|\mathbf{g}\|\delta)^2} \pm \sqrt{\left(\mathsf{ADC}_e - \mathsf{ADC}_i + \frac{\eta_e - \eta_i}{(\gamma\|\mathbf{g}\|\delta)^2}\right)^2 + \frac{4\eta_i\eta_e}{(\gamma\|\mathbf{g}\|\delta)^4}}\right), \tag{1.61}$$

$$f_i' = \frac{f_i\mathsf{ADC}_i + f_e\mathsf{ADC}_e - D_e'}{D_i' - D_e'}. \tag{1.62}$$

The accuracy of the Kärger model is to the first order of δ/Δ. In[62, 74], a modified Kärger model is proposed, which eliminates the reliance on the narrow pulse approximation and extends to the finite pulse case.

1.3.6 Numerical simulation methods

Except for some limited cases, there are no general closed form solutions of the Bloch-Torrey PDE. The predominant numerical methods to solve the BT equation include:

- Monte Carlo simulations[75–81]. As discussed in the previous subsection, the diffusion MRI can be viewed from a probabilistic perspective. Then we can compute the signals by the expectation of a functional of a stochastic process. The stochastic process can be approximated by many random walkers inside the simulation domain;
- Finite differences, finite elements[82–87]. After discretizing the simulation domain by a regular or conforming mesh, the continuous Bloch-Torrey PDE is replaced by a set of linear equations and we can numerically compute its solution on the mesh node at each time step;
- Matrix Formalism (MF) representation[70, 88–92]. The idea of the Matrix Formalism representation is to decompose the magnetization into the eigenbasis of the Laplace operator. The equation is then reduced to a system of ODEs of the time-dependent coefficients corresponding to the eigenfunctions.

Apart from them, other existing simulation methods include the Lattice Boltzmann method[93], layer potential theory (boundary element method)[94], etc. In the following subsections, we will introduce in detail the finite elements method and Matrix Formalism, and its numerical implementation, which we use in this thesis.

1.3.6.1 Finite element method

The finite element method[51, 87, 95, 96] is a powerful computational technique to numerically solve partial differential equations. It is based on the variational formulation of the equations. By multiplying a test function w, integrating over the domain Ω, and applying the Green's identity, the weak formulation of the Bloch-Torrey PDE with homogeneous Neumann boundary condition is written as[51]

$$\begin{aligned}\frac{\partial}{\partial t}\int\limits_{\bigcup_{i=1}^{N_{cmpt}}\Omega_i} M w d\mathbf{x} = &- \int\limits_{\bigcup_{i=1}^{N_{cmpt}}\Omega_i} \mathcal{D}^i \nabla M \cdot \nabla w d\mathbf{x} - \imath\gamma f(t) \int\limits_{\bigcup_{i=1}^{N_{cmpt}}\Omega_i} \mathbf{g}\cdot\mathbf{x} M w d\mathbf{x} \\ &+ \int\limits_{\bigcup_{i=1}^{N_{cmpt}}\bigcup_{j=1}^{N_{cmpt}}\Gamma_{ij}} \mathcal{D}^i \nabla M \cdot \mathbf{n} w ds_{\mathbf{x}}.\end{aligned} \tag{1.63}$$

By discretizing the simulation domain Ω by a set of regular simple geometric shapes $\{\mathcal{T}^h\}$ (called finite elements), the continuous solution of the Bloch-Torrey equation can be transformed into a discretized form M^h, which is defined on the nodes of the discretized domain. For piece-wise linear (P1) finite elements, the number of finite elements is equal to the number of nodes. Then M^h can be expanded into a finite dimensional space defined on $\{\mathcal{T}^h\}$. The standard Galerkin method uses the same functional spaces for the trial and test function, denoted by $(\varphi_i)_{i=1,\dots,N_{node}}$, where N_{node} is the number of nodes. The discretized solution is written as

$$M^h(\mathbf{x},t) = \sum_{i=1}^{N_{node}} T_i(t)\varphi_i(\mathbf{x}). \tag{1.64}$$

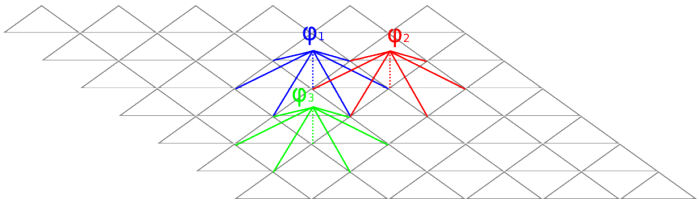

Figure 1.17: $P1$ linear function φ defined on a discretized domain $\{\mathcal{T}^h\}$ in two-dimensional space.

Replacing eq. (1.64) into eq. (1.63), one can obtain a system of the ordinary differential equations in matrix form:

$$\boldsymbol{M}\frac{d}{dt}\mathbf{T} = -(\boldsymbol{K} + \imath\gamma\boldsymbol{J} + \boldsymbol{Q})\mathbf{T}, \tag{1.65}$$

where $\mathbf{T} = [T_1, T_2, \dots, T_{N_{node}}]^T$ is the vector of time-dependent coefficients, $\boldsymbol{M}$ and $\boldsymbol{K}$ are the mass matrix and stiffness matrix in finite element literature, defined as

$$\boldsymbol{M}_{pq} = \int_\Omega \varphi_p(\mathbf{x})\varphi_q(\mathbf{x})d\mathbf{x}, \tag{1.66}$$

and

$$\boldsymbol{K}_{pq} = \begin{cases} \int_\Omega \mathcal{D}^i \nabla\varphi_p(\mathbf{x})\nabla\varphi_q(\mathbf{x})d\mathbf{x}, \ (p,q) \in \mathcal{I}_i^2, i \in \{1,\dots,N_{cmpt}\}, \\ 0, \ \text{otherwise}, \end{cases} \tag{1.67}$$

where $\mathcal{I}_i^2$ is the set of nodes index belonging to i-th compartment. $\boldsymbol{J}$ is the diffusion-encoding gradient matrix defined as

$$\boldsymbol{J}_{pq} = \int_\Omega \mathbf{g}\cdot\mathbf{x}\varphi_p(\mathbf{x})\varphi_q(\mathbf{x})d\mathbf{x}. \tag{1.68}$$

$\boldsymbol{Q}$ is the flux matrix. In order to implement the flux matrix, double nodes are placed at all the interfaces to enable the discontinuity of magnetization. When two finite elements, φ_p and φ_q, reside on the same side of an interface, their integral is positive; when on opposite sides, it is negative. We refer readers to the papers[51, 95] for the description in detail. $\boldsymbol{Q}$ is defined as

$$\boldsymbol{Q}_{pq} = \sum_{i=1}^{N_{cmpt}}\sum_{j=1}^{N_{cmpt}} \boldsymbol{Q}_{pq}^{ij}, \text{ where}$$

$$\boldsymbol{Q}_{pq}^{ij} = \begin{cases} \kappa^{ij}\int_{\Gamma_{ij}} \varphi_p(\mathbf{x})\varphi_q(\mathbf{x})d\Gamma(\mathbf{x}), & (p,q) \in \mathcal{I}_i^2, \ i \in \{1,\dots,N_{\text{cmpt}}\}, \\ \kappa^{ij}\int_{\Gamma_{ij}} \varphi_p(\mathbf{x})\varphi_q(\mathbf{x})d\Gamma(\mathbf{x}), & (p,q) \in \mathcal{I}_j^2, \ j \in \{1,\dots,N_{\text{cmpt}}\}, \\ -\kappa^{ij}\int_{\Gamma_{ij}} \varphi_p(\mathbf{x})\varphi_q(\mathbf{x})d\Gamma(\mathbf{x}), & (p,q) \in \mathcal{I}_i \times \mathcal{I}_j, \ (i,j) \in \{1,\dots,N_{\text{cmpt}}\}^2, \ i \neq j, \\ 0, & \Gamma_{ij} = \emptyset. \end{cases} \tag{1.69}$$

By applying a time discretization scheme, eq. (1.65) becomes a set of linear equations and one can obtain its discretized solution at each time step.

1.3.6.2 Matrix Formalism representation

The Matrix Formalism representation was derived twenty years ago[70, 88–90], and one recent numerical implementation of this method for irregular three-dimensional domains is proposed by[91, 92]. The idea of the Matrix Formalism representation is that on a bounded domain supplemented with Dirichlet, Neumann or Robin boundary conditions, the Laplace operator is complete[97]. This implies that the Laplace eigenbasis can represent any static function or time-dependent function at one moment on Ω. By decomposing the solution of the Bloch-Torrey PDE into this basis, one can separate the variables dependent on time from those dependent on space and reduce the equation to a system of ordinary differential equations (ODEs).

Let $\phi_k(\mathbf{x})$ and λ_k, $k = 1, \ldots$, be the L^2-normalized eigenfunctions and eigenvalues associated to the Laplace operator on Ω satisfying interface conditions and outer boundary condition above:

$$-\nabla \cdot \mathcal{D}^i \nabla \phi_k^i(\mathbf{x}) = \lambda_k \phi_k^i(\mathbf{x}), \qquad \mathbf{x} \in \Omega_i, \tag{1.70}$$

$$\mathcal{D}^i \nabla \phi_k^i(\mathbf{x}) \cdot \mathbf{n}_i(\mathbf{x}) = -\mathcal{D}^j \nabla \phi_k^j(\mathbf{x}) \cdot \mathbf{n}_j(\mathbf{x}), \mathbf{x} \in \Gamma_{ij}, \tag{1.71}$$

$$\mathcal{D}^i \nabla \phi_k^i(\mathbf{x}) \cdot \mathbf{n}_i(\mathbf{x}) = \kappa^{ij}(\phi_k^j(\mathbf{x}) - \phi_k^i(\mathbf{x})), \ \mathbf{x} \in \Gamma_{ij}, \tag{1.72}$$

$$\mathcal{D}^i \nabla \phi_k^i(\mathbf{x}) \cdot \mathbf{n}_i(\mathbf{x}) = 0, \qquad \mathbf{x} \in \Sigma_i, \tag{1.73}$$

where $\phi_k^i(\mathbf{x})$ denotes the restriction of $\phi_k(\mathbf{x})$ to compartment Ω_i for $i \in \{1, \ldots, N_{cmpt}\}$. Given these interface conditions and the outer boundary condition, all eigenvalues are real and non-negative. One remark is that this set of L^2-normalized eigenfunctions is orthogonal since the permeability coefficient is the same on both sides of interfaces. Assume that the eigenvalues are ordered in non-decreasing order:

$$0 = \lambda_1 \leq \lambda_2 \leq \lambda_3 \leq \ldots \tag{1.74}$$

Suppose that Ω is connected. If all permeability coefficients are strictly positive, then only the first eigenvalue will be zero and the corresponding eigenfunction will be the constant function on Ω. If all permeability coefficients are zero, then the first N_{cmpt} eigenvalues will be zero and there will be N_{cmpt} corresponding constant eigenfunctions supported on each compartment. We limit ourselves to these two cases, and define N_{group} as the number of constant eigenfunctions in the basis. Clearly, $N_{group} = 1$ in the former case, and $N_{group} = N_{cmpt}$ in the latter case.

When the eigenvalue is sufficiently large, over the length scale of diffusion, the oscillation of the corresponding eigenfunction will cancel itself out. Thus, we can obtain a reliable approximation of the diffusion MRI signals by using the first N_{eig} smallest eigenvalues.

Let $\boldsymbol{L}$ be the diagonal matrix containing the first N_{eig} Laplace eigenvalues:

$$\boldsymbol{L} = \text{diag}\left(\lambda_1, \lambda_2, \ldots, \lambda_{N_{eig}}\right) \in \mathbb{R}^{N_{eig} \times N_{eig}}. \tag{1.75}$$

Denote the vector of Laplace eigenfunctions corresponding to the first N_{eig} eigenvalues by

$$\Phi(\mathbf{x}) = \left(\phi_1(\mathbf{x}), \phi_2(\mathbf{x}), \ldots, \phi_{N_{eig}}(\mathbf{x})\right)^T. \tag{1.76}$$

Because $\{\phi_k(\mathbf{x})\}_{k=1,2,3,\ldots}$ is a complete basis on Ω with the correct interfaces and boundaries conditions, the magnetization $M(\mathbf{x}, t)$ can be decomposed in this basis as

$$M(\mathbf{x}, t) \approx \sum_{k=1}^{N_{eig}} T_k(t)\phi_k(\mathbf{x}) = \Phi(\mathbf{x}) \cdot \mathbf{T}(t), \tag{1.77}$$

with the time-dependent coefficient column vector

$$\mathbf{T}(t) = \left(T_1(t), T_2(t), \ldots, T_{N_{eig}}(t)\right)^T. \tag{1.78}$$

Substituting eq. (1.77) into the Bloch-Torrey equation, multiplying both sides with $\phi_l(\mathbf{x})$ and integrating over Ω gives

$$\frac{\partial}{\partial t} T_l(t) = -\lambda_l T_l(t) - \imath\gamma \sum_{k=1}^{N_{eig}} T_k(t) \int_\Omega \mathbf{g} \cdot \mathbf{x} \phi_k(\mathbf{x}) \phi_l(\mathbf{x}) d\mathbf{x}, \ l = 1, 2, \ldots, N_{eig}, \tag{1.79}$$

because of the orthogonality of the eigenbasis.

Define

$$\boldsymbol{W}(\mathbf{g}) := g_x \boldsymbol{A}^x + g_y \boldsymbol{A}^y + g_z \boldsymbol{A}^z, \tag{1.80}$$

where $\mathbf{g} = (g_x, g_y, g_z)^T$ is the diffusion-encoding gradient vector and $\boldsymbol{A}^x$, $\boldsymbol{A}^y$ and $\boldsymbol{A}^z$ are three symmetric $N_{eig} \times N_{eig}$ matrices whose entries are the first order moments in the coordinate directions of the product of pairs of eigenfunctions:

$$\boldsymbol{A}^r_{kl} := \int_{\mathbf{x}\in\Omega} r\phi_k(\mathbf{x})\phi_l(\mathbf{x})d\mathbf{x},\ (k,l) \in \{1,2,\ldots,N_{eig}\}^2,\ r \in \{x,y,z\}. \tag{1.81}$$

Then the Bloch-Torrey operator $-\nabla \cdot \mathcal{D}^i \nabla + \imath\gamma f(t)\mathbf{g}\cdot\mathbf{x}$ in the Laplace eigenfunctions basis is given by the complex-valued matrix

$$\boldsymbol{L} + \imath\gamma f(t)\boldsymbol{W}(\mathbf{g}), \tag{1.82}$$

and eq. (1.79) can be written as a system of ordinary differential equations:

$$\frac{d}{dt}\mathbf{T}(t) = -\left(\boldsymbol{L} + \imath\gamma f(t)\boldsymbol{W}(\mathbf{g})\right)\mathbf{T}(t). \tag{1.83}$$

For the PGSE sequence, define the actions of two pulses and the between-pulse by

$$\boldsymbol{H}(\mathbf{g}, f) = e^{-\delta(\boldsymbol{L}-\imath\gamma\boldsymbol{W}(\mathbf{g}))} \cdot e^{-(\Delta-\delta)\boldsymbol{L}} \cdot e^{-\delta(\boldsymbol{L}+\imath\gamma\boldsymbol{W}(\mathbf{g}))}, \tag{1.84}$$

and denote

$$\mathbf{T}(0) = \rho\left(\int_\Omega \phi_1(\mathbf{x})d\mathbf{x}, \int_\Omega \phi_2(\mathbf{x})d\mathbf{x}, \ldots, \int_\Omega \phi_{N_{eig}}(\mathbf{x})d\mathbf{x}\right)^T \in \mathbb{R}^{N_{eig},1},$$

the vector of coefficients of the initial condition projected onto the eigenfunctions of the Laplace operator, where ρ is a constant scalar. Because constant function is an eigenfunction and all eigenfunctions are L^2-orthogonal, the integral of the eigenfunctions over Ω will be zero except for the constant functions,

$$\int_\Omega \phi_i(\mathbf{x})d\mathbf{x} = \begin{cases} \sqrt{\Omega_i}, & \text{if } \phi_i(\mathbf{x}) \text{ is a constant function,} \\ 0, & \text{otherwise.} \end{cases}$$

The magnetization measured at the echo time is

$$M(\mathbf{x}, T_E) = \Phi(\mathbf{x})\boldsymbol{H}(\mathbf{g}, f)\mathbf{T}(0). \tag{1.85}$$

The signal is computed by integrating the magnetization over Ω:

$$S(\mathbf{g}, f; N_{eig}) = \int_\Omega \Phi(\mathbf{x})\boldsymbol{H}(\mathbf{g}, f)\mathbf{T}(0)d\mathbf{x}. \tag{1.86}$$

There are two benefits to using the Matrix Formalism signal representation[91]. First, once the Laplace eigendecomposition has been computed and saved, the diffusion MRI signal can be calculated for many experimental configurations at negligible additional cost. This makes it feasible to use the Matrix Formalism representation as the inner loop of optimization or parameter estimation procedures. Second, it makes explicit the link between the Laplace eigenvalues and eigenfunctions of the medium and its diffusion MRI signals. This clear link may help in the formulation of reduced models of the diffusion MRI signals.

1.3.6.3 The Numerical Matrix Formalism method

In order to numerically implement the Matrix Formalism method[91, 92], one may discretize the Laplace operator with permeable interface conditions using finite elements, for example, the $P1$ finite elements. Ω is discretized into a finite element mesh and use $P1$ basis functions $\{\varphi_p(\mathbf{x})\}_{p\in\{1,\ldots,N_{node}\}}$, where N_{node} is the number of nodes, to construct the mass, stiffness and flux matrices of finite element: $\boldsymbol{M}, \boldsymbol{K}, \boldsymbol{Q} \in \mathbb{R}^{N_{node}\times N_{node}}$. The definitions of these three matrices are given in section 1.3.6.1, eqs. (1.66), (1.67) and (1.69).

The discretized eigenfunctions of the Laplace operator with permeable interface condition in the $P1$ basis functions are expressed as

$$\phi_k(\mathbf{x}) = \sum_{n=1}^{N_{node}} \boldsymbol{P}_{n,k}\varphi_n(\mathbf{x}),\ n \in \{1,2,\ldots,N_{node}\},\ k \in \{1,\ldots,N_{eig}\}, \tag{1.87}$$

where $\boldsymbol{P} \in \mathbb{R}^{N_{node}\times N_{eig}}$, and the entry $\boldsymbol{P}_{n,k}$ is the coefficient of eigenfunction ϕ_k in the basis function φ_n.

By multiplying the $P1$ basis function on both sides of eq. (1.70), integrating over the whole domain Ω and applying the Green's identity, one can obtain the weak formulation of static Laplace's equation eqs. (1.70) to (1.73).

The finite elements discretization described above changes the continuous Laplace operator eigenvalue problem in eqs. (1.70) to (1.73) to a discrete, generalized matrix eigenvalues problem: Find the first N_{eig} eigenvalues $\lambda_1, \lambda_2, \ldots, \lambda_{N_{eig}}$ and corresponding eigenfunctions $\boldsymbol{P}$, such that

$$(\boldsymbol{K} + \boldsymbol{Q})\boldsymbol{P} = \boldsymbol{M}\boldsymbol{P}\boldsymbol{L}, \tag{1.88}$$

where $\boldsymbol{L} = \text{diag}\left(\lambda_1, \lambda_2, \ldots, \lambda_{N_{eig}}\right) \in \mathbb{R}^{N_{eig}\times N_{eig}}$ is a diagonal matrix whose diagonal terms are eigenvalues of Laplace operator with permeable interface conditions.

The integrals of the finite element discretized eigenfunctions are given by

$$\int_\Omega \Phi(\mathbf{x})d\mathbf{x} = \boldsymbol{P}^T\boldsymbol{M}\mathbf{1}_{N_{node},1}, \tag{1.89}$$

where $\mathbf{1}_{N_{node},1}$ is column vector of all ones with size N_{node} and

$$\mathbf{T}(0) = \rho\int_\Omega \Phi(\mathbf{x})d\mathbf{x} = \rho\boldsymbol{P}^T\boldsymbol{M}\mathbf{1}_{N_{node},1} = \left[\sqrt{\Omega_1}, \ldots \sqrt{\Omega_{N_{group}}}, 0, \ldots, 0\right]^T \in \mathbb{R}^{N_{eig},1}, \tag{1.90}$$

where N_{group} is the number of constant eigenfunctions.

Similarly, with this discretization, the matrices $\boldsymbol{A}^x$,$\boldsymbol{A}^y$ and $\boldsymbol{A}^z$ in eq. (1.81) can be rewritten as

$$\boldsymbol{A}^r = \boldsymbol{P}^T\boldsymbol{J}^r\boldsymbol{P},\ r \in \{x,y,z\}, \tag{1.91}$$

where the entries of $\boldsymbol{J}^r$ are

$$\boldsymbol{J}^r_{kl} = \int_\Omega r\varphi_k\varphi_l d\mathbf{x},\ r \in \{x,y,z\}. \tag{1.92}$$

Define

$$\boldsymbol{J}(\mathbf{g}) \equiv \mathbf{g}_x\boldsymbol{J}^x + \mathbf{g}_y\boldsymbol{J}^y + \mathbf{g}_z\boldsymbol{J}^z \in \mathbb{R}^{N_{node},N_{node}}, \tag{1.93}$$

$\boldsymbol{W}(\mathbf{g})$ can be rewritten as

$$\boldsymbol{W}(\mathbf{g}) = \sum_{r=\{x,y,z\}} g_r\boldsymbol{A}^r = \sum_{r=\{x,y,z\}} g_r\boldsymbol{P}^T\boldsymbol{J}^r\boldsymbol{P} = \boldsymbol{P}^T\boldsymbol{J}(\mathbf{g})\boldsymbol{P}. \tag{1.94}$$

Substituting $\boldsymbol{L}$, $\boldsymbol{P}$ and $\boldsymbol{J}(\mathbf{g})$ into $\boldsymbol{H}(\mathbf{g}, f)$:

$$\boldsymbol{H}(\mathbf{g}, f) = e^{-\delta(\boldsymbol{L}-\imath\gamma\boldsymbol{W}(\mathbf{g}))} \cdot e^{-(\Delta-\delta)\boldsymbol{L}} \cdot e^{-\delta(\boldsymbol{L}+\imath\gamma\boldsymbol{W}(\mathbf{g}))}. \tag{1.95}$$

The Numerical Matrix Formalism diffusion MRI signal at echo time is the following:

$$\begin{aligned} S^{\text{NMF}}(\mathbf{g}, f; N_{eig}) &= \rho\left(\mathbf{1}^T_{N_{node},1}\boldsymbol{M}\boldsymbol{P}\right)\boldsymbol{H}(\mathbf{g}, f)\left(\boldsymbol{P}^T\boldsymbol{M}\mathbf{1}_{N_{node},1}\right) \\ &= \rho\,\mathbf{T}(0)^T\boldsymbol{H}(\mathbf{g}, f)\mathbf{T}(0). \end{aligned} \tag{1.96}$$

When $N_{eig} = N_{node}$, the full set of discretized eigenfunctions will be used to compute the diffusion MRI signal. In practice, the eigenfunctions associated with large eigenvalues oscillate significantly and have little contribution to the physics of diffusion. Using the eigenfunctions whose spatial scales are on the order of the cell structure and the diffusion distance can yield a good approximation, and result in a $N_{eig} \ll N_{node}$.

When computing the diffusion MRI signal from the Numerical Matrix Formalism method, N_{eig} is not chosen arbitrarily. Rather, a length scale cut-off L_s will be introduced, that is appropriate for the geometry and for the MRI experiment. For realistic MRI experimental parameters and brain cell geometries, the smallest length scale that can influence the diffusion MRI signal is around 1 μm, comparable to the microstructure length/gradient length. Details about the Numerical Matrix Formalism method and how to choose the length scale cut-off refer to the works[91, 92]. To translate the eigenvalues λ into length scales, one can use the expression

$$l(\lambda) = \begin{cases} \infty, & \lambda = 0, \\ \pi\sqrt{/D_{ave}/\lambda}, & \lambda > 0, \end{cases} \tag{1.97}$$

where $/D_{ave}/$ is the volume averaged diffusion coefficient. Typically, $l(\lambda)$ is related to the wavelength of the oscillations in the corresponding eigenfunction. The number N_{eig} associated with this length scale choice is determined by the relation

$$\infty \geq l(\lambda_1) \geq \cdots \geq l(\lambda_{N_{eig}}) \geq L_s > l(\lambda_{N_{eig}+1}) \geq \cdots > 0. \tag{1.98}$$

Thus, N_{eig} or L_s are used interchangeably to indicate the truncation of the eigenfunctions for Numerical Matrix Formalism.

Remark 1. *It is to be noted that for the same geometry and the same L_s, when using the Numerical Matrix Formalism method, the resulting N_{eig} is smaller at higher permeability.*

Remark 2. *Even though eigendecomposition routines can accept an eigenvalue range (length scale cut-off) as input, it is more computationally efficient to input the number of desired eigenvalues and then keep those eigenvalues within the length scale cut-off. This is what the SpinDoctor do in practice to compute a subset of eigenfunctions.*

1.4 Diffusion MRI compartment signal models for microstructural imaging

Because the relationship between diffusion MRI signals and underlying tissue morphology, such as neurites orientation, volume fractions, neurons size etc., is not yet fully understood, microstructural imaging until now primarily relies on the concept of "compartmentalization"[3]. This idea suggests that the diffusion MRI signal from one voxel can be viewed as a sum of signal contributions from different compartments. These compartments can be effectively modeled by parameterized, simplified shapes, which have straightforward signal expressions under some assumptions. The parameters of these simplified shapes correspond to morphological parameters. By fitting the signals, one can identify the optimal combinations of these parameters, corresponding to the estimates of tissue morphology.

Here, we describe four state-of-the-art diffusion MRI compartment signal models used for the brain white matter and the brain gray matter microstructural imaging: Neurite Orientation Dispersion and Density Imaging (NODDI)[98], Axon diameter and density estimation (ActiveAx)[99], Soma and Neurite Density Imaging (SANDI)[28] and Neurite Exchange Imaging (NEXI)[100]. NODDI is designed for both the brain white and gray matter imaging. ActiveAx is designed for the brain white matter imaging. SANDI and NEXI are designed for the brain gray matter imaging.

1.4.1 NODDI

The NODDI model[98] is an advanced diffusion imaging technique developed to estimate the volume fraction of neurites and the dispersion of neurites orientations in the brain white matter on clinical MRI scanners. In the brain white matter, the primary component is axons, and somas are often neglected due to a relatively low volume fraction[66, 101], Based on this fact, the NODDI model assumes that (1) the brain white matter can be represented by three types of microstructural environment: intra-cellular space, extra-cellular space and cerebralspinal fluid and (2) there is no water exchange between them and the water diffusion is within the environment.

The normalized voxel signals by volume can be expressed as the sum of signals from each compartment:

$$S_{\text{NODDI}} = f_{\text{in}} S_{\text{in}} + f_{\text{ex}} S_{\text{ex}} + f_{\text{CSF}} S_{\text{CSF}}, \tag{1.99}$$

where f_{in}, f_{ex} and f_{CSF} are the volume fraction of each compartment and the sum equals to 1.

The intra-cellular space is modeled by a collection of orientation-dispersed sticks , i.e., infinity long cylinders of zero radius. The diffusion only occurs in the axial direction of the cylinders and satisfies the free diffusion assumption. S_{in} is given by

$$S_{\text{in}} = \int_{\|\mathbf{n}\|=1} p(\mathbf{n}) e^{-\text{b}\mathcal{D}_0(\mathbf{u_g}\cdot\mathbf{n})^2} d\mathbf{n}, \tag{1.100}$$

where $\mathbf{n}$ is the axial direction of the sticks, $\mathbf{u_g}$ is the gradient direction, b is the b-values, $\mathcal{D}_0$ is the intrinsic diffusion coefficient and $p(\mathbf{n})$ is the distribution of sticks orientation. In the original NODDI paper, $\mathcal{D}_0$ is fixed to 1.7×10^{-3} s/mm^2, estimated from corpus callosum, and $p(\mathbf{n})$ is modeled with a Watson distribution[102]:

$$p(\mathbf{n}) = M\left(\frac{1}{2}, \frac{3}{2}, \kappa\right)^{-1} e^{\kappa(\boldsymbol{\mu}\cdot\mathbf{n})^2}, \tag{1.101}$$

where M is a confluent hypergeometric function, $\boldsymbol{\mu}$ is a unit vector, representing the mean orientation, and κ is the concentration parameter measuring the extent of orientation dispersion about $\boldsymbol{\mu}$.

The extra-cellular space is modeled as an anisotropic Gaussian diffusion compartment and its signals is expressed as:

$$S_{\text{ex}} = \exp\left(-\text{b}\int_{\|\mathbf{n}\|=1} p(\mathbf{n})\left(\mathcal{D}_0(\mathbf{u_g}\cdot\mathbf{n})^2 + \mathcal{D}_\perp(1-(\mathbf{u_g}\cdot\mathbf{n})^2)\right) d\mathbf{n}\right), \tag{1.102}$$

where $\mathcal{D}_\perp$ is the diffusion coefficient perpendicular to the axial direction. $\mathcal{D}_\perp$ is set with a simple tortuosity model[103]

$$\mathcal{D}_\perp = \frac{f_{\text{ex}}}{f_{\text{in}} + f_{\text{ex}}} \mathcal{D}_0. \tag{1.103}$$

The CSF is modeled as a free diffusion compartment[104]:

$$S_{\text{CSF}} = e^{-\text{b}\mathcal{D}_{\text{CSF}}}, \tag{1.104}$$

where $\mathcal{D}_{\text{CSF}}$ is the diffusion coefficient of CSF. In the original NODDI paper, this coefficient is set to a fixed value 3×10^{-3} s/mm^2, corresponding to estimated value of free water diffusion at the body temperature.

The complete set of parameters includes 5 independent parameters: $\mathbf{p} = [f_{\text{in}}, f_{\text{CSF}}, \kappa, \boldsymbol{\mu}]^T$. By fitting the directional diffusion MRI signals in various gradient directions with multiple b-values (multiple shells of high-angular-resolution diffusion imaging),

$$\arg\min_{\mathbf{p}} \|S_{\text{measure}} - S_{\text{NODDI}}(\mathbf{p})\|_2,$$

NODDI can give estimated values of the volume fractions and the orientation dispersion distribution. In practice, a Rician loss is added to account for the noise. The orientation dispersion (OD) index is defined as

$$\text{OD} = \frac{2}{\pi}\arctan(1/\kappa). \tag{1.105}$$

1.4.2 ActiveAx

The ActiveAx[99] is another the brain white matter diffusion MRI compartment signal model, which focuses on the orientationally invariant indices of axon diameter and volume fractions. This model is based on the Gaussian phase approximation with PGSE sequence PGSE(δ, Δ). For *in vivo* imaging, it divides the voxel into three compartments: intra-axonal space, extra-axonal space and CSF. The normalized voxel signals is expressed as:

$$S_{\text{ActiveAx}} = f_{\text{in}} S_{\text{in}} + f_{\text{ex}} S_{\text{ex}} + f_{\text{CSF}} S_{\text{CSF}}, \tag{1.106}$$

where f_{in}, f_{ex} and f_{CSF} are the volume fraction of each compartment and the sum equals to 1.

The intra-axonal space is modeled by a bundle of parallel infinity long straight cylinders with equal radius R_{cyl}, and whose axial direction is set to $\mathbf{n}$. S_{in} is formulated under Gaussian phase approximation[72, 105]:

$$S_{\text{in}} = e^{-\text{b}\left(\mathcal{D}_0(\mathbf{u_g}\cdot\mathbf{n})^2 + 2c_{\text{cyl}}(1-(\mathbf{u_g}\cdot\mathbf{n})^2)/((\Delta-\delta/3)\delta^2)\right)}, \tag{1.107}$$

where $\mathcal{D}_0$ is the intrinsic diffusion coefficient, $\mathbf{u_g}$ is the gradient direction, and c_{cyl} is a coefficient depending on R_{cyl}, time profile and $\mathcal{D}_0$:

$$c_{\text{cyl}} = \sum_{m=1}^{\infty} \frac{2\mathcal{D}_0\alpha_m^2\delta - 2 + 2e^{-\mathcal{D}_0\alpha_m^2\delta} + 2e^{-\mathcal{D}_0\alpha_m^2\Delta} - e^{-\mathcal{D}_0\alpha_m^2(\Delta-\delta)} - e^{-\mathcal{D}_0\alpha_m^2(\Delta+\delta)}}{\mathcal{D}_0^2\alpha_m^6(R_{\text{cyl}}^2\alpha_m^2 - 1)}, \tag{1.108}$$

where α_m is the m-th root of

$$J_1'(\alpha_m R_{\text{cyl}}) = 0, \tag{1.109}$$

with $J_1'(\cdot)$ is the derivative of the Bessel function fo the first kind, order one.

Similar to NODDI, the extra-axonal space is modeled as an anisotropic Gaussian diffusion compartment and CSF is modeled as an isotropic Gaussian diffusion compartment:

$$S_{\text{ex}} = e^{-\text{b}(\mathcal{D}_0(\mathbf{u_g}\cdot\mathbf{n})^2 + \mathcal{D}_\perp(1-(\mathbf{u_g}\cdot\mathbf{n})^2))}, \tag{1.110}$$

$$S_{\text{CSF}} = e^{-\text{b}\mathcal{D}_{\text{CSF}}}. \tag{1.111}$$

The extra-axonal space is set to align with the intra-axonal space. $\mathcal{D}_\perp$ has the same expression as eq. (1.103) and $\mathcal{D}_{\text{CSF}}$ is also fixed to 3×10^{-3} s/mm^2

In practice, $\mathbf{n}$ is usually set to align with the principal direction of the best fit diffusion tensor, to simplify the fitting process. Therefore, the full set of independent parameters is $\mathbf{p} = [f_{\text{in}}, f_{\text{CSF}}, R_{\text{cyl}}]^T$. By fitting the directional signals, one can retrieve the indices of axon radius R_{cyl} and volume fractions.

1.4.3 SANDI

The SANDI model[28] is motivated by the deviation of the $1/\sqrt{\text{b}}$ power-law scaling observed in the brain gray matter. Morphologically, one key difference between the brain gray matter and the brain white matter is that the volume fraction of the soma in the brain gray matter is substantial. Thus, SANDI suggests this deviation is because the diffusion within the soma cannot be categorized as either anisotropic Gaussian diffusion or isotropic Gaussian diffusion. SANDI introduces a new compartment and models the brain gray matter as three separate compartments: intra-soma space, intra-neurite space, and extra-cellular space. The SANDI model is based on the Gaussian phase approximation as well. Unlike previous two models, SANDI model deals with the direction-averaged signal, i.e., $\overline{S} = \int_{\|\mathbf{u_g}\|=1} S(\mathbf{u_g}) d\mathbf{u_g}$. Its signal expression is

$$\overline{S}_{\text{SANDI}} = f_{\text{soma}}\overline{S}_{\text{soma}} + f_{\text{neurite}}\overline{S}_{\text{neurite}} + f_{\text{ECS}}\overline{S}_{\text{ECS}}, \tag{1.112}$$

where $f_{\text{soma}} + f_{\text{neurite}} + f_{\text{ECS}} = 1$.

The intra-soma space is modeled as one sphere of radius R_{sphere} and $\overline{S}_{\text{soma}}$ is computed under Gaussian phase approximation with PGSE(δ, Δ)[72, 106]:

$$\overline{S}_{\text{soma}} = e^{-2c_{\text{sphere}}\text{b}/((\Delta-\delta/3)\delta^2\mathcal{D}_0)}, \tag{1.113}$$

where $\mathcal{D}_0$ is the intrinsic diffusion coefficient and c_{sphere} is a coefficient depending on R_{sphere}, time profile and $\mathcal{D}_0$:

$$c_{\text{sphere}} = \sum_{m=1}^{\infty} \frac{\alpha_m^{-4}}{\alpha_m^2 R^2 - 2}\left[2\delta - \frac{2 + e^{-\alpha_m^2 D_0(\Delta-\delta)} - 2(e^{-\alpha_m^2\mathcal{D}_0\delta} + e^{-\alpha_m^2\mathcal{D}_0\Delta}) + e^{-\alpha_m^2\mathcal{D}_0(\Delta+\delta)}}{\alpha_m^2\mathcal{D}_0}\right], \tag{1.114}$$

where α_m is the m-th root of

$$\alpha_m R_{\text{sphere}} J'_{3/2}\left(\alpha_m R_{\text{sphere}}\right) - \frac{1}{2} J_{3/2}\left(\alpha_m R_{\text{sphere}}\right) = 0, \tag{1.115}$$

$J_{3/2}(\cdot)$ is the Bessel function of the first kind and $J'_{3/2}(\cdot)$ is its derivative.

The intra-neurite space is modeled as a bundle of sticks, similar to NODDI. After taking the average over diffusion-encoding gradient directions, $\overline{S}_{\text{neurite}}$ is given by:

$$\overline{S}_{\text{neurite}} = \sqrt{\frac{\pi}{4\mathsf{b}\mathcal{D}_{\text{neurite}}}} erf(\sqrt{\mathsf{b}\mathcal{D}_{\text{neurite}}}), \tag{1.116}$$

where $\mathcal{D}_{\text{neurite}}$ is the longitudinal diffusion coefficient inside the sticks.

The extra-cellular space is modeled as an isotropic Gaussian diffusion compartment:

$$\overline{S}_{\text{ECS}} = e^{-\mathsf{b}\mathcal{D}_{\text{ECS}}}, \tag{1.117}$$

where $\mathcal{D}_{\text{ECS}}$ is the scalar effective diffusion constant inside ECS.

The complete set of independent parameters is $\mathbf{p} = [f_{\text{soma}}, f_{\text{neurite}}, f_{\text{ECS}}, R_{\text{sphere}}, \mathcal{D}_{\text{neurite}}, \mathcal{D}_{\text{ECS}}]^T$. By fitting the SANDI model to measured direction-averaged signals, one can retrieve the volume fractions and an apparent soma radius in gray matter.

1.4.4 NEXI

The NEXI model[100] is a two-exchange compartment model for volume fractions and water exchange rate imaging in the brain gray matter. In the brain gray matter, under typical clinical experimental settings, water exchange across the neurite membrane is significant. It extends the classical the brain white matter diffusion MRI compartment signal models by accounting for water exchange between compartments. The water exchange process is described using the Kärger model under the narrow pulse approximation.

NEXI proposes that signals within a voxel arise from contributions of two compartments: (1) The intra-neurite compartment, represented as a bundle of sticks where diffusion occurs only in parallel direction (denoted by $\mathbf{n}$), characterized by $D_{i,\parallel}$; (2) the extra-neurite compartment, represented as an anisotropic Gaussian diffusion compartment, characterized by parallel and perpendicular diffusion coefficients $D_{e,\parallel}$ and $D_{e,\perp}$. The NEXI model deals with the direction-averaged signal as well. It assumes that the direction-averaged signal is expressed as:

$$\overline{S} = \int_{\|\mathbf{u_g}\|=1} \mathcal{K}(\mathbf{u_g}, b) d\mathbf{u_g}, \tag{1.118}$$

where $\mathcal{K}(\mathbf{u_g}, b)$ is the signal attenuation, which is given by

$$\mathcal{K}(\mathbf{u_g}, \mathsf{b}) = f' e^{-\mathsf{b}D'_i} + (1 - f')\, e^{-\mathsf{b}D'_e}. \tag{1.119}$$

with

$$f' = \frac{1}{D'_i - D'_e}(fD_i + (1-f)D_e - D'_e), \tag{1.120}$$

$$D'_{i/e} = \frac{1}{2}\left\{ D_i + D_e + \frac{1}{(t_{ex}/\Delta)\mathsf{b}} \mp \left[\left[D_e - D_i + \frac{2f-1}{(t_{ex}/\Delta)\mathsf{b}} \right]^2 + \frac{4f(1-f)}{((t_{ex}/\Delta)b)^2} \right]^{\frac{1}{2}} \right\}, \tag{1.121}$$

$$D_i \equiv D_{i,\parallel}(\mathbf{u_g} \cdot \mathbf{n})^2 \tag{1.122}$$

$$D_e \equiv D_{e,\parallel}(\mathbf{u_g} \cdot \mathbf{n})^2 + D_{e,\perp}(1 - (\mathbf{u_g} \cdot \mathbf{n})^2). \tag{1.123}$$

The independent parameters of NEXI are $\mathbf{p} = [f, D_{i,\parallel}, D_{e,\parallel}, D_{e,\perp}, t_{ex}]^T$, where f is the volume fraction of intra-neurite space and t_{ex} is a temporal quantity to characterize the water exchange rate.

Chapter 2

Permeable Matrix Formalism Representation using impermeable Laplace eigenfunctions

Contents

Chapter Overview

In this chapter, we present a novel approach to represent the diffusion MRI signals from a permeable medium using impermeable Laplace eigenfunctions. This idea is inspired by how the paper[97] treats surface relaxation. We derive our new method from the Numerical Matrix Formalism method. Our new method decomposes the transverse magnetization onto the impermeable Laplace eigenfunctions and treats the permeability separately during the signals computation process. Thus it requires only a single eigendecomposition on the impermeable configuration and re-uses the same Laplace eigenfunctions to compute the permeable signals, whereas the Numerical Matrix Formalism method necessitates re-running this process for each permeability value. The new method serves as a fast simulation approach when adjusting the membranes permeability values, which is beneficial for evaluating diffusion MRI compartment signal models or signal behaviors and designing microstructure estimation approaches that account for permeability.

We first present our new formulation using impermeable Laplace eigenfunctions and prove the equivalence between our new formulation and the Numerical Matrix Formalism method in the case that the full set of discretized eigenfunctions is used. We validate our method through simulations. When employing a partial eigendecomposition, at lower permeability values ($\kappa = 10^{-5}$ m/s), the relative errors of our new method are at the same level as the Numerical Matrix Formalism method. As the permeability increases, the relative errors by the new method using a partial set of discretized eigenfunctions (with the length scale cut-off $L_s = 1\mu$m) will increase accordingly but remain within

a reasonable range (less than $< 1\%$). We evaluate the computational efficiency of our new formulation in comparison to the Numerical Matrix Formalism method. In the signal computation step, the computational time for the new method is close to that of the Numerical Matrix Formalism method, but most importantly, the new method offers significant time savings during the eigendecomposition step.

To demonstrate the potential capabilities of our new method in studying the effects of permeability, we conduct a numerical analysis in a porous medium of the impact of permeability on (1) the diffusion MRI signals and (2) the ADC in the long time limit. The analysis suggests that:

1. The diffusion MRI signal has a mono-exponential relationship with permeability across a wide range of values ($10^{-6}\,\mathrm{m/s} \leq \kappa \leq 10^{-4}\,\mathrm{m/s}$), covering typical permeability values found in biological cells;

2. For a fixed PGSE sequenve, at low gradient strength, the impact of permeability is negligible. However, at high gradient strength, even a small permeability value would alter the diffusion MRI signals;

3. With high permeability, the dominant term of the long time limit ADC is $t^{-0.5}$, where t is diffusion time;

4. At low and high permeabilities, the long time limit ADC shows different rates of dependence on permeability.

Moreover, we evaluate a state-of-the-art diffusion MRI compartment signal model accounting for permeable membranes, the NEXI model, using the new method. To avoid falling into the local minimum, the NEXI model is fitted by an exhaustive search. The result indicates that the water exchange time of NEXI is correlated to permeability in a wide range ($10^{-6}\,\mathrm{m/s} \leq \kappa \leq 2 \times 10^{-5}\,\mathrm{m/s}$).

This work contributes to (1) fast numerical simulations accounting for permeability, (2) numerical studies on permeability effects in complicated geometries, (3) microstructural imaging model evaluation.

Compared to the published version[1], I incorporate two additional subsections: (1) Section 2.4.2 applies the new formulation to analyze the impact of permeability on the time-dependent ADC in the long time limit; (2) Section 2.4.3 uses simulated signals by our new method, to fit the NEXI model, showing the correlation between permeability and the water exchange time of NEXI.

2.1 Introduction

Probing cell membrane permeability using diffusion MRI is of research and clinical interest [59, 107, 108]. Additionally, cell membrane permeability can influence the interpretation of microstructure imaging. As discussed in the previous chapter, many diffusion MRI compartment signal models currently in use assume negligible water exchange between compartments, the validity of which remains unknown. Ignoring permeability effects could make micro-structural estimation hard to interpret. For example, a recent work[100] pointed out that ignoring permeability may under-estimate neurite volume fraction even at short diffusion times. Therefore, understanding this mechanism is vital for improving microstructure estimation. Some recent works in the diffusion MRI literature on tissue micro-structural estimation have begun to take cell membrane permeability into account, and have attempted to determine the permeability value using diffusion MRI data[59, 100, 109, 110].

In order to estimate the permeability coefficient from diffusion MRI data and validate diffusion MRI signal models, it is desirable that the Bloch Torrey PDE can be calculated efficiently for many values of membrane permeability. For simple geometries such as circles, spheres, plates, or one dimensional segments, analytical expressions of the diffusion MRI signal exist. The permeability effect is taken into account by a transition matrix[111] or the Kärger model[100] which is a two-compartment exchange approximation model. These analytical expressions have been used to estimate tissue micro-structure and interface permeability[59, 112]. However, for more complex and realistic cellular geometries, there are no explicit analytical expressions available and numerical simulations are needed.

The objective of this chapter is to develop a new approach, that facilitates the simulations when adjusting the membrane permeability value.

If only a small number of simulations are needed, the three main groups of approaches are (1) Monte Carlo/Random Walk simulations[78, 80, 81, 113, 114], (2) solving the discretized Bloch Torrey PDE[50, 86, 95, 115] and (3) spectral method, called the Matrix Formalism representation[70, 89, 90], as detailed in the preceding chapter in section 1.3.6. Monte Carlo simulation uses random walkers to mimic the diffusion process during a diffusion MRI experiment. It randomly places a large number of spins inside the complex geometry, and let them move according to the diffusion dynamics. To incorporate permeable membranes, the water exchange through interfaces is modeled via a transit probability P_{trans}, which is the probability that spins will either cross or reflect when they arrive at a permeable interface[116–119]. However, as the permeability increases, the time steps must become smaller (see the reasoning in the paper[116, 119]) to obtain the condition $P_{\text{trans}} \ll 1$ which results in a high demand of computational resources and computer memory. The discretization of the Bloch Torrey PDE can be used to directly solve for the magnetization in a geometrical configuration. The computational domain is discretized either by finite elements[50, 115, 120] or finite differences[86]. Since it deals with a deterministic equation, incorporating the permeability is straightforward. The details of finite element method implementation with permeability interfaces condition can be found in section 1.3.6.1.

In a recent work, Agdestein *et al.* presented a numerical implementation of the Matrix Formalism for permeable interfaces[92], called the Numerical Matrix Formalism method, where the permeability interface conditions are incorporated in the Laplace eigendecomposition step.

In this chapter, we aim to extend this work and present a new formulation, where the diffusion MRI signal of a permeable medium is computed using only impermeable Laplace eigenfunctions. We prove that the new method produces the same diffusion MRI signal as the original Numerical Matrix Formalism method, under the condition that the full set of eigenfunctions is used. We show the numerical convergence of the new method when the number of eigenfunctions used is much smaller than the full set. We also show the improved computational efficiency of the new method if simulations using many permeability coefficients are needed. Our approach means that the same basis (the impermeable set) can be used for all permeability values, which reduces the computational time significantly, enabling the study of the effects of the permeability coefficient on the diffusion MRI signal in the future.

2.2 New formulation using the impermeable Laplace eigenfunctions

In this section, we use the same geometry configuration as described in section 1.3.1 and the Numerical Matrix Formalism refers to section 1.3.6.3.

For the sake of simplicity, we use the PGSE sequence in this chapter to demonstrate the equivalence of our new method with Matrix Formalism. However, extending the results to other types of sequences is straightforward.

The main objective of this work is to derive a new formulation of the Numerical Matrix Formalism method for permeable interfaces, using the eigenvalues and eigenfunctions of Laplace operator from the impermeable case.

Suppose that all the interfaces are impermeable, then the discretized Laplace eigenvalues problem in eq. (1.88) becomes:

$$\boldsymbol{K}\boldsymbol{P}_{\text{imp}} = \boldsymbol{M}\boldsymbol{P}_{\text{imp}}\boldsymbol{L}_{\text{imp}}. \tag{2.1}$$

The subscript 'imp' indicates these matrices are from the impermeable case. We now want to use these two matrices $\boldsymbol{L}_{\text{imp}}$ and $\boldsymbol{P}_{\text{imp}}$ as well as

$$\boldsymbol{W}_{\text{imp}}(\mathbf{g}) \equiv g_x \boldsymbol{P}_{\text{imp}}^T \boldsymbol{J}^x \boldsymbol{P}_{\text{imp}} + g_y \boldsymbol{P}_{\text{imp}}^T \boldsymbol{J}^y \boldsymbol{P}_{\text{imp}} + g_z \boldsymbol{P}_{\text{imp}}^T \boldsymbol{J}^z \boldsymbol{P}_{\text{imp}} \tag{2.2}$$

$$= \boldsymbol{P}_{\text{imp}}^T \boldsymbol{J}(\mathbf{g}) \boldsymbol{P}_{\text{imp}}, \tag{2.3}$$

to obtain the diffusion MRI signal in the presence of permeable interfaces.

Assume that for $i \neq j, (i,j) \in \{1, \ldots, N_{cmpt}\}^2$, the interfaces are permeable: $\kappa_{ij} > 0$, and denoting the corresponding flux matrix by $\boldsymbol{Q}$. We recall that the flux matrix $\boldsymbol{Q}$ for the permeable case is defined by eq. (1.69). We define a new matrix,

$$\boldsymbol{Q}_{proj} \equiv \boldsymbol{P}_{\text{imp}}^T \boldsymbol{Q} \boldsymbol{P}_{\text{imp}} \in \mathbb{R}^{N_{eig}, N_{eig}}, \tag{2.4}$$

the projection of the flux matrix onto the eigenfunctions of the Laplace operator with impermeable interface conditions. Adding $\boldsymbol{Q}_{proj}$ to the diagonal matrix $\boldsymbol{L}_{\text{imp}}$, we define a new matrix (in general not diagonal)

$$\boldsymbol{L}_{proj} \equiv \boldsymbol{L}_{\text{imp}} + \boldsymbol{Q}_{proj},$$

as well as

$$\boldsymbol{H}_{proj}(\mathbf{g}, f) \equiv e^{-\delta\left(\boldsymbol{L}_{proj} - \imath\gamma \boldsymbol{W}_{\text{imp}}(\mathbf{g})\right)} \cdot e^{-(\Delta-\delta)\boldsymbol{L}_{proj}} \cdot e^{-\delta\left(\boldsymbol{L}_{proj} + \imath\gamma \boldsymbol{W}_{\text{imp}}(\mathbf{g})\right)}. \tag{2.5}$$

Theorem 1. *In the presence of permeable interfaces, the expression*

$$\begin{aligned} S^{NEW}(\mathbf{g}, f; N_{eig}) &\equiv \rho(\mathbf{1}_{N_{node},1}^T \boldsymbol{M} \boldsymbol{P}_{imp}) \boldsymbol{H}_{proj}(\mathbf{g}, f) (\boldsymbol{P}_{imp}^T \boldsymbol{M} \mathbf{1}_{N_{node},1}) \\ &= \rho \mathbf{T}_{imp}(0)^T \boldsymbol{H}_{proj}(\mathbf{g}, f) \mathbf{T}_{imp}(0), \end{aligned} \tag{2.6}$$

where

$$\mathbf{T}_{imp}(0) = \left[\sqrt{|\Omega_1|}, \sqrt{|\Omega_2|}, \ldots, \sqrt{|\Omega_{N_{cmpt}}|}, 0, \ldots, 0\right]^T \in \mathbb{R}^{N_{eig},1}, \tag{2.7}$$

is exactly equal to the diffusion MRI signal expression from the Numerical Matrix Formalism method, if the full set of the eigenvalues and eigenfunctions is used for both methods.

Proof. For a permeability matrix $\boldsymbol{Q} \in \mathbb{R}^{N_{node},N_{node}}$, let $\boldsymbol{L}_{\text{per}} \in \mathbb{R}^{N_{eig},N_{eig}}$ and $\boldsymbol{P}_{\text{per}} \in \mathbb{R}^{N_{node},N_{eig}}$ be the eigenvalues matrix and the eigenfunctions matrix, respectively,

$$(\boldsymbol{K} + \boldsymbol{Q})\boldsymbol{P}_{\text{per}} = \boldsymbol{M}\boldsymbol{P}_{\text{per}}\boldsymbol{L}_{\text{per}}. \tag{2.8}$$

The subscript 'per' indicates these matrices are from permeable case. Then the H matrix for the permeable case is

$$\boldsymbol{H}_{\text{per}}(\mathbf{g}, f) \equiv e^{-\delta(\boldsymbol{L}_{\text{per}} - \imath\gamma \boldsymbol{W}_{\text{per}}(\mathbf{g}))} e^{-(\Delta-\delta)\boldsymbol{L}_{\text{per}}} e^{-\delta(\boldsymbol{L}_{\text{per}} + \imath\gamma \boldsymbol{W}_{\text{per}}(\mathbf{g}))}, \tag{2.9}$$

where

$$\boldsymbol{W}_{\text{per}}(\mathbf{g}) = \boldsymbol{P}_{\text{per}}^T \boldsymbol{J}(\mathbf{g}) \boldsymbol{P}_{\text{per}},$$

and the signal is

$$S^{\text{NMF}}(\mathbf{g}, f; N_{eig}) = \left(\mathbf{1}_{N_{node},1}^T \boldsymbol{M} \boldsymbol{P}_{\text{per}}\right) \boldsymbol{H}_{\text{per}}(\mathbf{g}, f) \left(\boldsymbol{P}_{\text{per}}^T \boldsymbol{M} \mathbf{1}_{N_{node},1}\right) \rho. \tag{2.10}$$

We recall that all the eigenfunctions are L^2-normalized and orthogonal, so that

$$\boldsymbol{P}_{\text{imp}}^T M \boldsymbol{P}_{\text{imp}} = I_{N_{eig}}, \tag{2.11}$$

$$\boldsymbol{P}_{\text{per}}^T M \boldsymbol{P}_{\text{per}} = I_{N_{eig}}, \tag{2.12}$$

where $I_{N_{eig}}$ is the identity matrix, thus, multiplying $\boldsymbol{P}_{\text{imp}}^T$ on both sides of eq. (2.1) and $\boldsymbol{P}_{\text{per}}^T$ on both sides of eq. (2.8) gives

$$\boldsymbol{L}_{\text{imp}} = \boldsymbol{P}_{\text{imp}}^T \boldsymbol{K} \boldsymbol{P}_{\text{imp}}, \tag{2.13}$$

$$\boldsymbol{L}_{\text{per}} = \boldsymbol{P}_{\text{per}}^T (\boldsymbol{K} + \boldsymbol{Q}_{\text{per}}) \boldsymbol{P}_{\text{per}}. \tag{2.14}$$

We define a new matrix $\boldsymbol{C} \in \mathbb{R}^{N_{eig},N_{eig}}$, projecting the permeable Laplace eigenfunctions onto the impermeable Laplace eigenfunctions:

$$\boldsymbol{C} \equiv \boldsymbol{P}_{\text{imp}}^T M \boldsymbol{P}_{\text{per}}. \tag{2.15}$$

Knowing that the mass matrix $\boldsymbol{M}$ is real, symmetric and positive-definite, we apply the Cholesky factorization, $\boldsymbol{M} = \boldsymbol{R}^T \boldsymbol{R}$. Under the condition that $N_{eig} = N_{node}$ so that $\boldsymbol{P}_{\text{imp}}$ and $\boldsymbol{P}_{\text{per}}$ are full rank square matrices, we have

$$\begin{aligned} \boldsymbol{P}_{\text{imp}}^T (\boldsymbol{R}^T \boldsymbol{R}) \boldsymbol{P}_{\text{imp}} = I_{N_{eig}} &\Leftrightarrow (\boldsymbol{R}\boldsymbol{P}_{\text{imp}})(\boldsymbol{P}_{\text{imp}}^T \boldsymbol{R}^T) = I_{N_{node}}, \\ \boldsymbol{P}_{\text{per}}^T (\boldsymbol{R}^T \boldsymbol{R}) \boldsymbol{P}_{\text{per}} = I_{N_{eig}} &\Leftrightarrow (\boldsymbol{R}\boldsymbol{P}_{\text{per}})(\boldsymbol{P}_{\text{per}}^T \boldsymbol{R}^T) = I_{N_{node}}. \end{aligned} \tag{2.16}$$

Then, we can derive that $\boldsymbol{C}$ is a unitary matrix:

$$\begin{aligned}\boldsymbol{C}^T\boldsymbol{C} &= \boldsymbol{P}_{\text{per}}^T M \boldsymbol{P}_{\text{imp}} \boldsymbol{P}_{\text{imp}}^T M \boldsymbol{P}_{\text{per}} \\ &= \boldsymbol{P}_{\text{per}}^T (\boldsymbol{R}^T\boldsymbol{R}) \boldsymbol{P}_{\text{imp}} \boldsymbol{P}_{\text{imp}}^T (\boldsymbol{R}^T\boldsymbol{R}) \boldsymbol{P}_{\text{per}} \\ &= \boldsymbol{P}_{\text{per}}^T \boldsymbol{R}^T (\boldsymbol{R}\boldsymbol{P}_{\text{imp}} \boldsymbol{P}_{\text{imp}}^T \boldsymbol{R}^T) \boldsymbol{R}\boldsymbol{P}_{\text{per}} \\ &= I_{N_{eig}}.\end{aligned} \tag{2.17}$$

In addition, we can derive that

$$\boldsymbol{P}_{\text{per}} = \boldsymbol{P}_{\text{imp}}\boldsymbol{C}, \tag{2.18}$$

$$\boldsymbol{P}_{\text{imp}} = \boldsymbol{P}_{\text{per}}\boldsymbol{C}^T, \tag{2.19}$$

because

$$\begin{aligned}&\boldsymbol{P}_{\text{imp}}\boldsymbol{C} = \boldsymbol{P}_{\text{imp}}\boldsymbol{P}_{\text{imp}}^T M \boldsymbol{P}_{\text{per}} \\ \Leftrightarrow\ &\boldsymbol{R}\boldsymbol{P}_{\text{imp}}\boldsymbol{C} = \boldsymbol{R}\boldsymbol{P}_{\text{imp}}\boldsymbol{P}_{\text{imp}}^T \boldsymbol{R}^T \boldsymbol{R}\boldsymbol{P}_{\text{per}} \\ \Leftrightarrow\ &\boldsymbol{R}\boldsymbol{P}_{\text{imp}}\boldsymbol{C} = \boldsymbol{R}\boldsymbol{P}_{\text{per}} \\ \Leftrightarrow\ &\boldsymbol{P}_{\text{imp}}\boldsymbol{C} = \boldsymbol{P}_{\text{per}}\end{aligned}$$

since $\boldsymbol{R}$ is invertible.

Combining eq. (2.13), eq. (2.14),eq. (2.18),eq. (2.19) we have

$$\boldsymbol{L}_{proj} \equiv \boldsymbol{L}_{\text{imp}} + \boldsymbol{Q}_{proj} = \boldsymbol{P}_{\text{imp}}^T (K + Q_{\text{per}}) \boldsymbol{P}_{\text{imp}} = \boldsymbol{C}\boldsymbol{P}_{\text{per}}^T (K + Q_{\text{per}}) \boldsymbol{P}_{\text{per}} \boldsymbol{C}^T = \boldsymbol{C}\boldsymbol{L}_{\text{per}}\boldsymbol{C}^T, \tag{2.20}$$

and similarly,

$$\boldsymbol{W}_{\text{imp}} \equiv \boldsymbol{P}_{\text{imp}}^T \boldsymbol{J}(\mathbf{g}) \boldsymbol{P}_{\text{imp}} = \boldsymbol{C}\boldsymbol{P}_{\text{per}}^T \boldsymbol{J}(\mathbf{g}) \boldsymbol{P}_{\text{per}} \boldsymbol{C}^T = \boldsymbol{C}\boldsymbol{W}_{\text{per}}\boldsymbol{C}^T. \tag{2.21}$$

Then the matrix exponentials satisfy

$$\begin{aligned}e^{-(\Delta-\delta)\boldsymbol{L}_{proj}} &= e^{-(\Delta-\delta)\boldsymbol{C}\boldsymbol{L}_{\text{per}}\boldsymbol{C}^T} &&= \boldsymbol{C}e^{-(\Delta-\delta)\boldsymbol{L}_{\text{per}}}\boldsymbol{C}^T, \\ e^{-\delta\left(\boldsymbol{L}_{proj}+\imath\gamma\boldsymbol{W}_{\text{imp}}(\mathbf{g})\right)} &= e^{-\delta\boldsymbol{C}\left(\boldsymbol{L}_{\text{per}}+\imath\gamma\boldsymbol{W}_{\text{per}}(\mathbf{g})\right)\boldsymbol{C}^T} &&= \boldsymbol{C}e^{-\delta\left(\boldsymbol{L}_{\text{per}}+\imath\gamma\boldsymbol{W}_{\text{per}}(\mathbf{g})\right)}\boldsymbol{C}^T,\end{aligned}$$

because $\boldsymbol{C}\boldsymbol{C}^T = I$. Thus,

$$\begin{aligned}\boldsymbol{H}_{proj}(\mathbf{g}, f) &= e^{-\delta\left(\boldsymbol{L}_{proj}-\imath\gamma\boldsymbol{W}_{\text{imp}}(\mathbf{g})\right)} \cdot e^{-(\Delta-\delta)\boldsymbol{L}_{proj}} \cdot e^{-\delta\left(\boldsymbol{L}_{proj}+\imath\gamma\boldsymbol{W}_{\text{imp}}(\mathbf{g})\right)} \\ &= \boldsymbol{C}e^{-\delta\left(\boldsymbol{L}_{\text{per}}-\imath\gamma\boldsymbol{W}_{\text{per}}(\mathbf{g})\right)}\boldsymbol{C}^T\boldsymbol{C}e^{-(\Delta-\delta)\boldsymbol{L}_{\text{per}}}\boldsymbol{C}^T\boldsymbol{C}e^{-\delta\left(\boldsymbol{L}_{\text{per}}+\imath\gamma\boldsymbol{W}_{\text{per}}(\mathbf{g})\right)}\boldsymbol{C}^T \\ &= \boldsymbol{C}H_{\text{per}}(\mathbf{g}, f)\boldsymbol{C}^T.\end{aligned} \tag{2.22}$$

Substituting eq. (2.18) eq. (2.22) into eq. (2.6), we obtain the equivalence:

$$\begin{aligned}S^{\text{NEW}}(\mathbf{g}, f; N_{node}) &= \rho\left(\mathbf{1}_{N_{node},1}^T \boldsymbol{M}\boldsymbol{P}_{\text{imp}}\right) \boldsymbol{H}_{proj}(\mathbf{g}, f) \left(\boldsymbol{P}_{\text{imp}}^T \boldsymbol{M}\mathbf{1}_{N_{node},1}\right) \\ &= \rho\mathbf{1}_{N_{node},1}^T \cdot \boldsymbol{M} \cdot \left(\boldsymbol{P}_{\text{imp}} \cdot \boldsymbol{C}\right) \cdot \boldsymbol{H}_{\text{per}}(\mathbf{g}, f) \cdot \left(\boldsymbol{C}^T \cdot \boldsymbol{P}_{\text{imp}}^T\right) \cdot \boldsymbol{M} \cdot \mathbf{1}_{N_{node},1} \\ &= \rho\left(\mathbf{1}_{N_{node},1}^T \boldsymbol{M}\boldsymbol{P}_{\text{per}}\right) \boldsymbol{H}_{\text{per}}(\mathbf{g}, f) \left(\boldsymbol{P}_{\text{per}}^T \boldsymbol{M}\mathbf{1}_{N_{node},1}\right) \\ &= S^{\text{NMF}}(\mathbf{g}, f; N_{node}).\end{aligned} \tag{2.23}$$

Thus, when the full set of the discretized eigenfunctions is used, the new method using the impermeable eigenfunctions gives the same signal as the original Numerical Matrix Formalism method that uses permeable eigenfunctions.

□

2.2.1 Choice of number of eigenfunctions

As with the original Numerical Matrix Formalism method, the new method will not, in practice, require the use of the full set of eigenfunctions, and we will again have $N_{eig} \ll N_{node}$, with the choice of N_{eig} determined by the length scale cut-off L_s:

$$\infty \geq l(\lambda_1) \geq \cdots \geq l(\lambda_{N_{eig}}) \geq L_s > l(\lambda_{N_{eig}+1}) \geq \cdots > 0. \tag{2.24}$$

Remark 3. *It is to be noted that for the same geometry and the same L_s, when using the new method, the resulting N_{eig} is the same no matter what the interface permeability, and it is usually somewhat larger than the N_{eig} of the Numerical Matrix Formalism method (with the same value of L_s).*

Remark 4. *Any basis set, when it is complete, can represent any discretized solution in the finite elements basis. We used $P1$ finite elements, so any basis set is complete that has N_{node} elements. This means, the permeable Laplace eigenfunctions set and the impermeable Laplace eigenfunctions set are both sufficient to represent any PDE solution if $N_{eig} = N_{node}$.*

The discretized solution of the Bloch-Torrey equation, permeable or not, is usually piece-wise smooth on each compartment and so should be able to be represented by the smooth eigenfunctions in the impermeable basis. The discretized solution should not need to be represented by very oscillatory eigenfunctions, this means the vast majority of the oscillatory eigenfunctions in the impermeable basis are not needed. Thus, one can just keep the relatively smooth eigenfunctions in the impermeable basis and they are enough to represent any reasonable solution for the permeable problem. In short, for a discretized finite element solution of the Bloch-Torrey equation, one never needs to take N_{eig} to be anywhere close to N_{node} in any basis.

2.3 Numerical results

In this section we conduct a numerical validation of the new method. The generation of the computational geometries, the discretization into finite elements, and the numerical computation of the Laplace eigenfunctions in the finite element space were implemented into the SpinDoctor toolbox[87].

The simulations will be performed on a quasi-two dimensional multi-compartment geometry, denoted by Ω^I, shown in fig. 2.1, containing 20 axons. The axons are randomly placed and then wrapped by an extra-cellular space (ECS). The ECS is not a rectangle in order to keep the axons closely packed. The outer boundary condition is set to be impermeable, i.e. homogeneous Neumann boundary condition. The axon radii vary between 1μm and 3μm. The dimension of the whole geometry is $34\mu\text{m} \times 29\mu\text{m} \times 1\mu\text{m}$. The diffusion coefficients are set to be the same for all compartments: $\mathcal{D}_i = \mathcal{D}_0 = 2 \times 10^{-3}\,\text{mm}^2/\text{s}$ for $i \in \{1, N_{cmpt}\}$. The initial spin density is set to $\rho = 1.0$. SpinDoctor creates the geometrical configuration and the surface triangulation, then pass the surface triangulation to TetGen[121] to create a volume mesh. The finite elements mesh contains $N_{node} = 3455$ nodes and 6673 elements.

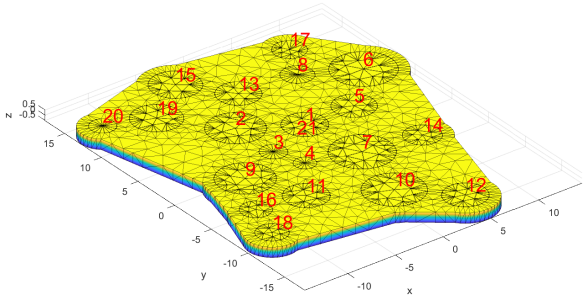

Figure 2.1: Finite element mesh of the geometry Ω^I. It contains 20 randomly placed cylindrical axons, wrapped in the extra-cellular space (ECS). The radii of all axons are between $1\mu m$ and $3\mu m$ and the height of all compartments is $1\mu m$. Dimension of the whole geometry is $34\mu m \times 29\mu m \times 1\mu m$. The geometry is generated by SpinDoctor and the finite elements mesh is created by Tetgen[121]. The mesh contains 3455 nodes and 6673 elements.

In the literature, the experimentally measured permeability coefficient κ in biological cells ranges from 10^{-6} m/s to 10^{-4} m/s[122], in particular, $\kappa = 10^{-5}$ m/s for axonal membranes without myelin sheath[37]. Therefore, our simulations are performed using permeability coefficients up to $\kappa = 10^{-4}$ m/s.

In this section, unless specified, we apply PGSE sequence for the simulations. The average displacement in free diffusion is $\sqrt{2\,\dim \mathcal{D}_0 T_E}$, where $\dim$ is the dimension. In order to limit the amount

of spins hitting the outer boundary and reduce the effects from the interaction of spins with the impermeable outer boundary, we keep the displacement to less than half of the geometry diameter, obtaining that $T_E \leq 20$ms. Thus, we limit $\delta + \Delta \leq 20$ms in the simulations on Ω^I. The gradient strength in *in-vivo* experiments does not exceed $1000\,\mathrm{mT/m}$[123], so we set the highest simulated g-value to $1000\,\mathrm{mT/m}$.

2.3.1 Computing the reference solution

For the geometry Ω^I, we do not have the analytical solution of the diffusion MRI signal. We propose using the Numerical Formalism method with the full set of permeable Laplace eigenfunctions as the reference solution. We have compared the reference solution to the finite elements solution of the discretized Bloch-Torrey PDE for $\|\mathbf{g}\| = 1000\,\mathrm{mT/m}, \mathrm{PGSE}(10\mathrm{ms}, 10\mathrm{ms})$ across all gradient directions and verified that the maximun relative differences between them are less than 0.002%. Thus, we estimate that the signals computed using the Numerical Matrix Formalism method with the full set of permeable eigenfunctions to be accurate to 0.002% from the true signal.

The reference solution is set to be the Numerical Matrix Formalism solution using the full set of permeable Laplace eigenfunctions i.e. $N_{eig} = N_{node} = 3455$ eigenfunctions for Ω^I,

$$S^{\mathrm{REF}}(\mathbf{g}, f) = S^{\mathrm{NMF}}(\mathbf{g}, f; N_{node}).$$

To avoid the dependence of the results on the gradient direction $\mathbf{g}$, we average the diffusion MRI signal over 18 gradient directions, uniformly distributed on a unit semicircle in the $x-y$ plane:

$$\overline{S}(\|\mathbf{g}\|, f; N_{eig}) = \frac{1}{|\Omega|}\frac{1}{18}\sum_{d=1}^{18} S(\mathbf{g}_d, f; N_{eig}),\ \mathbf{g}_d = \|\mathbf{g}\|\left[\cos\left(\pi\frac{d}{18}\right), \sin\left(\pi\frac{d}{18}\right), 0\right]^T, \tag{2.25}$$

normalized by the total volume. Figure 2.2 depicts the reference signals as a function of the g-value $\|\mathbf{g}\|$. The simulations are performed for g-value from $0\,\mathrm{mT/m}$ to $1000\,\mathrm{mT/m}$. The signals $\overline{S}$ have been normalized by the total volume so their maximum value is 1. We observe that diffusion MRI signal decays faster in the presence of more permeable membranes.

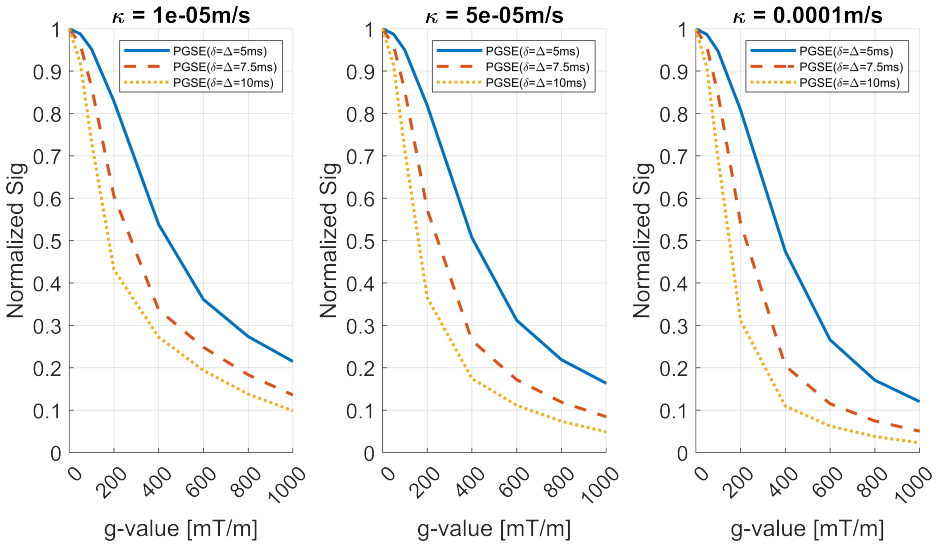

Figure 2.2: Normalized direction-averaged diffusion MRI signals as a function of the g-value $\|\mathbf{g}\|$. These are the reference solutions computed using the Numerical Matrix Formalism method with the full set of permeable Laplace eigenfunctions, i.e., $N_{eig} = N_{node} = 3455$ eigenfunctions for Ω^I.

2.3.2 Validation of the new method

We have shown in Theorem 1 that the new method yields the same signal as the Numerical Matrix Formalism method if the full set of basis functions is used. However, since in practice, $N_{eig} \ll$

N_{node}, we will now show the accuracy of the two methods for fixed values of the length scale cut-off L_s.

In fig. 2.3, we show the relative errors produced by the two methods compared to the reference solution. The relative error is defined as:

$$\epsilon_{rel}(\%) = 100 \times \frac{|\overline{S}(\|\mathbf{g}\|, f; N_{eig}) - \overline{S}^{\text{REF}}(\|\mathbf{g}\|, f)|}{\overline{S}^{\text{REF}}(\|\mathbf{g}\|, f)}. \tag{2.26}$$

First, we see that the relative errors of the original Numerical Matrix Formalism method where the length scale cut-off is $L_s = 1\mu$m are under 0.03% for all the simulated sequences. The number of the eigenfunctions differs with permeability: when $\kappa = 10^{-5}$ m/s, 5×10^{-5} m/s, 10^{-4} m/s, $N_{eig} = 538,\ 535,\ 532$, respectively. Second, for the new method, with a length scale cut-off of $L_s = 1\mu$m, resulting in $N_{eig} = 538$, the relative error is under 1.5% for all the sequences. The relative error increases as permeability increases, as the g-value $\|\mathbf{g}\|$ increases, and as the diffusion time increases.

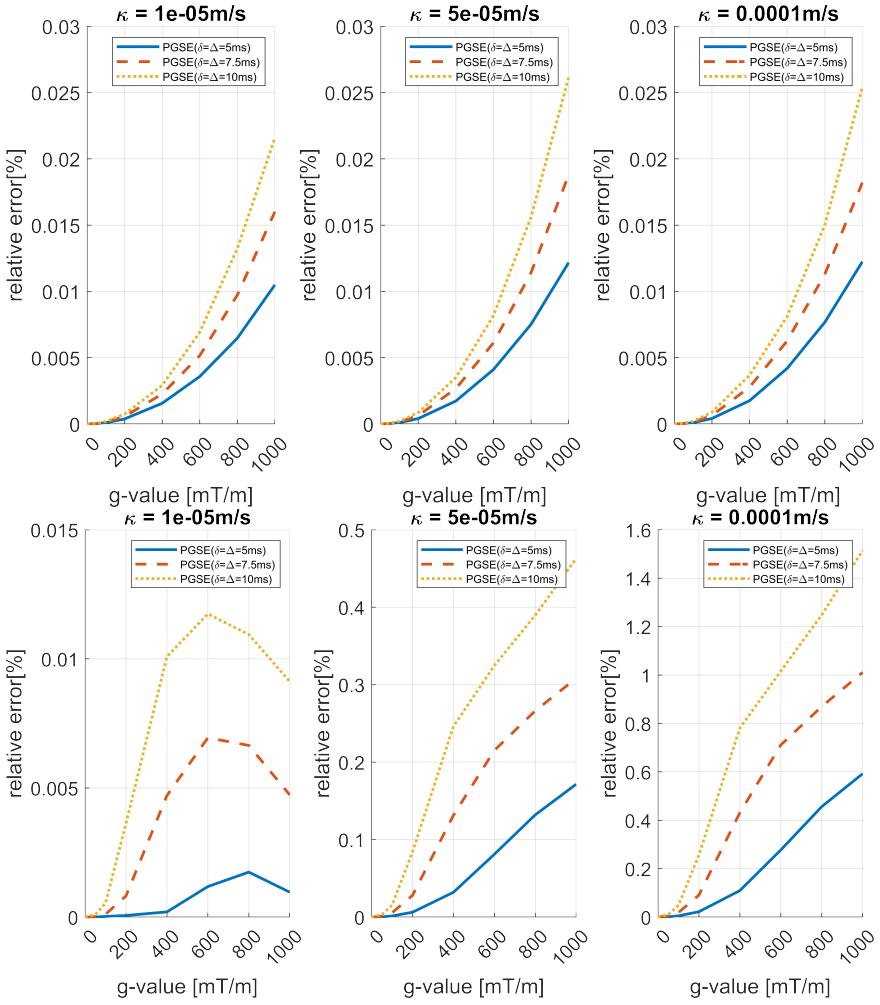

Figure 2.3: First row: Relative errors of direction averaged signals of the Numerical Matrix Formalism with the length scale cut-off $L_s = 1\mu$m ($\kappa = 10^{-4}$ m/s,$N_{eig} = 532$; $\kappa = 5 \times 10^{-5}$ m/s,$N_{eig} = 535$; $\kappa = 10^{-5}$ m/s,$N_{eig} = 538$). Second row: Relative errors of direction averaged signals of the new method with the length scale cut-off $L_s = 1\mu$m ($N_{eig} = 538$). The relative errors are in percent. Simulations are performed on Ω^I, by SpinDoctor. Left: $\kappa = 10^{-5}$ m/s; Middle: $\kappa = 5 \times 10^{-5}$ m/s; Right: $\kappa = 10^{-4}$ m/s.

Now we study the convergence behavior of the new method as L_s decreases (N_{eig} increases) and compare it to the original Numerical Matrix Formalism method. The simulated gradient direction is fixed in $[\sqrt{2}/2, \sqrt{2}/2, 0]^T$ and we use the longest sequence PGSE$(10\text{ms}, 10\text{ms})$, which yields the

biggest errors. We define the normalized error between the computed signal and reference signal to be

$$\epsilon_{abs} = \frac{|S(\mathbf{g}, f; N_{eig}) - S^{\text{REF}}(\mathbf{g}, f)|}{|\Omega|}. \tag{2.27}$$

It is a normalized error because $S/|\Omega|$ is always bounded by 1. Note this is not a relative error, we do not divide by S^{REF}, because we do not want the error to increase due to the decrease in the signal itself, we simply want to show the convergence of the signals.

Figure 2.4 shows the normalized errors of the diffusion MRI signals computed by the new method and by the original Numerical Matrix Formalism method, compared to the reference solution. The x-axis gives N_{eig}. The two vertical lines indicate where the truncations occur for $L_s = 2\mu$m and $L_s = 1\mu$m in the impermeable case:

$$L_s = 2\mu\text{m}, N_{eig} = 193,$$
$$L_s = 1\mu\text{m}, N_{eig} = 538.$$

As more eigenfunctions are used, the errors are reduced for both the new method and the original Numerical Matrix Formalism method. When $\kappa \leq 10^{-5} m/s$, the new method converges at a similar rate as the original Numerical Matrix Formalism. At the higher permeabilities, the new method converges more slowly than Numerical Matrix Formalism, but it is clear that if we are interested 2 or 3 digits of accuracy, which is reasonable given that the diffusion MRI signal noise is at least of order 0.01, using the length scale cut-off of $L_s = 2\mu$m is sufficient. As far as we know, there is not an analytical way to relate the truncation size and the signal error. The truncation is defined on the impermeable Laplace eigenfunctions, whereas the signal is related to the operator including the term $I\mathbf{g} \cdot \boldsymbol{x}$ as well as the permeability. We observe that though the errors of the Numerical Matrix Formalism method increase with lower permeability due to the large variations of the permeable eigenfunctions around the interfaces, the errors of the new method increase with higher permeability due to the fact that the new method uses impermeable eigenfunctions for all permeability values.

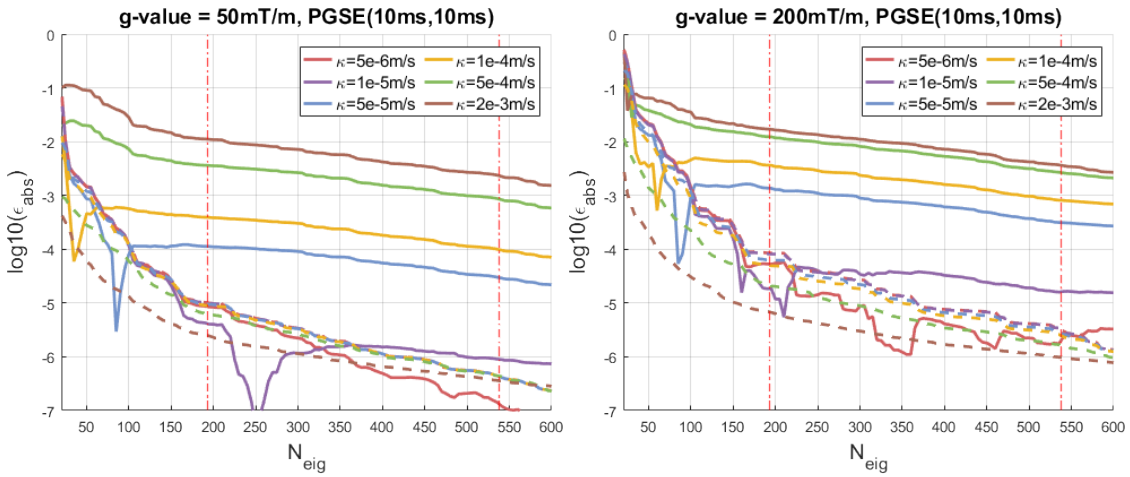

Figure 2.4: Normalized signal errors of the new method (in solid line) and the Numerical Matrix Formalism method (in dashed line), compared to the reference solution, as a function of N_{eig}. The two vertical lines indicate where the truncations occur for $L_s = 2\mu$m ($N_{eig} = 193$) and $L_s = 1\mu$m ($N_{eig} = 538$). The simulations are performed on Ω^I, with gradient direction fixed in $[\sqrt{2}/2, \sqrt{2}/2, 0]^T$ and the sequence PGSE$(10\text{ms}, 10\text{ms})$. Left: g-value$= 50\,$mT/m; Right: g-value$= 200\,$mT/m.

2.3.3 Computational time

An advantage of the new method to compute the diffusion MRI signal is the savings in computational time. To show the efficiency of the new method, we compare the computational times of the Numerical Matrix Formalism method and our new method on a bigger geometry $\Omega^{axons200}$

that contains 200 cylindrical axons enclosed in the ECS, as shown in fig. 2.5. Its dimensions are 98μm $\times$ 118μm $\times$ 1μm and there are 62145 elements and $N_{node} = 32023$ nodes in total, of which 16924 nodes in the ECS. The gradient direction of simulations is fixed in $[\sqrt{2}/2, \sqrt{2}/2, 0]^T$. Two PGSE sequences PGSE$(5\text{ms}, 5\text{ms})$ and PGSE$(10\text{ms}, 10\text{ms})$ and four g-value $= [50, 200, 500, 1000]$ mT/m are used. The simulations are performed with 3 different values of $N_{eig} = 2000, 4000, 5000$ (we fixed N_{eig} rather than L_s to make easier comparisons of computational time). All the simulations are performed on a computing server with 20 cores of frequency 2.4 GHz, and RAM of 256GB. The operating system is Rocky Linux 8 and the Matlab version is R2021a.

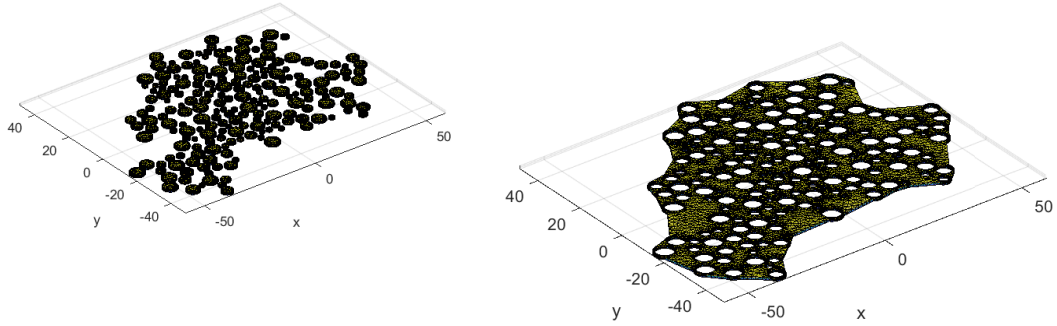

Figure 2.5: Finite element meshes of the geometry Ω^{axons200} for the computational times comparison. The geometry contains 200 randomly placed cylindrical axons, whose radii vary between 1μm and 3μm, and one tightly wrapped ECS. All compartments are 1μm in height. The dimensions are 98μm $\times$ 118μm $\times$ 1μm. This mesh has 32023 nodes and 62145 elements in total. Left: 200 axons compartments; Right: ECS compartment, which contains 16924 nodes and 34258 elements.

Numerical Matrix Formalism with the full set of eigenfunctions is set to be the reference solution. Both Matrix Formalism and the new method compute the diffusion MRI signal in two steps: Laplace eigendecomposition and matrix exponential computations. The first step is independent of the encoding sequence settings, involving only sparse matrices of size $N_{node} \times N_{node}$. The second step involves dense matrices of size $N_{eig} \times N_{eig}$. In practice, we have $N_{eig} \ll N_{node}$.

Table 2.1 shows the computational times of the Laplace eigendecomposition by the new method and the Numerical Matrix Formalism method. The eigenmodes are computed by the Matlab built-in function 'eigs', which computes the first smallest N_{eig} eigenmodes by Lanczos iteration. To obtain the full set of the eigenmodes, the Matlab built-in function 'eig' can be used to conduct a complete eigen-decomposition. The computational complexity of 'eig' for the generalized eigenvalue problem, $Ay = By\lambda$, is $O(N_{node}^3)$ in theory, and $O(N_{node}^{2.376})$ in practice using the Coppersmith and Winograd algorithm[124]. The computational complexity of 'eigs' is $O(N_{eig}N_{node}^2 + N_{node}N_{eig}^2)$, the first term is due to the computation of $B\backslash Ay$ at each Lanczos iteration and the second term is due to the orthogonalization of the new Krylov vectors at each Lanczos iteration[125]. In fact, because A and B are sparse matrices, the computation of $B\backslash Ay$ is $O(N_{eig}N_{node})$ rather than $O(N_{eig}N_{node}^2)$, so the dominant term of the computational complexity for 'eigs' is $O(N_{node}N_{eig}^2)$. We can see in the table that going from $N_{eig} = 2000$ to $N_{eig} = 4000$, the computational times increase by 4 in all the rows.

The original Numerical Matrix Formalism method needs to recalculate permeable Laplace eigenfunctions when the permeability changes. On the contrary, the new method only computes the impermeable Laplace eigenfunctions once. In addition, the impermeable Laplace eigendecomposition can be achieved compartment by compartment. The computational complexity of the permeable eigendecomposition is $\mathcal{O}(N_{node}^{2.376})$ ('eig') or $\mathcal{O}(N_{node}N_{eig}^2)$ ('eigs'), compared to the impermeable case, where it is $\mathcal{O}(\sum_i^{N_{cmpt}} N_{i,node}^{2.376})$ ('eig') or $\mathcal{O}(\sum_i^{N_{cmpt}}(N_{i,node}N_{eig}^2))$ ('eigs'), $N_{i,node}$ being the number of finite elements nodes in compartment i. In table 2.1, we can see that for the same N_{eig}, the impermeable eigendecomposition is two times faster than the permeable eigendecomposition. If we consider the simulation of three permeability values, using the new method, the full set eigendecomposition can be done in 141 seconds, whereas the Numerical Matrix Formalism method takes 301 seconds at $N_{eig} = 2000$.

	Computational time (seconds)			
	$N_{eig} = 2000$	$N_{eig} = 4000$	$N_{eig} = 5000$	Full set ($N_{eig} = 32023$)
	New method			
Total	41	171	278	141
$\kappa(m/s)$	Numerical Matrix Formalism method			
10^{-5}	99	419	646	723
5×10^{-5}	100	389	518	727
10^{-4}	102	353	625	734
Total	301	1161	1789	2184

Table 2.1: Computational times of Laplace eigen-decomposition at different permeabilities for Ω^{axons200}, given in seconds. The full set contains $N_{node} = 32023$ nodes.

On the question of whether to call 'eigs' or 'eig' to compute the eigenmodes, we remind the reader that the theoretical complexities are $O(N_{node}N_{eig}^2)$ and $O(N_{node}^{2.376})$, respectively. It is clear that, at some point, as N_{eig} increases, it would be more computationally efficient to compute the full eigendecomposition instead of a partial eigendecomposition. Some further considerations are that (1) the 'eig' implementation in Matlab is well optimized for parallel computing using all the computer's cores, unlike the 'eigs', (2), the 'eig' function in MATLAB only accepts dense matrices whereas the 'eigs' function allows the designation of sparse matrices so the matrix-vector multiplications are faster and take less memory. In summary, 'eigs' is useful when: (1) Only a small number of eigenmodes (for example, less than 15%) are needed, such as for simple geometries, longer diffusion times, lower gradient amplitudes; (2) When the computer RAM is limited. For 'eig', the input and output matrices are full, when $N_{node} = 32023$, 'eig' requires 22.9GB of RAM. In contrast, the inputs of 'eigs' are sparse matrices, when $N_{node} = 32023$, 'eigs' requires 1.2GB of RAM. For other cases, using 'eig' and selecting a subset of eigenmodes is preferred.

Table 2.2 shows the computational times of the matrix exponential computations in one gradient direction with different settings. In order to accelerate the computation, instead of computing the matrix exponential explicitly, we use the algorithm 'expmv'[126], which computes the action of matrix exponential on a vector, without explicitly forming the matrix exponential. The number of eigenfunctions is set to $N_{eig} = 2000$. With this choice, the errors of the normalized signals of the original Numerical Matrix Formalism method is less than 0.0008, and the error of the new method is less than 0.0013. We can see from the table that for the original Numerical Matrix Formalism method, the computational time is between 0.7 to 4.7 seconds. For the new method, the computational time is between 0.8 and 3.8 seconds. Thus, the two methods are similar in the signal computational step, however, the new method offers substantial computational time advantage over the original Numerical Matrix Formalism method due to the savings in the eigendecomposition step. In the table, we are also include the cost of solving the Bloch-Torrey PDE directly using finite elements rather than computing eigenfunctions, labeled "FE", clearly, this approach is much more costly than either of the two eigenfunctions based methods.

2.3.4 Application to other diffusion MRI sequences

Our methodology can be applied to other sequences, such as double PGSE[55], OGSE[54], flow compensation sequence[127] and long-narrow pore imaging sequence[128]. One should represent or approximate the sequence profile $f(t)$ as a piece-wise constant function defined on n intervals:

$$f(t) = \sum_{i=0}^{n-1} f(t_i)\mathbb{1}_{[t_i,t_{i+1}]}, \tag{2.28}$$

where $\{t_0, \ldots, t_n\}$ is a strictly increasing sequence between 0 and T_E and $\mathbb{1}_{[t_i,t_{i+1}]}$ is the indicator function on the interval $[t_i, t_{i+1}]$.

We illustrate the application of our method to the long-narrow pore imaging sequence[128], which consists of two rectangular pulses of duration $T_E\delta_1$ and $T_E\delta_2$, of gradient strengths $-\|g\|$ and $\|g\|\delta_1/\delta_2$, respectively, separated by a time interval $T_E(1 - \delta_1 - \delta_2)$, for which the temporal profile

				NMF		New method		FE	
κ	δ	Δ	$\|\mathbf{g}\|$	Time	ϵ_{abs}	Time	ϵ_{abs}	Time	S^{REF}
10^{-5}	5	5	50	0.9	0.000004	0.8	0.000001	16.2	0.99
			200	1.2	0.00006	1.1	0.00002	34.0	0.82
			500	1.4	0.0002	1.6	0.00008	68.9	0.43
			1000	1.8	0.0006	2.3	0.0001	117.3	0.22
	10	10	50	1.1	0.000008	1.3	0.000008	22.1	0.91
			200	1.2	0.00007	1.5	0.00009	53.1	0.43
			500	1.8	0.0003	2.3	0.0002	106.9	0.24
			1000	3.5	0.0008	3.8	0.0001	199.0	0.10
5×10^{-5}	5	5	50	0.7	0.000004	0.8	0.00002	16.6	0.99
			200	0.9	0.00005	0.9	0.0003	34.0	0.81
			500	1.4	0.0002	1.4	0.001	67.2	0.38
			1000	2.1	0.0004	1.8	0.001	106.6	0.16
	10	10	50	1.2	0.000007	1.1	0.0002	24.6	0.90
			200	1.4	0.00005	1.1	0.001	59.2	0.35
			500	2.3	0.0001	2.2	0.002	103.7	0.14
			1000	3.7	0.0003	2.6	0.0009	184.8	0.05
10^{-4}	5	5	50	0.9	0.000004	0.8	0.00007	16.0	0.99
			200	1.2	0.00005	1.0	0.0009	37.7	0.80
			500	1.7	0.0002	1.3	0.003	70.0	0.33
			1000	2.7	0.0002	1.7	0.0003	94.6	0.12
	10	10	50	1.4	0.000007	1.0	0.0005	24.9	0.90
			200	1.7	0.00004	1.2	0.004	56.6	0.28
			500	2.6	0.00006	1.7	0.0003	103.9	0.08
			1000	4.7	0.00008	3.1	0.0013	179.9	0.02

Table 2.2: Computational times and normalized signal errors of the Numerical Matrix Formalism (NMF) method and the new method in Ω^{axons200}, given in seconds. The number of eigenfunctions is $N_{eig} = 2000$. The encoding gradient direction is fixed in $[\sqrt{2}/2, \sqrt{2}/2, 0]^T$. The units are κ: m/s, δ:ms, Δ:ms and $\|\mathbf{g}\|$: mT/m. We also include the cost of solving the Bloch-Torrey PDE directly using finite elements rather than computing eigenfunctions, labeled "FE", and the value of the reference signal, labeled "S^{REF}".

$f_{pore}(t)$ is

$$f_{pore}(t) = \begin{cases} -1, & 0 \leq t \leq T_E\delta_1, \\ \delta_1/\delta_2, & T_E(1-\delta_2) < t \leq T_E, \\ 0, & \text{otherwise,} \end{cases} \tag{2.29}$$

where $\delta_1 > 0$ and $\delta_2 > 0$ are two dimensionless positive time coefficients, with $\delta_1 + \delta_2 \leq 1$.

We perform the simulations on Ω^I, with long-narrow pore imaging parameters below:

- $T_E = 20$ms, $\delta_1 = 1 - \delta_2$ and $\delta_2 = [0.5, 0.2, 0.1, 0.05]$;
- g-values from 0 to 200 mT/m;
- 18 gradient directions uniformly distributed on a unit semicircle.

We show in fig. 2.7 the simulated reference signals. We note that when $\delta_2 = 0.5$, we are in the PGSE case. When $\delta_2 \neq 0.5$, while this sequence meets the rephasing condition, it does not satisfy the anti-symmetric condition. Therefore, we see that the signals have a non-zero imaginary part. This extra phase information can serve to infer pore size information[129].

We show in fig. 2.8 the relative errors between the new method with the length scale cut-off $L_s = 1\mu$m ($N_{eig} = 538$) and the reference signals. The errors in the real part of the signal are between 0.01% and 1%, the errors in the imaginary part of the signal are between 2% and 3%.

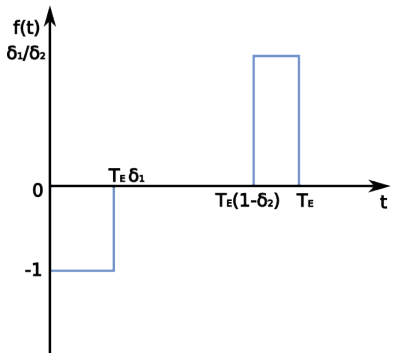

Figure 2.6: Time profile of long-narrow pore imaging sequence. The first pulse has longer duration and an amplitude of 1. The second pulse is shorter in duration but has a higher amplitude, given by δ_1/δ_2.

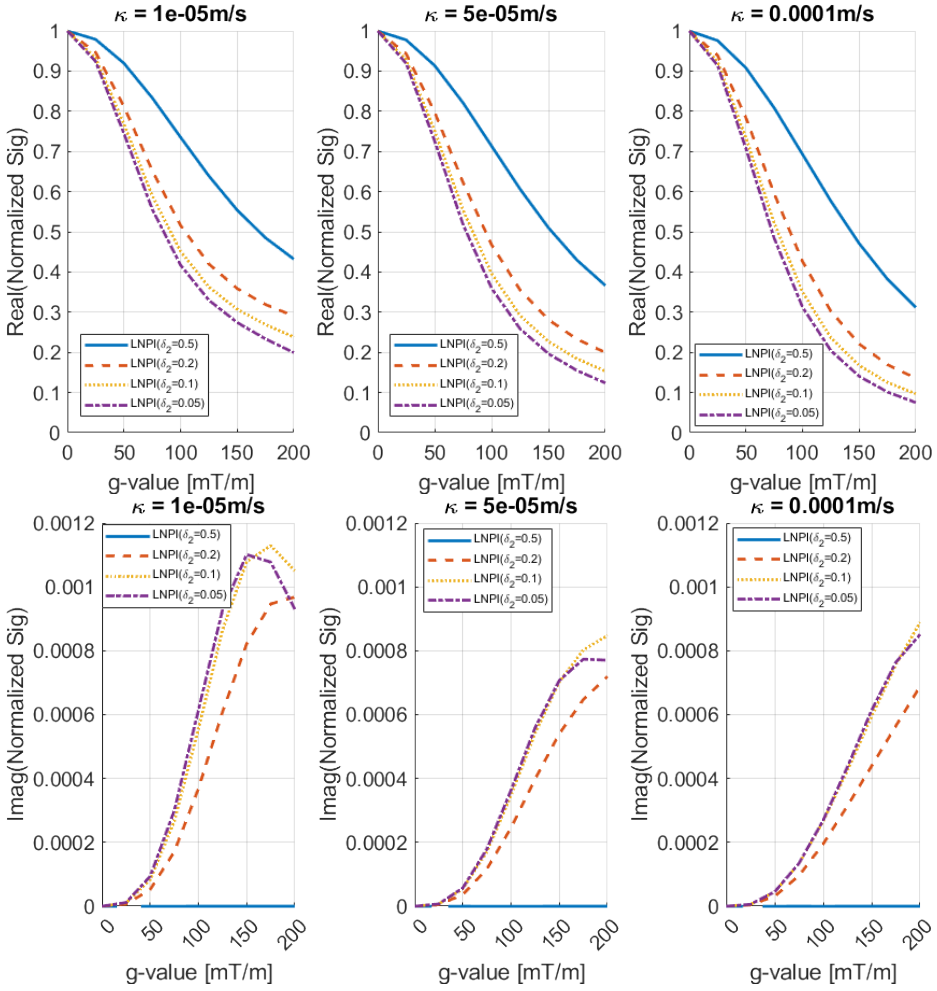

Figure 2.7: Real part (first row) and imaginary part (second row) of normalized direction-averaged diffusion MRI signals using the long-narrow pore imaging sequence, with ($\delta_1 = 1 - \delta_2$ and $T_E = 20$ms). Simulations are performed on Ω^I, by SpinDoctor. Left: $\kappa = 10^{-5}$ m/s; Middle: $\kappa = 5 \times 10^{-5}$ m/s; Right: $\kappa = 10^{-4}$ m/s.

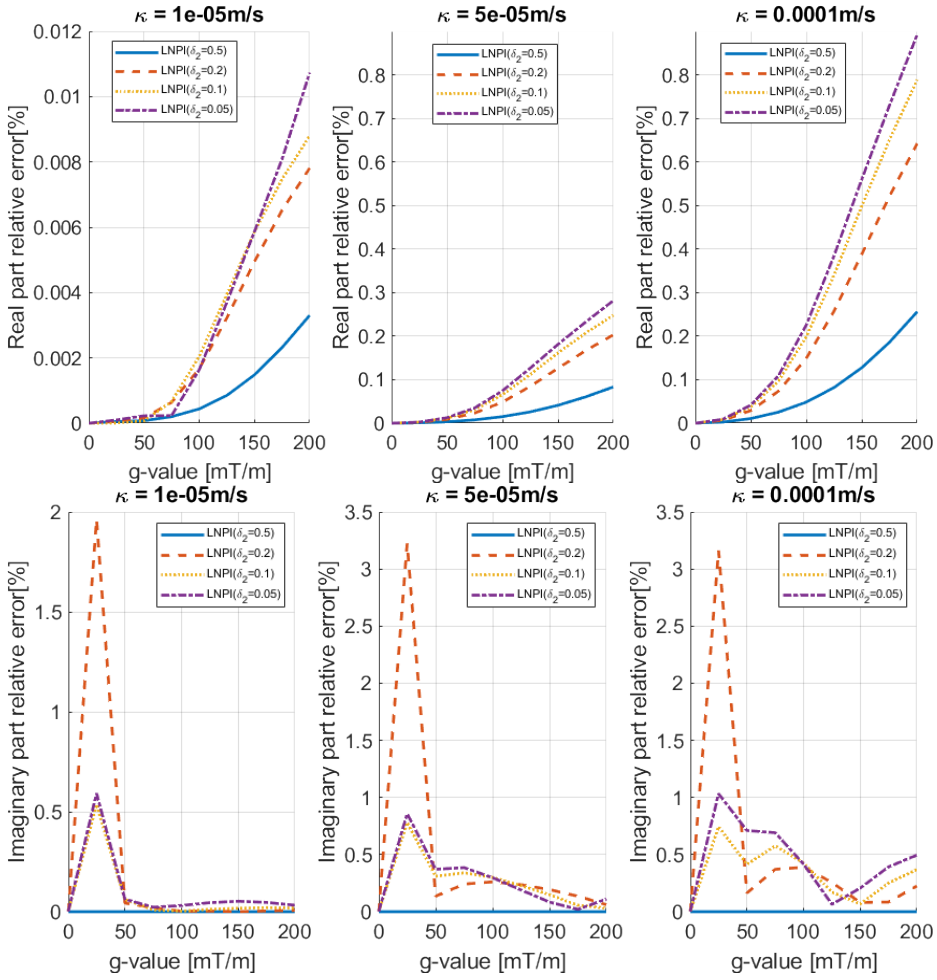

Figure 2.8: Relative errors of the real part (first row) and the imaginary part (second row) of the direction averaged signals of the new method with the length scale cut-off $L_s = 1\mu$m ($N_{eig} = 538$). The relative errors are in percent. Simulations are performed on Ω^I, by SpinDoctor. Left: $\kappa = 10^{-5}$ m/s; Middle: $\kappa = 5 \times 10^{-5}$ m/s; Right: $\kappa = 10^{-4}$ m/s.

2.4 Permeability models evaluation

To illustrate a way that the new method we developed in this paper can be used to study permeability, in this section, we apply the proposed method to evaluate several models that take account of permeability. Concretely, we will study (1) a mono-exponential model on diffusion MRI signals regarding permeability and (2) ADC in long time limit relative to permeability. In addition, we test a novel diffusion MRI compartment signal model, the NEXI model, to show the correlation between its exchange water time and permeability.

2.4.1 Numerical study of permeability effects on signal

Suppose we want to test the hypothesis that the dependence of the signal on the permeability can be approximated by the following expression for a range of values of permeability found in biological tissues:

$$S^{\text{APPROX}}(\mathbf{g}, f; N_{eig}) = e^{-\beta(\mathbf{g},f)\cdot\kappa} \cdot \left(S_{\text{imp}}(\mathbf{g}, f; N_{eig}) - S_{\text{free}}(\mathbf{g}, f; N_{eig})\right) + S_{\text{free}}(\mathbf{g}, f; N_{eig}), \quad (2.30)$$

where $\beta(\mathbf{g}, f)$ is a positive fitted coefficient depending on the encoding gradient and the geometry, $S_{\text{imp}}(\mathbf{g}, f; N_{eig})$ is the signal in the impermeable case and $S_{\text{free}}(\mathbf{g}, f; N_{eig})$ is the signal in absence of all interior interfaces. Both $S_{\text{imp}}(\mathbf{g}, f; N_{eig})$ and $S_{\text{free}}(\mathbf{g}, f; N_{eig})$ are independent of permeability. By construction, (1) $S = S_{\text{imp}}$ when $\kappa = 0\,\text{m/s}$; (2) $\lim_{\kappa\to+\infty} S = S_{\text{free}}$; (3) the signal is subject to exponential decay in κ;

We computed the permeable signals using the new method and in fig. 2.9 we show the computed $S^{\text{NEW}}/S_{\text{imp}}$ and $S^{\text{APPROX}}/S_{\text{imp}}$ with the fitted values of $\beta(\mathbf{g}, f)$. The good fit of the exponential dependence on κ is evident for the range of κ tested. At low gradient strength (b $= 500\,\text{s/mm}^2$), diffusion MRI signal depends very little on κ. As the gradient strength increases, the signal is more sensitive to κ. This result is consistent with the signal behavior at high gradients for one dimensional problems in the presence of multiple semi-permeable barriers discussed in[122].

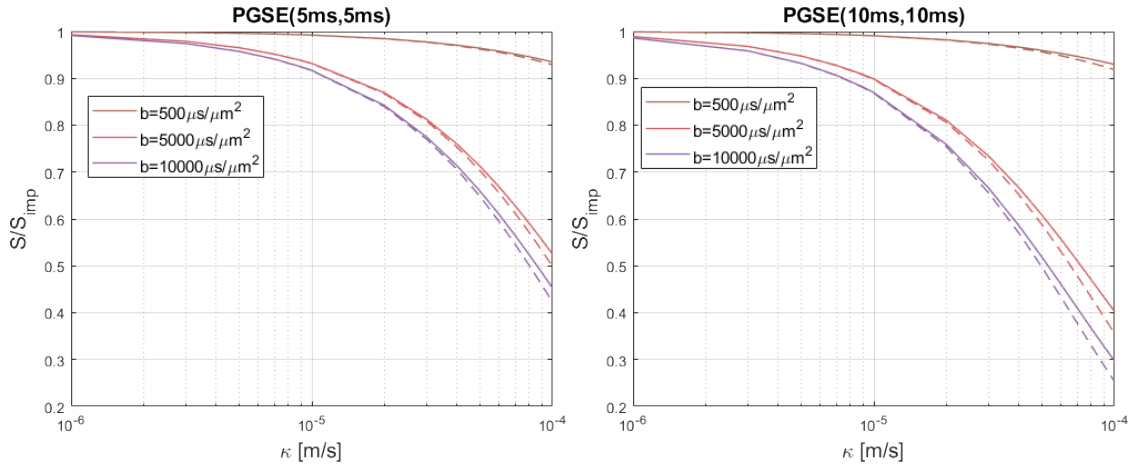

Figure 2.9: The simulations are performed on Ω^I, with the gradient direction fixed in $[\sqrt{2}/2, \sqrt{2}/2, 0]^T$, using the new method with length scale cut-off $L_s = 1\mu\text{m}$ ($N_{eig} = 538$). The solid and dashed lines represent $S^{\text{NEW}}/S_{\text{imp}}$ and $S^{\text{APPROX}}/S_{\text{imp}}$, respectively. Left: short diffusion time case, PGSE$(5\text{ms}, 5\text{ms})$. The fitted coefficients are $\beta = 2424(\,\text{m/s})^{-1}$ (b $= 500\,\text{s/mm}^2$), $\beta = 7497(\,\text{m/s})^{-1}$ (b $= 5000\,\text{s/mm}^2$), $\beta = 8984(\,\text{m/s})^{-1}$ (b $= 10000\,\text{s/mm}^2$). The normalized impermeable signals are $S_{\text{imp}} = 0.7$ (b $= 500\,\text{s/mm}^2$), $S_{\text{imp}} = 0.256$ (b $= 5000\,\text{s/mm}^2$), $S_{\text{imp}} = 0.162$ (b $= 1000\,\text{s/mm}^2$); Right: long diffusion time case, PGSE$(10\text{ms}, 10\text{ms})$. The fitted coefficient $\beta = 3185(\,\text{m/s})^{-1}$ (b $= 500\,\text{s/mm}^2$), $\beta = 11536(\,\text{m/s})^{-1}$ (b $= 5000\,\text{s/mm}^2$), $\beta = 14535(\,\text{m/s})^{-1}$ (b $= 10000\,\text{s/mm}^2$). The normalized impermeable signals are $S_{\text{imp}} = 0.734$ (b $= 500\,\text{s/mm}^2$), $S_{\text{imp}} = 0.341$ (b $= 5000\,\text{s/mm}^2$), $S_{\text{imp}} = 0.281$ (b $= 1000\,\text{s/mm}^2$).

The evolution of the fitted values of $\beta(\mathbf{g}, f)$ as functions of b and $\sqrt{\delta}$ is plotted in fig. 2.10. At low gradient strength, $\beta \propto \sqrt{\delta}$.

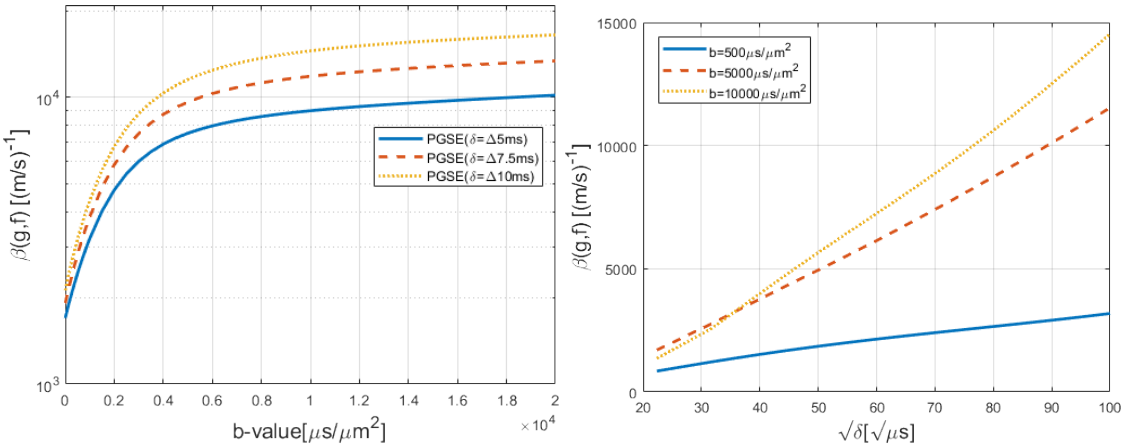

Figure 2.10: The evolution of $\beta(\mathbf{g}, f)$ as a function of b-value (left) for three tested sequences, PGSE$(5\text{ms}, 5\text{ms})$, PGSE$(7.5\text{ms}, 7.5\text{ms})$ and PGSE$(10\text{ms}, 10\text{ms})$, and as a function of $\sqrt{\delta}$ (right) for three tested gradient strengths, b=500 s/mm^2, b=5000 s/mm^2 and b=10000 s/mm^2. The simulations are performed on Ω^I, with the gradient direction fixed in $[\sqrt{2}/2, \sqrt{2}/2, 0]^T$, using the new method with length scale cut-off $L_s = 1\mu$m ($N_{eig} = 538$).

2.4.2 Long time limit ADC

For an open boundary geometry formed by pore structures with impermeable membranes, the ADC has an asymptotic approximation in the long time limit toward diffusion time t[130, 131]:

$$\text{ADC}_{\text{long}}(t) \approx \text{ADC}_\infty + \frac{k_1 \mathcal{D}_0}{t} + \frac{k_{3/2}\mathcal{D}_0}{t^{3/2}} + \mathcal{O}(\frac{1}{t^{5/2}}), \tag{2.31}$$

where $\mathcal{D}_0$ is the intrinsic diffusion coefficient, k_1 and $k_{3/2}$ are coefficients depending on the confining geometry, and ADC_∞ is the ADC at infinity time. In the presence of permeable membranes, a new leading term $1/\sqrt{t}$ needs to be added[132]. In particular, for one-dimensional diffusion case, separated by equally spaced permeable barriers with a spacing of a, ADC_∞ can be expressed as[133]

$$\frac{1}{\text{ADC}_\infty} = \frac{1}{\mathcal{D}_0} + \frac{1}{a\kappa}. \tag{2.32}$$

This approximation is useful to infer the permeability in the one dimensional case. Studying the time dependent ADC behavior in the long time limit for other geometrical configurations, like two dimensional or three dimensional, is intriguing.

To examine whether the long time limit ADC behavior of a complex permeable medium matches the two aforementioned relationships, we perform simulations on Ω^I. The experimental settings are as below:

- Diffusion coefficient $\mathcal{D}_0$ is 2×10^{-3} mm^2/s for all compartments;
- The gradient direction is fixed in $[\sqrt{2}/2, \sqrt{2}/2, 0]^T$;
- PGSE sequence is applied, with $\delta = 5$ms and 10 Δ values varying from 60ms to 150ms;
- ADC value is calculated by fitting the diffusion MRI signals at five low b-values, $[25, 50, 100, 150, 200]$ s/mm^2;
- The range of tested permeability values is from 10^{-6} m/s to 10^{-4} m/s;
- Length scale cut-off $L_s = 1\mu$m, i.e. $N_{eig} = 538$.

In fig. 2.11, we plot the time dependent ADC as a function of $1/\sqrt{t}$. We observe that in the case of $\kappa \to +\infty$ m/s (the purple line), ADC_{long} shows a clearly linear relationship with $1/\sqrt{t}$. This aligns with the finding presented in [132] As the permeability decreases, this relationship becomes less clear, suggesting that the leading term should be $t^{-\theta}$, where $0 \leq \theta \leq 0.5$.

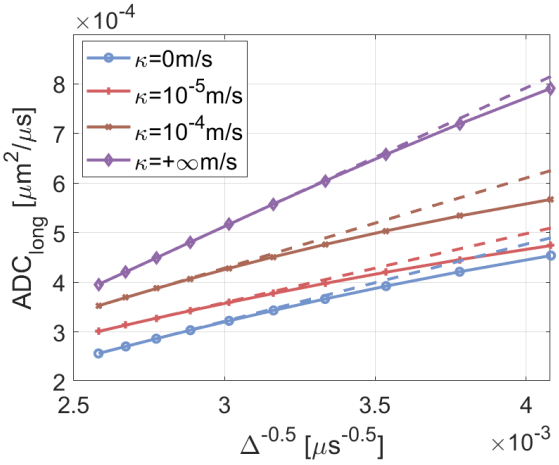

Figure 2.11: ADC_{long} as a function of $\Delta^{-0.5}$. The simulations are performed on Ω^I, with the gradient direction fixed in $[\sqrt{2}/2, \sqrt{2}/2, 0]^T$, using the new method with length scale cut-off $L_s = 1\mu$m ($N_{eig} = 538$). The blue, red, brown and purple solid lines represent $\kappa = 0$ m/s, $\kappa = 10^{-5}$ m/s, $\kappa = 10^{-4}$ m/s and $\kappa = +\infty$ m/s, respectively. The dashed lines represent the linear fit, using the three highest simulated Δ values, 130ms, 140ms and 150ms. The markers represent values computed by the new method.

In fig. 2.12, we plot a normalized time-dependent ADC, denoted as ADC_{norm}, against κ^{-1} in logarithm, with the longest simulated sequence PGSE$(5\text{ms}, 150\text{ms})$. The normalized ADC is defined as

$$\text{ADC}_{\text{norm}} = \frac{\text{ADC}_{\text{long}} - \text{ADC}_{\text{imp}}}{\text{ADC}_{\text{free}} - \text{ADC}_{\text{imp}}}, \tag{2.33}$$

where ADC_{free} is the ADC when $\kappa = +\infty$ m/s and ADC_{imp} is the ADC in the presence of impermeable interfaces ($\kappa = 0$ m/s). This choice of normalization eliminates the effect of interface shapes and allows to study purely the impact of permeability value on the ADC. At two ends of permeability, we have the asymptotic behaviors:

$$\lim_{\kappa \to +\infty} \text{ADC}_{\text{norm}} = 1, \tag{2.34}$$

$$\lim_{\kappa \to 0} \text{ADC}_{\text{norm}} = 0. \tag{2.35}$$

We can observe that $\text{ADC}_{\text{norm}}^{-1}$ shows different rates at low and high permeabilities. When $\kappa \leq 8 \times 10^{-6}$ m/s, we have $\text{ADC}_{\text{norm}}^{-1} \propto \kappa^{-1.1045}$, whereas when $\kappa \geq 3 \times 10^{-5}$ m/s, $\text{ADC}_{\text{norm}}^{-1} \propto \kappa^{-0.5934}$.

In summary, at low permeability, the dependence rate of $\text{ADC}_{\text{norm}}^{-1}$ becomes $\kappa^{-1.1045}$, which is similar to eq. (2.32).. As high permeability, we observe that $\text{ADC}_{\text{norm}}^{-1} \propto \kappa^{-0.5934}$ and $\text{ADC}_{\text{long}} \propto 1/\sqrt{t}$.

2.4.3 Neurite Exchange Imaging (NEXI) evaluation

Neurite Exchange Imaging (NEXI) is a state-of-the-art diffusion MRI compartment signal model to estimate the volume fractions and water exchange time between compartments in the brain gray matter, as presented in section 1.4.4. It fits the direction-averaged signals to estimate the five parameters: $\boldsymbol{p} = [f, D_{i,\parallel}, D_{e,\parallel}, D_{e,\perp}, t_{ex}]$, where f is the volume fraction of intra-neurite space. $D_{i,\parallel}$ is the parallel diffusivity of the intra-neurite space. $D_{e,\parallel}$ and $D_{i,\parallel}$ are the parallel and perpendicular diffusivity of the extra-neurite space. t_{ex} is a temporal quantity to characterize the water exchange rate. The details of NEXI expression refer to section 1.4.4.

To illustrate what this model effectively quantifies and to understand the relationship between t_{ex} and κ, we perform the simulations on a simple geometry Ω^{nexi}, containing four straight cylinders encapsulated in a tight wrapped ECS, as shown in fig. 2.13. The height of the cylinders is 30μm. The radii are selected to be small, ranging from 0.5μm to 0.9μm. The volume fraction of the neurites is 63.3%. We adopt one of the experimental settings consistent with the original NEXI paper[100]:

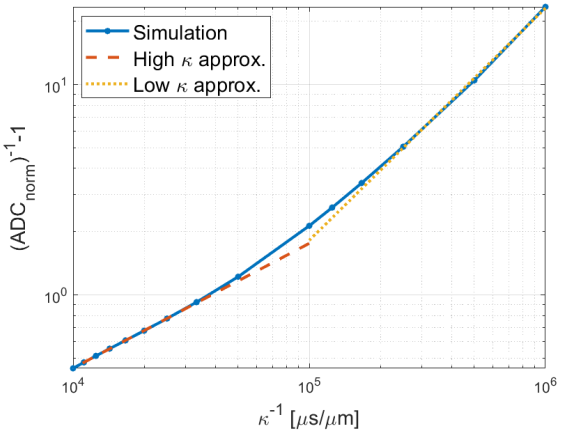

Figure 2.12: $\text{ADC}_{\text{norm}}^{-1} - 1$ as a function of κ^{-1} in logarithm. The simulations are performed on Ω^I, with the gradient direction fixed in $[\sqrt{2}/2, \sqrt{2}/2, 0]^T$, using the new method with length scale cut-off $L_s = 1\mu$m ($N_{eig} = 538$). The sequence is PGSE$(5\text{ms}, 150\text{ms})$. The blue solid line represents the simulated ADC, the dashed red line represents the linear fit at high permeability values and the dotted yellow line represents the linear fit at low permeability values. The slopes of the low and high permeability fitted lines are -1.1045 and -0.5934, respectively. The markers represent values computed by the new method.

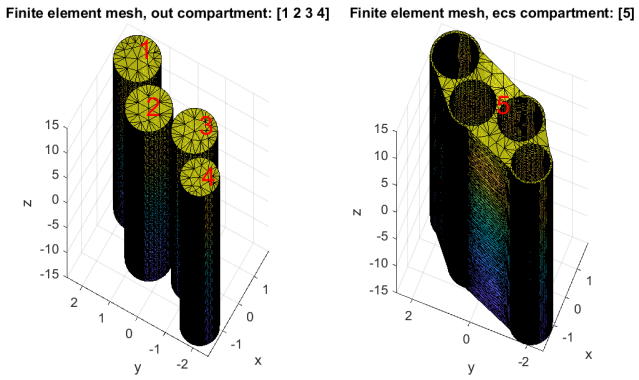

Figure 2.13: Geometry Ω^{nexi} for NEXI estimation. Left: finite element mesh of the four cylinders, with a height of 30μm and a radius from 0.5μm to 0.9μm; Right: finite element mesh of the tight wrapped ECS. The volume fraction of the ECS is 36.7%. The whole domain contains 65,720 nodes and 191,403 elements, among them, there are 41,362 nodes and 128,836 elements in ECS.

- 64 gradient directions uniformly distributed in unit sphere;
- One PGSE sequence is applied, with $\delta = 4.5$ms and $\Delta = 20$ms;
- Seven shells at b-values$= [1, 2.5, 4, 5.5, 7, 8.5, 10] \times 10^3$ s/mm^2;
- Seven tested permeability values $[10^{-6}, 5\times10^{-6}, 7.5\times10^{-6}, 10^{-5}, 2\times10^{-5}, 5\times10^{-5}, 10^{-4}]$ m/s;
- Length scale cut-off $L_s = 1\mu$m, i.e. $N_{eig} = 341$.

This choice of diffusion time limits the amount of spins hitting the upper and bottom outer boundaries.

To avoid local minimum due to the non-convex optimization, We fit NEXI model by an exhaustive search within a saved signal library. The NEXI signal library is populated along all five parameters: $f \in [0, 2, 0.8]$, with an equal spacing 0.01, $D_{i,\parallel} \in [1, 2] \times 10^{-3}$ mm^2/s, with an equal spacing 0.05, $D_{e,\parallel} \in [0.1, 2] \times 10^{-3}$ mm^2/s, with an equal spacing 0.05, $D_{e,\perp} \in [0, 1] \times 10^{-3}$ mm^2/s with an equal spacing 0.1, and $t_{ex}/\Delta \in [0.1, 6.1]$, with an equal spacing 0.1. Besides, one constraint $D_{e,\parallel} > D_{e,\perp}$

is applied. We pick the model parameters combination $\mathbf{p} = [f, D_{i,\parallel}, D_{e,\parallel}, D_{e,\perp}, t_{ex}]^T$ that yields the minimum mean squared error of the direction-averaged signals as the best fit.

Figure 2.14a illustrates the estimated exchange time t_{ex} against κ in logarithm. It is clear that within the range of 10^{-6} m/s $\leq \kappa \leq 2 \times 10^{-5}$ m/s, there is a linear relation between them, i.e. $t_{ex} \propto \kappa^{-1}$. It suggests that NEXI can be effectively used to probe the permeability within this range.

Figure 2.14b shows the estimated volume fraction f against κ. Typically, we obtain an overestimation for f when $\kappa \leq 5 \times 10^{-6}$ m/s.

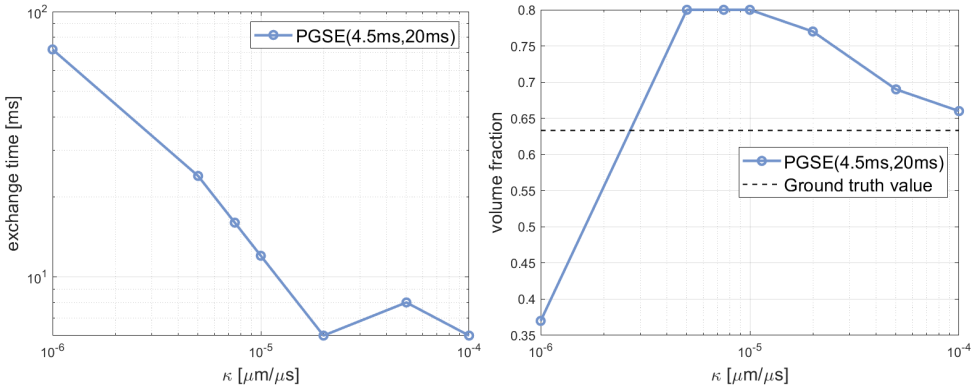

(a) Estimated exchange time t_{ex} against κ in logarithm.

(b) Estimated volume fraction against κ.

Figure 2.14: Estimated parameters of NEXI as functions of κ.The circles represent the estimated values at permeability of 10^{-6} m/s, 5×10^{-6} m/s, 8×10^{-6} m/s, 10^{-5} m/s, 2×10^{-5} m/s, 5×10^{-5} m/s and 10^{-4} m/s.The dashed black line on the right plot is the ground truth volume fraction value ($f = 63.3\%$).

2.5 Discussion

The Numerical Matrix Formalism method produces a diffusion MRI signal representation using the Laplace eigenfunctions basis computed on a domain with permeable interfaces. In this work, we formulated a new representation of the diffusion MRI signal using the Laplace eigenfunctions in the same domain while making the interfaces impermeable. This means our new method can use the same set of eigenfunctions for many different values of permeability, thus saving computational time in the eigendecomposition step. While the new method requires more eigenfunctions than the original Numerical Matrix Formalism method to achieve the same accuracy, we have shown that if the permeability is not too high (while still staying in the realistic range for biological cell membranes), the total computational time is still significantly lower than the original Numerical Matrix Formalism method.

The reduction in computational time makes possible the study of permeability effects on diffusion MRI and the evaluation of microstructure estimation methods on complex geometry via numerical simulations. Using the new formulation, we conduct a study on the permeability effect and demonstrate that the permeable diffusion MRI signals can be approximated by an exponential relation across a wide range of permeabilities. When the gradient strength is low, the permeability effect is negligible for the typical axon permeability value 10^{-5} m/s. The ratio between permeable signals and impermeable signals is higher than 90%. Therefore, the impermeable membranes assumption for diffusion MRI compartment signal models based on the low b-values should hold. When the gradient strength is high, the signals are sensitive to the permeability even at short diffusion time, which poses new challenges to microstructural imaging at high b-values. In the long time limit, the ADC exhibits different dependence rates between high and low permeabilities. In addition, as permeability increases, we have $\text{ADC}_{\text{long}} \propto 1/\sqrt{t}$. Even though in practice, we could not obtain S_{free} and S_{imp} or ADC_{free} and ADC_{imp}, these observations may aid in the development of new microstructure estimation methods.

The equivalence is proved for the PGSE sequence, it can easily be extended to other sequences, which is valuable for sequences specifically designed to measure permeability. An example is the filter-exchange imaging[59], which applies a double PGSE sequence to indirectly probe the permeability, by firstly eliminating the ECS contribution through the first PGSE sequence.

We employ the new method to assess the NEXI model. Numerical analysis indicates a strong correlation between permeability and the water exchange time of the NEXI model.

Chapter 3

Asymptotic expansion of diffusion MRI and ADC accounting for geometrical deformations

Contents

Chapter Overview

In this chapter, we develop asymptotic expansions of the diffusion MRI signal and the ADC accounting for bending and twisting deformations, derived from the Bloch-Torrey PDE and the HADC model. This work is inspired by how the papers[134, 135] treat heart movement in cardiac diffusion MRI.

In section 3.2, we first present the HADC model, and give the analytical expressions of bending and twisting deformations. We derive the transformed Bloch-Torrey PDE and the transformed HADC model accounting for these two deformations, and expand the solutions of those transformed PDEs as a second-order asymptotic series in deformation parameters. We conduct numerical simulations in section 3.4, to validate our asymptotic expansions and illustrate the effects of the geometrical deformations. The simulations suggest that: (1) For both the HADC model and the Bloch-Torrey PDE, at least second-order corrections are needed to significantly improve the accuracy; (2) From the HARDI

plots we observe that bending causes the ADC and signals to be less directional whereas twisting will rotate their maximal direction; (3) the analysis of computational time demonstrates the efficiency of the asymptotic expansions in terms of performing simulations when adjusting geometrical parameters.

This work contributes to explicitly linking the diffusion MRI signal to cellular structures and providing a numerical tool to study the impact of shape imperfections on the diffusion MRI signal and the ADC.

Compared to the published version[2], I make the following modifications: (1) I extend the asymptotic expansion of the Bloch-Torrey PDE by including the permeable case. I provide the numerical results of the asymptotic expansion of the Bloch-Torrey PDE using $\kappa = 10^{-5}\,\mathrm{m/s}$; (2) I extend the asymptotic expansions to the case when both deformations are applied, and add this case in the numerical results; (3) I add section 3.4.4 that compares the computational time to show the efficiency of the asymptotic expansions; (4) I change to use an alternative form of the HADC model, which requires a less stringent time step to maintain the same accuracy during numerical simulations.

3.1 Introduction

Due to the complexity of solving Bloch Torrey PDE, the predominant approach up to now has been adding the diffusion MRI signal from simple geometrical components and extracting model parameters of interest. Numerous tissue compartment models subdivide the tissue into compartments described by sticks, anisotropic Gaussian space, spheres, ellipsoids, cylinders, and the extracellular space (ECS)[99, 102, 136–141]. Some parameters of interest include axon diameter and orientation, neurite density, dendrite structure, the volume fraction and size distribution of cylinder and sphere components and the effective diffusion coefficient or tensor of the ECS could be retrieved from the model's compartments[142].

In the brain white matter microstructure estimation, the axons or the brain white matter fibers are modeled most either by a bundle of sticks, such as the NODDI model[98], or a collection of cylinders, in the same direction or dispersion in the orientation, such as the ActiveAx$_{\mathrm{ADD}}$ model[27]. These assumptions neglect the geometrical imperfection of realistic fiber shape on the diffusion MRI signal, including diameters variations[143], irregular section shapes[144], undulation[145], bending[146] etc, which may cause inaccuracy issue in some MRI experimental settings[147, 148]. In the work by Lee *et al.*[149], an overestimation of axon diameter was found at low b-values due to the undulation of axons.

The purpose of this chapter is to propose a reduced model to facilitate the studies on geometrical deformation and to further reveal the relationship between the tissue geometrical parameters and the diffusion MRI signal in the brain white matter via the simulations. Relevant works can be found in the works[110, 149]. In the paper[110], Olsen *et al.* analyzed the impact of realistic neurite shapes at high b-values via Monte-Carlo simulation on numerical neuron phantoms.

In this chapter, we continue the Bloch-Torrey PDE-based simulation work to further reveal the relationship between the cellular structure and the diffusion MRI signal in the brain white matter. We analyze the Bloch-Torrey PDE and the HADC model in the context of parameterized deformation mappings, starting from a canonical configuration. The canonical configuration we have in mind is a set of straight parallel axons contained in the extra-cellular space. Our idea is to model realistic axons as spatial deformations of canonical configurations of parallel axons.

To be more concrete, we focus on two analytically defined deformations: bending and twisting. We will derive asymptotic models of the diffusion MRI signal and the ADC where the asymptotic parameter indicates the extent of the geometrical deformation. The purpose of this work is to relate the diffusion MRI signal more directly with tissue geometrical parameters.

One potential application of this asymptotic model is to serve as a validation model to study the robustness of the brain white matter microstructure imaging, such as axons radii and volume fraction estimation, towards shape imperfections. Furthermore, one may use these asymptotic models to establish the relation between the deformations and diffusion MRI signals.

This work uses similar mathematical tools as several previous papers focused on the mathematical analysis of the Bloch-Torrey PDE subject to geometrical deformations. In[150], a new mathematical model of Bloch-Torrey PDE in moving and deforming media was introduced. In[134], a rigorous mathematical formalism was introduced to quantify the effect of macroscopic-scale tissue motion

and deformation in cardiac diffusion MRI. In[135], a new model of the ADC of cardiac diffusion MRI was formulated in the presence of microscopic-scale tissue motion and deformation.

3.2 Theory

In this section, we briefly present the HADC model and give the definition of two analytical deformations.

3.2.1 Geometrical description

To reveal the relationship between the geometrical structure and the diffusion MRI signal, we propose to describe the brain white matter fibers as a deformation of a canonical configuration. For ease of mesh generation, we ignore myelin sheathes and consider the canonical the brain white matter configuration as a set of straight parallel axons encapsulated in one extra-cellular space.

Let the whole canonical simulation domain be $\mathcal{C} = \bigcup_{i=1}^{N_{cmpt}} \mathcal{C}_i \in \mathbb{R}^3$, containing $N_{cmpt} - 1$ axons $\{\mathcal{C}_i\}_{1\leq i\leq N_{cmpt}-1}$ and one ECS $\mathcal{C}_{N_{cmpt}}$, without any overlap. The interface between one axon and ECS is denoted by $\mathcal{F}_{ij} = \mathcal{C}_i \cap \mathcal{C}_j$ for $(i,j) \in \{1,\ldots,N_{cmpt}-1\} \times \{N_{cmpt}\}$ or $(i,j) \in \{N_{cmpt}\} \times \{1,\ldots,N_{cmpt}-1\}$. And the interfaces between axons are $\mathcal{F}_{ij} = \emptyset$, for $i \neq j$, $(i,j) \in \{1,\ldots,N_{cmpt}-1\}^2$. Let $\partial\mathcal{C}$ be the outer boundary of the domain $\mathcal{C}$, we denote the restriction of the outer boundary in compartment $\mathcal{C}_i$ by $\mathcal{B}_i = \partial\mathcal{C} \cap \mathcal{C}_i$, $i \in \{1,\ldots,N_{cmpt}\}$.

We denote the simulation domain after applying analytical deformation as $\Omega = \bigcup_{i=1}^{N_{cmpt}} \Omega_i \in \mathbb{R}^3$, and the interfaces and restriction of the outer boundary of the deformed domain become Γ_{ij} and Σ_i, respectively.

The Bloch Torrey PDE on the deformed domain Ω remains the same as eqs. (1.27) to (1.31) defined in section 1.3.2.

3.2.2 HADC Model

When water exchange between compartments is negligible, a homogenized model, called the HADC model, is derived, to compute time-dependent apparent diffusion coefficient using homogenization techniques[151]. In this chapter, we use an alternative formula of the HADC model, which differs from the one presented in the original paper. This alternative formula requires less finer time steps in numerical computation. The ADC of compartment Ω_i by the HADC model is

$$\mathsf{ADC}^i = \frac{\mathcal{D}^i}{|\Omega_i| \int_0^{T_E} F(t)^2 dt} \int_0^{TE} F(t) \int_{\partial\Omega_i} \omega^i(\mathbf{r},t)\,(\mathbf{u_g}\cdot\mathbf{n}(\mathbf{r}))\,ds_{\mathbf{r}}dt, \tag{3.1}$$

where $\mathbf{u_g}$ is the diffusion-encoding gradient direction, $\mathbf{n}$ is the outward normal, ω^i is the solution of the non-homogeneous diffusion equation on the deformed domain Ω with homogeneous Neumann boundary condition and zero initial condition:

$$\frac{\partial}{\partial t}\omega^i(\mathbf{r},t) = \nabla\cdot\mathcal{D}^i\nabla\omega^i(\mathbf{r},t) - f(t)\mathbf{u_g}\cdot\mathbf{r}, \mathbf{r}\in\Omega_i \tag{3.2}$$

$$\mathcal{D}^i\nabla\omega^i(\mathbf{r},t)\cdot\mathbf{n}^i(\mathbf{r}) = 0, \quad \mathbf{r}\in\partial\Omega_i \tag{3.3}$$

$$\omega^i(\mathbf{r},0) = 0, \quad \mathbf{r}\in\Omega_i, \tag{3.4}$$

The above set of equations, eqs. (3.2) to (3.4), comprise the HADC model.

The ADC of the whole domain Ω is determined by the volume-weighted sum of each compartment:

$$\mathsf{ADC} = \sum_{i=1}^{N_{cmpt}} |\Omega_i|\mathsf{ADC}^i/|\Omega|. \tag{3.5}$$

See appendix A.1 for the derivation of this alternative formula of the HADC model.

3.2.3 Canonical configuration and analytical geometrical deformations

The two basic types of deformations that we implement in this chapter are (1) bending, and (2) twisting. Both types of deformations will be described by one single parameter, called α_b and α_t. The geometrical structure of the brain white matter fibers will be defined by these two deformation parameters.

Let $\mathbf{r}$ be the space variable in the deformed (by bending, twisting, or both of them) configuration, whose domain is Ω. The coordinate transformation,

$$\mathcal{T} : \mathcal{C} \to \Omega,$$

maps the canonical configuration defined on $\mathcal{C}$ to the deformed configuration on Ω:

$$\mathbf{x} \to \mathbf{r} = \mathcal{T}(\mathbf{x}).$$

Bending on the $x - z$ plane with a bending parameter α_b is defined by

$$\mathcal{T}_b : \begin{bmatrix} x \\ y \\ z \end{bmatrix} \to \begin{bmatrix} x + \alpha_b z^2 \\ y \\ z \end{bmatrix}. \tag{3.6}$$

Twisting around the z-axis with a twisting parameter α_t is defined by

$$\mathcal{T}_t : \begin{bmatrix} x \\ y \\ z \end{bmatrix} \to \begin{bmatrix} \cos(\alpha_t z) & -\sin(\alpha_t z) & 0 \\ \sin(\alpha_t z) & \cos(\alpha_t z) & 0 \\ 0 & 0 & 1 \end{bmatrix} \begin{bmatrix} x \\ y \\ z \end{bmatrix}. \tag{3.7}$$

The subscript b indicates this term is related to bending and t indicates this term is related to twisting. When both two deformations are applied, the canonical configuration will firstly perform bending, then twisting:

$$\mathcal{T}_{tb} := \mathcal{T}_t \circ \mathcal{T}_b : \begin{bmatrix} x \\ y \\ z \end{bmatrix} \to \begin{bmatrix} \cos(\alpha_t z) & -\sin(\alpha_t z) & 0 \\ \sin(\alpha_t z) & \cos(\alpha_t z) & 0 \\ 0 & 0 & 1 \end{bmatrix} \begin{bmatrix} x + \alpha_b z^2 \\ y \\ z \end{bmatrix}. \tag{3.8}$$

It is worth mentioning that the order of deformation is just a choice we have taken. Switching this order would modify the transformation operator, but the asymptotic derivation process remains valid.

We plot in fig. 3.1 a geometrical configuration of 20 cylindrical axons and the ECS before and after deformation, with two different deformation parameter values. Since all the compartments are the same in height, the bending deformation affects each axon uniformly, whereas the twisting deformation depends on the position in the x-y plane. We can observe that when α_b or α_t reach a value of 0.07, the deformation already exceeds the regime of small deformation, compared to straight configuration. Thus, in this thesis, we limit the maximum deformation parameters to 0.07. By adjusting these deformation parameters, we can emulate a configuration closer to the realistic axons.

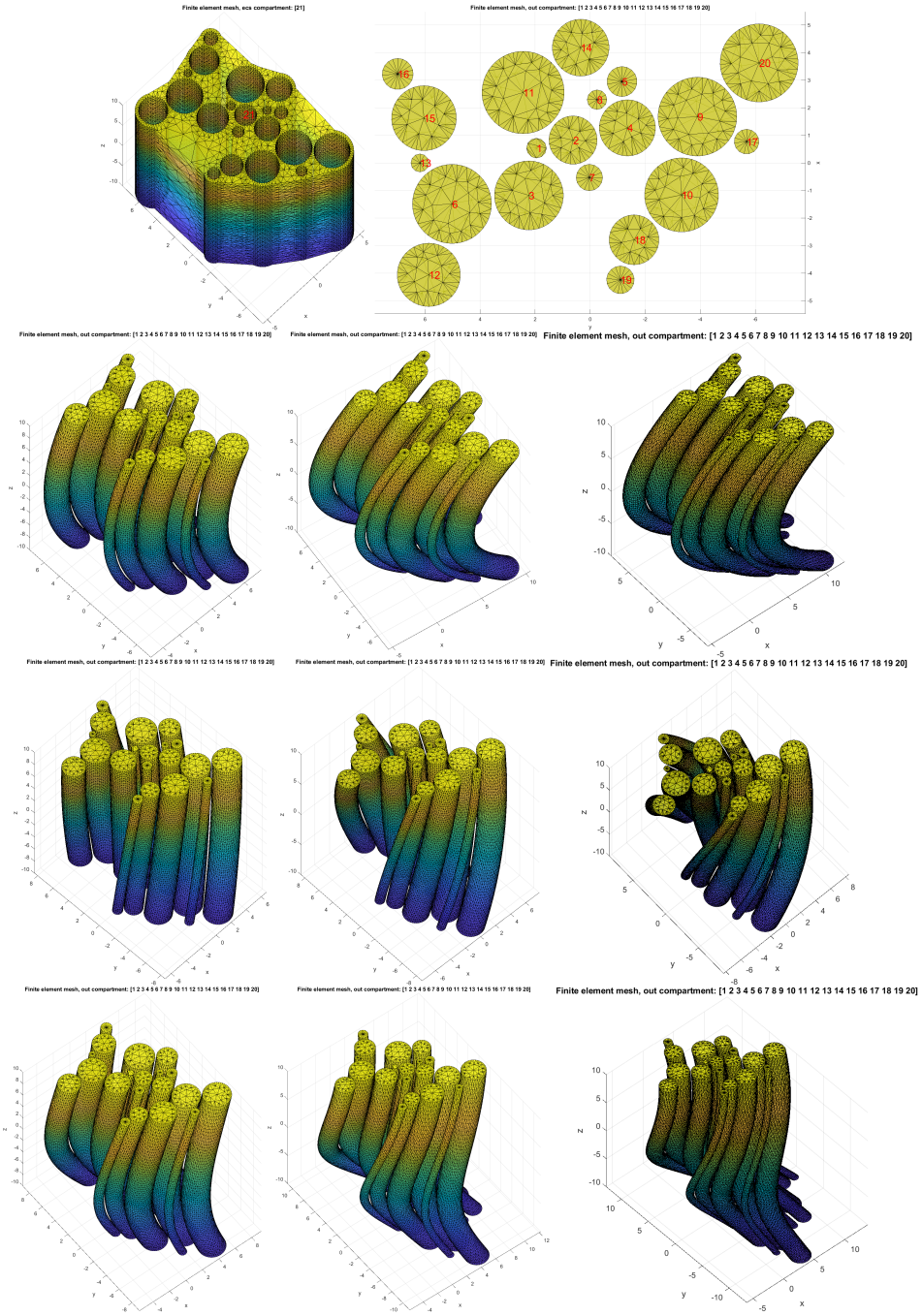

Figure 3.1: First row: canonical configuration, ECS (left), and all 20 cylindrical axons on top view (right).
Second row: 20 cylindrical axons with, bend deformation with $\alpha_b = 0.025$ (left), 20 cylindrical axons with $\alpha_b = 0.05$ (middle), 20 cylindrical axons with $\alpha_b = 0.07$ (right).
Third row: 20 cylindrical axons with, twist deformation with $\alpha_t = 0.025$ (left), 20 cylindrical axons with $\alpha_t = 0.05$ (middle), 20 cylindrical axons with $\alpha_t = 0.07$ (right).
Fourth row: 20 cylindrical axons with, deformation with $\alpha_b = 0.025$ and $\alpha_t = 0.025$ (left), 20 cylindrical axons with $\alpha_b = 0.05$ and $\alpha_t = 0.05$ (middle), 20 cylindrical axons with $\alpha_b = 0.07$ and $\alpha_t = 0.07$ (right).
The radii of all axons are between $0.25\mu m$ and $2\mu m$, the mean radius is $0.9\mu m$, and the height is $20\mu m$.

3.3 Derivation of asymptotic models on the deformation parameter

The main objective of this work is to construct appropriate models to describe the relationship between the deformation parameters α_b, α_t and the diffusion MRI signal as well as the ADC. We will expand the solutions of the Bloch-Torrey PDE and the HADC model as asymptotic series in the deformation parameters α_b and α_t. This approach is expected to work well in the regime of small deformations, i.e. $\alpha_b z \ll 1$ and $\alpha_t z \ll 1$.

3.3.1 Formulation of the PDEs on the canonical configuration

First, we transform the Bloch-Torrey PDE and the HADC model posed on the deformed geometry Ω into PDEs that are posed on the canonical geometry C.

Let J be the Jacobian of the transformation $\mathcal{T}$:

$$J = \begin{bmatrix} \frac{\partial \mathcal{T}}{\partial x} & \frac{\partial \mathcal{T}}{\partial y} & \frac{\partial \mathcal{T}}{\partial z} \end{bmatrix}. \tag{3.9}$$

We define the composite function for the Bloch-Torrey PDE to be $N(\mathbf{x}, t) : \mathcal{C} \to \mathbb{R}$, where

$$N = M \circ \mathcal{T}, \tag{3.10}$$

and for the HADC model to be $\eta(\mathbf{x}, t) : \mathcal{C} \to \mathbb{R}$, where

$$\eta = \omega \circ \mathcal{T}. \tag{3.11}$$

$M(\mathbf{r}, t)$ and $\omega(\mathbf{r}, t)$ are solutions on the deformed domain Ω, thus, $N(\mathbf{x}, t)$ and $\eta(\mathbf{x}, t)$ are the solutions of the respective transformed PDEs.

It is easy to show that the transformed gradient operator of transformed PDE in the i-th compartment is

$$\nabla_{\mathbf{r}} = J^{-T} \nabla_{\mathbf{x}}, \tag{3.12}$$

and the transformed Laplacian operator is

$$\nabla_{\mathbf{r}} \cdot \mathcal{D}^i \nabla_{\mathbf{r}} = \nabla_{\mathbf{x}} \cdot J^{-1} \mathcal{D}^i J^{-T} \nabla_{\mathbf{x}}, \tag{3.13}$$

by performing the chain rule. The matrix J^{-T} is the transpose inverse of the Jacobian matrix.

Thus, we can define the transformed diffusion tensor as:

$$\beta^i := J^{-1} \mathcal{D}^i J^{-T}. \tag{3.14}$$

For the bend deformation, the inverse of the Jacobian matrix is

$$J_b^{-1} = \begin{bmatrix} 1 & 0 & -2\alpha_b z \\ 0 & 1 & 0 \\ 0 & 0 & 1 \end{bmatrix}, \quad \det(J_b) = 1, \tag{3.15}$$

and the transformed diffusion tensor is

$$\beta_b^i = J_b^{-1} \mathcal{D}^i J_b^{-T} = \mathcal{D}^i \begin{bmatrix} 4\alpha_b^2 z^2 + 1 & 0 & -2\alpha_b z \\ 0 & 1 & 0 \\ -2\alpha_b z & 0 & 1 \end{bmatrix}. \tag{3.16}$$

For the twist deformation, the inverse of the Jacobian matrix is

$$J_t^{-1} = \begin{bmatrix} \cos(\alpha_t z) & \sin(\alpha_t z) & \alpha_t y \\ -\sin(\alpha_t z) & \cos(\alpha_t z) & -\alpha_t x \\ 0 & 0 & 1 \end{bmatrix}, \quad \det(J_t) = 1, \tag{3.17}$$

and the transformed diffusion tensor is

$$\beta_t^i = J_t^{-1} \mathcal{D}^i J_t^{-T} = \mathcal{D}^i \begin{bmatrix} \alpha_t^2 y^2 + 1 & -\alpha_t^2 yx & \alpha_t y \\ -\alpha_t^2 yx & \alpha_t^2 x^2 + 1 & -\alpha_t x \\ \alpha_t y & -\alpha_t x & 1 \end{bmatrix}. \tag{3.18}$$

In the case of both two deformations are applied:

$$J_{tb}^{-1} = (J_t J_b)^{-1} = J_b^{-1} J_t^{-1} = \begin{bmatrix} \cos(\alpha_t z) & \sin(\alpha_t z) & \alpha_t y - 2\alpha_b z \\ -\sin(\alpha_t z) & \cos(\alpha_t z) & -\alpha_t x \\ 0 & 0 & 1 \end{bmatrix}, \quad \det(J_{tb}) = 1, \tag{3.19}$$

and the transformed diffusion tensor is

$$\begin{aligned} \beta_{tb} &= (J_t J_b)^{-1} \mathcal{D}^i (J_t J_b)^{-T} \\ &= J_b^{-1} J_t^{-1} \mathcal{D}^i J_t^{-T} J_b^{-T} \\ &= \mathcal{D}^i \begin{bmatrix} 4\alpha_b^2 z^2 + \alpha_t^2 y^2 - 4\alpha_b \alpha_t yz + 1 & -\alpha_t^2 yx + 2\alpha_b \alpha_t xz & -2\alpha_b z + \alpha_t y \\ -\alpha_t^2 yx + 2\alpha_b \alpha_t xz & \alpha_t^2 x^2 + 1 & -\alpha_t x \\ -2\alpha_b z + \alpha_t y & -\alpha_t x & 1 \end{bmatrix}. \end{aligned} \tag{3.20}$$

According to[152], the transformed outward normals on the canonical configuration are the product of the transpose inverse of the Jacobian matrix and the normals on transformed configuration

$$\mathbf{n}^i(\mathbf{r}) = J^{-T} \mathbf{n}^i(\mathbf{x}). \tag{3.21}$$

Using eq. (3.21), the right-hand side of eq. (1.29) becomes

$$\begin{aligned} \kappa^{ij}(M^j(\mathbf{r},t) - M^i(\mathbf{r},t)) &= \kappa^{ij} \left(M^j(\mathbf{r},t)\mathbf{n}^i(\mathbf{r}) + M^i(\mathbf{r},t)(-\mathbf{n}^i(\mathbf{r})) \right) \cdot \mathbf{n}^i(\mathbf{r}) \\ &= J^{-1} \kappa^{ij} J^{-T} \mathbf{n}^i(\mathbf{x}) \cdot \mathbf{n}^i(\mathbf{x}) (N^j(\mathbf{x},t) - N^i(\mathbf{x},t)). \end{aligned} \tag{3.22}$$

We define the transformed permeability coefficient as

$$\mu^{ij} := J^{-1} \kappa^{ij} J^{-T} \mathbf{n}^i(\mathbf{x}) \cdot \mathbf{n}^i(\mathbf{x}). \tag{3.23}$$

Combining eqs. (3.14) and (3.23), the transformed Bloch-Torrey PDE in $\mathcal{C}$ is then:

$$\frac{\partial}{\partial t} N^i(\mathbf{x},t) = \left(\nabla \cdot \beta^i \nabla - \imath\gamma f(t) \mathbf{g} \cdot \mathcal{T}(\mathbf{x}) \right) N^i(\mathbf{x},t), \mathbf{x} \in \mathcal{C}_i, \tag{3.24}$$

$$\beta^i \nabla N^i(\mathbf{x},t) \cdot \mathbf{n}^i(\mathbf{x}) = -\beta^j \nabla N^j(\mathbf{x},t) \cdot \mathbf{n}^j(\mathbf{x}), \quad \mathbf{x} \in \mathcal{F}_{ij}, \tag{3.25}$$

$$\beta^i \nabla N^i(\mathbf{x},t) \cdot \mathbf{n}^i(\mathbf{x}) = \mu^{ij}(N^j(\mathbf{x},t) - N^i(\mathbf{x},t)), \quad \mathbf{x} \in \mathcal{F}_{ij}, \tag{3.26}$$

$$\beta^i \nabla N^i(\mathbf{x},t) \cdot \mathbf{n}^i(\mathbf{x}) = 0, \quad \mathbf{x} \in \mathcal{B}_i, \tag{3.27}$$

$$N^i(\mathbf{x},0) = \rho, \quad \mathbf{x} \in \mathcal{C}_i, \tag{3.28}$$

The transformed HADC model is:

$$\frac{\partial}{\partial t} \eta^i(\mathbf{x},t) = \nabla \cdot \beta^i \nabla \eta^i(\mathbf{x},t) - f(t) \mathbf{u_g} \cdot \mathcal{T}(\mathbf{x}), \mathbf{x} \in \Omega_i \tag{3.29}$$

$$\beta^i \nabla \eta^i(\mathbf{x},t) \cdot \mathbf{n}^i(\mathbf{x}) = 0, \quad \mathbf{x} \in \partial\Omega_i \tag{3.30}$$

$$\eta^i(\mathbf{x},0) = 0, \quad \mathbf{x} \in \Omega_i. \tag{3.31}$$

3.3.2 Asymptotic expansion of HADC according to one deformation parameter

We now expand the solution of the HADC model in one deformation parameter (α_b or α_t) and match the terms to get the first three terms of the asymptotic expansion.

We write the solution η of eqs. (3.29) to (3.31) as a three-term asymptotic expansion:

$$\eta_k(\mathbf{x},t) = \eta_{k,0}(\mathbf{x},t) + \alpha_k \eta_{k,1}(\mathbf{x},t) + \alpha_k^2 \eta_{k,2}(\mathbf{x},t) + \mathcal{O}(\alpha_k^2),$$

where $k \in \{b,t\}$. Replacing eq. (3.29) by the expansion above, we obtain:

$$\partial_t \eta_{k,0} + \alpha_k \partial_t \eta_{k,1} + \alpha_k^2 \partial_t \eta_{k,2} = \nabla \cdot \beta^i \nabla \eta_{k,0} + \alpha_k \nabla \cdot \beta^i \nabla \eta_{k,1} + \alpha_k^2 \nabla \cdot \beta^i \nabla \eta_{k,2} - f(t) \mathbf{u_g} \cdot \mathcal{T}(\mathbf{x}).$$

Using eq. (3.16) for the bending transformation, the transformed Laplacian operator is:

$$\begin{aligned}\nabla \cdot \beta_b^i \nabla &= \nabla \cdot \left[\mathcal{D}^i \begin{bmatrix} 4\alpha_b^2 z^2 + 1 & 0 & -2\alpha_b z \\ 0 & 1 & 0 \\ -2\alpha_b z & 0 & 1 \end{bmatrix} \begin{bmatrix} \partial_x \\ \partial_y \\ \partial_z \end{bmatrix} \right] \\ &= \nabla \cdot \mathcal{D}^i \nabla + \mathcal{D}^i \left(\alpha_b(-2\partial_x - 4z\partial_{xz}) + \alpha_b^2(4z^2\partial_{xx}) \right).\end{aligned} \tag{3.32}$$

To simplify the notation, we define two second-order differential operators:

$$\mathbf{K}_{b,1}^i := \mathcal{D}^i(-2\partial_x - 4z\partial_{xz}), \;\; \mathbf{K}_{b,2}^i := \mathcal{D}^i 4z^2\partial_{xx}. \tag{3.33}$$

Similarly, in the case of the twisting transformation, using eq. (3.18), the transformed Laplacian operator is:

$$\begin{aligned}\nabla \cdot \beta_t^i \nabla &= \nabla \cdot \left[\mathcal{D}^i \begin{bmatrix} \alpha_t^2 y^2 + 1 & -\alpha_t^2 yx & \alpha_t y \\ -\alpha_t^2 yx & \alpha_t^2 x^2 + 1 & -\alpha_t x \\ \alpha_t y & -\alpha_t x & 1 \end{bmatrix} \begin{bmatrix} \partial_x \\ \partial_y \\ \partial_z \end{bmatrix} \right] \\ &= \nabla \cdot \mathcal{D}^i \nabla + \mathcal{D}^i \left(2\alpha_t(y\partial_{xz} - x\partial_{yz}) + \alpha_t^2(y^2\partial_{xx} - y\partial_y - 2yx\partial_{xy} - x\partial_x + x^2\partial_{yy}) \right).\end{aligned} \tag{3.34}$$

Also, we define:

$$\mathbf{K}_{t,1}^i := \mathcal{D}^i(2y\partial_{xz} - 2x\partial_{yz}), \;\; \mathbf{K}_{t,2}^i := \mathcal{D}^i(y^2\partial_{xx} - y\partial_y - 2yx\partial_{xy} - x\partial_x + x^2\partial_{yy}). \tag{3.35}$$

So the transformed Laplacian operator acts as the first and the second correction operators for the Laplacian:

$$\nabla \cdot \beta_k^i \nabla = \nabla \cdot \mathcal{D}^i \nabla + \alpha_k \mathbf{K}_{k,1}^i + \alpha_k^2 \mathbf{K}_{k,2}^i, \tag{3.36}$$

where $k \in \{b, t\}$.

Using eq. (3.16) for the bending transformation, the transformed gradient operator is:

$$\beta_b^i \nabla = \mathcal{D}^i \begin{bmatrix} 4\alpha_b^2 z^2 + 1 & 0 & -2\alpha_b z \\ 0 & 1 & 0 \\ -2\alpha_b z & 0 & 1 \end{bmatrix} \begin{bmatrix} \partial_x \\ \partial_y \\ \partial_z \end{bmatrix} = \mathcal{D}^i \nabla + \mathcal{D}^i \left(\alpha_b \begin{bmatrix} -2z\partial_z \\ 0 \\ -2z\partial_x \end{bmatrix} + \alpha_b^2 \begin{bmatrix} 4z^2\partial_x \\ 0 \\ 0 \end{bmatrix} \right). \tag{3.37}$$

Similarly, we define two correction operators for the transformed gradient operator:

$$\mathbf{G}_{b,1}^i := \mathcal{D}^i \begin{bmatrix} -2z\partial_z \\ 0 \\ -2z\partial_x \end{bmatrix}, \;\; \mathbf{G}_{b,2}^i := \mathcal{D}^i \begin{bmatrix} 4z^2\partial_x \\ 0 \\ 0 \end{bmatrix}. \tag{3.38}$$

For the twist transformation, using eq. (3.18), the transformed gradient operator is:

$$\beta_t^i \nabla = \mathcal{D}^i \begin{bmatrix} \alpha_t^2 y^2 + 1 & -\alpha_t^2 yx & \alpha_t y \\ -\alpha_t^2 yx & \alpha_t^2 x^2 + 1 & -\alpha_t x \\ \alpha_t y & -\alpha_t x & 1 \end{bmatrix} \begin{bmatrix} \partial_x \\ \partial_y \\ \partial_z \end{bmatrix} = \mathcal{D}^i \nabla + \mathcal{D}^i \left(\alpha_t \begin{bmatrix} y\partial_z \\ -x\partial_z \\ y\partial_x - x \end{bmatrix} + \alpha_t^2 \begin{bmatrix} y^2\partial_x - xy\partial_y \\ x^2\partial_y - xy\partial_x \\ 0 \end{bmatrix} \right). \tag{3.39}$$

Also, we define:

$$\mathbf{G}_{t,1}^i := \mathcal{D}^i \begin{bmatrix} y\partial_z \\ -x\partial_z \\ y\partial_x - x \end{bmatrix}, \;\; \mathbf{G}_{t,2}^i := \mathcal{D}^i \begin{bmatrix} y^2\partial_x - xy\partial_y \\ x^2\partial_y - xy\partial_x \\ 0 \end{bmatrix}. \tag{3.40}$$

The expansion of the transformation operator $\mathcal{T}(\mathbf{x})$ until the second-order is

$$\mathcal{T}(\mathbf{x}) = \mathbf{x} + \alpha_k \mathbf{P}_{k,1} + \alpha_k^2 \mathbf{P}_{k,2}, \tag{3.41}$$

where $k \in \{b, t\}$,

$$\mathbf{P}_{b,1} = \begin{bmatrix} z^2 \\ 0 \\ 0 \end{bmatrix}, \; \mathbf{P}_{b,1} = [0]_{3\times 1}, \tag{3.42}$$

and

$$\mathbf{P}_{t,1} = \begin{bmatrix} -yz \\ xz \\ 0 \end{bmatrix}, \mathbf{P}_{t,2} = \begin{bmatrix} -xz^2 \\ -yz^2 \\ 0 \end{bmatrix}, \tag{3.43}$$

using Taylor expansion to trigonometrical functions. It is evident that for twisting deformation, the error bound of the Taylor expansion depends on both the twisting parameters α_t and the length of axons. Therefore, for the twisting deformation, in the regime of large deformation (long axons or large twisting transformation value), a higher asymptotic order is required to obtain accurate results.

For simplicity of notation, we note the normals on the canonical configuration as $\mathbf{n}^i$ below, and except for the initial condition equation, we note $\eta^i_{k,0}(\mathbf{x},t)$, $\eta^i_{k,1}(\mathbf{x},t)$ and $\eta^i_{k,2}(\mathbf{x},t)$ as $\eta^i_{k,0}$, $\eta^i_{k,1}$ and $\eta^i_{k,2}$, respectively.

Finally, we obtain the following equations after matching the terms α^j_k, with $j = 0, 1, 2$ and $k \in \{b, t\}$.

For α^0_k, we get the solution of the HADC on the canonical configuration:

$$\begin{aligned}
\frac{\partial}{\partial t}\eta^i_{k,0} &= \nabla \cdot \mathcal{D}^i \nabla \eta^i_{k,0} - f(t)\mathbf{u_g} \cdot \mathbf{x}, \mathbf{x} \in \mathcal{C}_i, && (3.44)\\
\mathcal{D}^i \nabla \eta^i_{k,0} \cdot \mathbf{n}^i &= 0, \qquad \mathbf{x} \in \partial\mathcal{C}_i, && (3.45)\\
\eta^i_{k,0}(\mathbf{x},0) &= 0, \qquad \mathbf{x} \in \mathcal{C}_i. && (3.46)
\end{aligned}$$

For α^1_k, we get a PDE that depends on the solution of the previous equation, $\eta_{k,0}$:

$$\begin{aligned}
\frac{\partial}{\partial t}\eta^i_{k,1} &= \nabla \cdot \mathcal{D}^i \nabla \eta^i_{k,1} + \mathbf{K}^i_{k,1}\eta^i_{k,0} - f(t)\mathbf{u_g} \cdot \mathbf{P}_{k,1}, \mathbf{x} \in \mathcal{C}_i, && (3.47)\\
\mathcal{D}^i \nabla \eta^i_{k,1} \cdot \mathbf{n}^i &= -\mathbf{G}^i_{k,1}\eta^i_{k,0} \cdot \mathbf{n}^i, \qquad \mathbf{x} \in \partial\mathcal{C}_i, && (3.48)\\
\eta^i_{k,1}(\mathbf{x},0) &= 0, \qquad \mathbf{x} \in \mathcal{C}_i. && (3.49)
\end{aligned}$$

For α^2_k, we get a PDE that depends on the solutions of both the above PDEs:

$$\begin{aligned}
\frac{\partial}{\partial t}\eta^i_{k,2} &= \nabla \cdot \mathcal{D}^i \nabla \eta_{k,2} + \mathbf{K}^i_{k,1}\eta^i_{k,1} + \mathbf{K}^i_{k,2}\eta^i_{k,0} - f(t)\mathbf{u_g} \cdot \mathbf{P}_{k,2}, \mathbf{x} \in \mathcal{C}_i, && (3.50)\\
\mathcal{D}^i \nabla \eta^i_{k,2} \cdot \mathbf{n}^i &= -(\mathbf{G}^i_{k,1}\eta^i_{k,1} + \mathbf{G}^i_{k,2}\eta^i_{k,0}) \cdot \mathbf{n}^i, \qquad \mathbf{x} \in \partial\mathcal{C}_i, && (3.51)\\
\eta^i_{k,2}(\mathbf{x},0) &= 0, \qquad \mathbf{x} \in \mathcal{C}_i. && (3.52)
\end{aligned}$$

3.3.3 Asymptotic expansion of Bloch-Torrey PDE according to one deformation parameter

Similar to the asymptotic expansion of the HADC model, we write the solution $N(\mathbf{x},t)$ of eqs. (3.24) to (3.28) as a three-term expansion:

$$N_k(\mathbf{x},t) = N_{k,0}(\mathbf{x},t) + \alpha_k N_{k,1}(\mathbf{x},t) + \alpha^2_k N_{k,2}(\mathbf{x},t) + \mathcal{O}(\alpha^2_k), \quad k \in \{b,t\}.$$

The transformed Laplacian operator $\nabla\beta^i\nabla$, the transformed gradient operator $\beta^i\nabla$ and the expansion of transformation operator $\mathcal{T}(\mathbf{x})$ here are identical to the case of HADC asymptotic expansion. Only the transformed permeability coefficient is needed to be treated.

For the bend transformation, the expansion of transformed permeability coefficient in α_b is:

$$\begin{aligned}
\mu^{ij}_b &= \kappa^{ij} \begin{bmatrix} 4\alpha^2_b z^2 + 1 & 0 & -2\alpha_b z \\ 0 & 1 & 0 \\ -2\alpha_b z & 0 & 1 \end{bmatrix} \mathbf{n}^i(\mathbf{x}) \cdot \mathbf{n}^i(\mathbf{x}) \\
&= \kappa^{ij} + \kappa^{ij}\left(\alpha_b(-4z\boldsymbol{n_x}^i\boldsymbol{n_z}^i) + \alpha^2_b(4z^2\boldsymbol{n_x}^i\boldsymbol{n_x}^i)\right),
\end{aligned} \tag{3.53}$$

where $\boldsymbol{n_x}^i$ and $\boldsymbol{n_z}^i$ are the x and z components of the normal vector $\mathbf{n}^i(\mathbf{x})$ in the canonical configuration. We define

$$\mu^{ij}_{b,1} := \kappa^{ij}(-4z\boldsymbol{n_x}^i\boldsymbol{n_z}^i), \quad \mu^{ij}_{b,2} := 4\kappa^{ij}z^2\boldsymbol{n_x}^i\boldsymbol{n_x}^i \tag{3.54}$$

Similarly, for the twist transformation, the expansion of transformed permeability coefficient is:

$$\begin{aligned}\mu_t^{ij} &= \kappa^{ij}\begin{bmatrix}\alpha_t^2y^2+1 & -\alpha_t^2yx & \alpha_t y\\ -\alpha_t^2yx & \alpha_t^2x^2+1 & -\alpha_t x\\ \alpha_t y & -\alpha_t x & 1\end{bmatrix}\mathbf{n}^i(\mathbf{x})\cdot\mathbf{n}^i(\mathbf{x})\\ &= \kappa^{ij}+\kappa^{ij}\left(\alpha_t(2y\boldsymbol{n_x}^i\boldsymbol{n_z}^i-2x\boldsymbol{n_y}^i\boldsymbol{n_z}^i)+\alpha_t^2(y^2\boldsymbol{n_x}^i\boldsymbol{n_x}^i-2xy\boldsymbol{n_x}^i\boldsymbol{n_y}^i+x^2\boldsymbol{n_y}^i\boldsymbol{n_y}^i)\right).\end{aligned} \tag{3.55}$$

Also, we define

$$\mu_{t,1}^{ij}:=2\kappa^{ij}(y\boldsymbol{n_x}^i\boldsymbol{n_z}^i-x\boldsymbol{n_y}^i\boldsymbol{n_z}^i),\quad \mu_{t,2}^{ij}:=\kappa^{ij}(y^2\boldsymbol{n_x}^i\boldsymbol{n_x}^i-2xy\boldsymbol{n_x}^i\boldsymbol{n_y}^i+x^2\boldsymbol{n_y}^i\boldsymbol{n_y}^i). \tag{3.56}$$

So for $k\in\{b,t\}$, the transformed permeability coefficient also gets two correction terms:

$$\mu_k^{ij}=\kappa^{ij}+\alpha_k\mu_{k,1}^{ij}+\alpha_k^2\mu_{k,2}^{ij}. \tag{3.57}$$

For simplicity of notation, we define the Bloch-Torrey operator $\mathbf{BT}^i:=\nabla\mathcal{D}^i\nabla-\imath\gamma f(t)\mathbf{g}\cdot\mathbf{x}$, and except the initial condition equation, we omit the variable dependence $(\mathbf{x},t)$ for all the orders of magnetizations.

We obtain the following equations after matching for α_k^j, with $j=0,1,2$, and $k\in\{b,t\}$:

For α_k^0, this is the solution of the Bloch-Torrey PDE on the canonical geometry $\mathcal{C}_i$:

$$\frac{\partial}{\partial t}N_{k,0}^i = \mathbf{BT}^iN_{k,0}^i, \qquad \mathbf{x}\in\mathcal{C}_i, \tag{3.58}$$

$$\mathcal{D}^i\nabla N_{k,0}^i\cdot\mathbf{n}^i = -\mathcal{D}^j\nabla N_{k,0}^j\cdot\mathbf{n}^j, \quad \mathbf{x}\in\mathcal{F}_{ij}, \tag{3.59}$$

$$\mathcal{D}^i\nabla N_{k,0}^i\cdot\mathbf{n}^i = \kappa^{ij}(N_{k,0}^j-N_{k,0}^i), \mathbf{x}\in\mathcal{F}_{ij}, \tag{3.60}$$

$$\mathcal{D}^i\nabla N_{k,0}^i\cdot\mathbf{n}^i = 0, \qquad \mathbf{x}\in\mathcal{B}_i, \tag{3.61}$$

$$N_{k,0}^i(\mathbf{x},0) = \rho, \qquad \mathbf{x}\in\mathcal{C}_i. \tag{3.62}$$

For α_k^1, the solution depends on the solution of the above PDE, N_0:

$$\frac{\partial}{\partial t}N_{k,1}^i = \mathbf{BT}^iN_{k,1}^i+(\mathbf{K}_{k,1}^i-\imath\gamma f(t)\mathbf{g}\cdot\mathbf{P}_{k,1})N_{k,0}^i, \qquad \mathbf{x}\in\mathcal{C}_i, \tag{3.63}$$

$$\mathcal{D}^i\nabla N_{k,1}^i\cdot\mathbf{n}^i = -\mathcal{D}^j\nabla N_{k,1}^j\cdot\mathbf{n}^j, \qquad \mathbf{x}\in\mathcal{F}_{ij}, \tag{3.64}$$

$$\mathcal{D}^i\nabla N_{k,1}^i\cdot\mathbf{n}^i = \kappa^{ij}(N_{k,1}^j-N_{k,1}^i)+\mu_{k,1}^{ij}(N_{k,0}^j-N_{k,0}^i)-\mathbf{G}_{k,1}^iN_{k,0}^i\cdot\mathbf{n}^i, \mathbf{x}\in\mathcal{F}_{ij}, \tag{3.65}$$

$$\mathcal{D}^i\nabla N_{k,1}^i\cdot\mathbf{n}^i = -\mathbf{G}_{k,1}^iN_{k,0}^i\cdot\mathbf{n}^i, \qquad \mathbf{x}\in\mathcal{B}_i, \tag{3.66}$$

$$N_{k,1}^i(\mathbf{x},0) = 0, \qquad \mathbf{x}\in\mathcal{C}_i. \tag{3.67}$$

For α_k^2, the solution depends on the solutions of both of the above PDEs:

$$\begin{aligned}\frac{\partial}{\partial t}N_{k,2}^i &= \mathbf{BT}^iN_{k,2}^i+(\mathbf{K}_{k,1}^i-\imath\gamma f(t)\mathbf{g}\cdot\mathbf{P}_{k,1})N_{k,1}^i\\ &\quad+(\mathbf{K}_{k,2}^i-\imath\gamma f(t)\mathbf{g}\cdot\mathbf{P}_{k,2})N_{k,0}^i, \qquad \mathbf{x}\in\mathcal{C}_i,\end{aligned} \tag{3.68}$$

$$\mathcal{D}^i\nabla N_{k,2}^i\cdot\mathbf{n}^i = -\mathcal{D}^j\nabla N_{k,2}^j\cdot\mathbf{n}^j, \qquad \mathbf{x}\in\mathcal{F}_{ij}, \tag{3.69}$$

$$\begin{aligned}\mathcal{D}^i\nabla N_{k,2}^i\cdot\mathbf{n}^i &= \kappa^{ij}(N_{k,2}^j-N_{k,2}^i)+\mu_{k,1}^{ij}(N_{k,1}^j-N_{k,1}^i)+\mu_{k,2}^{ij}(N_{k,0}^j-N_{k,0}^i)\\ &\quad-(\mathbf{G}_{k,1}^iN_{k,1}^i+\mathbf{G}_{k,2}^iN_{k,0}^i)\cdot\mathbf{n}^i, \qquad \mathbf{x}\in\mathcal{F}_{ij},\end{aligned} \tag{3.70}$$

$$\mathcal{D}^i\nabla N_{k,2}^i\cdot\mathbf{n}^i = -(\mathbf{G}_{k,1}^iN_{k,1}^i+\mathbf{G}_{k,2}^iN_{k,0}^i)\cdot\mathbf{n}^i, \qquad \mathbf{x}\in\mathcal{B}_i, \tag{3.71}$$

$$N_{k,2}^i(\mathbf{x},0) = 0, \qquad \mathbf{x}\in\mathcal{C}_i. \tag{3.72}$$

3.3.4 Asymptotic expansion of HADC according to two deformation parameters

In this subsection, we expand the solution of the HADC model when two deformation parameters (α_b and α_t) are applied, and match the first six terms of the asymptotic expansion.

We write the solution η of eqs. (3.29) to (3.31) as a six term asymptotic expansion:

$$\eta(\mathbf{x},t)=\eta_0(\mathbf{x},t)+\alpha_b\eta_{0,1}(\mathbf{x},t)+\alpha_b^2\eta_{0,2}(\mathbf{x},t)+\alpha_t\eta_{1,0}(\mathbf{x},t)+\alpha_t^2\eta_{2,0}(\mathbf{x},t)+\alpha_t\alpha_b\eta_{1,1}(\mathbf{x},t)+\mathcal{O}(\alpha_b^2+\alpha_t^2),$$

where the first subscript indicates the order of twist deformation and the second subscript indicates the order of bend deformation.

The transformed diffusion tensor β_{tb} can be decomposed into four terms: an identity matrix, a pure bending term, a pure twisting term, and a coupling-effect term.

$$\beta_{tb}=\mathcal{D}^i\left(Id+\begin{bmatrix}4\alpha_b^2z^2 & 0 & -2\alpha_bz\\ 0 & 0 & 0\\ -2\alpha_bz & 0 & 0\end{bmatrix}+\begin{bmatrix}\alpha_t^2y^2+1 & -\alpha_t^2yx & \alpha_ty\\ -\alpha_t^2yx & \alpha_t^2x^2+1 & -\alpha_tx\\ \alpha_ty & -\alpha_tx & 1\end{bmatrix}+\begin{bmatrix}-4\alpha_b\alpha_tyz & 2\alpha_b\alpha_txz & 0\\ 2\alpha_b\alpha_txz & 0 & 0\\ 0 & 0 & 0\end{bmatrix}\right). \tag{3.73}$$

If we switch to applying firstly the twisting transformation, and then bending transformation, the first three terms will be unchanged, and only the coupling effect term will be different.

Replacing eq. (3.73) into the transformed Laplace operator, we obtain

$$\nabla\cdot\beta_{tb}^i\nabla=\nabla\cdot\mathcal{D}^i\nabla+\alpha_b\mathbf{K}_{b,1}^i+\alpha_b^2\mathbf{K}_{b,2}^i+\alpha_t\mathbf{K}_{t,1}+\alpha_t^2\mathbf{K}_{t,2}^i+\alpha_b\alpha_t\mathcal{D}^i(-4yz\partial_{xx}+4xz\partial_{xy}). \tag{3.74}$$

We define a new second-order differential operator for the coupling effect term:

$$\mathbf{K}_{tb,1,1}^i:=\mathcal{D}^i(-4yz\partial_{xx}+4xz\partial_{xy}). \tag{3.75}$$

Similarly, using eq. (3.73), the transformed gradient operator is:

$$\beta_{tb}^i\nabla=\mathcal{D}^i\nabla+\alpha_b\mathbf{G}_{b,1}^i+\alpha_b^2\mathbf{G}_{b,2}^i+\alpha_t\mathbf{G}_{t,1}^i+\alpha_t^2\mathbf{G}_{t,2}^i+\alpha_t\alpha_b\mathcal{D}^i\begin{bmatrix}-4yz\partial_x+2xz\partial_y\\ 2xz\partial_x\\ 0\end{bmatrix}. \tag{3.76}$$

We define

$$\mathbf{G}_{tb}^i=\mathcal{D}^i\begin{bmatrix}-4yz\partial_x+2xz\partial_y\\ 2xz\partial_x\\ 0\end{bmatrix}. \tag{3.77}$$

In the same manner, the transformation operator $\mathcal{T}(\mathbf{x})$ can also be divided into four terms:

$$\mathcal{T}_{tb}(\mathbf{x})=\left(\mathbf{x}+\begin{bmatrix}\alpha_bz^2\\ 0\\ 0\end{bmatrix}+\begin{bmatrix}x(\cos(\alpha_tz)-1)-y\sin(\alpha_tz)\\ x\sin(\alpha_tz)+y(\cos(\alpha_tz)-1)\\ 0\end{bmatrix}+\begin{bmatrix}\alpha_bz^2(\cos(\alpha_tz)-1)\\ \alpha_bz^2\sin(\alpha_tz)\\ 0\end{bmatrix}\right). \tag{3.78}$$

When we expand it to the second-order term:

$$\mathcal{T}(\mathbf{x})=\mathbf{x}+\alpha_b\mathbf{P}_{b,1}+\alpha_b^2\mathbf{P}_{b,2}+\alpha_t\mathbf{P}_{t,1}+\alpha_t^2\mathbf{P}_{t,2}+\alpha_t\alpha_b\begin{bmatrix}0\\ z^3\\ 0\end{bmatrix}, \tag{3.79}$$

using Taylor expansion to trigonometrical functions. The error bound of the coupling effect term is of the second-order of α_tz, whereas the error bound of the pure twisting term is higher, of the third order.

We define a new vector

$$\mathbf{P}_{tb,1,1}:=\begin{bmatrix}0\\ z^3\\ 0\end{bmatrix}. \tag{3.80}$$

After matching the order of deformation parameters, we obtain that η_0 is equivalent to the solution of eqs. (3.44) to (3.46), $\eta_{0,1}$, $\eta_{1,0}$ are equivalent to the solution of eqs. (3.47) to (3.49) and $\eta_{0,2}$, $\eta_{2,0}$ are equivalent to the solution of eqs. (3.50) to (3.52):

$$\eta_0\equiv\eta_{b,0}\equiv\eta_{t,0},\qquad \eta_{0,1}\equiv\eta_{b,1},\qquad \eta_{0,2}\equiv\eta_{b,2},\qquad \eta_{1,0}\equiv\eta_{t,1},\qquad \eta_{2,0}\equiv\eta_{t,2}.$$

For $\alpha_t\alpha_b$, the solution $\eta_{1,1}$ depends on three lower order solutions η_0, $\eta_{0,1}$ and $\eta_{1,0}$:

$$\frac{\partial}{\partial t}\eta_{1,1}^i = \nabla\cdot\mathcal{D}^i\nabla\eta_{1,1}+\mathbf{K}_{t,1}^i\eta_{0,1}^i+\mathbf{K}_{b,1}^i\eta_{1,0}^i+\mathbf{K}_{tb,1,1}^i\eta_0^i-f(t)\mathbf{u_g}\cdot\mathbf{P}_{tb,1,1},\ \mathbf{x}\in\mathcal{C}_i, \tag{3.81}$$

$$\mathcal{D}^i\nabla\eta_{1,1}^i\cdot\mathbf{n}^i=-(\mathbf{G}_{t,1}^i\eta_{0,1}^i+\mathbf{G}_{b,1}^i\eta_{1,0}^i+\mathbf{G}_{tb,1,1}^i\eta_0^i)\cdot\mathbf{n}^i,\qquad \mathbf{x}\in\partial\mathcal{C}_i, \tag{3.82}$$

$$\eta_{1,1}^i(\mathbf{x},0)=0,\qquad \mathbf{x}\in\mathcal{C}_i. \tag{3.83}$$

3.3.5 Asymptotic expansion of Bloch-Torrey PDE according to two deformation parameters

Similar to the asymptotic expansion of the HADC model, we write the solution $N(\mathbf{x},t)$ of eqs. (3.24) to (3.28) as a six-term expansion:

$$N(\mathbf{x},t) = N_0(\mathbf{x},t)+\alpha_b N_{0,1}(\mathbf{x},t)+\alpha_b^2 N_{0,2}(\mathbf{x},t)+\alpha_t N_{1,0}(\mathbf{x},t)+\alpha_t^2 N_{2,0}(\mathbf{x},t)+\alpha_t\alpha_b N_{1,1}(\mathbf{x},t)+\mathcal{O}(\alpha_b^2+\alpha_t^2),$$

where the first subscript indicates the order of twist deformation and the second subscript indicates the order of bend deformation.

Similarly, we only need to treat the transformed permeability coefficient.

The expansion of transformed permeability coefficient is:

$$\begin{aligned}\mu_{tb}^{ij} &= \kappa^{ij}\begin{bmatrix} 4\alpha_b^2 z^2+\alpha_t^2 y^2-4\alpha_b\alpha_t yz+1 & -\alpha_t^2 yx+2\alpha_b\alpha_t xz & -2\alpha_b z+\alpha_t y \\ -\alpha_t^2 yx+2\alpha_b\alpha_t xz & \alpha_t^2 x^2+1 & -\alpha_t x \\ -2\alpha_b z+\alpha_t y & -\alpha_t x & 1\end{bmatrix}\mathbf{n}^i\cdot\mathbf{n}^i \\ &= \kappa^{ij}++\alpha_b\mu_{b,1}^{ij}+\alpha_b^2\mu_{b,2}^{ij}+\alpha_t\mu_{t,1}^{ij}+\alpha_t^2\mu_{t,2}^{ij}+\alpha_t\alpha_b\kappa^{ij}(-4yz\boldsymbol{n_x}^i\boldsymbol{n_x}^i+4xz\boldsymbol{n_x}^i\boldsymbol{n_y}^i),\end{aligned} \tag{3.84}$$

We define the coupling permeability coefficient as

$$\mu_{tb,1,1}^{ij} := \kappa^{ij}(-4yz\boldsymbol{n_x}^i\boldsymbol{n_x}^i+4xz\boldsymbol{n_x}^i\boldsymbol{n_y}^i). \tag{3.85}$$

After matching the order of deformation parameters, we obtain

$$N_0\equiv N_{b,0}\equiv N_{t,0},\qquad N_{0,1}\equiv N_{b,1},\qquad N_{0,2}\equiv N_{b,2},\qquad N_{1,0}\equiv N_{t,1},\qquad N_{2,0}\equiv N_{t,2}.$$

For $\alpha_b\alpha_t$, the solution $N_{1,1}$ depends on N_0, $N_{0,1}$ and $N_{1,0}$:

$$\begin{aligned}\frac{\partial}{\partial t}N_{1,1}^i &= \mathbf{B}\mathbf{T}^i N_{1,1}^i+(\mathbf{K}_{b,1}^i-\imath\gamma f(t)\mathbf{g}\cdot\mathbf{P}_{0,1})N_{1,0}^i+(\mathbf{K}_{t,1}^i-\imath\gamma f(t)\mathbf{g}\cdot\mathbf{P}_{1,0})N_{0,1}^i \\ &\quad+(\mathbf{K}_{tb,1,1}^i-\imath\gamma f(t)\mathbf{g}\cdot\mathbf{P}_{1,1})N_0^i, && \mathbf{x}\in\mathcal{C}_i, \quad (3.86)\\ \mathcal{D}^i\nabla N_{1,1}^i\cdot\mathbf{n}^i &= -\mathcal{D}^j\nabla N_{1,1}^j\cdot\mathbf{n}^i, && \mathbf{x}\in\mathcal{F}_{ij}, \quad (3.87)\\ \mathcal{D}^i\nabla N_{1,1}^i\cdot\mathbf{n}^i &= \kappa^{ij}(N_{1,1}^j-N_{1,1}^i)+\mu_{t,1}^{ij}(N_{0,1}^j-N_{0,1}^i)+\mu_{b,1}^{ij}(N_{1,0}^j-N_{1,0}^i) \\ &\quad+\mu_{tb,1,1}^{ij}(N_0^j-N_0^i)-(\mathbf{G}_{t,1}^i N_{0,1}^i+\mathbf{G}_{b,1}^i N_{1,0}^i+\mathbf{G}_{tb,1,1}^i N_0^i)\cdot\mathbf{n}^i, && \mathbf{x}\in\mathcal{F}_{ij}, \quad (3.88)\\ \mathcal{D}^i\nabla N_{1,1}^i\cdot\mathbf{n}^i &= -(\mathbf{G}_{t,1}^i N_{0,1}^i+\mathbf{G}_{b,1}^i N_{1,0}^i+\mathbf{G}_{tb,1,1}^i N_0^i)\cdot\mathbf{n}^i, && \mathbf{x}\in\mathcal{B}_i, \quad (3.89)\\ N_{1,1}^i(\mathbf{x},0) &= 0, && \mathbf{x}\in\mathcal{C}_i. \quad (3.90)\end{aligned}$$

3.3.6 Asymptotic expansion using Matrix Formalism and numerical implementation

To compute efficiently the asymptotic expansion, we aim to apply Matrix Formalism representation for the asymptotic expansion. The solutions of zeroth order terms of HADC and Bloch-Torrey PDE asymptotic expansion η_0 and N_0 are identical to the solutions on the canonical geometry. So we can naturally decompose these terms into the Laplace basis with the same interfaces and boundary conditions. For the solutions of first and second-order terms accompanied by a non-homogeneous boundary condition, they can be transformed into homogeneous case. We decompose these high-order solutions on the same Laplace eigenfunctions, consider the forcing terms on the boundaries and interfaces as a perturbation, and add the projection of the forcing terms onto the Laplace eigenbasis into the matrix exponentials. By construction, we can decompose the solution η and N into the Laplace basis of canonical configuration, and write the time-dependent coefficient vector as an expansion of six terms:

$$\eta(\mathbf{x},t)\approx\mathbf{\Phi}(\mathbf{x})\boldsymbol{\zeta}(t),\qquad N(\mathbf{x},t)\approx\mathbf{\Phi}(\mathbf{x})\boldsymbol{T}(t),$$

where $\mathbf{\Phi}(\mathbf{x})$ is the eigenfunctions and

$$\begin{aligned}\boldsymbol{\zeta}(t) &= \boldsymbol{\zeta}_0(t)+\alpha_b\boldsymbol{\zeta}_{0,1}(t)+\alpha_b^2\boldsymbol{\zeta}_{0,2}(t)+\alpha_t\boldsymbol{\zeta}_{1,0}(t)+\alpha_t^2\boldsymbol{\zeta}_{2,0}(t)+\alpha_t\alpha_b\boldsymbol{\zeta}_{1,1}(t)+\mathcal{O}(\alpha_b^2+\alpha_t^2),\\ \boldsymbol{T}(t) &= \boldsymbol{T}_0(t)+\alpha_b\boldsymbol{T}_{0,1}(t)+\alpha_b^2\boldsymbol{T}_{0,2}(t)+\alpha_t\boldsymbol{T}_{1,0}(t)+\alpha_t^2\boldsymbol{T}_{2,0}(t)+\alpha_t\alpha_b\boldsymbol{T}_{1,1}(t)+\mathcal{O}(\alpha_b^2+\alpha_t^2).\end{aligned}$$

Another concern regarding RAM limitation is that the solution for each asymptotic order relies on the solution of a lower order. Solving them individually necessitates the storage of intermediate solutions for each order at every time step. To address this issue, one approach is to concatenate these PDEs into one system of PDEs. The solution of this system of PDEs is

$$\boldsymbol{\zeta}^{\text{all}} = [\boldsymbol{\zeta}_0, \boldsymbol{\zeta}_{0,1}, \boldsymbol{\zeta}_{1,0}, \boldsymbol{\zeta}_{0,2}, \boldsymbol{\zeta}_{1,1}, \boldsymbol{\zeta}_{2,0}]^T, \qquad \boldsymbol{T}^{\text{all}} = [\boldsymbol{T}_0, \boldsymbol{T}_{0,1}, \boldsymbol{T}_{1,0}, \boldsymbol{T}_{0,2}, \boldsymbol{T}_{1,1}, \boldsymbol{T}_{2,0}]^T.$$

After solving it, we can break it into pieces again and obtain the final result. Further details about the numerical implementation are found in appendix A.2.

The numerical computations of the asymptotic expansions in Matrix Formalism representation are already integrated into SpinDoctor[87, 92]. We use SpinDoctor to create the geometries, generate finite element (FE) meshes, and compute the orders 0, 1, and 2 asymptotic expansions.

Firstly, we use SpinDoctor to create a canonical geometry, containing several straight cylindrical axons parallel to the z-axis and an extracellular space wrapped around the axons. Then a finite element mesh is generated for the canonical geometry. The deformed geometries will have finite element meshes that are the analytical deformations of the canonical finite element mesh, described in eqs. (3.6) and (3.7).

The finite element discretization is based on continuous piece-wise linear basis functions (the $P1$ finite elements), with a numerically efficient implementation from[153].

The eigen-decomposition and matrix exponential steps are identical to the previous chapter.

3.4 Numerical results

The numerical validation of the asymptotic expansions of the Bloch-Torrey PDE and the HADC model will be conducted in this section. The geometry we use is composed of 20 cylindrical axons and a tightly wrapped ECS, as depicted in fig. 3.1. The radii of the axons are between 0.25μm and 2μm, with a mean value of 0.7μm. This range selection is based on the histological study of axon size[154, 155]. The volume fraction of the ECS is 50.4%. The height of all the compartments is 20μm. The diffusion coefficients are set to $\mathcal{D}^{\text{axon}} = \mathcal{D}^{\text{ECS}} = \mathcal{D}_0 = 2 \times 10^{-3}\,\text{mm}^2/\text{s}$ and the permeability coefficient is set to $\kappa = 10^{-5}\,\text{m/s}$, which is the permeability value for axonal membranes[37, 122]. The gradient sequence is PGSE$(5\text{ms}, 15\text{ms})$ and the gradient strength is b-value=$500\,\text{s/mm}^2$ (g-value=$145\,\text{mT/m}$) and b-value=$1000\,\text{s/mm}^2$ (g-value=$205\,\text{mT/m}$), within the range of commercial used MRI scanner gradient strength (up to $300\,\text{mT/m}$)[156].

The reference values are either the ADC obtained by solving the HADC model (eqs. (3.2) to (3.4)) on the deformed geometry Ω or the diffusion MRI signal obtained by solving the Bloch-Torrey PDE (eqs. (1.27) to (1.31)) on the deformed domain using Numerical Matrix Formalism. Both of these reference values are obtained using SpinDoctor. To ensure a fair comparison, We fix the length scale cut-off L_s to 1.5μm. Given that the HADC model is based on an impermeable geometry assumption, the number of eigenfunctions corresponding to the same length scale cut-off is greater than that for the Bloch-Torrey PDE with permeable interfaces, as we saw in the previous chapter. For the asymptotic expansion which deals with Laplace eigenfunctions on canonical configuration, the corresponding number of eigenfunctions is $N_{eig} = 917$ for Bloch-Torrey PDE and $N_{eig} = 922$ for the HADC model. For the reference results obtained by using Laplace eigenfunctions on deformed configuration, the corresponding number of eigenfunctions N_{eig} increases as the deformed angle increases. In table 3.1, we list the required N_{eig} for each configurations.

Because pure bending and pure twisting are two special cases of the last case, in practice, we only need to solve the asymptotic expansion in the case when both two deformations are applied and set one deformed angle to zero to obtain one deformation result.

$[\alpha_t, \alpha_b]$	canonical	$[0, 0.05]$	$[0, 0.07]$	$[0.05, 0]$	$[0.07, 0]$	$[0.05, 0.05]$	$[0.07, 0.07]$
$\kappa = 10^{-5}$	917	945	956	927	936	951	958
$\kappa = 0$	922	949	958	934	940	952	961

Table 3.1: Corresponding number of eigens N_{eig} to a length scale cut-off $L_s = 1.5\mu$m with different permeability values and deformed angles on the simulation domain. The unit of permeability κ is m/s.

3.4.1 HADC model

First, we show the effects of bending and twisting in multiple gradient directions for the HADC model. Being that 0^{th} order term η_0 gives the ADC of the canonical configuration, η_1 and η_2 could be considered as two corrections. In all the plots that follow, the ADC is normalized by the intrinsic diffusion coefficient 2×10^{-3} mm^2/s.

In fig. 3.2 we show ADC and the contribution from 0^{th}, 1^{st} and 2^{nd} order terms in multiple gradient directions in 3 dimensions. For bend deformation, we can see that 1^{st} order term provides maximal negative correction along the z direction. On the other hand, 2^{nd} order term provides maximal positive correction along the $x-z$ plane. As a result, the ADC figure will be thicker in x directions compared with canonical case and be lower in the axial direction.

For twist deformation, 1^{st} and 2^{nd} provide different maximal correction directions, because of the different orders of Taylor expansion of trigonometrical functions. This will change the maximum ADC direction. The final ADC is titled toward to maximal correction direction of the 2^{nd} order correction. When both two deformations are applied, the effects of high order correction terms look like the convolution of bend and twist effects.

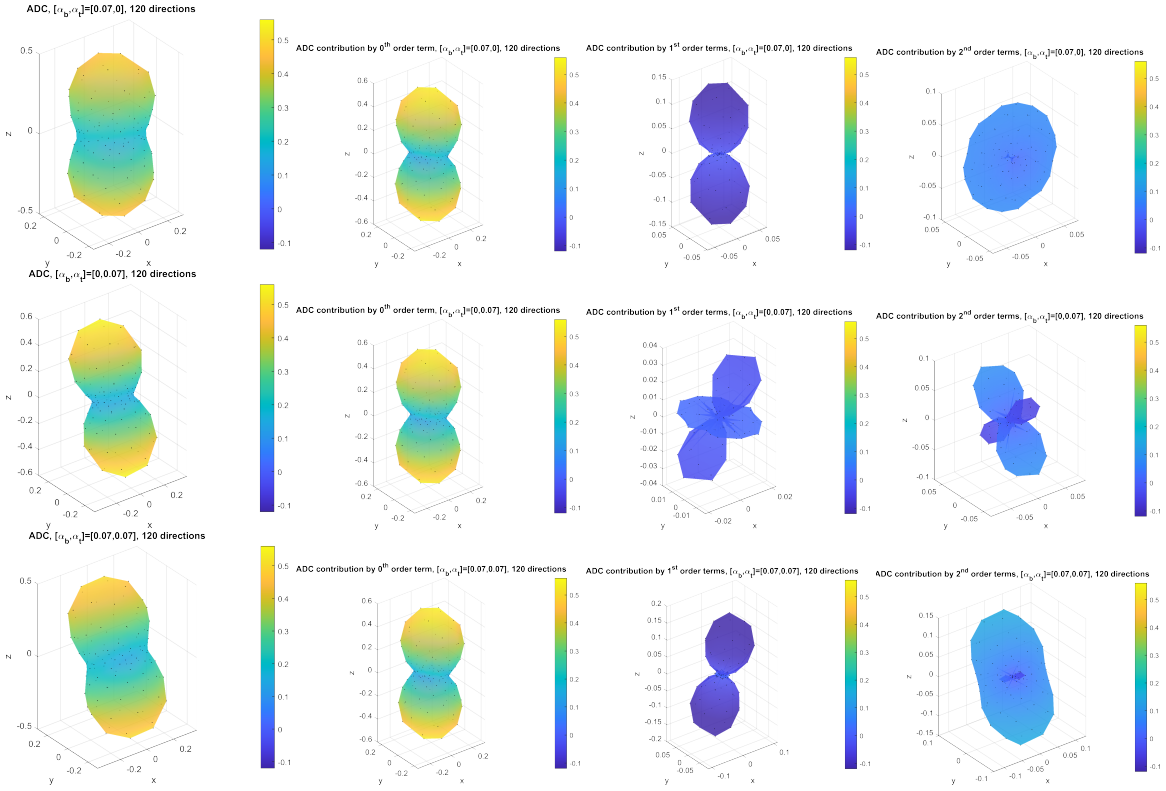

Figure 3.2: The components of the HADC asymptotic model in 120 gradient-directions, which are uniformly distributed on the sphere. The black dots indicate the ADC values. The distances from the origin of the dots as well as the colors are proportional to the ADC (normalized by the intrinsic diffusion coefficient $\mathcal{D}_0 = 2 \times 10^{-3}$ mm^2/s). The gradient sequence is PGSE$(5\text{ms}, 15\text{ms})$. Top: the bend deformation with $\alpha_b = 0.07$. Middle: the twist deformation with $\alpha_t = 0.07$. Bottom: bend then twist deformation with $[\alpha_b, \alpha_t] = [0.07, 0.07]$. From left to right: ADC, contribution from 0^{th}, 1^{st} and 2^{nd} order terms.

For the clarity of display, we show further results, which concern the accuracy of our asymptotic model, using two dimensional plots, where a uniform distribution of gradient directions is taken from the $x-z$ plane ($y=0$). The reference value is the ADC obtained by solving the HADC model on the deformed geometry Ω. The error of the asymptotic model is the difference between different order approximations and the reference value.

In fig. 3.3, we show four curves: the reference value, the asymptotic model (the second-order approximation), the zeroth order approximation (the ADC from the canonical geometry), and the

first-order approximation (sum of the zeroth and first-order terms). We see that frequently, for bend deformation, the first-order correction is an over-correction on η_0 and that our second-order correction brings the result closer to the reference value. As the deformation parameter increases, the difference between our asymptotic model and the reference value increases, as expected. We note that even though η_0 is the same function on the canonical geometry for both the bend and twist deformations, after integrating over the surface of deformed geometry, its contribution to the ADC is different depending on the specific deformation. This causes that the computed zeroth order ADC is different for each deformation despite the fact that η_0 is the same function on the canonical geometry $\mathcal{C}$.

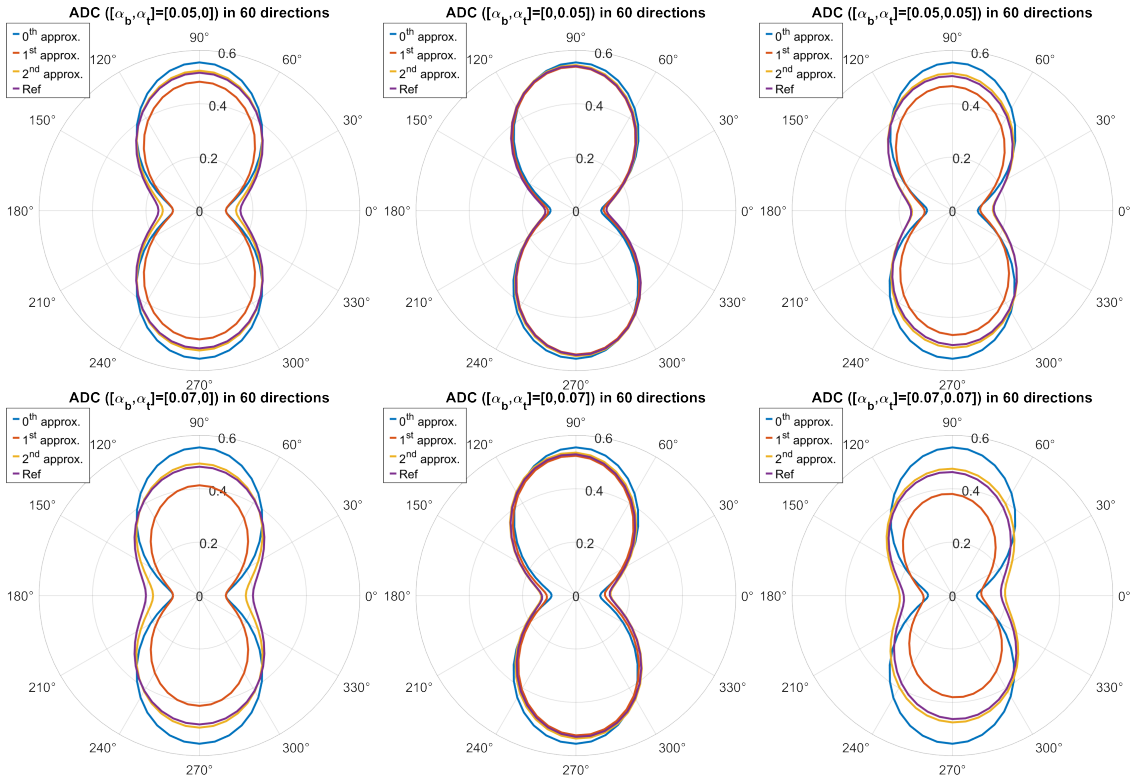

Figure 3.3: 2D HARDI simulations of the ADC in 60 gradient-directions, which are uniformly distributed in the $x-z$ plane ($y=0$). The ADC values are normalized by the intrinsic diffusion coefficient $\mathcal{D}_0 = 2\times10^{-3}\,\mathrm{mm}^2/\mathrm{s}$ and labeled on the gray circles. The displayed angle (from 0 to 360 degrees) is the angle between positive x-axis and the diffusion gradient direction. The blue, red, yellow lines represent 0^{th}, 1^{st} and 2^{nd} order approximations, respectively. The reference value is shown in purple. The gradient sequence is PGSE$(5\mathrm{ms}, 15\mathrm{ms})$. Top left: $\alpha_b = 0.05$; Top middle: $\alpha_t = 0.05$ (where the first-order, second-order approximations and the reference value are indistinguishable); Top right: $[\alpha_b, \alpha_t] = [0.05, 0.05]$ Bottom left: $\alpha_b = 0.07$; Bottom middle: $\alpha_t = 0.07$; Bottom right: $[\alpha_b, \alpha_t] = [0.07, 0.07]$.

In fig. 3.4, we show the relative errors of the 0^{th}, 1^{st} and 2^{nd} order approximations, normalized by the reference values. At $\alpha_b = 0.05$, the maximum 2^{nd} order approximation error is 11%, and the maximum 0^{th} order approximation error is 35%. At $\alpha_b = 0.07$, the maximum 2^{nd} order approximation error is 11%, and the maximum 0^{th} order approximation error is 65%. At $\alpha_t = 0.05$, the maximum 2^{nd} order approximation error is 2%, and the maximum 0^{th} order approximation error is 18%. At $\alpha_t = 0.07$, the maximum 2^{nd} order approximation error is 4%, and the maximum 0^{th} order approximation error is 30%. At $[\alpha_b, \alpha_t] = [0.05, 0.05]$, the maximum 2^{nd} order approximation error is 2%, and the maximum 0^{th} order approximation error is 39%. At $[\alpha_b, \alpha_t] = [0.07, 0.07]$, the maximum 2^{nd} order approximation error is 9%, and the maximum 0^{th} order approximation error is 50%.

Next, we show in fig. 3.5 the relative errors for the axons compartment and for the ECS separately. For axons compartment, the maximum relative errors lie in x-axis, where the ADC values are the smallest (less than 0.2). In general, the axons compartment is much less accurately modeled

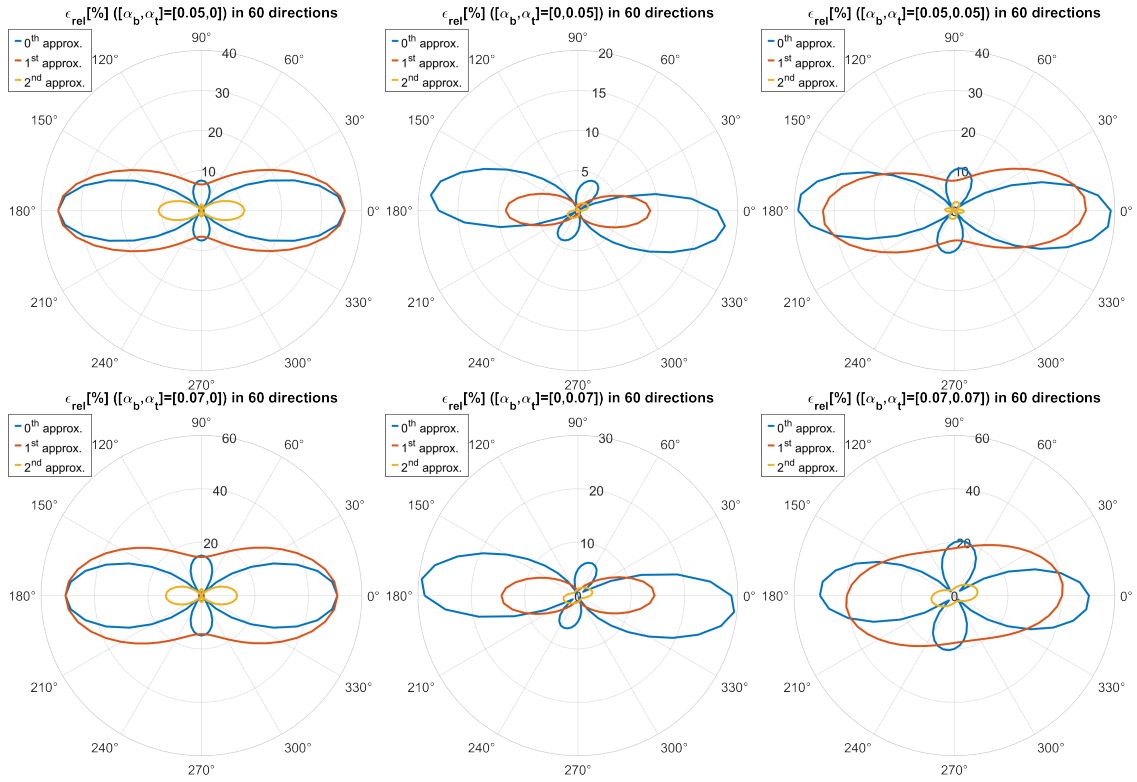

Figure 3.4: The relative ADC error between 0^{th}, 1^{st} and 2^{nd} order approximations and the reference value in 60 gradient directions, which are uniformly distributed in the $x-z$ plane ($y=0$). The labeled values on the gray circles are given in percent. The gradient sequence is PGSE$(5\text{ms}, 15\text{ms})$. The displayed angle (from 0 to 360 degrees) is the angle between positive x-axis and the diffusion gradient direction. The blue, red, yellow lines represent 0^{th}, 1^{st} and 2^{nd} order approximations, respectively. Top left: $\alpha_b = 0.05$; Top middle: $\alpha_t = 0.05$; Top right: $[\alpha_b, \alpha_t] = [0.05, 0.05]$ Bottom left: $\alpha_b = 0.07$; Bottom middle: $\alpha_t = 0.07$; Bottom right: $[\alpha_b, \alpha_t] = [0.07, 0.07]$.

than the ECS compartment (which is more isotropic), except the case $\alpha_t = 0.07$.

3.4.2 Bloch-Torrey PDE

Now we validate our asymptotic model for the Bloch-Torrey PDE in the same geometries. We show firstly the deformation effects on the diffusion MRI signals. In fig. 3.6 we show the normalized signals at b $= 1000\,\text{s/mm}^2$ in the canonical geometry, as well as in the bend and twist deformed geometries. We can observe that the maximum diffusion MRI signal will decrease in the presence of any kind of deformation, compared to the canonical configuration. When both two deformations are applied, it is clear that the signals HARDI plot is titled.

In fig. 3.7, we depicted the diffusion MRI signals and each order approximations in x-z plane. It is evident that the second-order approximation is close to the reference signal, except the case of $[\alpha_b, \alpha_t] = [0.07, 0.07]$.

In fig. 3.8, we show the relative errors between the 0^{th}, the 1^{st}, the 2^{nd} order approximations and the reference value, for b $= 1000\,\text{s/mm}^2$. For the bend deformation, the 0^{th} and the 1^{st} order approximations are indistinguishable for α_b from 0.05 to 0.07, whose maximum relative error angles align with x-axis. Therefore, at least a second-order approximation is needed to obtain an accurate simulation. The overall relative error of 2^{nd} approximation is under 5.6% and the relative error in x-axis direction is well reduced.

For the twist deformation, in the case of $\alpha_t = 0.05$, the relative error by first-order approximation is about the same level as zeroth order approximation. Thus a higher order approximation is also required. The overall relative error of 2^{nd} approximation is under 1.6%.

When both two deformations are applied, the first-order approximation does not have signifi-

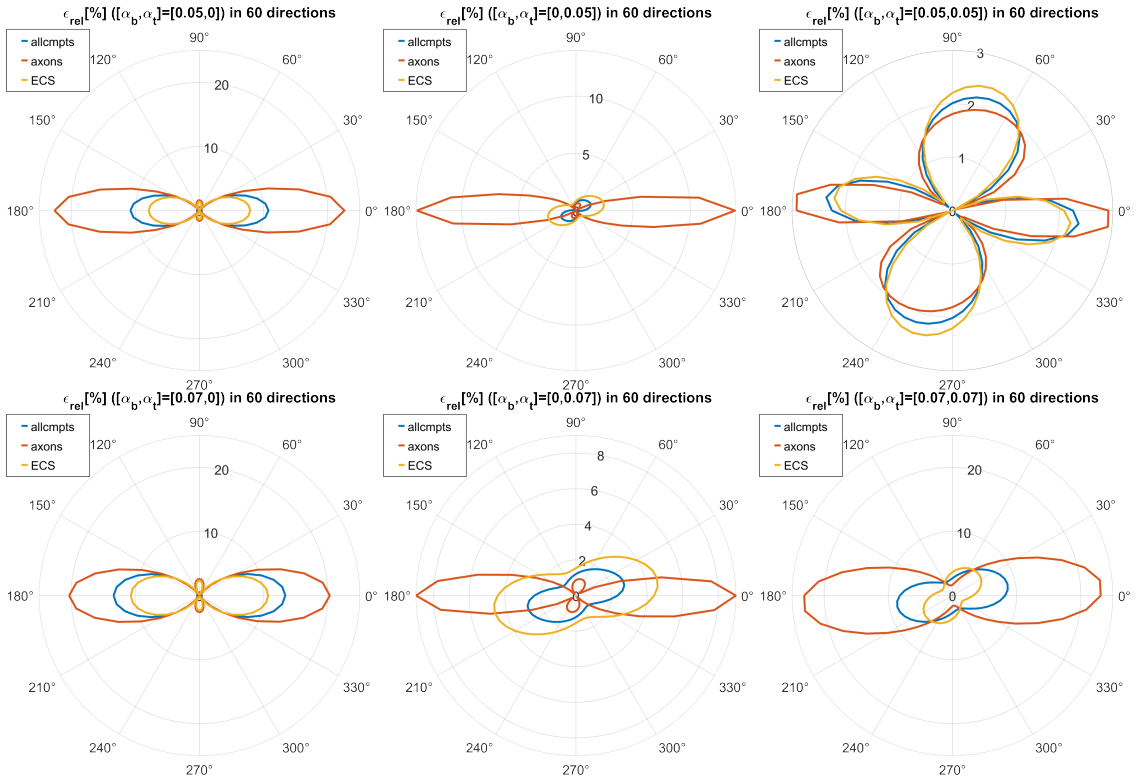

Figure 3.5: The relative ADC errors between the reference solution and the asymptotic model in 60 gradient directions in the $x-z$ plane ($y=0$), in all compartments (blue line), in the axons (red line), and in the ECS (yellow line). The labeled values on the gray circles are given in percent. The displayed angle (from 0 to 360 degrees) is the angle between positive x-axis and the diffusion gradient direction. The gradient sequence is PGSE$(5\text{ms}, 15\text{ms})$. The volume fraction of ECS is 50.4%. Top left: $\alpha_b = 0.05$; Top middle: $\alpha_t = 0.05$; Top right: $[\alpha_b, \alpha_t] = [0.05, 0.05]$ Bottom left: $\alpha_b = 0.07$; Bottom middle: $\alpha_t = 0.07$; Bottom right: $[\alpha_b, \alpha_t] = [0.07, 0.07]$.

cant improvement because of the bending deformation. For $[\alpha_b, \alpha_t] = [0.07, 0.07]$, the relative error in x-axis is the same level for all three approximations, which means that second-order approximation is not accurate enough to approximate this extent of deformation.

In fig. 3.9, we show the relative errors of the asymptotic model for the axons compartment and for the ECS separately, for b $= 500$ s/mm^2 and b $= 1000$ s/mm^2. For bend deformation, the relative errors of axons and ECS are at the same level.

3.4.3 Convergence order of the asymptotic models

Next, we show the convergence order of the asymptotic models. In fig. 3.10, we show the relative errors in the direction-averaged ADC of 0^{th}, 1^{st}, and 2^{nd} approximations, as α_b and α_t decrease. The first-order approximation yields almost the same errors as the zeroth-order approximation for bend deformation. We see a lower error level for our second order asymptotic model.

In fig. 3.11, we show the relative errors in the direction-averaged signal of 0^{th}, 1^{st}, and 2^{nd} approximations, as α_b and α_t decrease, for b $= 1000$ s/mm^2. We see a convergence order of 3, $O(\alpha^3)$, for our second order asymptotic model.

Finally, in fig. 3.12, we show the convergence of our asymptotic models with b-value is first-order, $O(\text{b})$.

3.4.4 Computational time comparison

In terms of the computation time, the asymptotic offers two benefits when conducting the simulations with multiple deformation parameter values. First, the Laplace decomposition just needs

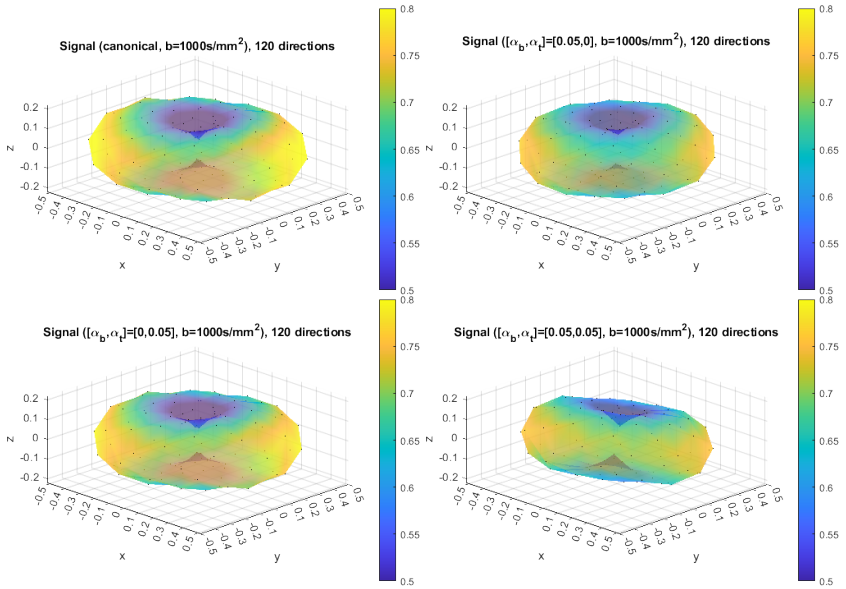

Figure 3.6: Normalized diffusion MRI signal at b-value = $1000\,\mathrm{s/mm}^2$, in 120 gradient-directions, which are uniformly distributed on the sphere. The distances from the origin of the black dots as well as the colors are normalized by S_0, equivalent to the volume of the simulation domain. The gradient sequence is PGSE$(5\mathrm{ms}, 15\mathrm{ms})$. The diffusion MRI signals of the canonical configuration (left top). The signals of the bend deformation by asymptotic model, with $\alpha_b = 0.05$ (right top). The signals of the twist deformation by asymptotic model, with $\alpha_t = 0.05$ (left bottom). The signals of two deformations by asymptotic model with $[\alpha_b, \alpha_t] = [0.05, 0.05]$ (right bottom).

to be done once. In contrast to the classical Matrix Formalism, where changing the deformation angles necessitates regenerating the Laplace eigenbasis, the asymptotic approach is based on the canonical configurations, which saves time in this step. Second, although solving the system of ODEs (or computing the matrix exponential) is more time-consuming than the classical way because the larger matrix size is related to the asymptotic order, it also requires only a single computation. After obtaining and storing the solution for each asymptotic order, calculating the diffusion MRI signal or ADC for various deformed configurations is immediate.

To show this efficiency, we compare the computational time of the classical Matrix Formalism and the asymptotic expansion on the same geometry in fig. 3.1 with the same experimental settings. There are 335,284 elements and $N_{node} = 99,414$ nodes in total, of which 52,563 nodes in the ECS. All the simulations are performed on a computing server with 20 cores of frequency 2.4 GHz, and RAM of 256GB. The operating system is Rocky Linux 8 and the Matlab version is R2021a. All the simulations are performed on a Dell laptop with 6 cores of frequency 1.1 GHz and RAM of 32GB/@. The operating system is Windows 11 and the Matlab version is R2022b.

Table 3.2 shows the computational times of the Laplace eigendecomposition with different configurations, using the same routine as the previous chapter. Numerical Matrix Formalism needs to perform the Laplace eigendecomposition on each deformed configuration, whereas the asymptotic expansion only needs to perform once on the canonical configuration.

Table 3.3 shows the computational times of the matrix exponential computations in one gradient direction with different settings. The number of eigenfunctions is set to $N_{eig} = 1,000$. We can see from the table that the asymptotic expansion is much slower than the Numerical Matrix Formalism. It takes around 36 times longer to compute one value compared to the Numerical Matrix Formalism because the matrix size is six times bigger. However, the asymptotic expansion requires computing the matrix exponentials just once for each sequence setting. After that, signal computations for different deformed configurations become instant. Thus, when various deformed angles are simulated, both two methods will consume similar time. In the table, we also include the cost of solving the Bloch-Torrey PDE directly using finite elements rather than computing eigenfunctions, labeled “FE”. It is much more costly than either of the two eigenfunction based methods, if multiple diffusion encoding gradient directions and shells are needed.

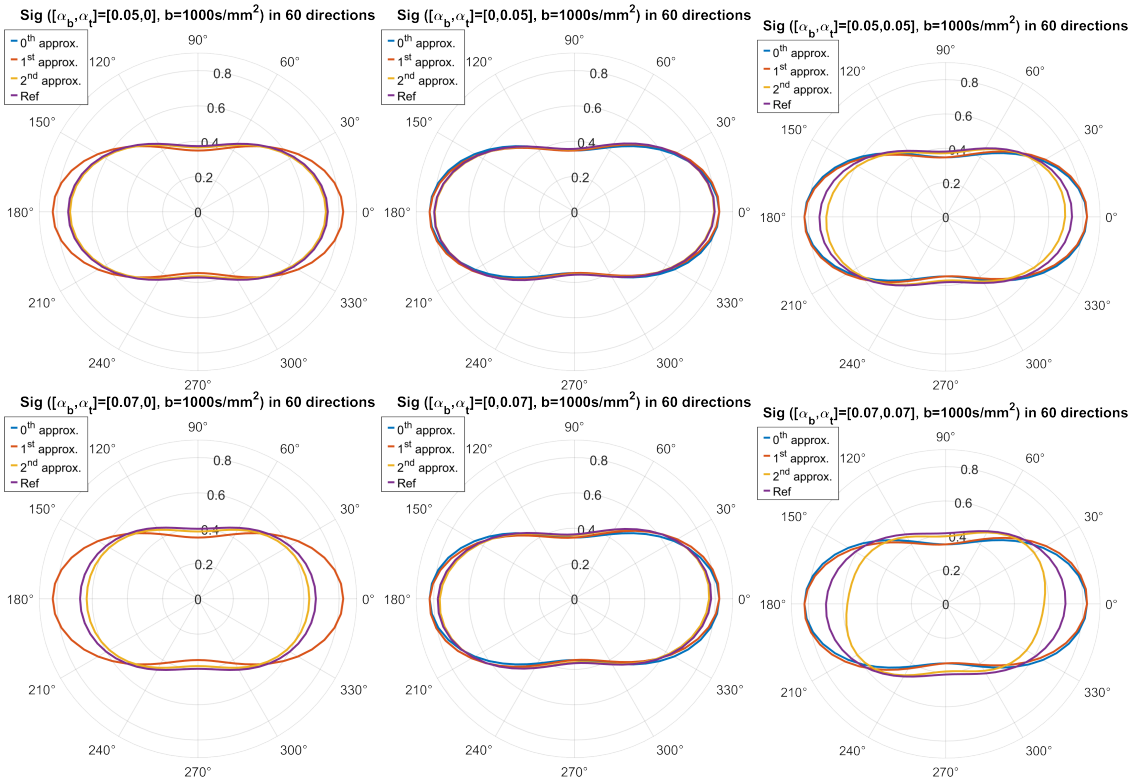

Figure 3.7: The diffusion MRI signal by 0^{th}, 1^{st} and 2^{nd} order approximations and the reference in 60 directions gradient-directions in the $x-z$ plane ($y=0$). The diffusion MRI signal is normalized by the initial signal S_0. The labeled values on the gray circles are the normalized signal values from 0 to 1. The displayed angle (from 0 to 360 degrees) is the angle between positive x-axis and the diffusion gradient direction. The b-value = $1000\,\text{s/mm}^2$ and the gradient sequence is PGSE$(5\text{ms}, 15\text{ms})$. The blue, red, yellow, purple lines represent 0^{th}, 1^{st}, 2^{nd} order approximations and reference signal, respectively. Top (from left to right): $\alpha_b = 0.05$, $\alpha_t = 0.05$ and $[\alpha_b, \alpha_t] = [0.05, 0.05]$; Bottom (from left to right): $\alpha_b = 0.07$, $\alpha_t = 0.07$ and $[\alpha_b, \alpha_t] = [0.07, 0.07]$.

	Computational time (seconds)					
$[\alpha_t, \alpha_b]$	$N_{eig} = 1,000$		$N_{eig} = 1,500$		$N_{eig} = 2,000$	
	HADC	$\kappa = 10^{-5}$	HADC	$\kappa = 10^{-5}$	HADC	$\kappa = 10^{-5}$
Canonical	219	258	367	490	455	725
$[0, 0.05]$	216	290	319	548	426	799
$[0.05, 0]$	205	297	314	512	438	781
$[0.05, 0.05]$	216	292	303	534	471	834
Total (NMF)	856	1137	1303	2084	1790	3139
Total (asymptotic)	219	258	367	490	455	725

Table 3.2: Computational times of Laplace eigen-decomposition with different deformation angles, given in seconds. The unit of permeability κ is m/s. The full set contains $N_{node} = 99,414$ nodes.

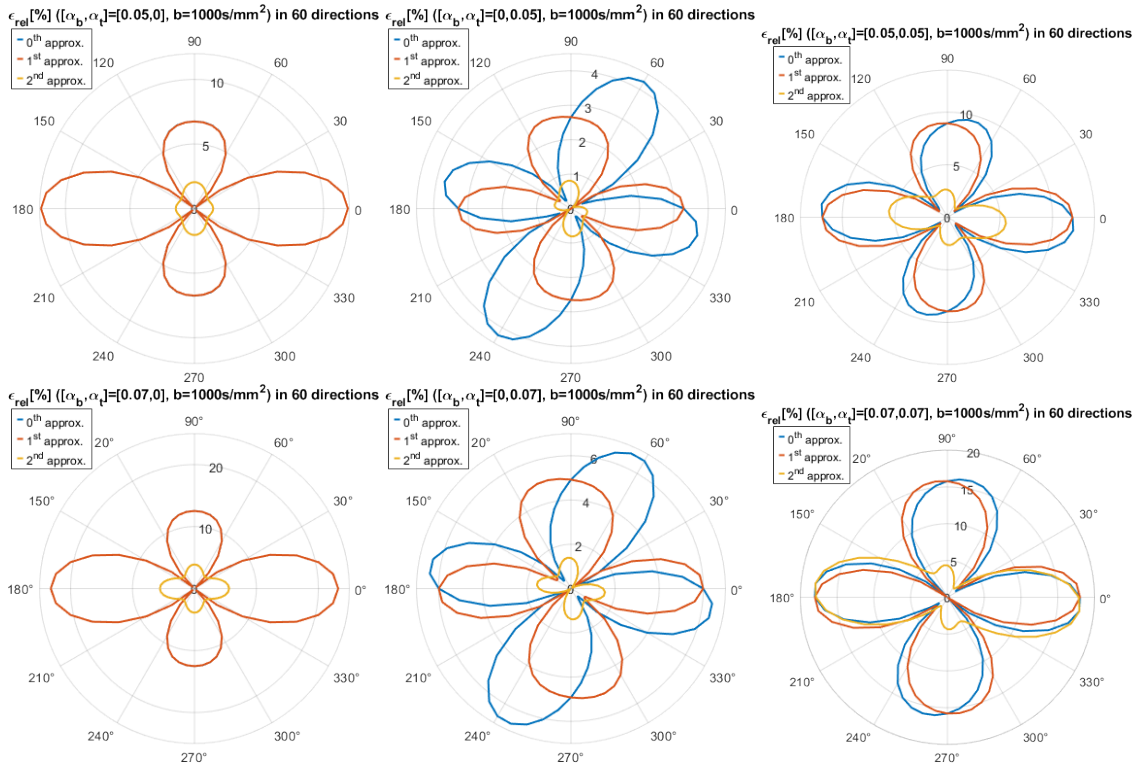

Figure 3.8: The relative signal error between 0^{th}, 1^{st} and 2^{nd} order approximations and reference value in 60 directions gradient-directions in the $x-z$ plane ($y=0$). The labeled values on the gray circles are given in percent. The displayed angle (from 0 to 360 degrees) is the angle between positive x-axis and the diffusion gradient direction. The b-value = $1000\,$s/mm^2 and the gradient sequence is PGSE$(5\text{ms}, 15\text{ms})$. The diffusion MRI signal is normalized by the initial signal S_0. The blue, red, yellow lines represent 0^{th}, 1^{st} and 2^{nd} order approximations, respectively. Top (from left to right): $\alpha_b = 0.05$, $\alpha_t = 0.05$ and $[\alpha_b, \alpha_t] = [0.05, 0.05]$; Bottom (from left to right): $\alpha_b = 0.07$, $\alpha_t = 0.07$ and $[\alpha_b, \alpha_t] = [0.07, 0.07]$.

	b	NMF				asym	FE
$[\alpha_t, \alpha_b]$		[0,0]	[0,0.05]	[0.05,0]	[0.05,0.05]		[0,0]
	500	2.4	2.4	2.3	2.3	186	734
	1000	3.6	3.5	3.5	3.5	189	1363
	HADC	1.1	0.9	0.4	0.5	105	579

Table 3.3: Computational times of the Numerical Matrix Formalism (NMF) method, and the asymptotic expansion, given in seconds. The number of eigenfunctions is $N_{eig} = 1,000$. The encoding gradient direction is fixed in $[\sqrt{3}/3, \sqrt{3}/3, \sqrt{3}/3]^T$. The gradient sequence is PGSE$(5\text{ms}, 15\text{ms})$. We also include the cost of solving the Bloch-Torrey PDE directly using finite elements rather than computing eigenfunctions in canonical configuration, labeled "FE" The units are κ: m/s and b: s/mm^2.

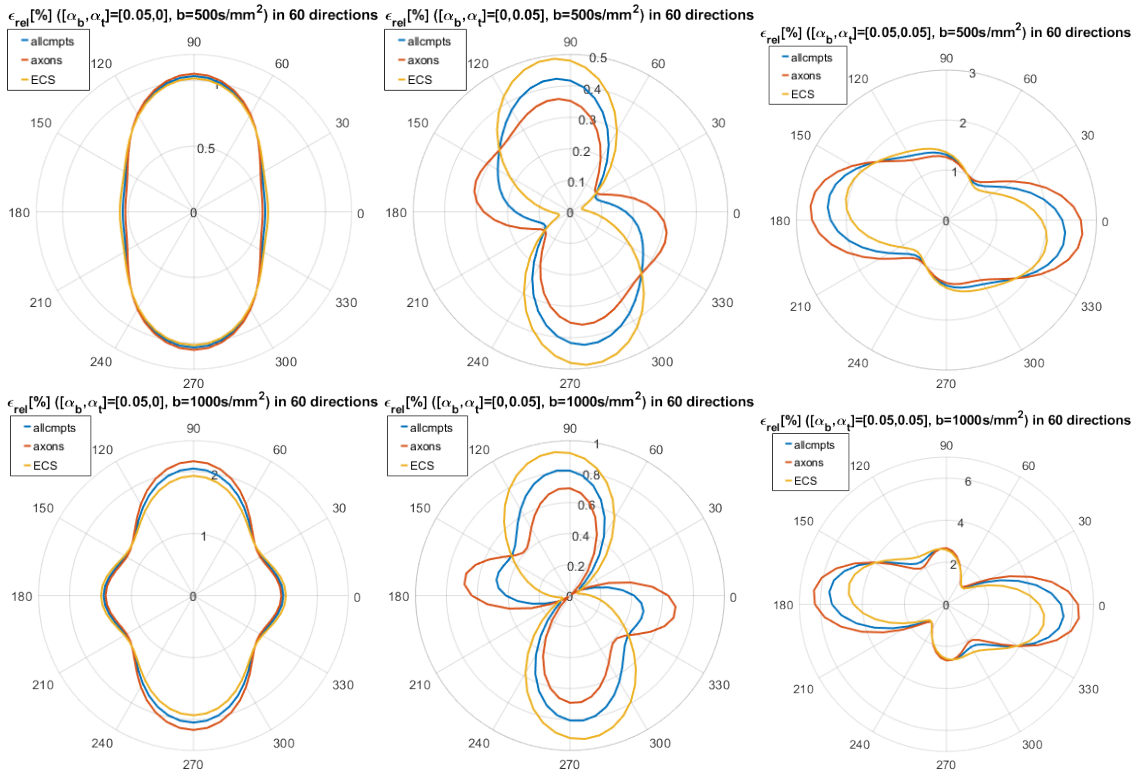

Figure 3.9: The relative signal errors between the reference solution and the asymptotic model in 60 gradient directions in the $x-z$ plane ($y=0$), in all compartments (blue line), in the axons (red line), and in the ECS (yellow line). The labeled values on the gray circles are given in percent. The displayed angle (from 0 to 360 degrees) is the angle between positive x-axis and the diffusion gradient direction. The gradient sequence is PGSE$(5\text{ms}, 15\text{ms})$. The volume fraction of ECS is 50.4%. Left: $\alpha_b = 0.05$. Middle: $\alpha_t = 0.05$. Right: $[\alpha_b, \alpha_t] = [0.05, 0.05]$. Top: b $= 500\,\text{s/mm}^2$. Bottom: b $= 1000\,\text{s/mm}^2$.

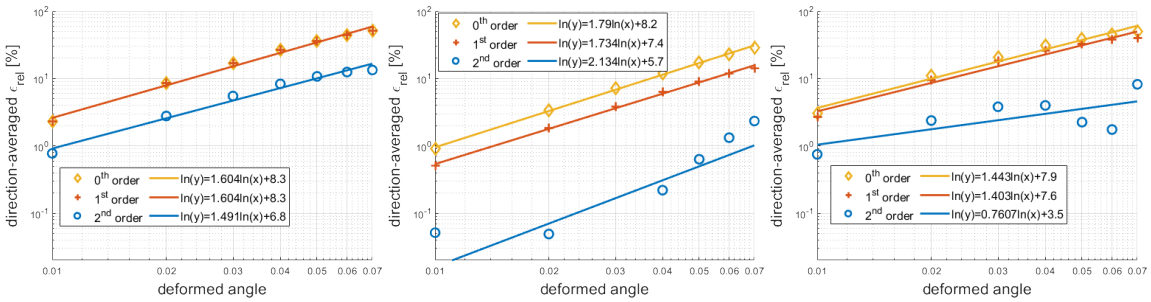

Figure 3.10: The direction-averaged ADC relative error (in percent) against the deformation angle. The yellow, red and blue circles represent zeroth order, first-order and second-order approximations, respectively. The lines with the same color are the linear fitting functions. Top: ADC relative error against bend angle; Middle: ADC relative error against twist angle; Right: two angles with the same values applied.

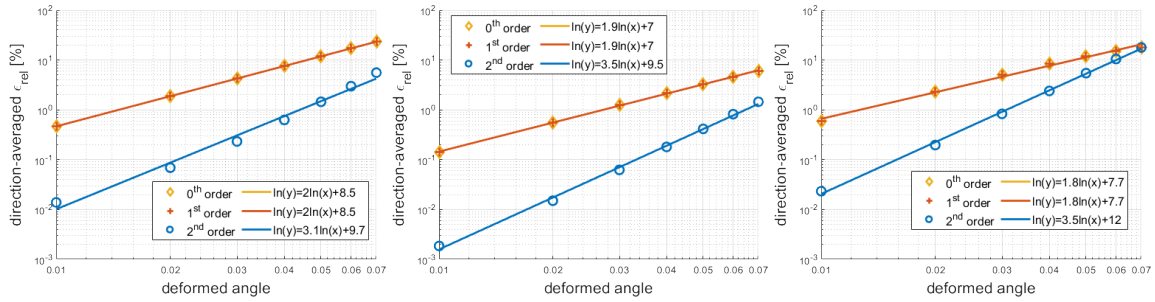

Figure 3.11: The direction-averaged signal relative error (in percent) against deformation angle.The yellow, red and blue circles represent zeroth order, first-order and second-order approximations, respectively. The lines with the same color are the linear fitting functions. Top: Signal relative error against bend angle; Middle: Signal relative error against twist angle; Right: two angles with the same values applied.

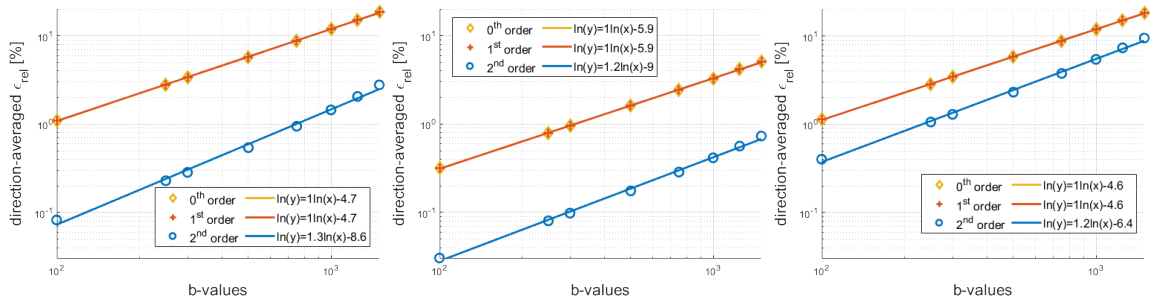

Figure 3.12: The direction-averaged signal relative error (in percent) against b-values. The yellow, red and blue circles represent zeroth order, first-order and second-order approximations, respectively. The lines with the same color are the linear fitting functions. Top: Signal relative error against b-value, with $\alpha_b = 0.05$; Middle: Signal relative error against b-value, with $\alpha_t = 0.05$; Right: Signal relative error against b-value, with $\alpha_b = 0.05$ and $\alpha_t = 0.05$.

3.5 Discussion

We analyzed the Bloch-Torrey PDE and the HADC model in the context of geometrical deformations starting from a canonical configuration, focusing on two analytically defined deformations, bending and twisting. We derived asymptotic models of the diffusion MRI signal and the ADC where the asymptotic parameter indicates the extent of the geometrical deformation. We computed numerically the first three orders of the asymptotic models, the zeroth order model based on the canonical configuration, and two orders of corrections.

In section 3.4, we have shown the accuracy levels of the second-order asymptotic models for four geometrical deformations. From fig. 3.1 we can see that at the smaller deformation values, $\alpha_b = 0.05$ and $\alpha_t = 0.05$, there are already visually significant deformations compared to the canonical geometry. It seems that this range of values is sufficient to model significant deviations from straight cylinders and is therefore biologically relevant to describe the geometry of the brain white matter. At the higher values that we simulated, $\alpha_b = 0.07$ and $\alpha_t = 0.07$, the asymptotic models resulted in much higher errors, but by visual inspection, this larger range of values seems beyond the level of geometrical deviations from straight cylinders that we can expect in the brain white matter.

We have shown that for biologically relevant geometrical deviations, the ADC and the diffusion MRI signal are accurately described as the sum of a zeroth order value (signal or ADC from the straight cylinders) and two orders of corrections. We showed that a first-order correction is not sufficient to improve on the zeroth order model, at least two orders of corrections are needed to significantly improve on the zeroth order model. With the second-order corrections, the asymptotic models are second order accurate in the geometrical deformation parameters. In addition, the model errors were shown to come mainly from the axons, with the errors from the ECS compartment a much smaller source of error.

Through HARDI plot, We observe that: (1) The bending deformation causes the HARDI plot in x-z plane to become thicker; (2) The twisting deformation will rotate the direction of maximal ADC, which might potentially introduce challenges in orientation estimation; (3) Applying both two deformations simultaneously, the final effect is the superposition of them.

Compared to traditional approaches computing diffusion MRI signals on deformed domains, the proposed asymptotic expansions only need to solve the PDE once on the canonical geometry and can yield the results immediately for all the combination of deformation angles, which facilitate the study of deformation effects. This method can be used to quantitatively examine how realistic axons shapes affect the microstructure estimation in the brain white matter.

The purpose of this work is to contribute to relating the diffusion MRI signal more directly with the tissue geometrical parameters. The idea is that the diffusion MRI signal and ADC differences between nearby voxels and regions of interest can be modeled by second-order corrections due to geometrical deformations with respect to a canonical configuration of straight brain white matter fibers. Even though the two correction terms we described in this paper are in the forms of partial differential equations and hence are complicated to solve, an intriguing possible future direction is the use of machine learning algorithms to directly map diffusion MRI signals to some geometrical deformation parameters relevant to the brain white matter fibers in the regions of interest.

Chapter 4

Soma size and volume fractions estimation using inflection point-derived biomarkers

Contents

Chapter Overview

In this chapter, we investigate the underlying cause of the breakdown of the $1/\sqrt{b}$ power-law scaling in the brain gray matter. Following the investigation, we propose a novel soma size and compartment volume fractions estimation approach.

This work is inspired by the numerical study on the signal behavior of individual realistic neurons at high b-values in[5]. By fixing the gradient strength and varying the diffusion time (using PGSE with $\delta = \Delta$), Fang *et al.*[5] observed that the direction-averaged neuron signal will change its concavity in the region where $1/\sqrt{b}$ power-law is expected. From this observation, potential biomarkers were derived from this signal inflection point (IP). In the PhD thesis of Chengran Fang[3], he presented a simulation-driven supervised learning framework for microstructural imaging, which uses the inflection point-derived biomarkers (and alternatively, a large number of signal values) as inputs to Multi-layer Perceptrons (MLPs). Also from that PhD thesis are the following needed elements for this thesis described in section 4.1: the experimental settings, the constructions of the *NeuronSet*, the Synthetic Voxels Set, and the spline interpolation method.

In this work, we first examine the signal behaviors of various geometrical shapes using PGSE sequences with fixed δ and Δ ($\delta < \Delta$) and adjusting the gradient strength. This choice is more in accordance with practical MRI experimental settings than the fixed gradient strength setting above. We found that individual neurons still show the same signal pattern as observed in[5]. Thus, we can identify the IP-derived biomarkers in the fixed δ, Δ setting as well. In addition, we found that single spheres exhibit a similar signal pattern as individual neurons, hence we would like to link the signal deviation in realistic neurons to the presence of spherical structures. To be able to accurately compute IP-derived biomarkers, we derive their mathematical expressions using the Numerical Matrix Formalism method. Then, by analyzing the relationship between IP-derived biomarkers and volume fractions and soma size, we demonstrate that:

1. In the single sphere case, the b-value at the inflection point is uniquely determined by the soma radius, with a monotonic relationship;

2. For the case of a single sphere combined with a bundle of sticks, the y-intercept of the linear fit at the inflection point is related to the soma volume fraction;

3. In the case comprising a single sphere, sticks, and one free diffusion compartment, the signal value at the inflection point correlates with the volume fraction of the free diffusion compartment.

These investigations suggest that we can retrieve the soma size and volume fractions information from IP-derived biomarkers.

To demonstrate the ability to use the IP-derived biomarkers for practical microstructure estimation, we propose an exhaustive search method, using similar parameters to the Synthetic Voxels Set constructed in[3]. On the single neuron dataset, we evaluate an iterative method based on the IP-derived biomarkers. On a synthetic test set and on an *in vivo* dataset, we evaluate this exhaustive search method. It is shown that the estimated values are similar to those of the SANDI model and the exhaustive search method based on using a large number of direction-averaged signal values.

This work contributes to the interpretation of the deviation from the $1/\sqrt{\mathrm{b}}$ power-law scaling at high b-values in the brain gray matter with IP-derived biomarkers corresponding to physically meaningful parameters, and leveraging this understanding for microstructure estimation. Compared to signal-based estimation, the estimation errors by the biomarker-based estimation are at the same level. Because it requires only three biomarkers as inputs instead of signal values of multiple shells, the estimation takes less time.

Certain sections from this chapter have been published in the paper[4]. This includes

1. the experimental settings, the constructions of the *NeuronSet*, the Synthetic Voxels Set, and the spline interpolation method, described in section 4.1 (which originated in the PhD thesis of Chengran Fang[3]);

2. the exhaustive search method in section 4.3.2;

3. the estimation results on the Synthetic Voxels Set in section 4.4.2

4. the *in vivo* parameters estimation in section 4.4.3.

The rest of the chapter is new to this thesis and has not been published elsewhere.

4.1 Introduction

In the brain white matter, a recent study by Veraart *et al.*[64, 65] found that the direction-averaged signals

$$\overline{S} \equiv \int_{\|\mathbf{u_g}\|=1} S d\mathbf{u_g}$$

decay at a linear rate with the inverse of the square root of the b-values, $1/\sqrt{\mathrm{b}}$, at high gradient strength. This behavior, called $1/\sqrt{\mathrm{b}}$ power-law scaling, is prevalent in the brain white matter. Subsequent explanation of this observation is achieved through the numerical simulations on sticks,

cylinders as well as realistic neurites phantoms[110, 157]. However, in the brain gray matter, a deviation from this $1/\sqrt{\mathrm{b}}$ power-law scaling is observed. Several explanations have been proposed for this deviation. The three primary ones are: (1) the curvature of neurites[158], (2) the presence of soma[28], and (3) the significant water exchange between neurites and the extracellular space[100].

In a recent work[5], Fang *et al.* conducted a numerical study on individual realistic neurons and their neurite branches, using PGSE sequences with $\delta = \Delta$, keeping the gradient strength constant and adjusting the pulse duration δ. It was revealed that: (1) For the neurite branches, the $1/\sqrt{\mathrm{b}}$ power-law scaling holds true and the slope of this linear fit exhibits a correlation with the inverse of the square root of the intrinsic diffusion coefficient $1/\sqrt{\mathcal{D}_0}$; (2) In contrast, $\overline{S}$ of neurons exhibits a change of the concavity. Thus, potential biomarkers were proposed based on the inflection point (IP) of the direction-averaged signal curve.

In follow up work, in the PhD thesis of Chengran Fang[3], he presented a simulation-driven supervised learning framework for microstructural imaging, showing the potential applications of the inflection point derived biomarkers. In order to fit the *in vivo* dataset, the IP-derived biomarkers are defined based on the signal curve using a fixed PGSE sequence and varying gradient strength, which is different from the original paper[5]. He constructed a Synthetic Voxels Set from realistic neurons and used multilayer perceptrons (MLPs) to approximate the underlying mappings between (1) a large number of signals or (2) IP-derived biomarkers plus ADC and microstructure parameters.

The objective of this chapter is to further investigate the relationship between the IP-derived biomarkers and the volume fractions and soma size, then employ the findings for estimation. Different sequence configurations might result in different relationships. Because practical experiments usually employ PGSE sequences with fixed δ and Δ, adjust only the gradient strength, we adopt the latter definition of IP-derived biomarkers from[3]. Figure 4.1 depicts the $\overline{S}$ of an individual realistic neuron as a function of $1/\sqrt{\mathrm{b}}$ within the regime where the $1/\sqrt{\mathrm{b}}$ power-law scaling is expected, using a fixed PGSE sequence PGSE$(8\mathrm{ms}, 49\mathrm{ms})$ with varying gradient strength. Four IP-derived biomarkers are:

- x_0: the x-coordinate of the inflection point;
- y_0: the y-coordinate of the inflection point;
- c_0: the y-intercept of the power-law fit at the inflection point;
- c_1: the slope of the fit.

This chapter addresses the challenges of interpreting signals in relation to microstructures in the brain gray matter and seeks to provide insights into the design of microstructure estimation algorithms. We analyze the relationship between these four IP-derived biomarkers and volume fractions and soma size. To conduct accurate estimation in practice, we use an exhaustive search method rather than optimization algorithms or machine learning algorithms such as MLPs. The reason for this choice is that the exhaustive search approach eliminates the need for difficult computations of nonconvex fitting. Our library will use similar parameters to the Synthetic Voxels Set constructed in the work[3].

In the remainder of this section, we will present the simulation-driven supervised learning framework proposed in the thesis of Fang[3], including the *in vivo* data, the construction of Synthetic Voxels Set, and the computation of IP-derived biomarkers using spline interpolation. Detailed information regarding the MLP configurations can be found in appendix B.2. We will employ the same datasets to validate our exhaustive search method and compare its performance with the simulation-driven supervised learning framework in a later section.

4.1.1 MGH CDMD data and experimental settings

We first introduce the *in vivo* data and corresponding experimental settings. All subsequent investigations and estimations will be presented using these experimental parameters.

The MGH Connectome Diffusion Microstructure Dataset (CMCD)[156] is a publicly accessible dataset designed to serve as a test platform for the new diffusion MRI microstructure models working at high gradient strengths. The diffusion MRI data are acquired from 26 healthy participants on the 3T Connectome MRI scanner (Magnetom CONNECTOM, Siemens Healthineers). The experiment settings are:

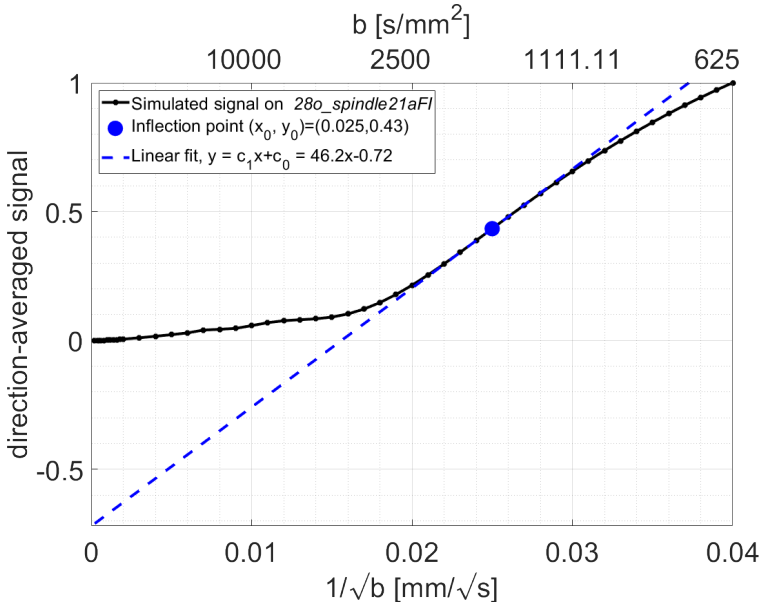

Figure 4.1: Four inflection point derived biomarkers values. The inflection point is characterized as the location where the concavity of the signals changes. The simulation is performed on the neuron *"20171005A01"* from neuromorpho.org[159] using SpinDoctor. Different from the original paper[5], the curve is plotted with fixed sequence PGSE$(8\text{ms}, 49\text{ms})$ and varying gradient strengths. Signal values are normalized by the neuron volume and averaged over 32 uniformly distributed diffusion-encoding gradient directions. The black dots indicate values computed by Numerical Matrix Formalism.

- Two PGSE sequences are applied. The pulse duration $\delta = 8$ms, and two different between pulse duration $\Delta = [19, 49]$ms. The echo time $T_E = 77$ms;
- Eight gradient strengths are used, g-values=$[31, 68, 105, 142, 179, 216, 253, 290]$ mT/m, corresponding to b-values $[72, 346, 825, 1509, 2400, 3491, 4789, 6292]$ s/mm^2 for $\Delta = 19$ ms and $[204, 981, 2340, 4279, 6800, 9902, 13584, 17848]$ s/mm^2 for $\Delta = 49$ms;
- 32 diffusion encoding directions uniformly distributed on a sphere for b < 2400 s/mm^2 and 64 uniform directions for b ≥ 2400 s/mm^2.

The acquired image parameters are: field of view (FOV) = 216×216 mm; slice thickness = 2mm; and voxel size = $2 \times 2 \times 2$ mm^3.

The diffusion MRI data were already pre-processed to correct gradient non-linearity, eddy currents, and susceptibility-induced distortions. The estimated median signal-to-noise ratio (SNR) is 21[156, 160]. MGH CDMD recorded only the real part of the signals for some subjects. Further details regarding data acquisition and processing can be found in the initial publication associated with this dataset[156].

Accordingly, the simulated experiments are designed based on the *in vivo* dataset in use:

- Two PGSE sequences PGSE$(8\text{ms}, 19\text{ms})$ and PGSE$(8\text{ms}, 49\text{ms})$ are applied, referred in the following as the short and long sequences;
- 64 gradient strengths $\|\mathbf{g}\|$ linearly space between 0 and 290 mT/m are simulated;
- 32 diffusion encoding gradient directions $\mathbf{u_g}$ uniformly distributed on a hemisphere are used, which are equivalent to 64 directions on a sphere because the signals are anti-symmetric;
- The simulations are performed using the Numerical Matrix Formalism. The length scale cut-off L_s is chosen to be 1.5μm, which corresponds to a characteristic time scale of 76μs;
- The intrinsic diffusion coefficient $\mathcal{D}_0$ is set to be 3×10^{-3} mm^2/s;

- Interfaces are supposed to be impermeable.

The initial condition is assumed to be a uniformly distributed density. The signals are normalized by the initial density, denoted as $S(\|\boldsymbol{G}\|, \mathbf{u_g}, \delta, \Delta)$. The direction-averaged signals are computed as the average value over all the 32 diffusion encoding directions:

$$\overline{S}(\|\boldsymbol{G}\|, \delta, \Delta) = \frac{1}{32} \sum_{i=1}^{32} S(\|\boldsymbol{G}\|, \mathbf{u_g}, \delta, \Delta). \tag{4.1}$$

4.1.2 *NeuronSet*

The quality of the estimation using MLP is tightly coupled with the quality of the diffusion MRI signal data in the training set. Furthermore, accurate microstructural parameters are required for the validation as well. To be able to acquire high-fidelity data, it is desired that simulations are performed on neurons with realistic shapes. In [4], a neuron database, named *NeuronSet*, was established using digitally reconstructed real human neurons sourced from neuromorpho.org[159], via an automatic generator. This dataset is now available at `https://github.com/SpinDoctorMRI`. To ensure diversity and avoid potential biases arising from similarities in shapes, *NeuronSet* includes neurons covering a wide range of brain regions and encompassing a diverse range of shapes. This dataset contains simulation-ready surface meshes of 1,163 real human neurons and 50 glia, independently recorded by 11 laboratories, stored in 11 archives, and reported on 22 papers[161–182]. For simplicity of notation, we refer to both neurons and glia as neurons in the following since they have the same neuronal shapes.

To be able to perform the simulations (compute the signals and their second-order derivatives), surface meshes will be transformed into volume meshes. This process is done by Tetgen[121] using SpinDoctor. Figure 4.2 displays the distributions of the number of triangles on surface meshes and the number of nodes on volume meshes. The average numbers of faces and nodes are around $150,000$ and $80,000$, respectively. The maximum number of nodes is $200,000$, which is within the capability of our computer.

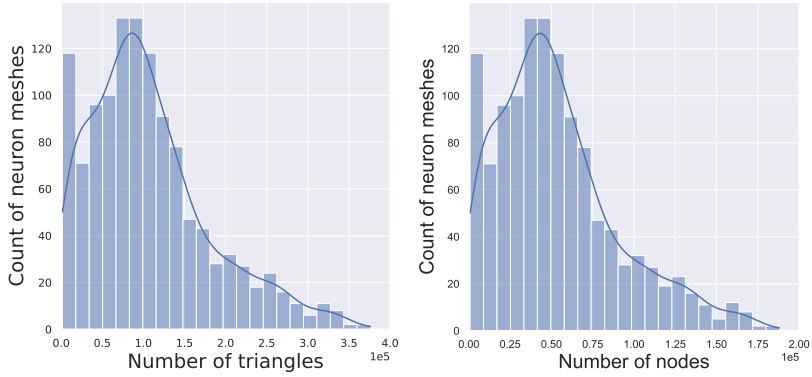

Figure 4.2: Distributions of surface meshes and finite element meshes information of the *NeuronSet* which contains 1213 neurons. Left: The distribution of the number of triangles; Right: The distribution of the number of nodes. The blue solid line is the probability density function of the distributions calculated by Seaborn[183].

In addition, the volume meshes will be used to accurately measure the neuron's shape information. The soma is represented as a sphere with a radius of R_{soma}. Thus, its volume is approximated as $V_{\text{soma}} \simeq 4\pi R_{\text{soma}}^3/3$ and the volume fraction of soma is $f_{\text{soma}} = V_{\text{soma}}/V_{\text{neuron}}$, where V_{neuron} is the neuron volume. The volume fraction of neurite is $f_{\text{neurite}} = (V_{\text{neuron}} - V_{\text{soma}})/V_{\text{neuron}}$.

Figure 4.3 shows the distributions of these four different morphological parameters of the $1,213$ neurons in the *NeuronSet*. The soma radius ranges from 2 to 28 micrometers, with the majority of neurons having a soma radius of 8 or 21 micrometers in this one-neuron dataset. More than 50% of neurons have a f_{soma} value between 40% and 60%.

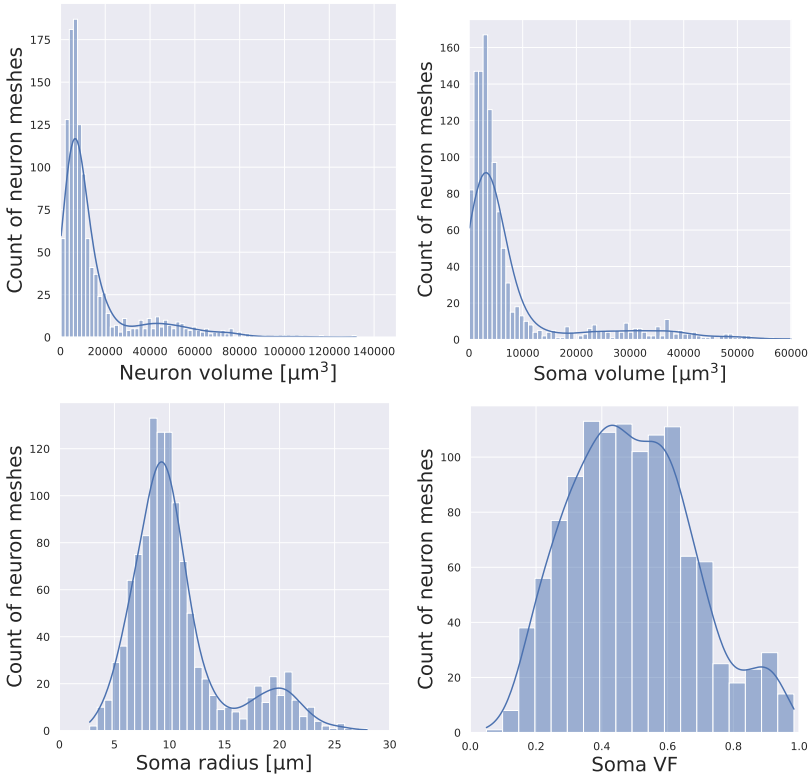

Figure 4.3: Distributions of morphological parameters of the *NeuronSet* which contains $1,213$ cells. All the morphological parameters are measured on the finite elements meshes. Top left: The distribution of neuron volume; Top right: The distribution of soma volume; Bottom left: The distribution of R_{soma}; Bottom right: The distribution of f_{soma}. The blue solid line is the probability density function of the distributions calculated by Seaborn[183].

4.1.3 Synthetic Voxels Set

The Synthetic voxels set is constructed based on the following assumptions:

- The blood vessels compartment and the stationary water are negligible because their volume fractions in the brain gray matter are relatively small;
- The intracellular compartment is modeled as a combination of neurons randomly selected from the *NeuronSet*. Each neuron comprises a soma and neurites, all of which are correctly interconnected;
- Due to the complexities of accurately packing neurons into extracellular space (ECS) and maintaining a volume fraction close to the actual value, as well as the intensive computational costs for simulating the permeability effects, the signal contribution from ECS is modeled as one isotropic Gaussian diffusion compartment. To reduce the model complexity, its diffusion coefficient is fixed to be the same value of the intrinsic diffusion coefficient, $\mathcal{D}_0$;
- Water exchange between neurons and the free diffusion compartment is negligible. Therefore, each neuron and ECS are disconnected.

The Synthetic voxels set is constructed by randomly selecting M neurons from the *NeuronSet* to make 145,000 artificial intercellular spaces. The number M ranges from 1 to 500 and there are no duplicate neurons by choice. Each combination of M neurons is then supplemented with 10 different free diffusion compartments whose diffusion coefficient is fixed to $\mathcal{D}_0$ but the volume fraction follows a Gaussian distribution $\mathcal{N}(\mu = 0.5, \sigma^2 = 0.25^2)$. The choice of the Gaussian distribution is empirical. In total, 1.45 million distinct artificial brain voxels are made.

Since the orientation of the neurons has no impact on the direction-averaged signal, all the compartments in one voxel are uncoupled. Therefore, the signal is simply represented as the sum of all the contained compartments. Suppose an artificial brain voxel contains M neurons and a free diffusion compartment, the direction-averaged signal inside one voxel is expressed as

$$\overline{S}_{\text{voxel}}(\delta, \Delta, \|\boldsymbol{G}\|) = f_{\text{neuron}} \times \frac{\sum_{i=1}^{M} V_i \cdot \overline{S}_i}{\sum_{i=1}^{M} V_i} + f_{\text{free}} \times e^{-\mathcal{D}_0 b}, \tag{4.2}$$

where the subscription i indicates the i-th cell, V_i is the neuronal volume, $\overline{S}_i$ is the direction-averaged signal, and $\mathcal{D}_0$ is the intrinsic diffusion coefficient. f_{neuron} and f_{free} are the volume fraction of the neuron and free compartment, respectively. The sum of them is 1.

The microstructural parameters of the synthetic voxel can be determined by the contained neurons. Here, we focus on the volume fractions and the soma radius. Given the neuroanatomical parameters of one synthetic voxel of M neurons, the soma volume fraction is

$$f_{\text{soma}} = f_{\text{neuron}} \frac{\sum_{m=1}^{M} V_{\text{soma}}^m}{\sum_{m=1}^{M} V_{\text{neuron}}^m}, \tag{4.3}$$

the neurite volume fraction is

$$f_{\text{neurite}} = f_{\text{neuron}} \frac{\sum_{m=1}^{M} V_{\text{neurite}}^m}{\sum_{m=1}^{M} V_{\text{neuron}}^m}, \tag{4.4}$$

and the volume-averaged soma radius is

$$\overline{R}_{\text{soma}} = \frac{\sum_{m=1}^{M} V_{\text{soma}}^m R_{\text{soma}}^m}{\sum_{m=1}^{M} V_{\text{soma}}^m}. \tag{4.5}$$

Figure 4.4 presents the distributions of the volume fractions and volume-averaged soma radius in the Synthetic voxels set. f_{soma} and f_{neurite} are not very correlated after adding the free diffusion compartment. Two peaks of $\overline{R}_{\text{soma}}$ are 10μm and 18μm.

Figure 4.4: The distributions of the volume fractions and volume-averaged soma radius in the Synthetic voxels set. Left: The distributions of f_{soma}, f_{neurite}, f_{free}. Middle: The joint distributions of f_{soma} and f_{neurite}. Right: The distributions of $\overline{R}_{\text{soma}}$. The Synthetic voxels set contains 1.45 million artificial voxels, where f_{free} follows a Gaussian distribution $\mathcal{N}(\mu = 0.5, \sigma^2 = 0.25^2)$, f_{soma} and f_{neurite} are derived from realistic neuron meshes. The contour lines in the joint distributions contain 50%, 75%, and 90% of the data points.

4.1.4 Spline interpolation

The spline interpolation is used for:

- The MLPs are trained using 64 gradient strengths, in order to be designed as a dataset-independent framework. To perform estimation on the *in vivo* data, 8 measured signals need to be interpolated into 64 signals;

- The IP-derived biomarkers need to be computed using spline interpolation.

Because a vanilla cubic spline suffers a large fluctuation, which may cause inaccuracy and produce spurious inflection point, the fourth-order B-spline interpolation implemented in Scipy[184] is adopted. To moderate the fluctuation, the Gaussian phase approximation is applied when b-values are smaller than 35 s/mm^2, which provides two boundary conditions which are the continuity of the first and second-order derivatives at the lowest b-values $\mathrm{b_{low}}$:

$$\overline{S}'(1/\sqrt{\mathrm{b_{low}}}) = 2\mathrm{ADC}\sqrt{\mathrm{b_{low}^3}}e^{-\mathrm{ADC}\cdot\mathrm{b_{low}}}, \tag{4.6}$$

$$\overline{S}''(1/\sqrt{\mathrm{b_{low}}}) = 2\mathrm{ADC}\cdot\mathrm{b_{low}^2}(2\mathrm{ADC}\cdot\mathrm{b_{low}}-3)e^{-\mathrm{ADC}\cdot\mathrm{b_{low}}}. \tag{4.7}$$

At the high b-value end $\mathrm{b_{high}}$, the "natural" boundary condition[185] is adopted:

$$\overline{S}''(1/\sqrt{\mathrm{b_{high}}}) = 0. \tag{4.8}$$

The boundary conditions help moderate the fluctuation of the interpolation and allow to sample of gradient strength up to its maximum value in the real data and find the inflection point. Figure 4.5 demonstrates the measured and interpolated signals. It is worth mentioning that if the inflection point exceeds the maximum gradient strength, it will be capped at the maximum value, due to the considerable extrapolation error of this method.

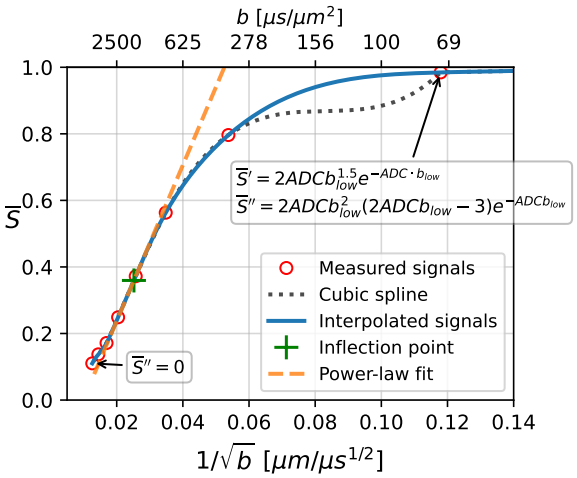

Figure 4.5: Fourth-order B-spline interpolation of direction-averaged signals. Red circles represent the direction-averaged signals at eight non-zero b-values measured from a voxel of the second subject (`sub_002`) in MGH CDMD. The voxel index is (19, 25, 73). A vanilla cubic spline interpolation represented by the dotted black line suffers a large fluctuation. The inflection point is marked by the green cross. The orange dash line represents the power-law fit at the inflection point. By incorporating the three boundary conditions annotated in the boxes, the fourth-order B-spline method interpolates the eight measured signals giving the solid blue line.

4.2 Analysis of the deviation of power-law scaling in gray matter

To start, we examine the direction-averaged signal behavior at high b-values for different geometries, from simple shapes, such as sticks, cylinders, and spheres, to realistic neurons, as shown in fig. 4.6. Two numerically reconstructed neurons from *NeuronSet* are used. The first one is located in the fronto-insula region, labeled as "neuron1", which has a radius of 15.65μm and a soma volume fraction of 83%. The second one is located in the occipital lobe, labeled as "neuron2", which has a

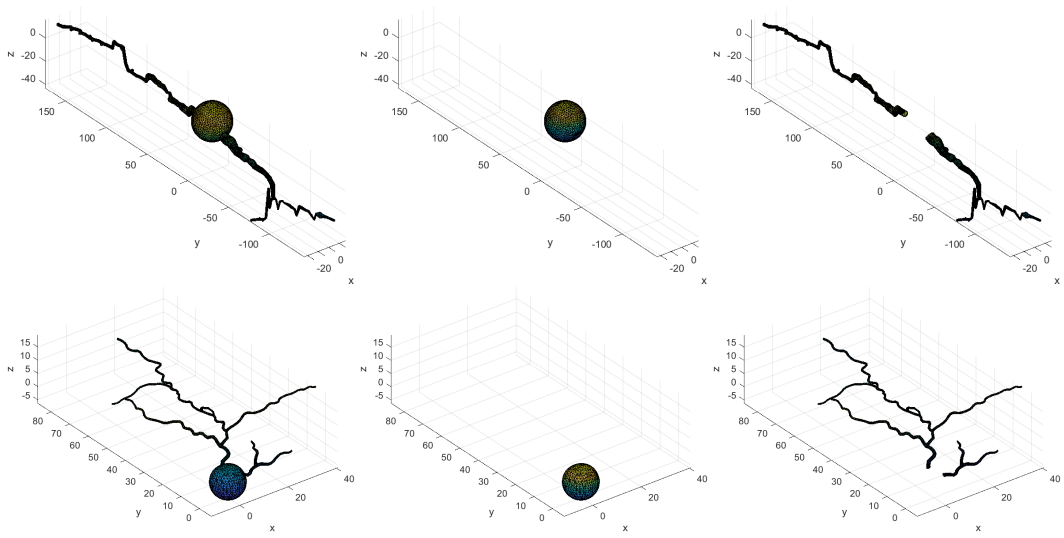

Figure 4.6: Finite element meshes of two numerically reconstructed neurons from *NeuronSet*. From left to right: The whole neurons, the soma part, and the neurites part. The neuron is cut manually in Blender and its volume is conservative. Top row: The name of the neuron is *"28o_spindle21aFl"* (from the *allman* archive, located in the fronto-insula region). Its soma radius is 15.65μm and its soma volume fraction is 83%; Bottom row: The name of the neuron is *"H17-06-012-14-08-03_680980293_m"* (from the *allen* archive, located in the occipital lobe). Its soma radius is 5.5μm and its soma volume fraction is 91%.

radius of 5.5μm and a soma volume fraction of 91%. This analysis employs fixed PGSE sequence and varying $\|\boldsymbol{G}\|$, which differs from[5].

In fig. 4.7, we plot the direction-averaged signals using two sequences for eight cases: (1) a bundle of sticks, (2) one sphere, (3) one sphere + sticks (4) a collection of infinity long cylinders, (5) connected neuron, (6) disconnected neuron, (7) soma part and (8) neurites part. The direction-averaged signal of sticks has an analytical expression:

$$\overline{S}_{sticks} = \int_{-1}^{1} e^{-\mathcal{D}_0 b z^2} dz = \sqrt{\frac{\pi}{4\mathcal{D}_0 \mathsf{b}}} \mathrm{erf}(\sqrt{\mathcal{D}_0 \mathsf{b}}) \tag{4.9}$$

where erf$(\cdot)$ is the error function. For the other shapes, $\overline{S}$ is computed by the Matrix Formalism. We observe that:

1. The $1/\sqrt{\mathsf{b}}$ power-law scaling holds true for all tubular structures, from simple shapes such as sticks and straight cylinders to realistic neurite branches, implying that the curvature and branching won't break this relationship. For sticks, at high b-values, erf$(\sqrt{\mathcal{D}_0 \mathsf{b}}) \approx 1$, thus we have $\overline{S}_{sticks} \approx \sqrt{\pi/4\mathcal{D}_0 \mathsf{b}}$, which results in the power-law relationship;
2. At ultra-high b-values, the signal of the collection of cylinders starts to become sensitive to the perpendicular diffusion inside the neurite, resulting in deviation from the linear relationship[66];
3. All the shapes containing spherical structures do not exhibit the power-law in the range where we should observe it. Furthermore, for all of them, we notice the signals will change the concavity at a specific point, suggesting that the inflection point is related to the inclusion of spherical structures;
4. As the diffusion time increases, the point of concavity change occurs at a higher b-value;
5. Signal of the whole neuron is similar to those of the case comprising one sphere and sticks;
6. The signals from disconnected neurons are similar to those from the connected neurons, indicating that water exchange between the soma and neurites has minimal influence on the global signal behavior pattern.

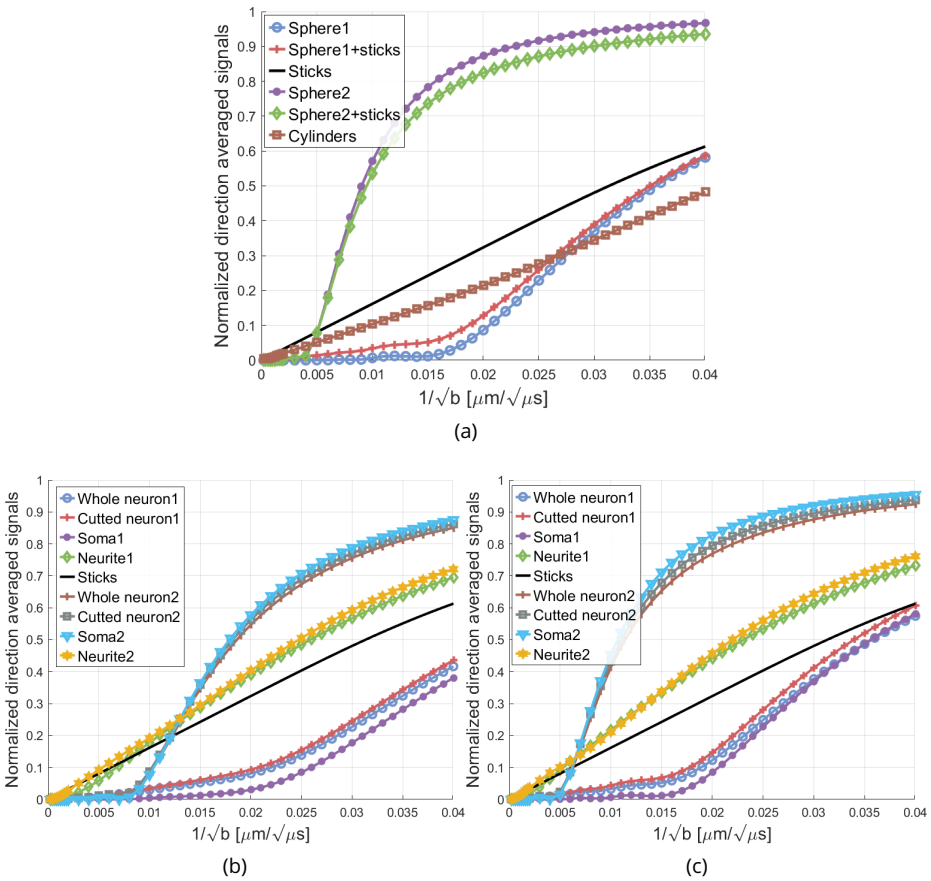

Figure 4.7: $\overline{S}$ against $1/\sqrt{\text{b}}$. Top: Results for simple shapes, using the long sequence, The blue, red, purple, green, and brown lines represent the case of (1) one sphere with a radius of 15.65μm, labeled 'Sphere1', (2) 'Sphere1'+sticks, (3) one sphere with a radius of 5.5μm, labeled 'Sphere2', (4) 'Sphere2'+sticks and (5) a collection of cylinders with radii from 0.5μm to 1.5μm; Bottom left: Results for realistic shapes, using the short sequence; Right: Results for realistic shapes, using the long sequence. The blue, red, purple, green, brown, gray, light blue, and yellow lines represent the case of (1) connected neuron1, (2) disconnected neurons1, (3) the soma of neuron1, (4) the neurites of neuron1, (5) the connected neuron2, (6) the disconnected neuron2, (7) the soma of neuron2 and (8) the neurite of neuron2. The black line is the pure sticks case. The markers indicate values computed by Numerical Matrix Formalism.

4.2.1 IP-derived biomarkers

In the previous subsection, we demonstrate that the presence of spherical structures will cause the deviation of the $1/\sqrt{\text{b}}$ power-law scaling. In the following, we adopt the same definition of the four IP-derived biomarkers in section 4.1 and investigate the relationship between these biomarkers and the soma size and volume fractions. Notably, among these four IP-derived biomarkers, only three are truly independent. The slope c_1 can be computed by $(y_0 - c_0)/x_0$. Mathematically, the x-coordinate of the inflection point x_0 corresponds to the gradient strength value making the second-order derivative of $\overline{S}$ against $1/\sqrt{\text{b}}$ equal to zero. The y-coordinate y_0 is the corresponding normalized signal value and the slope c_1 is the corresponding first-order derivative value. The y-intercept c_0 signifies that, starting from the inflection point, the signals begin to decay at their peak rate c_1, and this trend continues as the gradient strength approaches infinity.

Because of the high b-values resonance, the second-order derivative of $\overline{S}$ perhaps has multiple zeros. In that case, we take the lowest b-values point as the target inflection point, where the first-order derivative of $\overline{S}$ against $1/\sqrt{\text{b}}$ is maximum.

4.2.2 Mathematical computation of IP-derived biomarkers from Numerical Matrix Formalism

In this subsection, we provide the mathematical expressions of the four IP-derived biomarkers, x_0, y_0, c_1 and c_0, using Numerical Matrix Formalism. Compared to find them by fourth-order spline interpolation, these expressions ensure precise computation of these biomarkers during numerical analysis.

Using the first N_{eig} smallest Laplace eigenfunctions $(\phi_i)_{i=1,\dots,N_{eig}}$, the diffusion MRI signals of PGSE(δ, Δ) have the expression as below by the Numerical Matrix Formalism:

$$\begin{aligned} S(\|\boldsymbol{G}\|, \mathbf{u_g}, \delta, \Delta; N_{eig}) &= \left(\mathbf{1}_{N_{node},1}^T \boldsymbol{M}\boldsymbol{P}\right) \boldsymbol{H}(\|\boldsymbol{G}\|, \mathbf{u_g}, \delta, \Delta) \left(\boldsymbol{P}^T \boldsymbol{M} \mathbf{1}_{N_{node},1}\right) \\ &= \mathbf{T}_0^T \boldsymbol{H}(\|\boldsymbol{G}\|, \mathbf{u_g}, \delta, \Delta) \mathbf{T}_0, \end{aligned} \tag{4.10}$$

where $\cdot^T$ is the transposed conjugate, $\mathbf{1}_{N_{node},1}$ is an all-one vector, $\boldsymbol{M}$ is the mass matrix, and $\boldsymbol{P}$ is the coefficient of Laplace eigenfunctions in the $P1$ finite element functions. We denote the initial magnetization coefficient on the Laplace eigenfunctions as $\mathbf{T}_0 \equiv \boldsymbol{P}^T \boldsymbol{M} \mathbf{1}_{N_{node},1}$, which is independent of the imposed gradient sequence. $\boldsymbol{H}(\|\boldsymbol{G}\|, \mathbf{u_g}, \delta, \Delta)$ is expressed as

$$\boldsymbol{H}(\|\boldsymbol{G}\|, \mathbf{u_g}, \delta, \Delta) = e^{-\delta(\boldsymbol{L} - \imath\gamma\|\boldsymbol{G}\|\boldsymbol{W}(\boldsymbol{g_u}))} \cdot e^{-(\Delta-\delta)\boldsymbol{L}} \cdot e^{-\delta(\boldsymbol{L} + \imath\gamma\|\boldsymbol{G}\|\boldsymbol{W}(\boldsymbol{g_u}))}, \tag{4.11}$$

where $\boldsymbol{L}$ is a diagonal matrix of Laplace eigenvalues, $\|\boldsymbol{G}\|$ is the gradient strength, $\boldsymbol{g_u}$ is the diffusion encoding gradient direction and $\boldsymbol{W}(\mathbf{u_g})$ is the projection of encoding gradient term onto the Laplace eigenfunctions:

$$\boldsymbol{W}(\boldsymbol{g_u}) = \sin(\phi)(\cos(\theta)\boldsymbol{A}^x + \sin(\theta)\boldsymbol{A}^y) + \cos(\phi)\boldsymbol{A}^z, \tag{4.12}$$

$$\boldsymbol{A}^r_{kl} = \int_{\mathbf{x}\in\Omega} r\phi_k(\mathbf{x})\phi_l(\mathbf{x})d\mathbf{x},\ (k,l) \in \{1, 2, \dots, N_{eig}\}^2,\ r \in \{x, y, z\}, \tag{4.13}$$

with

$$\boldsymbol{g_u} = [\sin(\phi)\cos(\theta), \sin(\phi)\sin(\theta), \cos(\phi)]^T. \tag{4.14}$$

The matrices $\boldsymbol{L}$ and $\boldsymbol{W}$ are symmetric. The details of the Numerical Matrix Formalism representation can be found in chapter 2.

For ease of notation, we introduce a new variable q, defined as $q = \gamma\|\boldsymbol{G}\|$. For PGSE, the $\sqrt{\mathsf{b}}$ holds a linear relation with q:

$$\sqrt{\mathsf{b}} = \delta\sqrt{\Delta - \delta/3}\gamma\|\boldsymbol{G}\| = \delta\sqrt{\Delta - \delta/3}q. \tag{4.15}$$

Here, we represent $\boldsymbol{H}$ as the product of a matrix $\boldsymbol{G}$ and its transpose conjugate:

$$\boldsymbol{H} = \boldsymbol{G}^T\boldsymbol{G}, \tag{4.16}$$

with $\boldsymbol{G}$ defined as

$$\boldsymbol{G} = e^{-0.5\cdot(\Delta-\delta)\boldsymbol{L}} \cdot e^{-\delta(\boldsymbol{L} + \imath q\boldsymbol{W})}. \tag{4.17}$$

In the case of δ and Δ fixed, and the gradient strength $\|\boldsymbol{G}\|$ varying, the direction-averaged signals exclusively depend on the gradient strength and can be written as

$$\overline{S}(\|\boldsymbol{G}\|) = \frac{1}{4\pi}\int_0^{\pi}\int_0^{2\pi} S(\|\boldsymbol{G}\|, \mathbf{u_g})d\theta d\phi \tag{4.18}$$

$$= \mathbf{T}_0^T \frac{1}{4\pi}\int_0^{\pi}\int_0^{2\pi} \boldsymbol{H} d\theta d\phi \mathbf{T}_0 \tag{4.19}$$

$$= \mathbf{T}_0^T \frac{1}{4\pi}\int_0^{\pi}\int_0^{2\pi} \boldsymbol{G}^T\boldsymbol{G} d\theta d\phi \mathbf{T}_0. \tag{4.20}$$

The first-order derivative of $\overline{S}$ with respect to $1/\sqrt{\mathsf{b}}$ is

$$\begin{aligned}\frac{d\overline{S}}{d(1/\sqrt{\mathsf{b}})} &= \frac{d\overline{S}}{dq}\frac{dq}{d(1/\sqrt{\mathsf{b}})} \\ &= -q^2\delta\sqrt{\Delta-\delta/3}\frac{d\overline{S}}{dq} \\ &= \frac{-q^2\delta\sqrt{\Delta-\delta/3}}{4\pi}\mathbf{T}_0^T\left(\int_0^{\pi}\int_0^{2\pi}\frac{d(\boldsymbol{G}^T\boldsymbol{G})}{dq}d\theta d\phi\right)\mathbf{T}_0 \\ &= \frac{-q^2\delta\sqrt{\Delta-\delta/3}}{4\pi}\mathbf{T}_0^T\left(\int_0^{\pi}\int_0^{2\pi}\boldsymbol{G}^T\frac{d\boldsymbol{G}}{dq}+\left(\boldsymbol{G}^T\frac{d\boldsymbol{G}}{dq}\right)^T d\theta d\phi\right)\mathbf{T}_0.\end{aligned} \tag{4.21}$$

where the first-order derivative of $\boldsymbol{G}$ with respect to q can be computed by the theorem[186]

$$\frac{d\boldsymbol{G}}{dq} = e^{-0.5\cdot(\Delta-\delta)\boldsymbol{L}}\int_0^1 e^{-\alpha\delta(\boldsymbol{L}+\imath q\boldsymbol{W})}(-\imath\delta\boldsymbol{W})e^{-(1-\alpha)\delta(\boldsymbol{L}+\imath q\boldsymbol{W})}d\alpha. \tag{4.22}$$

For simplicity in notation, we define one new variable depending on q:

$$a \equiv \frac{1}{4\pi}\mathbf{T}_0^T\left(\int_0^{\pi}\int_0^{2\pi}\boldsymbol{G}^T\frac{d\boldsymbol{G}}{dq}d\theta d\phi\right)\mathbf{T}_0. \tag{4.23}$$

Therefore, the first-order derivative $d\overline{S}/d(1/\sqrt{\mathsf{b}})$ is expressed as

$$\frac{d\overline{S}}{d(1/\sqrt{\mathsf{b}})} = -q^2\delta\sqrt{\Delta-\delta/3}(a+a^T) = -2q^2\delta\sqrt{\Delta-\delta/3}\Re(a). \tag{4.24}$$

The second-order derivative of $\overline{S}$ with respect to $1/\sqrt{\mathsf{b}}$ is

$$\begin{aligned}\frac{d^2\overline{S}}{d(1/\sqrt{\mathsf{b}})^2} &= \frac{d}{dq}\left(\frac{d\overline{S}}{d(1/\sqrt{\mathsf{b}})}\right)\frac{dq}{d(1/\sqrt{\mathsf{b}})} \\ &= q^2\delta^2(\Delta-\delta/3)\frac{d(q^2(a+a^T))}{dq} \\ &= q^4\delta^2(\Delta-\delta/3)\left(\frac{2(a+a^T)}{q}+\frac{da}{dq}+\left(\frac{da}{dq}\right)^T\right).\end{aligned} \tag{4.25}$$

The derivative da/dq is expressed as

$$\begin{aligned}\frac{da}{dq} &= \frac{1}{4\pi}\mathbf{T}_0^T\left(\int_0^{\pi}\int_0^{2\pi}\frac{d}{dq}\left(\boldsymbol{G}^T\frac{d\boldsymbol{G}}{dq}\right)d\theta d\phi\right)\mathbf{T}_0 \\ &= \frac{1}{4\pi}\mathbf{T}_0^T\left(\int_0^{\pi}\int_0^{2\pi}\frac{d\boldsymbol{G}^T}{dq}\frac{d\boldsymbol{G}}{dq}+\boldsymbol{G}^T\frac{d^2\boldsymbol{G}}{dq^2}d\theta d\phi\right)\mathbf{T}_0.\end{aligned} \tag{4.26}$$

The second-order derivative of $\boldsymbol{G}$ with respect to q is

$$\frac{d^2\boldsymbol{G}}{dq^2} = e^{-0.5\cdot(\Delta-\delta)\boldsymbol{L}}\cdot(\boldsymbol{B}+\boldsymbol{B}^T), \tag{4.27}$$

where $\boldsymbol{B}$ can be computed using the same theorem[186]

$$\boldsymbol{B} = \int_0^1\alpha\left(\int_0^1 e^{-\beta\alpha\delta(\boldsymbol{L}+\imath q\boldsymbol{W})}(-\imath\delta\boldsymbol{W})e^{-(1-\beta)\alpha\delta(\boldsymbol{L}+\imath q\boldsymbol{W})}d\beta\right)(-\imath\delta\boldsymbol{W})e^{-(1-\alpha)\delta(\boldsymbol{L}+\imath q\boldsymbol{W})}d\alpha. \tag{4.28}$$

For simplicity in notation, we define two new variables depending on q:

$$b = \frac{1}{4\pi}\mathbf{T}_0^T\left(\int_0^{\pi}\int_0^{2\pi}\frac{d\boldsymbol{G}^T}{dq}\frac{d\boldsymbol{G}}{dq}d\theta d\phi\right)\mathbf{T}_0, \tag{4.29}$$

$$c = \frac{1}{4\pi}\mathbf{T}_0^T\left(\int_0^{\pi}\int_0^{2\pi}\boldsymbol{G}^T\frac{d^2\boldsymbol{G}}{dq^2}d\theta d\phi\right)\mathbf{T}_0. \tag{4.30}$$

Thus, the second-order derivative $d^2\overline{S}/d(1/\sqrt{\mathsf{b}})^2$ is expressed as

$$\begin{aligned}\frac{d^2\overline{S}}{d(1/\sqrt{\mathsf{b}})^2} &= q^4\delta^2(\Delta-\delta/3)\left(\frac{2(a+a^T)}{q}+b+c+b^T+c^T\right)\\ &= 2q^4\delta^2(\Delta-\delta/3)\left(\frac{2\Re(a)}{q}+\Re(b+c)\right).\end{aligned} \tag{4.31}$$

The x-coordinate of the inflection point x_0 is the b-value where eq. (4.31) equals to 0:

$$\frac{2\Re(a)}{q}+\Re(b+c)=0. \tag{4.32}$$

This formulation of x_0 is valid for all kinds of geometries with a fixed PGSE sequence, except in the presence of the non-equilibrium permeable interfaces. Even though it is difficult to solve directly this equation due to the complex dependence of a, b, and c on gradient strength, we can numerically compute it by root-finding algorithms[187].

y_0 is the corresponding $\overline{S}$ value at the b-value of x_0:

$$y_0=\overline{S}_{|\mathsf{b}=x_0}. \tag{4.33}$$

c_1 is the corresponding first-order derivative value of $\overline{S}$ with respect to $1/\sqrt{\mathsf{b}}$ at b-value of x_0:

$$c_1=\frac{d\overline{S}}{d(1/\sqrt{\mathsf{b}})_{|\mathsf{b}=x_0}}. \tag{4.34}$$

c_0 can be given by

$$c_0=y_0-c_1x_0. \tag{4.35}$$

In summary, to accurately compute the IP-derived biomarkers, we use root-finding algorithms to find the zero of eq. (4.32), which is x_0. Once we obtain the value of x_0, y_0 and c_1 can be calculated by eq. (4.33) and eq. (4.34) respectively, then c_0 can be obtained by eq. (4.35).

Figure 4.8 depicts $d^2\overline{S}/d(1/\sqrt{\mathsf{b}})^2$ and $2\Re(a)/q+\Re(b+c)$ against q, for a single sphere with varying radius. The inflection point is marked by the transition of $2\Re(a)/q+\Re(b+c)$ from a negative to a positive value. As R_{soma} increases, the q value at the inflection point decreases. Additionally, in the regime near zero, $2\Re(a)/q+\Re(b+c)$ exhibits a quasi-linear behavior, whereas $d^2\overline{S}/d(1/\sqrt{\mathsf{b}})^2$ appears more curved, in order of q^5. This implies that using spline interpolation to compute the IP-derived biomarkers may be less accurate.

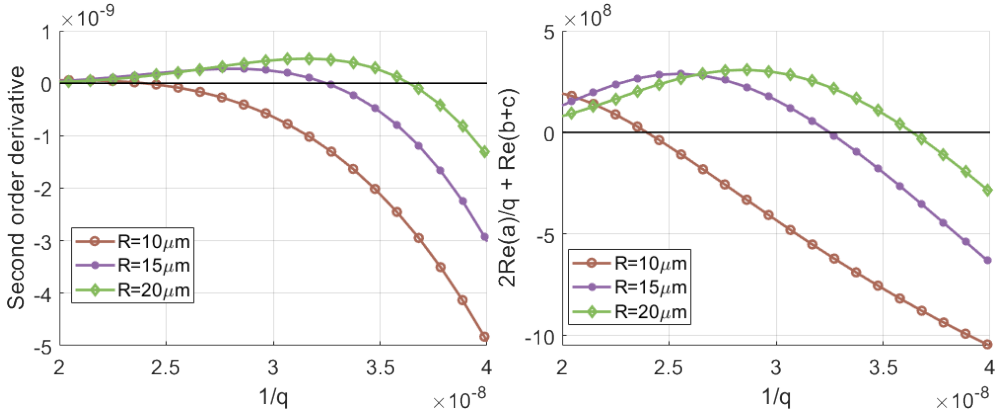

Figure 4.8: $d^2\overline{S}/d(1/\sqrt{\mathsf{b}})^2$ (left) and $2\Re(a)/q+\Re(b+c)$ (right) against $1/q$, using the short sequence. The simulations are performed on a single sphere with varying radii. The markers indicate values computed by Numerical Matrix Formalism.

The numerical implementation of the first and second-order derivatives of the direction-averaged signals using Numerical Matrix Formalism refers to appendix B.1.

Remark 5. *The a, b, and c are real numbers in the case of uniformly distributed initial density. Therefore, in practice, the operator $\Re(\cdot)$ in eq.* (4.32) *isn't necessary.*

4.2.3 Analysis IP-derived biomarkers on simplified shapes

In this subsection, we investigate the relationship between the four IP-derived biomarkers and the soma size and volume fractions on some simplified shapes. As shown in fig. 4.7, we observe that the signals from the neuron can be roughly approximated as a combination of signals from the soma and the neurites. Furthermore, the soma can be represented as a sphere and the neurites can be represented as a bundle of sticks. Throughout this subsection, we use the terms "soma" and "sphere" as synonyms and "neurite" and "sticks" as synonyms. We will examine four simplified shapes: a single sphere, a sphere accompanied by sticks, a sphere combined with sticks and a free diffusion compartment, and multiple spheres.

4.2.3.1 One sphere case

The soma is often modeled as a perfect sphere with a radius of R_{soma}. Our initial effort is to relate the four IP-derived biomarkers with R_{soma} in the single sphere case. In that case, the diffusion MRI signals are identical in all the diffusion encoding directions, so we can remove the integral in eq. (4.32).

The Laplace operator in spherical coordinates (r, θ, ϕ) can be separated into an axial term and spherical harmonic term

$$\Delta = \frac{\partial^2}{\partial r^2} + \frac{2}{r}\frac{\partial}{\partial r} + \frac{1}{r^2}\left(\frac{1}{\sin\theta}\frac{\partial}{\partial\theta}\sin\theta\frac{\partial}{\partial\theta} + \frac{\partial^2}{\partial\varphi^2}\right). \tag{4.36}$$

The eigenvalues and eigenfunctions of the Laplace operator with Neumann boundary condition are expressed as[70]

$$\lambda_{nk} = \frac{\mathcal{D}_0\alpha_{nk}^2}{R_{\text{soma}}^2}, \text{ with } j_n'(\alpha_{nk}) = 0, \tag{4.37}$$

$$\phi_{lnk}(r,\theta,\varphi) = \frac{\beta_{nk}}{\sqrt{2\pi}j_n(\alpha_{nk})}j_n(\alpha_{nk}\frac{r}{R_{\text{soma}}})Y_l^n(\theta,\varphi), \tag{4.38}$$

where $j(\cdot)_n$ and $j_n'(\cdot)$ are the spherical Bessel function of the first kind of order n and its derivative, β_{nk} is the L^2-norm normalized constant, which can be expressed as $\beta_{nk} = \frac{1}{R_{\text{soma}}^{3/2}}\sqrt{\frac{(2n+1)\lambda_{nk}}{\lambda_{nk}-n(n+1)}}$, $Y_l^n(\theta,\varphi)$ is the spherical harmonics. The eigenvalues are degenerates ($2l+1$ eigenfunctions for one eigenvalues), and hold a linear relation with R_{soma}^{-2}, $\boldsymbol{L} \propto R_{\text{soma}}^{-2}$.

We have also the analytical expression of the matrix of the projection of encoding gradient term $\boldsymbol{W}$[70]:

$$\boldsymbol{W}_{nk,n'k'} = \beta_{nk}\beta_{n'k'}\frac{(n+n'+1)\,\delta_{n,n'\pm1}}{(2n+1)\,(2n'+1)}\frac{\lambda_{nk}+\lambda_{n'k'}-n\,(n'+1)-n'(n+1)+1}{\left(\lambda_{nk}-\lambda_{n'k'}\right)^2} \tag{4.39}$$

It is clear that in this case, the eigenvalues matrix $\boldsymbol{L}$ and encoding gradient projection matrix $\boldsymbol{W}$ only depend on R_{soma}. In fig. 4.9, we illustrate the four IP-derived biomarkers as functions of R_{soma}. The blue and red lines represent the results for the short and long sequences, respectively. From the plot, we have the following observations:

1. x_0 and c_1 are one-to-one mappings with R_{soma}, implying that we can retrieve the radius value from either of them;
2. For a R_{soma} value, the longer the sequence, the smaller the values of x_0. Besides, with a longer sequence, the relationship between x_0 and R_{soma} appears increasingly linear;
3. For large radius ($R > 20\mu$m), the curve x_0 tends to flatten with shorter PGSE sequence, making it challenging to differentiate between different large radius values;
4. Conversely, c_1 remains consistent for $3\mu\text{m} \leq R_{\text{soma}} \leq 10\mu$m across two sequences. With a longer sequence, the mapping between c_1 and R_{soma} in logarithm also tends toward linearity;
5. y_0 and c_0 are fluctuated around 0.22 and 0.45, preventing us from establishing one-to-one mappings between y_0 or c_0 with the radius R_{soma}.

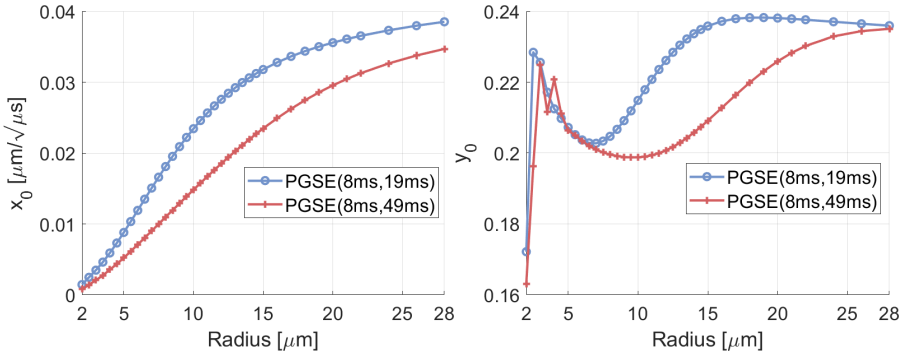

(a) x_0 against R_{soma}

(b) y_0 against R_{soma}

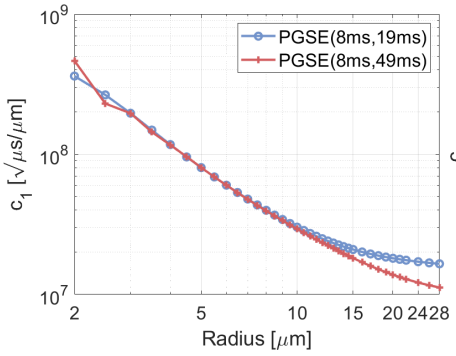

(c) c_1 against R_{soma}

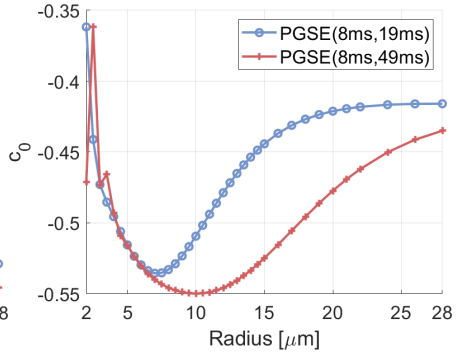

(d) c_0 against R_{soma}

Figure 4.9: Four IP-derived biomarkers as functions of R_{soma}. The blue and red lines are the results using short and long sequences, respectively. The markers indicate values computed by Numerical Matrix Formalism.

4.2.3.2 One sphere + sticks

A common simplification about neuronal shape is to model the soma as one sphere, and the neurites as a collection of infinitely long sticks[188]. These two compartments are distinct and disconnected. Its direction-averaged signal can be written as

$$\overline{S} = f_{\text{soma}}\overline{S}_{\text{soma}} + f_{\text{neurite}}\overline{S}_{\text{neurite}}, \tag{4.40}$$

with $f_{\text{soma}} + f_{\text{neurite}} = 1$. The direction-averaged sphere signal is the same as discussed in the previous subsection, and the sticks signal is given by eq. (4.9). Its first and second-order derivatives are

$$\frac{d\overline{S}_{\text{neurite}}}{d(1/\sqrt{\mathsf{b}})} = \sqrt{\frac{\pi}{4\mathcal{D}_0}}\text{erf}(\sqrt{\mathcal{D}_0\mathsf{b}}) - \sqrt{\mathsf{b}}e^{-\mathcal{D}_0\mathsf{b}}, \tag{4.41}$$

$$\frac{d^2\overline{S}_{\text{neurite}}}{d(1/\sqrt{\mathsf{b}})^2} = -2\mathcal{D}_0\mathsf{b}^2e^{-\mathcal{D}_0\mathsf{b}}. \tag{4.42}$$

In fig. 4.10, we plot the first and second-order derivatives of sticks compartment against $1/\sqrt{\mathsf{b}}$. The second-order derivative of the sticks is a strictly negative monotone function. Thus, the sticks compartment does not have an inflection point itself. In the regime of high b-values ($1/\sqrt{\mathsf{b}} \leq 0.02\mu\text{m}\cdot\mu\text{s}^{-1/2}$), the second-order derivative is almost zero ($-2\mathcal{D}_0\mathsf{b}^2e^{-\mathcal{D}_0\mathsf{b}} \approx 0$), manifesting the power-law scaling. The first-order derivative converges to $\sqrt{\pi/(4\mathcal{D}_0)} \approx 16.18$.

However, adding the sticks to single sphere will change the relationship between our IP-derived biomarkers and morphological parameters. In this case, the x-coordinate of the inflection point is given by the expression:

$$f_{\text{soma}}\left(\frac{2\Re(a_{\text{soma}})}{q} + \Re(b_{\text{soma}} + c_{\text{soma}})\right) - f_{\text{neurite}}\mathcal{D}_0\delta^2(\Delta - \delta/3)e^{-\mathcal{D}_0\delta^2(\Delta-\delta/3)q^2} = 0. \tag{4.43}$$

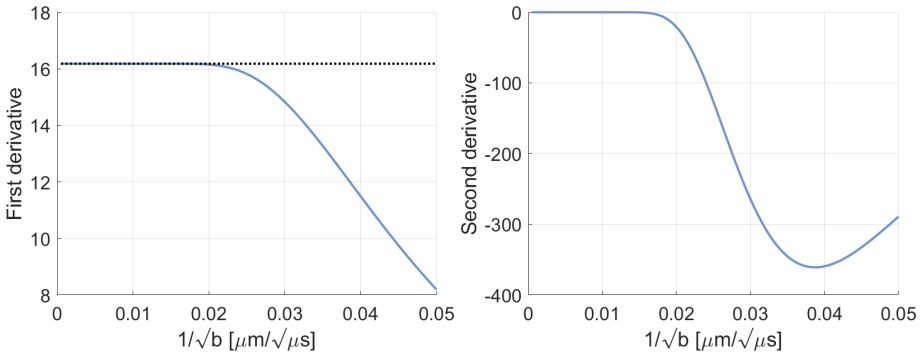

Figure 4.10: The first-order derivative (left) and second-order derivative (right) of $\overline{S}_{\text{neurite}}$ as functions of $1/\sqrt{b}$. The dotted black line represents $\sqrt{\pi/(4\mathcal{D}_0)}$.

Because of incorporating a negative term into the second-order derivative, x_0 will be smaller than in the single sphere case. In fig. 4.11, we illustrate x_0 as a function of the radius for various soma volume fraction values, using two sequences. From fig. 4.3, we note that realistic values for f_{soma} range from 0.1 to 1. We clearly observe this downward shift for spheres with a large radius. With increasing the diffusion time, the influence of the soma volume fraction on x_0 becomes negligible for spheres with small radius.

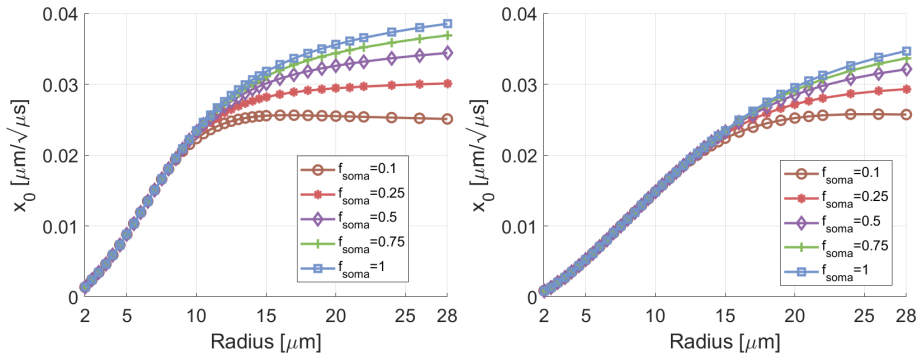

Figure 4.11: x_0 as a function of R_{soma} for various values of f_{soma}. Left: results using short PGSE sequence; Right: results using long PGSE sequence. The blue, green, purple, red, and brown lines represent $f_{\text{soma}} = [100\%, 75\%, 50\%, 25\%, 10\%]$. The markers indicate x_0 values computed by Numerical Matrix Formalism.

In fig. 4.12, we plot the other three IP-derived biomarkers against the radius across various soma volume fraction values, using the short sequence. Similarly, as f_{soma} increases, the c_1 curve tends to flatten, making it challenging to differentiate between larger radius values. Besides, the c_0 curve against R_{soma} maintains the same trend. At very low f_{soma}, c_0 is nearly independent of the radius.

In fig. 4.13, we plot the four IP-derived biomarkers against f_{soma}, across various values of R_{soma}, using the short sequence. We can observe that both c_1 and c_0 show a quasi-linear relationship with f_{soma}. Besides, x_0 is quite independent of f_{soma}. As R_{soma} increases, the slope of the c_1 curve diminishes, while the slope of c_0 remains consistent. Therefore, c_0 could be a good indicator for f_{soma}. In fig. 4.14, We plot the curves of c_1 and c_0 when using the long sequence. As diffusion time increases, we note a more linear relationship between c_0 and f_{soma}.

When δ is sufficiently short, the soma and neurites can be considered as disconnected compartments, allowing the values of the four IP-derived biomarkers to be expressed as the sum of the contributions from each of them. At high b-values, the second-order derivative of $\overline{S}_{\text{neurite}}$ is nearly zero and its y-intercept of linear fit is virtually zero. Thus, the contribution of neurites to c_0 is negligible. As observed in fig. 4.1, when this shift of the x-coordinate of the inflection point remains within a small range, $\overline{S}_{\text{soma}}$ is linear towards $1/\sqrt{b}$, ensuring that its contribution to c_0 remains unchanged. Therefore, we have $c_0 \approx c_{0,\text{soma}} f_{\text{soma}}$, where $c_{0,\text{soma}}$ is the y-intercept in the single sphere case.

Also, $\overline{S}_{\text{neurite}}$ decays at a near-constant rate $\sqrt{\pi/(4\mathcal{D}_0)}$ in the regime of high b-values. As a

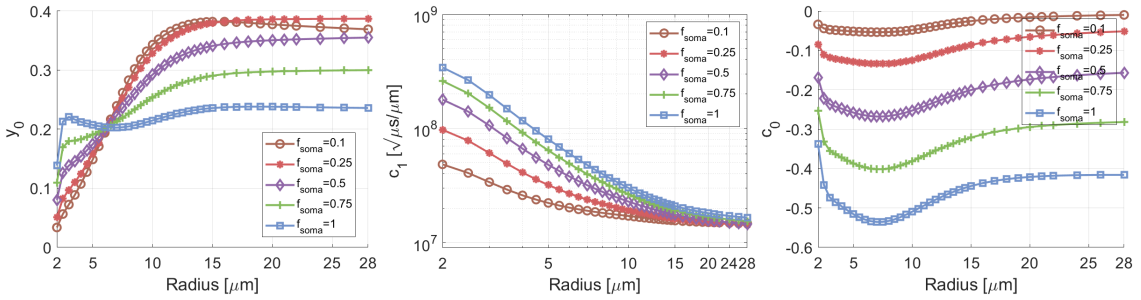

Figure 4.12: y_0 (left), c_1 (middle), and c_0 (right) as functions of R_{soma}, across various values of f_{soma}, using the short sequence. The blue, green, purple, red, and brown lines represent $f_{\text{soma}} = [100\%, 75\%, 50\%, 25\%, 10\%]$. The markers indicate values computed by Numerical Matrix Formalism.

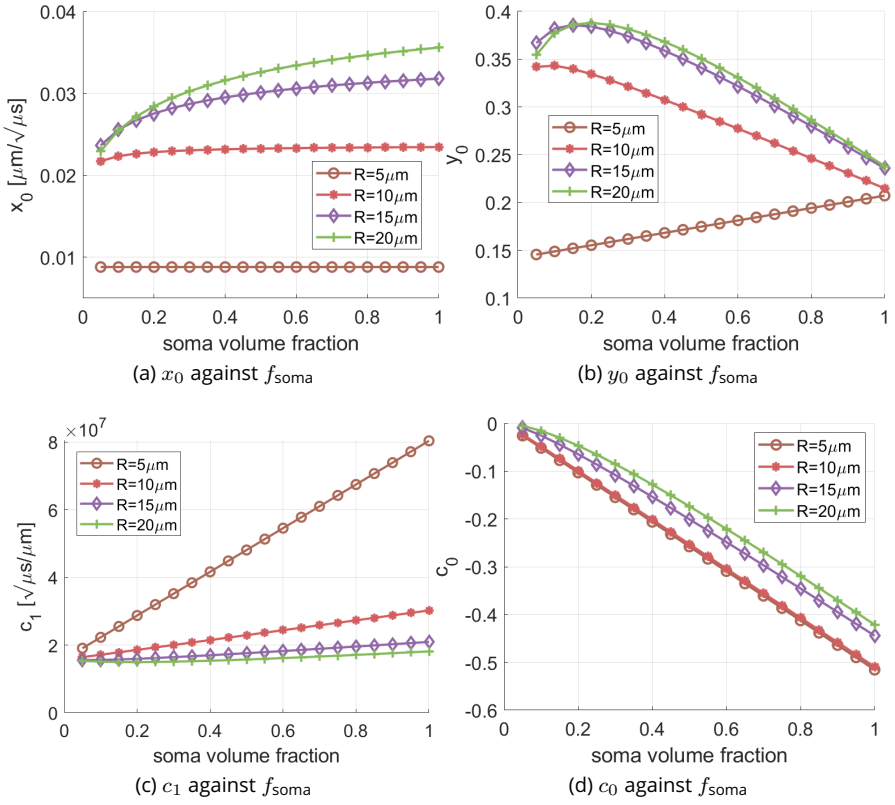

Figure 4.13: Four IP-derived biomarkers against f_{soma}, across various values of R_{soma}, using the short sequence. The brown, red, purple, and green lines represent radius of 5μm, 10μm, 15μm, and 20μm. The markers indicate values computed by Numerical Matrix Formalism. In the c_0 plot, The curves 5μm and 10μm coincide each other.

result, the contribution of neurites to c_1 is $(1 - f_{\text{soma}})\sqrt{\pi/(4\mathcal{D}_0)}$. So, we have $c_1 \approx (c_{1,soma} - \sqrt{\pi/(4\mathcal{D}_0)})f_{\text{soma}} + \sqrt{\pi/(4\mathcal{D}_0)}$, where $c_{1,\text{soma}}$ is the slope of linear fit at the inflection point in the single sphere case. The longer the diffusion time, the more linear the c_0 and c_1. As the diffusion time increases, c_0 and c_1 become more linearly related to f_{soma}.

In summary, when using a sequence with infinitely long diffusion time, the one-to-one relationship between x_0 and R_{soma} remains, and c_0 is linear to f_{soma}. Hence, using only x_0 and c_0 is sufficient to determine the soma radius and its volume fraction. Besides, c_1 depends on both R_{soma} and f_{soma}.

In practice, it is not feasible to use infinitely long sequence. Moreover, as we discuss in the previous subsection, the x_0 curve will become less steep toward R_{soma} as the diffusion time increases,

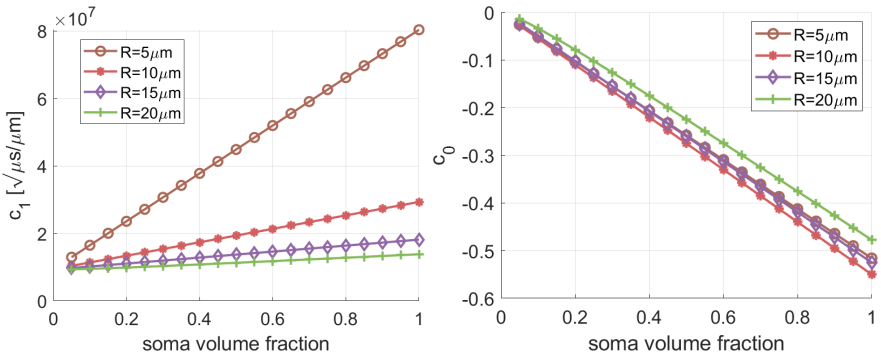

Figure 4.14: c_1 (left) and c_0 (right) against soma volume fraction, using the long sequence. The brown, red, purple, and green lines represent radius of 5μm, 10μm, 15μm, and 20μm. The markers indicate values computed by Numerical Matrix Formalism.

making accurate estimation difficult.

To be able to obtain a more precise estimation based on our IP-derived biomarkers under practical sequence configurations, we proposed an iterative method based on IP-derived biomarkers. We define firstly two groups of functions. For a given x_0 value, the function

$$f_{x_0} : f_{\text{soma}} \rightarrow R$$

describes the mapping from f_{soma} to R_{soma}, determined by eq. (4.43). And for a given c_0, the function

$$f_{c_0} : R \rightarrow f_{\text{soma}}$$

describes the mapping from R_{soma} to f_{soma}. This choice ensures a good initial guess. Figure 4.15a depicts these two functions across various x_0 and c_0 values by numerical simulations. The solid line and dash line represent f_{x_0} and f_{c_0}, respectively. For each possible combination of (x_0, c_0), there is a unique intersection between f_{x_0} and f_{c_0}, corresponding to the actual values of R_{soma} and f_{soma}. It guarantees a unique solution for the iterative method. The algorithm begins with an initial estimation of the soma radius $R^0_{\text{soma}} = f_{x_0}(1)$, and calculates the soma volume fraction by $f^0_{\text{soma}} = f_{c_0}(R^0)$. In each iteration, the values of R_{soma} and f_{soma} are alternately updated until convergence. The procedure of this algorithm is plotted in fig. 4.15b.

Algorithm 1: Iterative method for estimating R_{soma} and f_{soma} in the case of one sphere + sticks

Data: X-coordinate x_0, y-intercept c_0, initial values $R^0_{\text{soma}} = f_{x_0}(1)$ and $f^0_{\text{soma}} = f_{c_0}(R^0)$, tolerance ϵ_1 and ϵ_2, maximum number of iterations N

Result: Estimations f^*_{soma} and R^*

$n \leftarrow 0$;
while *n* < N *and not converged* **do**
  $R^{n+1}_{\text{soma}} \leftarrow f_{x_0}(f^n_{\text{soma}})$;
  $f^{n+1}_{\text{soma}} \leftarrow f_{c_0}(R^{n+1}_{\text{soma}})$;
  if $|f^{n+1}_{soma} - f^n_{soma}| < \epsilon_1$ *and* $|R^{n+1}_{soma} - R^n_{soma}| < \epsilon_2$ **then**
    converged $\leftarrow$ true;
  $n \leftarrow n + 1$;
if *converged or n*>N **then**
  $f^*_{\text{soma}} \leftarrow f^{n+1}_{\text{soma}}$;
  $R^*_{\text{soma}} \leftarrow R^{n+1}_{\text{soma}}$;
  return f^*_{soma}, R^*_{soma};

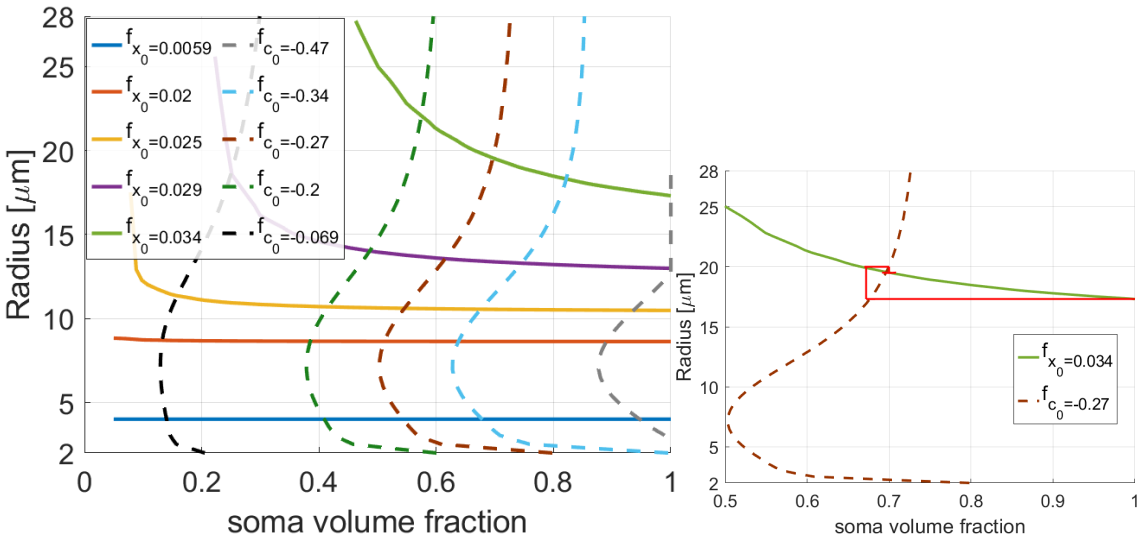

(a) f_{x_0} and f_{c_0}. (b) Iteration method procedure.

Figure 4.15: Left: The mapping f_{x_0} and f_{c_0} across various x_0 and c_0 values, computed by numerical simulations. The solid line represents the mapping f_{x_0}, defined as the mapping from f_{soma} to R_{soma} for a given x_0 and the dash line represents f_{c_0}, defined as the mapping from R_{soma} to f_{soma} for a given c_0. Right: An illustrative picture on the procedure of the iterative method. Each red segment represents one iteration. The procedure starts from $f_{x_0}(1)$, where on the right end of the red line, and will converge to the intersection point.

4.2.3.3 One sphere+sticks+one free diffusion compartment

One simplified shape assumption about the brain gray matter is to represent it as the combination of three compartments: a single sphere, a collection of sticks, and one free diffusion compartment[28]. In that case, the direction-averaged signal is

$$\overline{S} = f_{\text{soma}}\overline{S}_{\text{soma}} + f_{\text{neurite}}\overline{S}_{\text{neurite}} + f_{\text{free}}\overline{S}_{\text{free}}, \tag{4.44}$$

where the signal of the free diffusion compartment is defined as isotropic Gaussian diffusion:

$$\overline{S}_{\text{free}} = e^{-\mathcal{D}_0 \text{b}}. \tag{4.45}$$

Its second-order derivative is

$$\frac{d^2\overline{S}_{\text{free}}}{d(1/\sqrt{\text{b}})^2} = 2\mathcal{D}_0\text{b}^2(2\mathcal{D}_0\text{b} - 3)e^{-\mathcal{D}_0\text{b}}. \tag{4.46}$$

In fig. 4.16, we plot the signals and second-order derivative of the free diffusion compartment. Its inflection point is fixed at $[\sqrt{2\mathcal{D}_0/3}, e^{-3/2}]$.

In fig. 4.17, we plot the four IP-derived biomarkers against f_{free}, for various pairings of $(f_{\text{soma}}, R_{\text{soma}})$ using the long PGSE sequence. It is evident that y_0 and c_1 are proportional to $(1 - f_{\text{free}})$. As shown in fig. 4.16, at high b-values ($1/\sqrt{\text{b}} \leq 0.015\mu\text{m} \cdot \mu\text{s}^{-1/2}$), $\overline{S}_{\text{free}}$ is almost zero, as well as the first and second-order derivatives, i.e. $\overline{S} \propto (1 - f_{\text{free}})$. Thus, we can link f_{free} to y_0.

In summary, c_1 depends on all these three morphological parameters $(R_{\text{soma}}, f_{\text{soma}}, f_{\text{free}})$ and from the values of (x_0, y_0, c_1), we can deduce a unique estimate of $(R_{\text{soma}}, f_{\text{soma}}, f_{\text{free}})$. We define a multivariate function:

$$f : (R_{\text{soma}}, f_{\text{soma}}, f_{\text{free}}) \to (100x_0, 10y_0, 10c_0).$$

The different coefficients before x_0, y_0 and c_0 are used to make the gradient smoother. A non-zero determinant of the Jacobian matrix suggests the invertibility of f. Consequently, $f^{-1}(100x_0, 10y_0, 10c_0)$ gives a unique solution of $(R_{\text{soma}}, f_{\text{soma}}, f_{\text{free}})$. In addition, A determinant significantly deviating from 1 indicates that inverting the function f is numerically challenging.

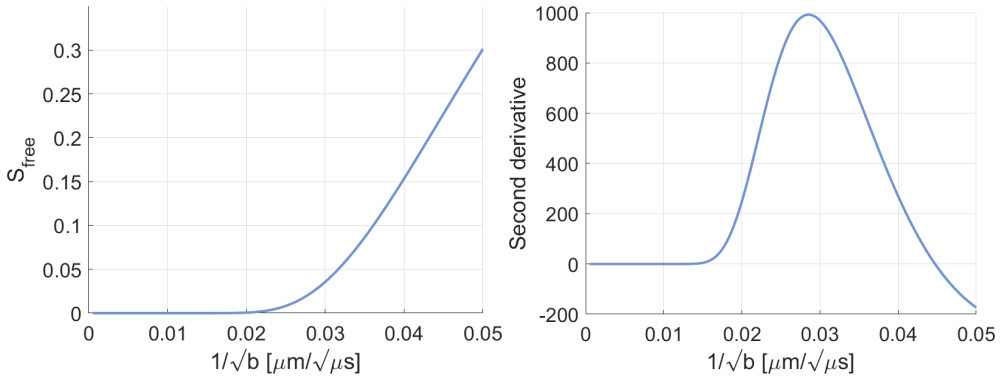

Figure 4.16: Left: $\overline{S}_{\text{free}}$ against $1/\sqrt{\text{b}}$. Right: second-order derivative of $\overline{S}_{\text{free}}$ with respect to $1/\sqrt{\text{b}}$.

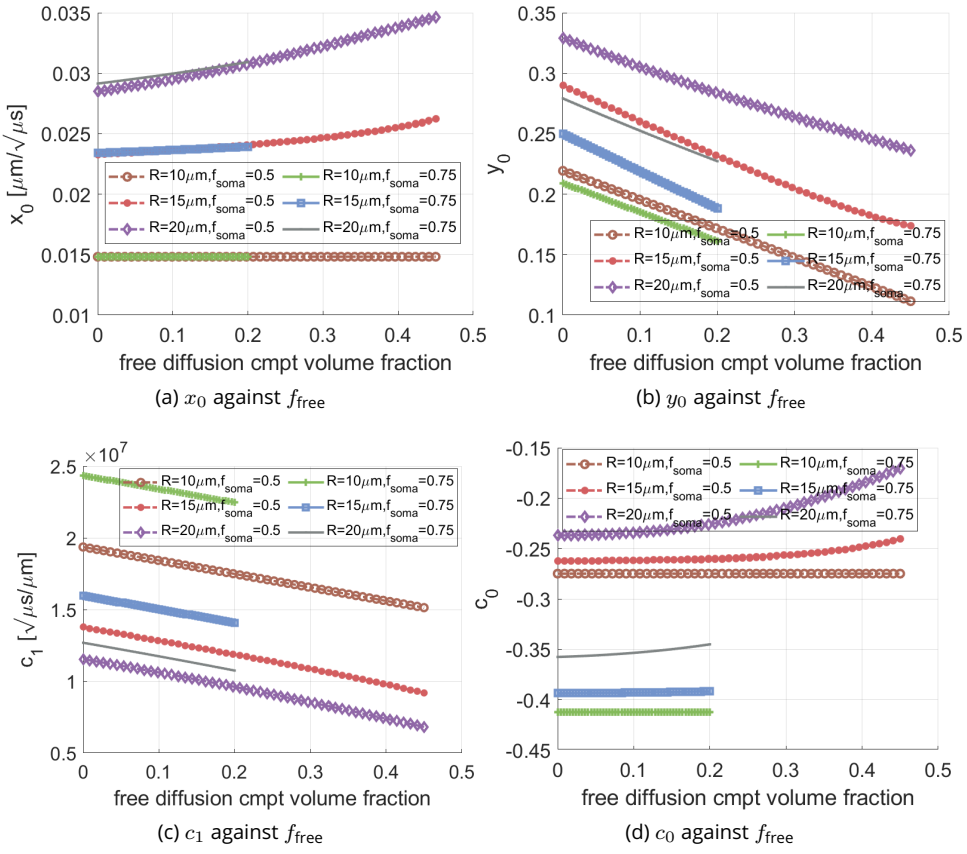

(a) x_0 against f_{free} (b) y_0 against f_{free}

(c) c_1 against f_{free} (d) c_0 against f_{free}

Figure 4.17: Four IP-derived biomarkers against f_{free} for various combinations of $(f_{\text{soma}}, R_{\text{soma}})$, using the long PGSE sequence. The markers indicate values computed by Numerical Matrix Formalism.

In fig. 4.18, we plot the determinant of its Jacobian matrix as a function of f_{free} for some pairings of R_{soma} and f_{soma}, using the long sequence. In a realistic brain tissue voxel, f_{free} should not exceed 50%. Notably, all determinant values for $f_{\text{free}} \leq 50\%$ are strictly positive. For small radii, the determinant is close to 1 and it is not dependent on the volume fractions, implying that inverting f is straightforward. As R_{soma} increases or f_{soma} decreases, it always exists a unique solution but inverting the function f may become more challenging.

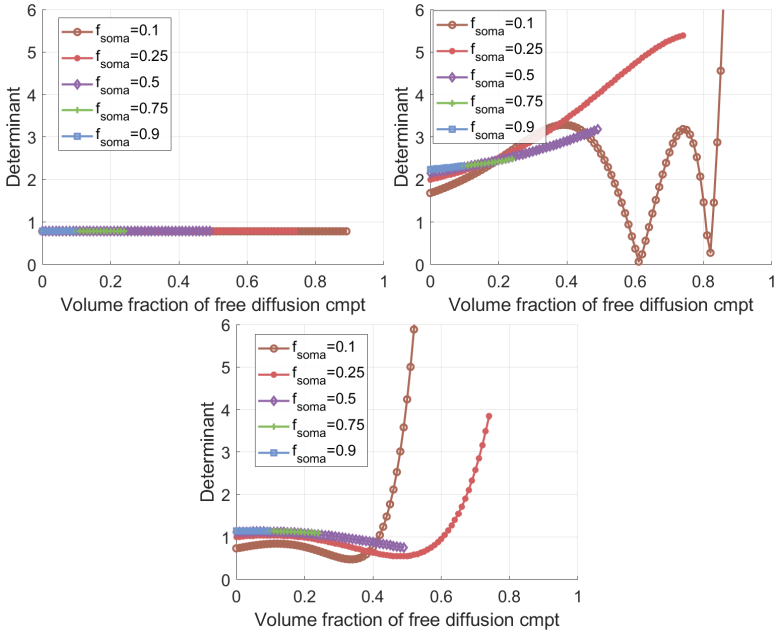

Figure 4.18: The determinant of the Jacobian matrix of f against f_{free} when using the long sequence. From left to right: $R_{\text{soma}} = 5\mu$m, $R_{\text{soma}} = 15\mu$m and $R_{\text{soma}} = 20\mu$m. The brown, red, purple, green, and blue lines represent $f_{\text{soma}} = 10\%$, $f_{\text{soma}} = 25\%$, $f_{\text{soma}} = 50\%$, $f_{\text{soma}} = 75\%$ and $f_{\text{soma}} = 90\%$. For $R_{\text{soma}} = 5\mu$m, all the lines coincide.

4.2.3.4 Multiple spheres case

Within one single voxel, there are a large number of neurons with different soma radii. It can be modeled as a composite of multiple spheres with different radii, complemented by a bundle of sticks and one free diffusion compartment. The impact of sticks and the free diffusion compartment on the four IP-derived biomarkers, especially c_0 and y_0, are the same as we discussed in previous subsections.

In the multiple spheres case, the x-coordinate of the inflection point x_0 satisfies the expression as below:

$$\frac{\sum_{m=1}^{M} \frac{4}{3}\pi (R_{\text{soma}}^m)^3 \left(\frac{2\Re(a_{R_{\text{soma}}^m})}{q} + \Re(b_{R_{\text{soma}}^m} + c_{R_{\text{soma}}^m})\right)}{\sum_{m=1}^{M} \frac{4}{3}\pi (R_{\text{soma}}^m)^3} = 0. \tag{4.47}$$

It is the zero of the volume-weighted sum of the function $2\Re(a_{R_{\text{soma}}^m})/q + \Re(b_{R_{\text{soma}}^m} + c_{R_{\text{soma}}^m})$. Therefore, x_0 is linked to one kind of volume-averaged radius. This effective soma radius lies between the minimum and maximum radii, and it closely approximates the radius associated with the highest volume fraction. We define the volume-averaged radius $\overline{R}_{\text{soma}}$ as:

$$\overline{R}_{\text{soma}} = \frac{\sum_{m=1}^{M} (R_{\text{soma}}^m)^4}{\sum_{m=1}^{M} (R_{\text{soma}}^m)^3}. \tag{4.48}$$

In fig. 4.19, we illustrate x_0 against $\overline{R}_{\text{soma}}$ in the two spheres case. We note that although x_0 and $\overline{R}_{\text{soma}}$ do not maintain a one-to-one mapping in this case, x_0 still follows the same trend as we observed in the single sphere case in fig. 4.9a.

Throughout the analysis, we conclude that:

1. In one single sphere case, x_0 is one-to-one mapping with R_{soma}. As the diffusion time increases, the mapping becomes more linear;
2. In the case of one sphere supplemented by a bundle of sticks, c_0 exhibits a linear relationship with f_{soma};
3. In the case of one sphere complemented by a bundle of sticks and a free diffusion compartment, when using a sequence with long diffusion time, ensuring that $x_0 \leq 0.015\mu\text{m} \cdot \mu\text{s}^{-1/2}$

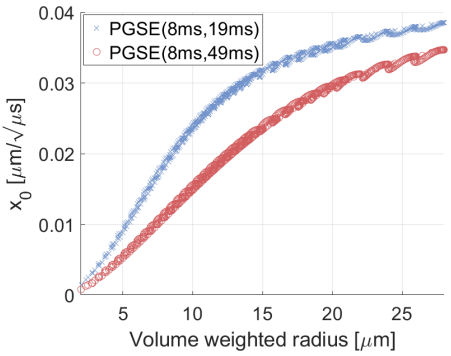

Figure 4.19: x_0 against the volume-averaged soma radius for two spheres case. Each scatter point represents one combination of $(R_1, R_2) \in [2, 28]^2$. The blue and red scatters represent the results using the short and long sequences.

and $\overline{S}_{\text{free}} \approx 0$, y_0 exhibits a linear relationship with f_{free}. Thus, x_0, y_0 and c_0 are each uniquely correlated to R_{soma}, f_{free} and f_{soma};

4. c_1 shows a dependence on all these three morphological parameters;

5. The determinant of the Jacobian matrix of the mapping f from $(R_{\text{soma}}, f_{\text{soma}}, f_{\text{free}})$ to (x_0, y_0, c_0) is invertible, indicating that three IP-derived biomarkers are sufficient to determine the soma radius and volume fraction;

6. In the cases of multiple spheres, the relationship between x_0 and volume-averaged radius $\overline{R}_{\text{soma}}$ will follow the same trend observed between x_0 and R_{soma} in the single sphere case.

4.3 Impact of realistic neuronal shapes and exhaustive search

In the previous section, we show the ability to use the IP-derived biomarkers to estimate soma size and volume fractions for simplified shapes. However, in real estimation, finding the accurate inverse of the mapping f presents challenges due to the following reasons:

1. As we can see in section 4.2, even though the actual neurites branches also exhibit the power-law scaling, their signals are not identical to those of sticks or cylinders. The slope is different and at ultra-high b-values, the signals will deviate from the linear relationship, which leads to a slightly different neurites contribution to the IP-derived biomarkers;

2. There are multiple somas with varied radii within one voxel, and representing them as one single sphere introduces an extra error in IP-derived biomarkers.

To be able to perform precise estimation using these IP-derived biomarkers, we propose an exhaustive search method with the Synthetic voxels set in section 4.1.3. The intra-neuronal space is modeled as a combination of several realistic neurons, accommodating both the authentic shapes of neurites and the presence of multiple soma radii. The second-order derivative of $\overline{S}_{\text{voxel}}$ on the Synthetic voxels set is computed by the volume-averaged second-order derivatives of all the neurons supplemented by the second-order derivative of $\overline{S}_{\text{free}}$. Then four biomarkers $(x_{0,\text{voxel}}, y_{0,\text{voxel}}, c_{1,\text{voxel}}, c_{0,\text{voxel}})$ are retrieved from the zero of $d^2\overline{S}_{\text{voxel}}/d(1/\sqrt{b})^2$.

In this section, we first plot the IP-derived biomarkers against volume fractions and soma radius on *NeuronSet* and 145,000 artificial intercellular spaces, to illustrate the impacts of the two effects above. Then, we present the exhaustive search approach.

4.3.1 Impact of realistic neuronal shapes on IP-derived biomarkers

In fig. 4.20, we plot the two IP-derived biomarkers x_0 and c_0 against the two morphological parameters R_{soma} and f_{soma} on the *NeuronSet*. We clearly observe the correlations between the IP-

derived biomarkers and the neuronal parameters. The effect of curvature and branches perturb c_0 more than x_0.

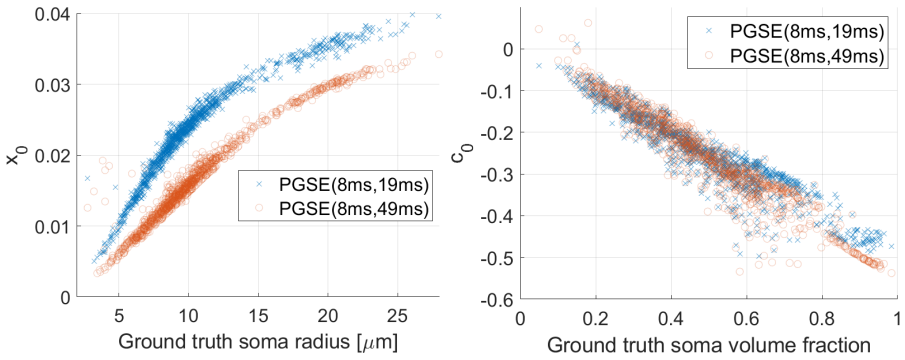

Figure 4.20: Left: x_0 against R_{soma} on the *NeuronSet*; Right: c_0 against f_{soma} on the *NeuronSet*. The blue cross represents the results by the short PGSE sequence and the red circle represents the results by the long PGSE sequence.

In fig. 4.21, we plot x_0 and c_0 against $\overline{R}_{\text{soma}}$ and f_{soma} on 145,000 artificial intercellular spaces. Compared to fig. 4.20, the scatter plots become thicker but maintain the same trends. Adding the free diffusion compartment will perturb the inflection point and these correlations, resulting in thicker scatter plots.

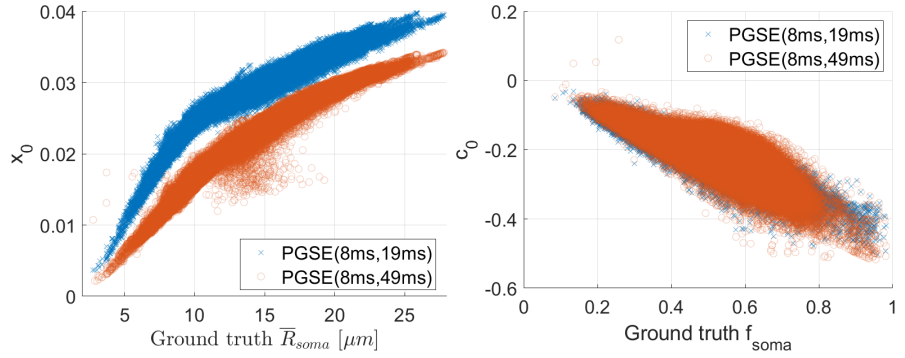

Figure 4.21: Left: x_0 against $\overline{R}_{\text{soma}}$; Right: c_0 against f_{soma}. The blue cross represents the results by the short PGSE sequence and the red circle represents the results by the long PGSE sequence.

4.3.2 Exhaustive search method

The exhaustive search method relies on a pre-constructed library for estimation. We randomly picked 0.45 million synthetic voxels in the Synthetic voxel set as the Synthetic test set. We used the remaining 1 million voxels to build the Synthetic library set, serving as the pre-built library for exhaustive search.

We restrict our exhaustive search to (x_0, y_0, c_0), given that only the fourth IP-derived biomarker is not independent. The difference between the IP-derived biomarkers of a test voxel, denoted as ($x_{0,\text{test}}$, $y_{0,\text{test}}$, $c_{0,\text{test}}$), and the IP-derived biomarkers of the i-th voxel from the Synthetic library set, denoted as $(x_{0,i}, y_{0,i}, c_{0,i})$ is defined as:

$$\epsilon_i = \frac{|x_{0,\text{test}} - x_{0,i}|}{|x_{0,i}|} + \frac{|y_{0,\text{test}} - y_{0,i}|}{|y_{0,i}|} + \frac{|c_{0,\text{test}} - c_{0,i}|}{|c_{0,i}|}. \tag{4.49}$$

Because multiple combinations of neurons and f_{free} can give similar IP-derived biomarkers values, we average the parameters from the elements of the Synthetic library set that give the 10 lowest ϵ_i. Thus, our IP-derived biomarkers-based exhaustive search fitted parameters $\{\overline{R}_{\text{soma}}, f_{\text{soma}}, f_{\text{neurite}}\}$ are the averages of 10 values from the Synthetic library set.

4.4 Estimation results

In this section, we will evaluate our estimation based on IP-derived biomarkers on the *NeuronSet*, the Synthetic test set, and the *in vivo* MGH CDMD dataset. On the *NeuronSet*, we employ the IP-derived biomarker-based iterative method and compare it to the SANDI model. This is due to the *NeuronSet* not being sufficiently large enough to conduct a complete library-test split and exhaustive search process. On both the Synthetic test set and the *in vivo* MGH CDMD dataset, we evaluate the exhaustive search within the Synthetic library set and compared it to (1) the SANDI model and (2) an exhaustive search approach within the same Synthetic library set but based on L^2 differences at 64 direction-averaged signal values.

The SANDI model[28] has an analytical signal expression, which allows one to recompute the direction averaged signals by substituting five SANDI's estimation parameters $\boldsymbol{p}$=[f_{soma}, f_{free}, R_{soma}, $\mathcal{D}_{\text{neurite}}$, $\mathcal{D}_{\text{free}}$] into the signal formula. Its signal expression is given in section 1.4.3.

To avoid the commonly encountered numerical instabilities due to the difficulty of finding the global minimum in optimization procedures, we chose to perform SANDI fitting using an exhaustive search approach on a saved signal library. Exhaustive search should be more numerically stable than a fast optimization method such as AMICO[189]. Also, this makes it possible to compare the models only, without having to account for errors that come from the optimization procedures. To make the library search computationally feasible, we further simplified the problem by fixing both $\mathcal{D}_{\text{neurite}}$ and $\mathcal{D}_{\text{free}}$ to 3×10^{-3} mm^2/s.

Thus, the signals library for SANDI is populated along three dimensions: the soma radius discretized on the interval $[0, 35]\mu$m in 0.35μm increments, the f_{soma} and f_{free} discretized on the interval $[0, 1]$ in 0.01 (1 percent) increments. The set of three parameters $\{\overline{R}_{\text{soma}}, f_{\text{soma}}, f_{\text{free}}\}$ that gives the smallest L^2 difference at the 64 direction-averaged signal values will be called the SANDI fitted parameters for that voxel. For the estimation on the *NeuronSet*, f_{free} is set to 0, so only two parameters $\{\overline{R}_{\text{soma}}, f_{\text{soma}}\}$ are left.

Besides, we compare our method to an exhaustive search applied to the simulated signals, which uses the same Synthetic library set, but operates directly on the signals. Its fitted parameters $\overline{R}_{\text{soma}}$, f_{soma}, f_{neurite} are the averages of values from the elements of the Synthetic library set that gave the 10 lowest L^2 differences at the 64 direction-averaged signal values. This comparison can help illustrate whether the low dimensional data (three IP-derived biomarkers) is as effective as the high dimensional data (64 signals) in estimating the soma size and volume fractions.

4.4.1 On NeuronSet

In fig. 4.22, we plot the estimated soma radius and soma volume fraction against the ground truth values on the *NeuronSet* by the biomarker-based iterative method shown in fig. 4.15 and SANDI library search, with $f_{\text{free}} = 0$. The iterative method uses the mappings f_{x_0} and f_{c_0} from the sphere-sticks model. Thus, the main difference between the IP-derived biomarker-based iterative method and SANDI library search is that the sphere-sticks model uses IP-derived biomarkers computed by Numerical Matrix Formalism, whereas SANDI employs signals under Gaussian phase approximation. At high b-values, due to non-Gaussian diffusion, SANDI signal expression may be less accurate than the sphere-sticks model. From the plots, it can be inferred that:

1. The overall estimation errors by SANDI are greater than the biomarker-based iterative method;
2. For the biomarker-based iterative method, the long PGSE sequence outperforms the short PGSE sequence in R_{soma} estimation, especially for the larger radii. As discussed in the previous section, for the short PGSE sequence, the curve x_0 against R_{soma} is less steep for large radii, posing challenges to distinguishing large radius values;
3. Both two sequences give a slight overestimation of R_{soma} using the iterative method. In fig. 4.7, we can see that the signals by sphere-sticks model are higher than the case of connected neuron, leading to an overestimation of the soma radius;
4. Using the SANDI library search, the short PGSE sequence tends to give a slight overestimation of R_{soma} whereas the long PGSE sequence gives a slight underestimation;
5. SANDI yields a larger bias than the iterative method in terms of f_{soma} estimation.

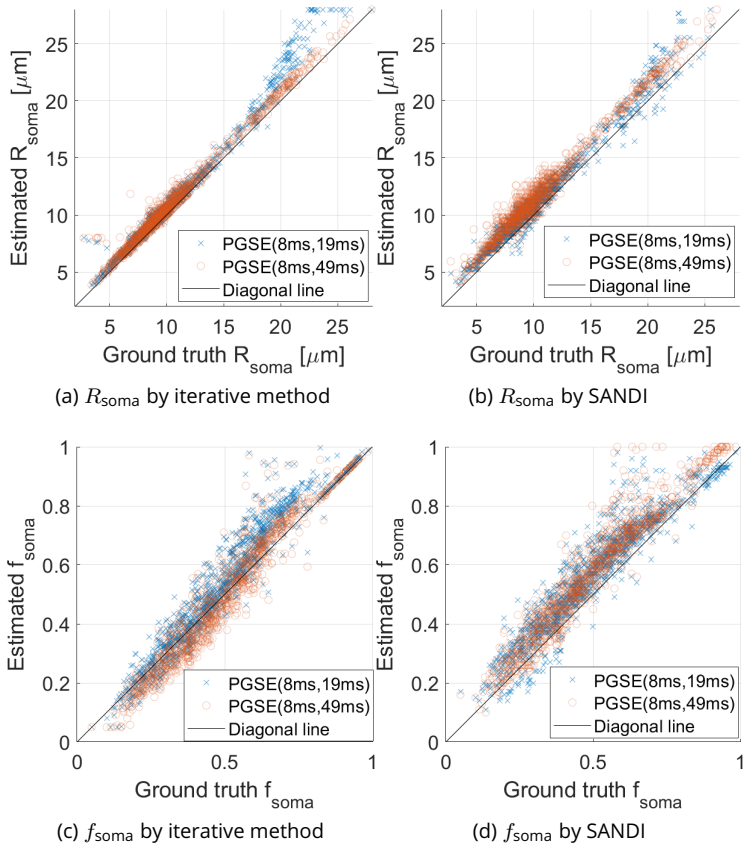

(a) R_{soma} by iterative method (b) R_{soma} by SANDI

(c) f_{soma} by iterative method (d) f_{soma} by SANDI

Figure 4.22: Estimated morphological parameters against ground truth values on the *NeuronSet*. The blue cross represents the results by the short PGSE sequence and the red circle represents the results by the long PGSE sequence.

4.4.2 On Synthetic voxels set

Next, we compare the estimation results of these methods on the Synthetic test set. In the Synthetic voxels set, we have the ground truth microstructural parameters. We compare the performance of the exhaustive search using IP-derived biomarkers (1 million elements) with the exhaustive search using the simulated signals (1 million elements) and the SANDI signals library (1 million elements, incremented in $\overline{R}_{\text{soma}}$, f_{soma} and f_{free}).

In fig. 4.23, we can see that there is a larger bias in f_{soma} and f_{free} in the SANDI library fit. The Synthetic library search based on signals yields the smallest errors among these three methods and is consistent through two sequences. Our Synthetic library search based on IP-derived biomarkers is unbiased, with slightly larger errors compared to the Synthetic library search based on signals for the long PGSE sequence, but not as big as the SANDI library search.

we now compare the estimated $\overline{R}_{\text{soma}}$ among these three methods. Infig. 4.24, Synthetic library search based on IP-derived biomarkers yields comparable results compared to the Synthetic library search based on signals, and the fitted $\overline{R}_{\text{soma}}$ errors are much smaller than the SANDI library search. There is no bias for the two Synthetic library search, whereas SANDI library search shows significant bias. The results using the long PGSE sequence outperform those the using short PGSE sequence for all three methods. These results of volume fraction estimation and volume-averaged radius estimation indicate that the IP-derived biomarker-based method is a good estimator in the Synthetic voxels set.

Figure 4.23 shows that significant errors occur in SANDI's estimation of soma and free diffusion compartment volume fractions. This is not surprising because the soma term in eq. (1.112) has the same form as the free diffusion term $f_{\text{free}}e^{-\mathcal{D}_{\text{free}}\text{b}}$, causing an indeterminacy problem. Based on the sum of the two exponentials alone ($f_1e^{-\mathcal{D}_1\text{b}} + f_2e^{-\mathcal{D}_2\text{b}}$), there is no way to tell which exponential

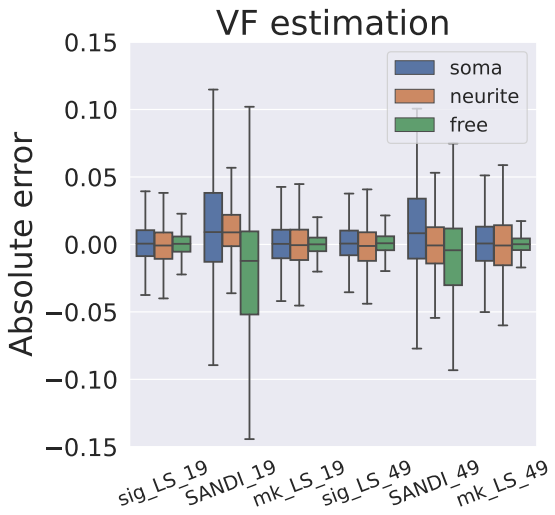

Figure 4.23: The box plots summarizing the distributions of the absolute errors of f_{soma}, f_{neurite}, f_{free}. The estimations are computed by (1) Synthetic library search based on signals, (2) SANDI library search, and (3) Synthetic library search based on IP-derived biomarkers on the Synthetic test set. The Synthetic voxels set has 1.45 million artificial voxels containing neurons and a free diffusion compartment. The Synthetic test set has 450,000 voxels from the Synthetic voxels set. A box plot denotes the median, interquartile range, and 1.5 times the interquartile range by the center line, hinges, and whiskers.

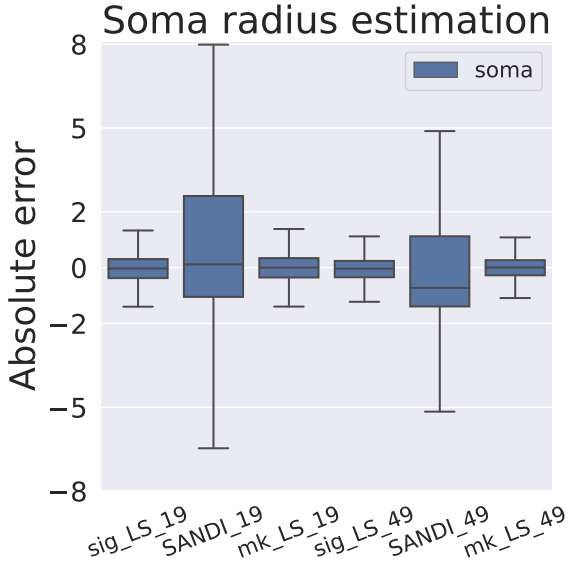

Figure 4.24: The box plots summarizing the distributions of the absolute errors of $\overline{R}_{\text{soma}}$. The estimations are computed by (1) Synthetic library search based on signals, (2) SANDI library search, and (3) Synthetic library search based on IP-derived biomarkers on the Synthetic test set. A box plot denotes the median, interquartile range, and 1.5 times the interquartile range by the center line, hinges, and whiskers.

belongs to soma and which belongs to the free diffusion compartment. The two exhaustive searches within the Synthetic library set do not suffer from such a problem. We note that in contrast to SANDI, the NODDI model[98] has two diffusion compartments, one is an ECS compartment with a low diffusion coefficient, another is a compartment labeled free water or CSF that has a much higher diffusion coefficient. It seems likely that if either of these compartments has a diffusion coefficient that is close in magnitude to the exponent of the signal term from the spheres, then an

indeterminacy can happen.

Concerning the estimation of the soma radius, fig. 4.24 shows that significant errors occur in SANDI's estimation of $\overline{R}_{\text{soma}}$, compared to the much smaller errors from the other two approaches.

4.4.3 In vivo parameters estimation

Finally, we compare the three methods on the MGH CDMD dataset. Specifically, the eight direction-averaged signals from a brain voxel are interpolated to get the 64 signals for SANDI and Synthetic library search base on signals, then we use the interpolated signals to compute the three IP-derived biomarkers x_0, y_0, and c_0 for Synthetic library search based on IP-derived biomarkers since directly computing the second-order derivative to identify those biomarkers derived from the inflection point isn't feasible on the *in vivo* data. We obtain an *in-vivo* parameter map by applying the three methods to every brain voxel of a subject in the MGH CDMD. In this subsection, the second subject in MGH CDMD (`sub_002`) serves as an exemplar.

4.4.3.1 Fitting brain white matter voxels

To be able to fit voxels that contain primarily axons, we created 20,000 random combinations of cylinders with radius from the interval $[0.2, 5]\mu$m and a free diffusion compartment, and added them to the Synthetic library set. Henceforth, the full Synthetic library has 1 million artificial voxels from the Synthetic voxels set plus 20,000 voxels that contain cylinders and a free diffusion compartment only. Then we generated a Synthetic Cylinders-only test set that has 10,000 voxels containing random combinations of cylinders. We fitted f_{soma}, f_{neurite}, f_{free} using SANDI library search and the Synthetic library search based on signals on the Synthetic Cylinders-only test set. In table 4.1, we see that with SANDI the mean of the fitted values are f_{soma} = 0.14, f_{neurite}=0.86, f_{free}=0, whereas with the Synthetic library search, f_{soma} = 0, f_{neurite}=1, f_{free}=0. This means the Synthetic library search based on signals will be able to fit axons-only voxels.

	f_{soma}		f_{neurite}		f_{free}	
	mean	std	mean	std	mean	std
SANDI_19	0.14	0.0076	0.86	0.0076	0	0
sig_Lib_Search_19	0	0	1	0.00024	0	0.00024
SANDI_49	0.14	0.0076	0.86	0.0076	0	0
sig_Lib_Search_49	0	0	1	0.00024	0	0.00024

Table 4.1: Fitted f_{soma}, f_{neurite}, f_{free} using SANDI library search and the Synthetic library search based on signals on the Synthetic Cylinders-only test set. The Synthetic Cylinders-only test set has 10,000 voxels containing random combinations of cylinders. The Synthetic library set has 1 million artificial voxels from the Synthetic voxels set plus 20,000 voxels that contain cylinders and a free diffusion compartment only. The SANDI library has 1 million elements, incremented in $\overline{R}_{\text{soma}}$, f_{soma} and f_{free}.

4.4.3.2 In vivo parameter maps

Figure 4.25 shows the volume fractions estimation by Synthetic library search based on IP-derived biomarkers, to the scanned data of `sub_002`. We also include the SANDI library search parameter maps as well as the Synthetic library search based on signals parameter maps.

There are no significant differences between the Synthetic library search based on based on IP-derived biomarkers and signals. The Synthetic library search based on IP-derived biomarkers gives a higher soma volume fraction and lower neurite volume fraction compared to the other two methods. Besides, it is less clean. This is because it uses only three inputs. In addition, the computation of the IP-derived biomarkers, especially the x_0 and y_0, is sensitive to noise. Nonetheless, the IP-derived biomarkers still manage to give reasonable volume fraction estimations.

The maps of f_{soma} properly highlight the brain gray matter and the cerebral nuclei. In contrast, the maps of f_{neurite} are prominent in the brain white matter, especially the brain white matter tracts located at the corpus callosum, the corona radiata, and the brain stem.

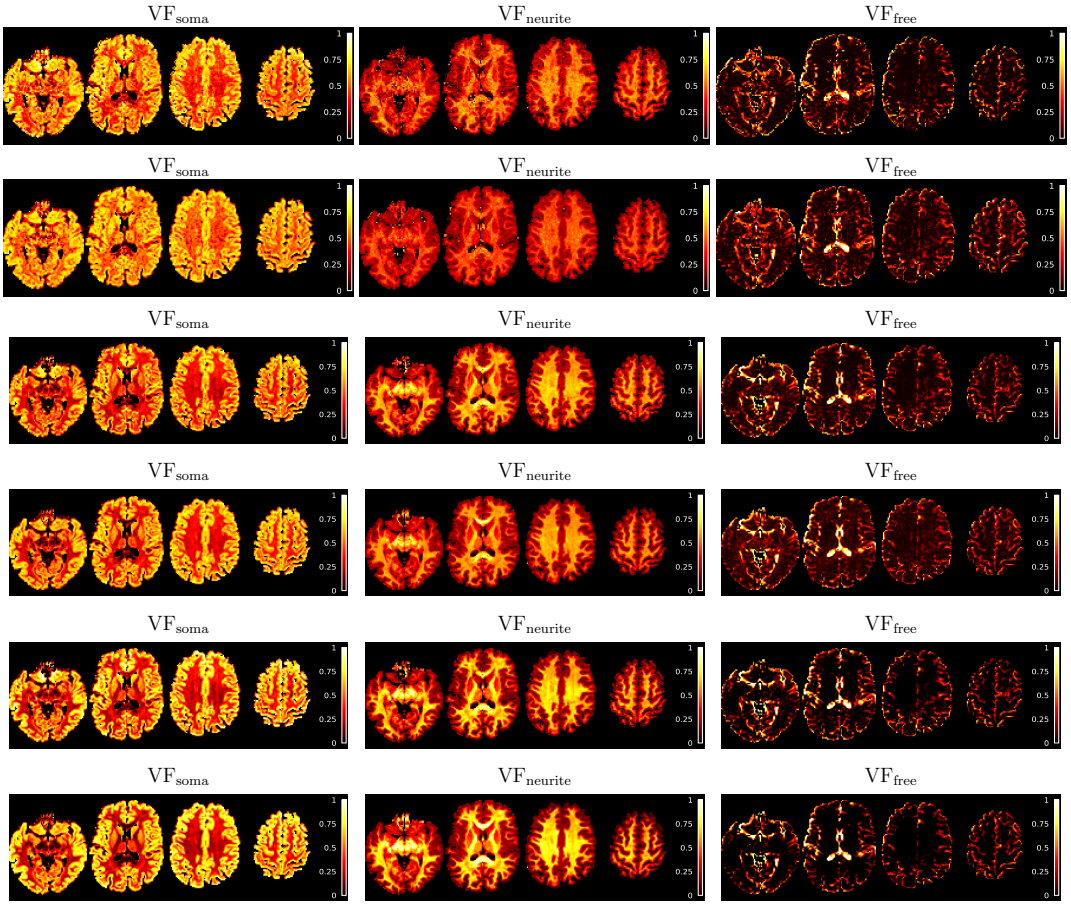

Figure 4.25: Parameter maps for MGH CDMD `sub_002`. The first column is f_{soma}, the second column is f_{neurite}, the third column is f_{free}. First row is the exhaustive search on Synthetic library based on IP-derived biomarkers at the short diffusion time ($\delta/\Delta = 8/19$ms), the second row is the exhaustive search on Synthetic library based on IP-derived biomarkers at the long diffusion time ($\delta/\Delta = 8/49$ms), third row is the exhaustive search on Synthetic library based on signals at the short diffusion time ($\delta/\Delta = 8/19$ms), the fourth row is the exhaustive search on Synthetic library based on signals at the long diffusion time ($\delta/\Delta = 8/49$ms), fifth row is SANDI library search at the short diffusion time ($\delta/\Delta = 8/19$ms), the sixth row is SANDI library search at the long diffusion time ($\delta/\Delta = 8/49$ms).

The above results qualitatively demonstrate that the proposed method can yield encouraging estimations even though it only uses three inputs. We further validate the parameter maps by investigating the consistency across diffusion times.

4.4.3.3 Independence of diffusion time

We present the voxel-wise joint distributions for the estimated parameters. All brain white and gray matter (WM and GM) voxels of `sub_002` are included. Due to the lack of real-world ground truth, validating parameter maps remains largely qualitative. Given this limitation, the community has begun to seek consistency across acquisition parameters, sequences, and scanners[190–192], instead of qualitative visual assessment. In our case, we focus on the dependence of the volume fractions and volume-averaged soma radius on the two diffusion times. Indeed, microstructure imaging aims to infer the objective properties based on diffusion MRI signals. If the estimated properties largely depend on the acquisition parameters, the estimation interpretation becomes non-trivial.

In fig. 4.26, we show the voxel-wise joint distributions of f_{soma}, f_{neurite}, f_{free} for all the three methods. For f_{soma} and f_{free}, the spread of the distributions of the Synthetic library search based on IP-derived biomarkers is wider than for the Synthetic library search based on signals. The estimated

volume fractions of both SANDI and Synthetic library searches lie on the identity line. The Synthetic library search based on signals produces lower f_{neurite} and higher f_{free} in the brain white matter than SANDI library search.

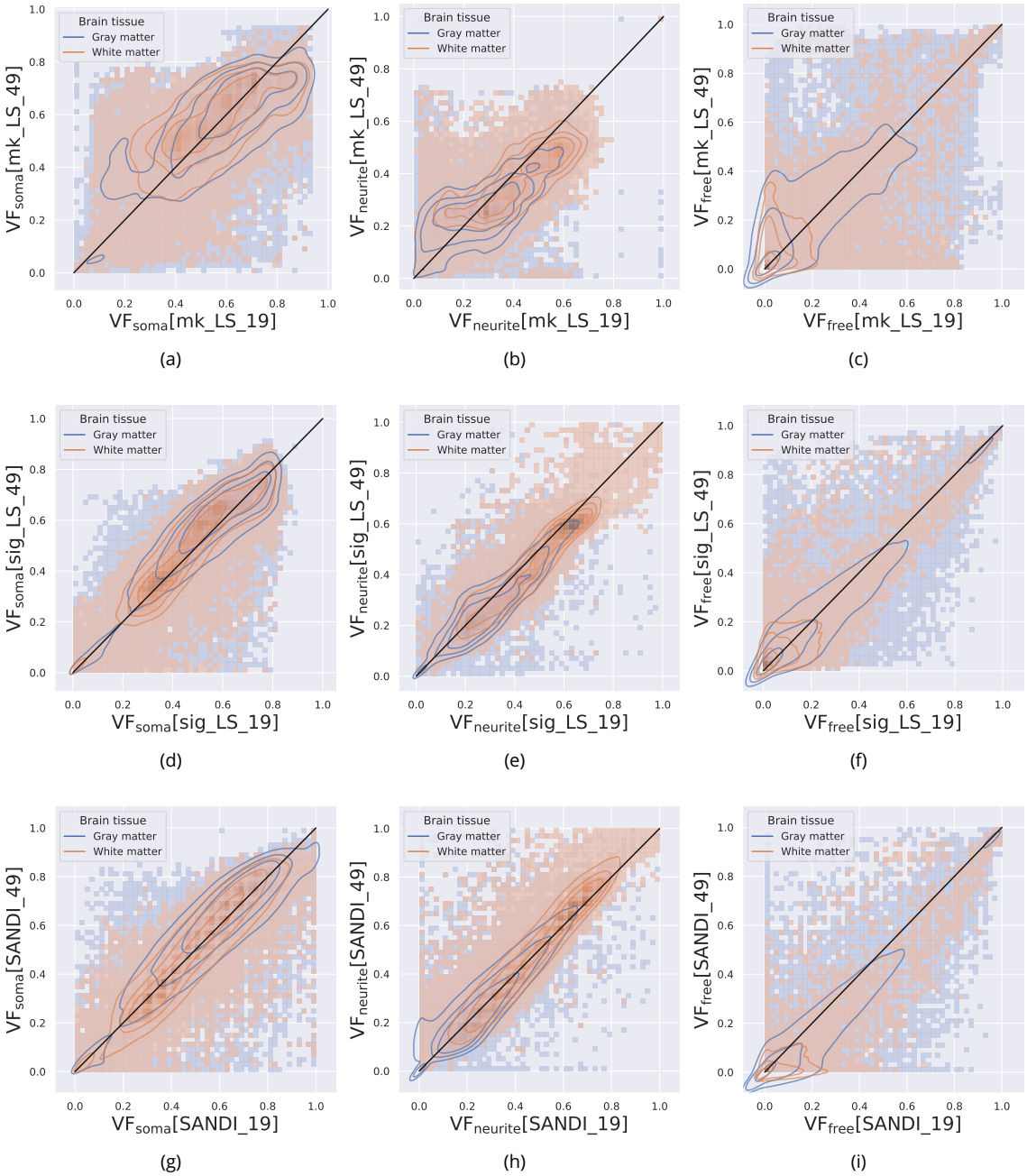

Figure 4.26: The voxelwise joint distribution of f_{soma}, f_{neurite}, f_{free} at two diffusion times. Top row: exhaustive search within the Synthetic library based on IP-derived biomarkers. Middle row: exhaustive search within the Synthetic library based on signals. Bottom row: SANDI library search. All brain white and gray matter voxels of `sub_002` are included. The x- and y-axes represent the estimated fractions at ($\delta/\Delta = 8/19$ms) and ($\delta/\Delta = 8/49$ms), respectively. The black lines are the identity lines. The contour lines represent 50%, 75%, and 90% of the data.

In figs. 4.27a to 4.27c, we show the diffusion time dependence in the estimation of $\overline{R}_{\text{soma}}$ for the three methods. At the lower diffusion time, $\overline{R}_{\text{soma}}$ ranges from $[8, 13]\mu$m for all the three methods, whereas at the longer diffusion time, $\overline{R}_{\text{soma}}$ ranges from $[10 - 18]\mu$m for the Synthetic library search

based on signals and from $[10-20]\mu$m for SANDI library search.

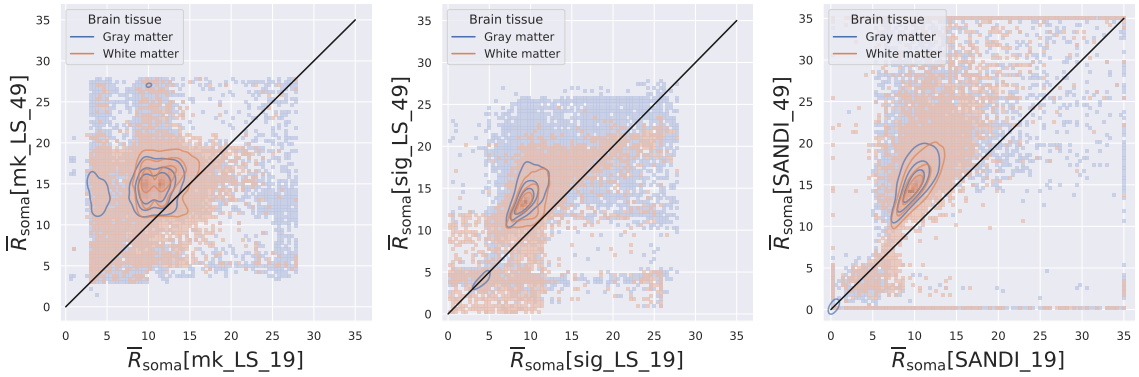

(a) $\overline{R}_{soma}$, Synthetic library search based on IP-derived biomarkers.

(b) $\overline{R}_{soma}$, Synthetic library search based on signals.

(c) $\overline{R}_{soma}$, SANDI library search.

Figure 4.27: The voxel-wise joint distribution of $\overline{R}_{soma}$ at two diffusion times. All brain white and gray matter voxels of `sub_002` are included. The x- and y-axes represent the estimated fractions at ($\delta/\Delta = 8/19$ms) and ($\delta/\Delta = 8/49$ms), respectively. The black lines are the identity lines. The contour lines represent 50%, 75%, and 90% of the data.

Figure 4.25 demonstrates that the parameter maps given by the proposed are consistent between the short and long diffusion times. For a more quantitative comparison, we plot the voxel-wise joint distribution of the estimated volume fractions at the two diffusion times in fig. 4.26. If the estimation is consistent, the scatter points should lie around the identity line.

Finally, figs. 4.27a to 4.27c show the diffusion time dependence of the three methods in estimating $\overline{R}_{soma}$. This means that the estimation of soma radius on the real data needs to be improved in the future.

4.5 Discussion

In this chapter, we propose an exhaustive search method for estimating soma size and volume fractions, based on the inflection point of diffusion MRI signals at high b-values. This approach is driven by the observation that the power-law scaling does not hold true in the brain gray matter because of the presence of the soma. We identify three independent biomarkers from the inflection point and give their mathematical expressions through the Numerical Matrix Formalism. Through the studies on simplified geometries, we demonstrate that these IP-derived biomarkers can link to soma size and volume fractions.

Similar to the simulation-driven supervised learning framework, the proposed method has two distinct features, compared to diffusion MRI compartment signal models:

1. The representation of intra-neuronal space is more realistic, by including numerically reconstructed neurons;

2. It employs the Numerical Matrix Formalism, while most state-of-the-art diffusion MRI compartment signal models to date rely on the Gaussian phase approximation. To be able to probe fine microstructure, strong gradient strength needs to be applied. However, at high b-values, the Gaussian phase approximation may lose accuracy due to the non-Gaussian diffusion effects.

Compared to signal-based estimation, which necessitates signal values across various b-values, biomarker-based estimation requires only three biomarkers, leading to a potentially rapid estimation process. For instance, the biomarker-based estimation would be 2.6 times faster than directly fitting the SANDI model to 8 measured signals on the MGH CDMD data.

The main differences between the proposed method and the simulation-driven learning framework proposed in[3] are (1) substituting the MLPs with an exhaustive search (2) using three IP-derived biomarkers instead of using four IP-derived biomarkers plus the ADC. In fig. 4.28, we plot the estimation errors on Synthetic voxels set using MLPs. It is clear that exhaustive search and MLPs yield very close results. This implies that ADC would not help enhancing volume fractions and soma size estimation. The benefits of exhaustive search are:

- It is easy to implement and robust, avoiding introducing fitting errors, like initialization, or falling into local optima;
- It does not require training before performing estimation;
- Even though it may not be as instantaneous as MLPs during the estimation process, exhaustive search within an ordered library remains efficient;
- Once we find the 10 elements giving the lowest ϵ_i, we can acquire all the estimated microstructures, whereas MLPs need to require re-training for each microstructure.

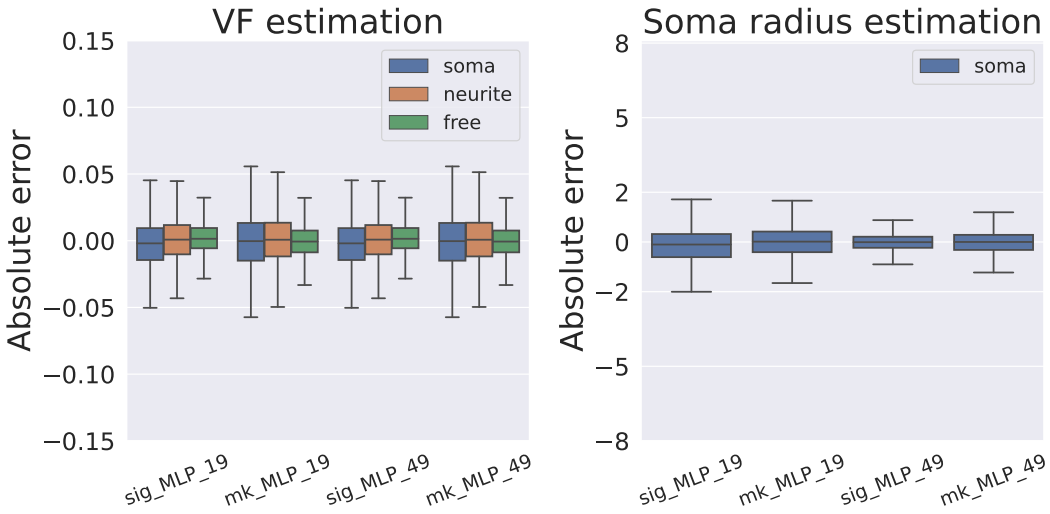

Figure 4.28: The box plots summarizing the distributions of the absolute errors of f_{soma}, f_{neurite}, f_{free} and $\overline{R}_{\text{soma}}$. The estimations are computed by (1) MLP with signals as inputs and (2) MLP with IP-derived biomarkers plus ADC as inputs. A box plot denotes the median, interquartile range, and 1.5 times the interquartile range by the center line, hinges, and whiskers.

We carried out an in-depth performance analysis comparing the IP-derived biomarker-based estimation with two other approaches, SANDI and Synthetic library search based on signals, on the *NeuronSet*, the Synthetic test set, and the *in vivo* dataset. On the *NeuronSet* and Synthetic test set, the IP-derived biomarker-based method outperforms SANDI. On the *in vivo* dataset, IP-derived biomarker-based estimation yields similar values but displays more noise compared to the other two methods and exhibited diminished performance concerning diffusion time independence. Because IP-derived biomarkers-based estimation is based on only three biomarkers, it is more sensitive. There are many factors that may deteriorate the performance of the IP-derived biomarker-based estimation:

1. The signal-to-noise ratio level. At high b-values, the signal-to-noise ratio decreases. The accuracy of inflection point computation is vital for the estimation;
2. Stationary water. When we construct the Synthetic voxel dataset, we exclude the stationary water compartment. However, in presence of the stationary water, the c_0 will be higher and also the y_0, introducing an extra error;
3. Inherent time-dependency. Biomarker-based estimation requires that the sequence should be long enough to ensure that the inflection point lies within the power-law scaling range and

that the signal contribution from extra-cellular space is almost negligible. Given a specific sequence, the method exhibits sensitivity to a particular range of soma radii, making it naturally dependent on diffusion time;

4. We observe that even though we include 20,000 voxels that contain cylinders and a free diffusion compartment only, the biomarker-based method could rarely make an estimation on f_{neurite} larger than 80%, implying that this method is not valid in the brain white matter. As we see in fig. 4.7, cylinders do not possess the inflection point.

Chapter 5

Diffusion MRI simulation with Streamline Upwind Petrov-Galerkin

Contents

Chapter Overview

In this chapter, we present a new finite element scheme for diffusion MRI blood flow imaging applications. The proposed technique addresses the instability issue of simulating perfusion MRI signal at high blood flow velocity, particularly in arterioles and venules. The new scheme combines the Streamline Upwind Petrov-Galerkin (SUPG) method and the theta time discretization method. The idea of the SUPG method is to add an artificial diffusion term only in the flow's direction, to smooth out the spurious oscillations arising near areas with sharp gradients. The amplitude of this regularization term is controlled by stabilization parameters τ_k. Numerical simulation results demonstrate that the standard Galerkin method leads to spurious oscillations at high blood flow velocity whereas the new scheme can provide a stable solution even on a coarse finite elements mesh. To provide guidance on selecting the stabilization parameters and diameter of elements for τ_k, we conduct a study evaluating the performance of different combinations of these two parameters.

This work is a collaboration with the computational medicine team at the University of Leeds, aiming to extend the existing finite elements solver of the SpinDoctor for diffusion MRI blood flow simulations.

5.1 Introduction

Another promising application of diffusion MRI beyond brain tissue imaging is the assessment of the blood perfusion (known as intravoxel incoherent motion (IVIM) MRI) and cardiac blood flow imaging[193–196]. As explored in the first chapter, at low b-values, diffusion MRI signals are sensitive to micro-circulation of blood in the cerebral capillary network, which makes the ADC deviate from the expected value[197]. This deviation has been widely used to measure the perfusion index in

clinics[198, 199]. In recent years, diffusion tensor imaging (DTI) has seen a growing application in the cardiac domain, highlighting its versatility in medical imaging[200–204].

Simulating the diffusion MRI involves treating a flow term. The velocity is typically determined by the Navier-Stokes equation through numerical simulations. It is then often provided as a pre-defined variable for diffusion MRI simulations[204].

When considering blood flow, the Bloch-Torrey PDE becomes a convection-diffusion-reaction PDE, with an imaginary reaction term[115, 205]. This PDE exhibits different behaviors based on the ratio of the velocity to diffusion coefficient. When the velocity is comparably low, such as in the capillaries, the molecules movement is mainly determined by the diffusion process and a signal pattern similar to classical diffusion MRI will be produced. On the contrary, when the velocity is comparably high, for example in the arteries or veins, the molecules are mainly transposed by the flow, and in this case, the numerical simulation would potentially encounter instability issues, reported in[206, 207].

Mesh refinement may enhance stability, but it doesn't always guarantee addressing it, especially when using the standard Galerkin finite element method. It depends on the maximum velocity and the finite element mesh. In some cases, an extremely fine mesh might be necessary, which could be impractical due to computational resource constraints. Or in some cases, the mesh is pre-defined and we could not modify it. Some studies suggest a local refinement strategy to improve the stability and maintain a reasonable size[208, 209]. Another issue is that with the standard Galerkin finite element method, spurious oscillations may be produced, leading to nonphysical results[210].

The objective of this chapter is to apply a stabilized simulation scheme for the diffusion MRI accounting for the blood flow. Many stabilization approaches were proposed to solve the time-dependent convection diffusion equation simulation in the computational fluid dynamics community, such as the Streamline Upwind Petrov-Galerkin (SUPG) method[210–213], symmetric stabilization method[214, 215] and Galerkin least-squares method (GLS)[216].

In this work, we present a new finite element scheme for diffusion MRI simulations that combines the Streamline Upwind Petrov-Galerkin method and the theta time discretization method. This new approach addresses the instability issue observed in diffusion MRI signal computation involving blood flow. It serves as a powerful simulation tool, paving the way for numerically studying signal behaviors and designing novel microstructure estimation models for future blood perfusion studies. We firstly introduce the generalized form of Bloch-Torrey PDE incorporating the convection term and the Péclet number, a metric indicative of the potential for instability. Then, we give the full expression of the proposed scheme. We compare the standard Galerkin method and the Streamline Upwind Petrov-Galerkin method via simulations, demonstrating its effectiveness. We conduct an analysis of the effect of the choice of the stabilization parameters and the diameters of elements on the performance.

5.2 Bloch Torrey PDE with blood flow term

In this chapter, we focus on blood flow within the intravascular space and disregard the contribution of water diffusion inside the extravascular space and the exchange between these two domains. The intravascular space is modeled as one connected space, denoted Ω, with its boundary given by $\partial\Omega = \partial\Omega_{wall} \bigcup \partial\Omega_{end}$. $\partial\Omega_{wall}$ is the vascular wall and $\partial\Omega_{end}$ is the artificial boundary on the inlet and outlet sections.

The presence of blood flow induces a change in the acquired phase of spins, introducing a convection term to the Bloch-Torrey PDE[205, 217]:

$$\frac{\partial}{\partial t} M(\mathbf{x}, t) = \left(\nabla \mathcal{D}_0 \nabla - \imath\gamma f(t) \mathbf{g} \cdot \mathbf{x} - \mathbf{v}(\mathbf{x}, t) \cdot \nabla\right) M(\mathbf{x}, t),\ \mathbf{x} \in \Omega, \tag{5.1}$$

where $\mathcal{D}_0$ is the intrinsic diffusion coefficient, $\mathbf{v}(\mathbf{x}, t)$ represents the velocity field of blood flow, which should satisfy $\nabla \mathbf{v}(\mathbf{x}, t) = 0$. This modified Bloch-Torrey PDE is called the generalized form of Bloch-Torrey PDE in some literature[115, 218]. In reality, the velocity field is complex. It varies spatially according to the vessel section, blood pressure, and viscosity, and its direction can change along both parallel and perpendicular axes of the vessel[219].

For the sake of simplicity, we assume that the vascular wall is impermeable and there is no surface relaxation thus $\partial\Omega_{wall}$ can be modeled as a homogeneous Neumann boundary condition:

$$\mathcal{D}_0 \nabla M(\mathbf{x}, t) \cdot \mathbf{n}(\mathbf{x}) = 0, \ \mathbf{x} \in \partial\Omega_{wall}. \tag{5.2}$$

We impose also the homogeneous Neumann boundary conditions at both end sections. To prevent molecules from reaching these artificial boundaries and inducing artificial reflect flows in the simulation domain, we constrain the initial density to a specific region close to the inlet section without touching it and make the simulation domain sufficiently long in the direction normal to the outlet section. This ensures that by the end of the simulation, spins won't approach the outlet section:

$$\mathcal{D}_0 \nabla M(\mathbf{x}, t) \cdot \mathbf{n}(\mathbf{x}) = 0, \qquad \mathbf{x} \in \partial\Omega_{end}, \tag{5.3}$$

$$M(\mathbf{x}, 0) = m_0(\mathbf{x}), \qquad \mathbf{x} \in \Omega, \tag{5.4}$$

where m_0 is the initial density, located near the inlet section.

Another possible boundary condition on the two end sections of the vessel for the convection equation is the inlet/outlet boundary condition[220]. It assigns one inlet velocity and one outlet velocity on the end sections and the initial condition can be set to uniform in the domain. However, with mass consistently entering and leaving the simulation domain, accurately "tracking" the acquired phase for diffusion MRI becomes challenging. Thus, in this chapter, we do not adopt this boundary condition. A further investigation of the inlet/outlet boundary condition on diffusion MRI is needed in the future.

One remark is that in the presence of the convection, the diffusion MRI signals of PGSE sequence are usually complex values. Some advanced techniques are needed to make the phases back to zero in practice.

5.2.1 Numerical instability for the standard Galerkin method

Considering the blood flow, the generalized form of Bloch-Torrey PDE is a time dependent convection-diffusion-reaction PDE with an imaginary reactive term. The solution exhibits different behaviors based on convection and diffusion terms. A prevalent metric used to predict the behavior is the mass Péclet number (Pe)[221], defined as $\text{Pe} = \|\mathbf{v}\|_2 h / \mathcal{D}_0$, where h is the characteristic length.

When $\text{Pe} \ll 1$, water molecular movement is mainly affected by the self diffusion effects. Conversely, when $\text{Pe} \gg 1$, molecules are mainly transported by the flow[222].In this case, the standard Galerkin method will suffer significant instability and spurious oscillations. Refining the mesh reduces the characteristic length as well as the Péclet number. However, this isn't always practical. The Péclet number is determined by the local finite element size. To keep the Péclet number low, all the finite elements might experiencing high velocities during the whole simulation time need to be reduced in size by the same scale as velocity increases, leading to significant computational demands.

In addition, the convective operator is inherently directional. In convection-dominated regions, the solution will align in the direction of the flow or against it. The standard Galerkin method does not account for this directionality and thus might produce non-physical oscillations near areas of very steep gradients. These oscillations can then propagate throughout the simulation domain and cause a numerical explosion.

We illustrate this numerical instability in the simulation section.

5.3 SUPG scheme with theta method

The Streamline Upwind Petrov-Galerkin finite element method is a technique to stabilize the convection-diffusion equation in convection-dominated regimes for incompressible flows. The term "Petrov-Galerkin" means that the trial and test space are different and the term "streamline upwind" signifies that a stabilization term is added in the direction of the velocity field (the streamline).

To begin, we present first the weak formulation of eq. (5.1) by the standard Galerkin method. After discretizing the domain Ω by a set of confirming tetrahedra $\mathcal{T}^h$, eq. (5.1) can be transformed

into a weak formulation of the generalized Bloch-Torrey equation by multiplying a test function w^h and integrating over the domain Ω. The finite element methods are employed now on the finite dimensional space W^h. The standard Galerkin method uses the same functional space for the trial and test function, to find the discretized solution $M^h \in W^h$, such that

$$(\frac{\partial M^h}{\partial t}, w^h) = -(\mathcal{D}_0 \nabla M^h, \nabla w^h) - (\imath\gamma f(t)\mathbf{g}\cdot\mathbf{x}M^h + \mathbf{v}\cdot\nabla M^h, w^h), \tag{5.5}$$

where $w^h \in W^h, w^h|_{\partial\Omega} = 0$ is the test function and $(\cdot,\cdot)$ is the inner product in the L^2-norm Lebesgue spaces.

We consider now θ-scheme as temporal discretization. At the discrete time t_n, eq. (5.5) is transformed into

$$\begin{aligned}
&(M_n^h, w^h) + \theta\Delta t_n \left((\mathcal{D}_0\nabla M_n^h, \nabla w^h) + (\imath\gamma f(t_n)\mathbf{g}\cdot\mathbf{x}M_n^h + \mathbf{v}\cdot\nabla M_n^h, w^h)\right) \\
&\quad = (M_{n-1}^h, w^h) - (1-\theta)\Delta t_n \left((\mathcal{D}_0\nabla M_{n-1}^h, \nabla w^h) + (\imath\gamma f(t_{n-1})\mathbf{g}\cdot\mathbf{x}M_{n-1}^h + \mathbf{v}\cdot\nabla M_{n-1}^h, w^h)\right),
\end{aligned} \tag{5.6}$$

where $0 \leq \theta \leq 1$ and $\Delta t = t_n - t_{n-1}$ is the time step. For the given parameter, when $\theta = 1$, it corresponds to the backward Euler scheme and when $\theta = 0.5$ it corresponds to the Crank-Nicolson scheme. Equation (5.6) can be viewed as a stationary convection-diffusion-reaction equation at t_n with the right-hand side as a source term and the following diffusion, convection, and reaction coefficients:

$$D = \theta\Delta t\mathcal{D}_0, \tag{5.7}$$

$$\boldsymbol{C} = \theta\Delta t\mathbf{v}, \tag{5.8}$$

$$R = 1 + \imath\gamma\theta\Delta t f(t_n)\mathbf{g}\cdot\mathbf{x}. \tag{5.9}$$

To recompense the upwind phenomenon, the SUPG method employs a different test functional space

$$V^h := \{v^h : v^h(w^h) = w^h + \sum_{k\in\mathcal{T}^h} \tau_k \boldsymbol{C}\cdot\nabla w^h; w^h \in W^h\}, \tag{5.10}$$

where τ_k is the stabilization parameter depending on finite elements. With this test function space, the SUPG method is expressed as

$$\begin{aligned}
&(M_n^h, w^h) + \sum_{k\in\mathcal{T}^h} \tau_k\theta\Delta t_n (M_n^h, \mathbf{v}\cdot\nabla w^h)_k \\
&\quad + \theta\Delta t_n \left((\mathcal{D}_0\nabla M_n^h, \nabla w^h) + (\imath\gamma f(t_n)\mathbf{g}\cdot\mathbf{x}M_n^h + \mathbf{v}\cdot\nabla M_n^h, w^h)\right) \\
&\quad + \sum_{k\in\mathcal{T}^h} \tau_k(\theta\Delta t_n)^2(-\nabla\mathcal{D}_0\nabla M_n^h + \imath\gamma f(t_n)\mathbf{g}\cdot\mathbf{x}M_n^h + \mathbf{v}\cdot\nabla M_n^h, \mathbf{v}\cdot\nabla w^h)_k \\
&= (M_{n-1}^h, w^h) + \sum_{k\in\mathcal{T}^h} \tau_k\theta\Delta t (M_{n-1}^h, \mathbf{v}\cdot\nabla w^h)_k \\
&\quad - (1-\theta)\Delta t_n \left((\mathcal{D}_0\nabla M_{n-1}^h, \nabla w^h) + (\imath\gamma f(t_{n-1})\mathbf{g}\cdot\mathbf{x}M_{n-1}^h + \mathbf{v}\cdot\nabla M_{n-1}^h, w^h)\right) \\
&\quad - \sum_{k\in\mathcal{T}^h} \tau_k(1-\theta)\Delta t(\theta\Delta t_n)(-\nabla\mathcal{D}_0\nabla M_{n-1}^h + \imath\gamma f(t_{n-1})\mathbf{g}\cdot\mathbf{x}M_{n-1}^h + \mathbf{v}\cdot\nabla M_{n-1}^h, \mathbf{v}\cdot\nabla w^h)_k.
\end{aligned} \tag{5.11}$$

The literature[223] has proven that for incompressible flow, i.e. $\nabla\boldsymbol{C} = 0$, this formulation is well-posed for each time-step with the Crank-Nicolson scheme.

5.3.1 Choice of stabilization parameters

How to choose appropriate stabilization parameters is a vital consideration in actual simulations. We can distinguish the convection and diffusion effects by their characteristic time:

$$t_{\text{convection}} = \frac{h_k}{\|\boldsymbol{C}\|_2} \quad \text{and} \quad t_{\text{diffusion}} = \frac{h_k^2}{D}, \tag{5.12}$$

where h_k is the diameter of finite element. These definitions are related to Péclet number by Pe $=$ $t_{\text{diffusion}}/t_{\text{convection}}$. When $t_{\text{convection}} \leq t_{\text{diffusion}}$, the solution is more sensitive to the convection effect.

The desired asymptotic behaviors of the stabilization parameters (or characteristic stabilization time) τ_k should be two-fold: (1) In the diffusion-dominated regions where the standard Galerkin method is effective, τ_k should tend to the diffusion characteristic time $t_{\text{diffusion}}$; (2) In the convection-dominated regions, τ_k should tend to the convection characteristic time $t_{\text{convection}}$ to stabilize the equation and prevent spurious oscillations. The stabilization parameters typically depend on the diameter of elements, the amplitude of velocity $\|\boldsymbol{C}\|_2$ and the diffusion coefficient $\mathcal{D}$. In[210], it also suggests taking the reaction term into consideration. However, for our equation eq. (5.1), the diffusion term always dominates the diffusion encoding gradient term in actual experimental settings. Consequently, the solution won't fall into a reaction-dominated region in the presence of the diffusion. Hence, we will not add the reaction coefficient R into the stabilization parameters in our study.

Various proposals for τ_k exist in the literature. We will specifically consider the following three.

In[224], τ_k is suggested to be set as:

$$\tau_k^I \sim \left(\frac{4}{t_{\text{diffusion}}} + \frac{2}{t_{\text{convection}}}\right)^{-1} = \frac{h_k^2}{\theta \Delta t_n (4 t_n \mathcal{D}_0 + 2 h_k \|\mathbf{v}\|_2)} \tag{5.13}$$

In[225], τ_k is suggested to be set as

$$\tau_k^{II} \sim \frac{h_k}{2\|\boldsymbol{C}\|_2} \xi\left(\frac{m_k \|\boldsymbol{C}\|_2 h_k}{2D}\right) = \frac{h_k}{2\theta \Delta t_n \|\mathbf{v}\|_2} \xi\left(\frac{m_k \|\mathbf{v}\|_2 h_k}{2\mathcal{D}_0}\right), \tag{5.14}$$

where m_k is a constant related to the finite element function. For piece-wise linear ($P1$) function, $m_k = 1/3$. And $\xi(x)$ function is

$$\xi(x) = \begin{cases} x, & 0 \leq x < 1, \\ 1, & x \geq 1. \end{cases}$$

In[226, 227], τ_k is suggested to be set as

$$\tau_k^{III} \sim \min\left\{\frac{h_k}{p_k \|\mathbf{C}\|_\infty}, \frac{h_k^2}{p_k^4 c_{\text{inv}}^2 \|D\|_\infty}\right\} = \min\left\{\frac{h_k}{p_k \theta \Delta t_n \|\mathbf{v}\|_\infty}, \frac{h_k^2}{p_k^4 c_{\text{inv}}^2 \theta \Delta t_n \mathcal{D}_0}\right\} \tag{5.15}$$

where p_k is the polynomial degree of the finite element function and c_{inv} is a constant from an inverse estimate. For $P1$ function, we have $p_k = 1$ and $c_{\text{inv}} = 1$.

All these three proposals satisfy the asymptotic behaviors of τ_k but they exhibit a slightly different in the intermediate regions. We will evaluate and compare these three stabilization parameters in the following section.

Another concern is that for tetrahedral elements, there is not a standard definition of the diameter h_k. In[228, 229], it is suggested that h_k should be chosen as the length of the elements in the direction of the velocity field, which should be re-calculated at each time step if the velocity is time dependent. Conversely, another study in[210] indicates that the specific direction chosen for the diameter isn't crucial. In our analysis, we evaluate both diameter definitions and will compare them through numerical simulations. The non-directional diameter $h_{k,1}$ is selected as the diameter of the inscribed sphere within the element, while the directional diameter $h_{k,2}$ is defined as follows:

$$h_{k,2} = \frac{3V_k}{2F_k(\mathbf{v})}, \tag{5.16}$$

where V_k is the volume of the tetrahedral element, and F_k is the average area of the projection of four tetrahedral faces onto the surface orthogonal to the velocity direction, as shown in fig. 5.1. When the direction of velocity is orthogonal to the face of the element, h_k is equal to the height of that face.

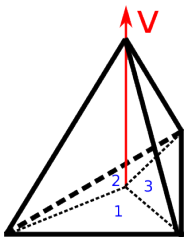

Figure 5.1: Projection of tetrahedral faces onto the perpendicular plane of velocity, in the case of the velocity is orthogonal to one face. For such a case, the projection of the bottom face is itself and the projection of the other three faces are labeled as 1, 2 and 3 (depicted in blue), respectively. The average area is equivalent to half the combined area of 1, 2 and 3.

5.4 Simulation

The numerical studies of the generalized Bloch-Torrey PDE using the SUPG method are conducted in this section. Due to the constraints of our computational resources, we only simulate one segment of the vessel, modeled as a straight cylinder with a radius of 2.1μm and a height of 100μm, denoted L, as depicted in fig. 5.2. The intrinsic diffusion coefficient is set to 2×10^{-3} mm^2/s.

Velocity is usually assumed to run in the tangent direction to the vessel wall. While the actual environment might be more intricate as discussed in[219]. Here, we adhere to the tangent direction assumption. Accordingly, we set the velocity direction as $[0, 0, 1]^T$, which aligns with the cylinder's axial direction. For simplicity, we use a constant velocity. The amplitude of velocity is set to be $\|\mathbf{v}\|_2 = [10^{-3}, 1.5\times10^{-2}, 3\times10^{-2}, 4\times10^{-2}]\mu$m/$\mu$s, corresponding to some typical blood flow velocity values inside capillaries, arterioles and venules[230–232].

To ensure that the initial density is concentrated near the inlet section at the bottom and remains a continuous function, we define it as an exponential function:

$$m_0(\mathbf{x}) = e^{-(z-(-L/2+4))^2}, \tag{5.17}$$

as shown in fig. 5.2. At the bottom section, $m_0(-L/2) = 1.1 \times 10^{-7} \approx 0$. The initial signal is $S_0 = 24.58$.

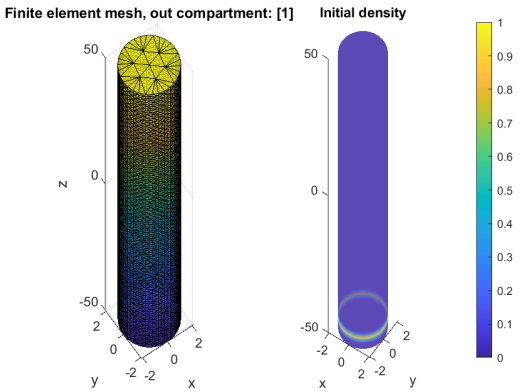

Figure 5.2: Left: Finite elements mesh of the simulation domain Ω, with a radius of 2.1μm and a height of 100μm. Right: The initial density on Ω. We adjusted the plot z-coordinate scale to enhance its visual representation.

To make sure that at the echo time, the spins will not reach the top artificial boundary, we limit the $T_E \leq 2 \times 10^3$ms and employ the sequence PGSE$(1\text{ms}, 1\text{ms})$.

The diffusion encoding gradient direction is set to $[0; 0; 1]^T$, parallel to the velocity field direction. Indeed, in the x-y plane perpendicular to the velocity, the diffusion encoding gradient term is entirely decoupled from the convection term, so we only need to consider the convection-diffusion in z-direction. In the simulations, three gradient strengths are used: $\|\mathbf{g}\| = [0, 200]$ mT/m. In the case of

$\|\mathbf{g}\| = 0\,\text{mT/m}$, the equation is reduced to a convection-diffusion equation and the magnetization should be real, which will make it easier to detect spurious oscillations.

The temporal discretization scheme is the Crank-Nicolson scheme $\theta = 0.5$. It requires that the ratio of time step Δt times diffusion coefficient to the square of element size should be small, in order to produce a stable solution in time discretization[233]. Thus, if not specific, we use a time step of 0.5μs, which is sufficient short.

The finite element mesh is generated by Tetgen[121]. The coarseness of the mesh is controlled by a parameter h. In table 5.1, we list the number of elements $N_{element}$, the number of nodes N_{node}, and the average inner radius $r_{in,ave}$ for different h values. In the application of brain diffusion MRI, the mesh of $h = 1$ can already yield an accurate solution.

h	1	0.2	0.1	0.07	0.05
N_{node}	4,593	8,981	10,379	11,731	24,783
$N_{element}$	15,411	28,332	38,402	47,266	104,156
$r_{in,ave}$	0.294	0.238	0.228	0.218	0.160
h	0.03	0.02	0.015	0.12	0.01
N_{node}	27,300	31,850	37,972	47,332	57,708
$N_{element}$	120,495	150,437	189,302	235,325	286,228
$r_{in,ave}$	0.157	0.148	0.140	0.130	0.122

Table 5.1: Number of nodes, Number of elements and the average inner radius [in μm] of the finite element meshes with different coarseness parameters.

There is no analytical solution for the generalized Bloch-Torrey PDE. Therefore, we take the stable solutions on the finest mesh as the reference solutions.

5.4.1 Numerical instability of the standard Galerkin method

First, we will show that the standard Galerkin method will encounter instability issues when simulating the convection-diffusion equation.

In fig. 5.3, we plot the magnetization at echo time $M(\mathbf{x}, T_E)$ simulated by the standard Galerkin method on the finite elements mesh of $h = 1$, using the four distinct velocity values, with $\|\mathbf{g}\| = 0\,\text{mT/m}$. In this case, the magnetization and signals at echo time should be real. With high velocities, the particles are less likely to reach the bottom section due to diffusion. Thus, the diffusion in z-direction is like the free diffusion transported by the flow and the signals should be closed to S_0. We can observe that in the diffusion-dominated regions (as in the case of $\|\mathbf{v}\|_2 = 1 \times 10^{-3}\mu\text{m}/\mu\text{s}$), particles disperse more rapidly than transport by the flow. As the flow velocity increases, the particles are transported together as a group. In the convection-dominated regions ($\|\mathbf{v}\|_2 = 4 \times 10^{-2}\mu\text{m}/\mu\text{s}$), we could not obtain stable solutions. Besides, even in the case $\|\mathbf{v}\|_2 = 3 \times 10^{-2}\mu\text{m}/\mu\text{s}$, the amplitude of magnetization does not exceed 1, spurious oscillations will arise, where negative values are present (between $z = 0\mu$m and $z = 10\mu$m).

In fig. 5.4, we plot the amplitude of transverse magnetization with $\|\mathbf{g}\| = 200\,\text{mT/m}$ for the two high velocities $\|\mathbf{v}\|_2 = [3 \times 10^{-2}, 4 \times 10^{-2}]\mu\text{m}/\mu\text{s}$. We can still see the spurious oscillations at high velocities.

In fig. 5.5, we depict normalized signals (divided by S_0) as a function of the number of nodes with $\|\mathbf{g}\| = 0\,\text{mT/m}$, across different velocity values. In the diffusion-dominated region, the signals are a little bit higher than S_0 due to interactions with the bottom boundary caused by flow. In this case, using the coarsest mesh is already capable of yielding a convergent solution. At high velocities, the signals simulated on the coarse meshes are not accurate. Moreover, spurious oscillations occur for $\|\mathbf{v}\|_2 = 1.5 \times 10^{-2}\mu\text{m}/\mu\text{s}$ on the two coarse meshes even though we do not observe that from the magnetization plot.

In fig. 5.6, we plot the amplitude, real part, and imaginary part of the normalized signals against the number of nodes with $\|\mathbf{g}\| = 200\,\text{mT/m}$, across different velocity values. We can see that at low gradient strengths, the signals have similar amplitude at three high velocities, but different real parts and imaginary parts due to the diffusion-encoding gradient.

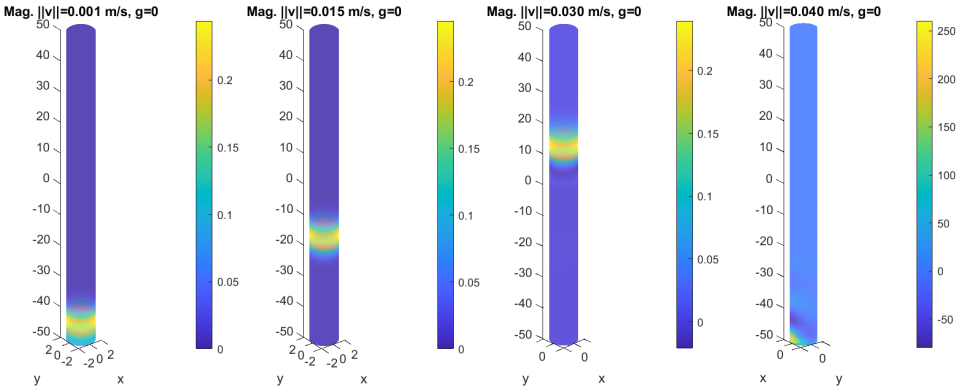

Figure 5.3: Transverse magnetization with various velocities on the finite element mesh of $h = 1$, at g-value of $0\,\mathrm{mT/m}$. The PGSE$(1\mathrm{ms}, 1\mathrm{ms})$ sequence is applied. The simulations are performed by the standard Galerkin finite elements method. From left to right: $\|\mathbf{v}\|_2 = [10^{-3}, 1.5 \times 10^{-2}, 3 \times 10^{-2}, 4 \times 10^{-2}]\mu\mathrm{m}/\mu\mathrm{s}$. A spurious oscillation (negative magnetization values) occurs between 0μm and 10μm for $\|\mathbf{v}\|_2 = 3 \times 10^{-2}\mu\mathrm{m}/\mu\mathrm{s}$.

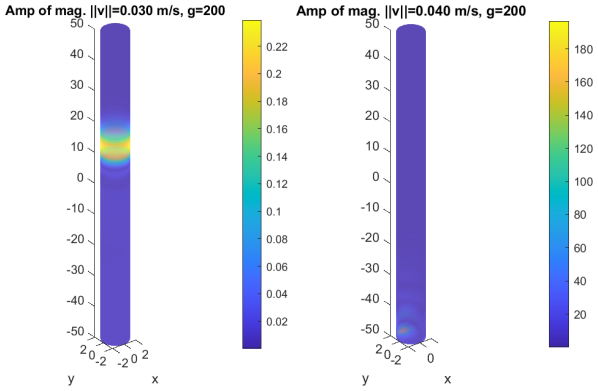

Figure 5.4: Transverse magnetization with various velocities on the finite element mesh of $h = 1$, at g-value of $200\,\mathrm{mT/m}$. The PGSE$(1\mathrm{ms}, 1\mathrm{ms})$ sequence is applied. The simulations are performed by the standard Galerkin finite elements method. From left to right: $\|\mathbf{v}\|_2 = [3 \times 10^{-2}, 4 \times 10^{-2}]\mu\mathrm{m}/\mu\mathrm{s}$. A spurious oscillation occurs between 0μm and 10μm for $\|\mathbf{v}\|_2 = 3 \times 10^{-2}\mu\mathrm{m}/\mu\mathrm{s}$.

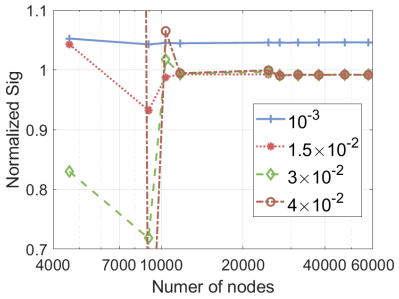

Figure 5.5: Normalized signals by the standard Galerkin method against the number of nodes, with $\|\mathbf{g}\| = 0\,\mathrm{mT/m}$. The signals are normalized by S_0. The solid, dotted, dashed, and dash-dot lines represent the velocity values of $10^{-3}\mu\mathrm{m}/\mu\mathrm{s}$, $1.5 \times 10^{-2}\mu\mathrm{m}/\mu\mathrm{s}$, $3 \times 10^{-2}\mu\mathrm{m}/\mu\mathrm{s}$ and $4 \times 10^{-2}\mu\mathrm{m}/\mu\mathrm{s}$.

We use the signals from the standard Galerkin method on the finest mesh as our reference, as it provides stable results in this example. One reminder is that the standard Galerkin method doesn't always guarantee stable solutions in other cases. In fig. 5.7, we plot the relative errors between the signals and reference. It is clear that to obtain stable solutions at high velocities, the number of nodes needs to be more than 27,300.

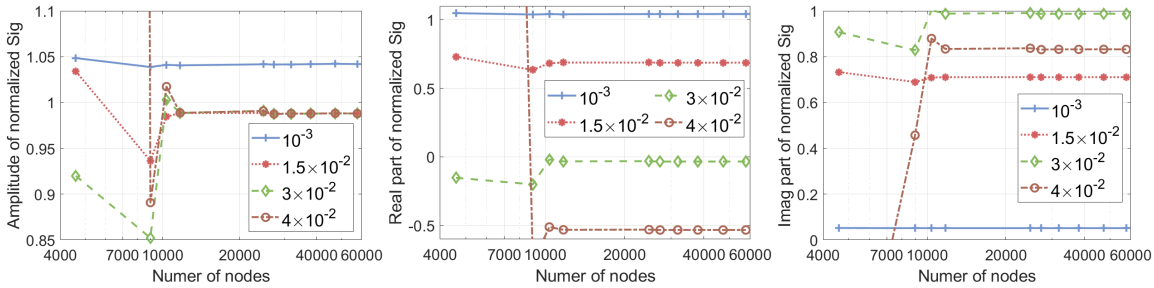

Figure 5.6: Amplitude (left), real part (middle), and imaginary part (right) of normalized signals by the standard Galerkin method against the number of nodes, with $\|\mathbf{g}\| = 200\,\mathrm{mT/m}$. The signals are normalized by S_0. The solid, dotted, dashed, and dash-dot lines represent the velocity values of $10^{-3}\mu\mathrm{m}/\mu\mathrm{s}$, $1.5\times10^{-2}\mu\mathrm{m}/\mu\mathrm{s}$, $3\times10^{-2}\mu\mathrm{m}/\mu\mathrm{s}$ and $4\times10^{-2}\mu\mathrm{m}/\mu\mathrm{s}$.

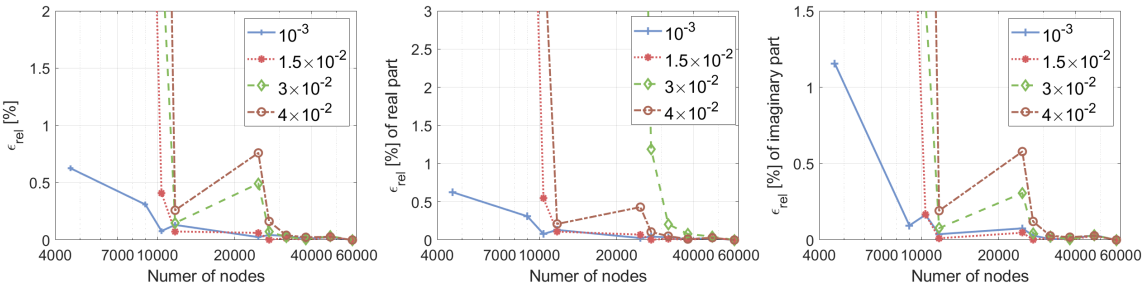

Figure 5.7: Relative errors by the standard Galerkin method against the number of nodes. Left: $\|\mathbf{g}\| = 0\,\mathrm{mT/m}$, computed by $100\% \times |S - S_{ref}|/|S_{ref}|$; Middle: Real part with $\|\mathbf{g}\| = 200\,\mathrm{mT/m}$, computed by $100\% \times |\Re(S) - \Re(S_{ref})|/|\Re(S_{ref})|$; Right: Imaginary part with $\|\mathbf{g}\| = 200\,\mathrm{mT/m}$, computed by $100\% \times |\Im(S) - \Im(S_{ref})|/|\Im(S_{ref})|$. The solid, dotted, dashed, and dash-dot lines represent the velocity values of $10^{-3}\mu\mathrm{m}/\mu\mathrm{s}$, $1.5\times10^{-2}\mu\mathrm{m}/\mu\mathrm{s}$, $3\times10^{-2}\mu\mathrm{m}/\mu\mathrm{s}$ and $4\times10^{-2}\mu\mathrm{m}/\mu\mathrm{s}$.

5.4.2 Using SUPG

Next, we employ the SUPG method on the simulations. At low velocities, the results by the SUPG method should be close to those by the standard Galerkin method, and at high velocities, we expect that the solutions are stable on a coarse mesh.

In fig. 5.8, we plot the magnetization calculated by the SUPG method, with stabilization parameters τ_k^I and directional diameter of elements $h_{k,2}$, on the finite elements mesh of $h = 1$ with $\|\mathbf{g}\| = 0\,\mathrm{mT/m}$. We can see that after adding the stabilization terms, the magnetization at high velocities is stable and there are no spurious oscillations.

In fig. 5.9, we plot the normalized signals by the SUPG method against the number of nodes, with $\|\mathbf{g}\| = 0\,\mathrm{mT/m}$ and $\|\mathbf{g}\| = 200\,\mathrm{mT/m}$. We can see that after adding the stabilization terms, the signals are stable for all velocities when $N_{node} \geq 8,981$, which is a significant improvement compared to the standard Galerkin method.

5.4.3 Choice of stabilization parameters and diameter of elements

The choice of the stabilization parameters and diameter of elements will affect the performance of the SUPG method. In fig. 5.10, we plot the signal relative errors using different combinations of stabilization parameters and diameters of elements, with $\|\mathbf{g}\| = 0\,\mathrm{mT/m}$. We use the solutions by the standard Galerkin method on the finest mesh as the reference solutions, same as the previous subsection. We observe that not every combination effectively stabilizes the equation. With the directional diameters of elements $h_{k,2}$, only the first stabilization parameter τ_k^I produces stable results. In contrast, for the non-directional diameter $h_{k,1}$, all three stabilization parameters can stabilize the solution, though with varying efficiency. Specifically, $(\tau_k^I, h_{k,1})$ and $(\tau_k^{II}, h_{k,1})$ are better than $(\tau_k^{III}, h_{k,1})$.

In summary, generally, the combination $(\tau_k^I, h_{k,2})$ is preferable, it could converge on coarse

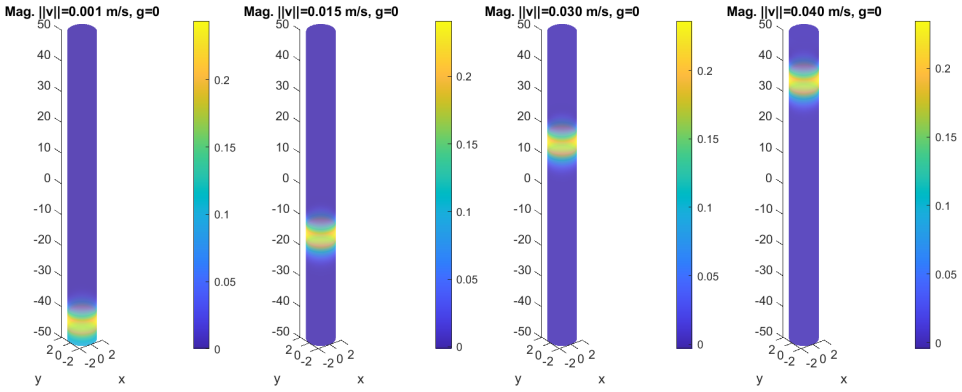

Figure 5.8: Transverse magnetization with various velocities on the finite element mesh of $h = 1$, at g-value of $0\,\mathrm{mT/m}$. The PGSE$(1\mathrm{ms}, 1\mathrm{ms})$ sequence is applied. The simulations are performed by the SUPG method, with stabilization parameters τ_k^I and diameter of elements $h_{k,2}$. From left to right: $\|\mathbf{v}\|_2 = [10^{-3}, 1.5 \times 10^{-2}, 3 \times 10^{-2}, 4 \times 10^{-2}]\mu\mathrm{m}/\mu\mathrm{s}$.

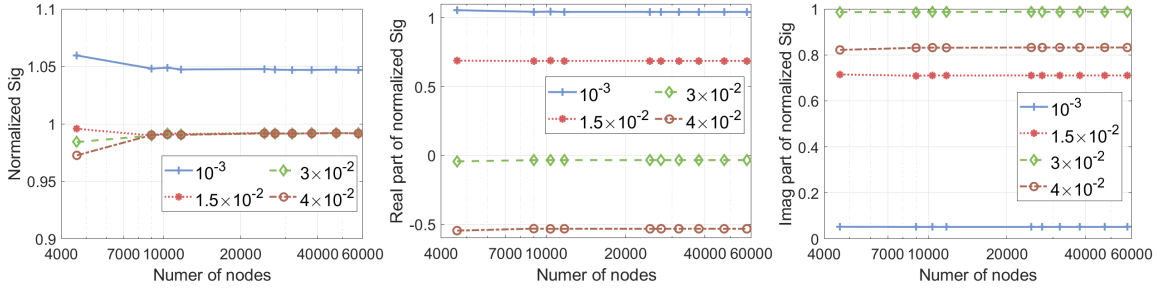

Figure 5.9: Normalized signals by the SUPG method with stabilization parameters τ_k^I and diameter of elements $h_{k,2}$, against the number of nodes. Left: $\|\mathbf{g}\| = 0\,\mathrm{mT/m}$. Left: Real part with $\|\mathbf{g}\| = 200\,\mathrm{mT/m}$; Right: Imaginary part with $\|\mathbf{g}\| = 200\,\mathrm{mT/m}$. The solid, dotted, dashed, and dash-dot lines represent the velocity values of $10^{-3}\mu\mathrm{m}/\mu\mathrm{s}$, $1.5 \times 10^{-2}\mu\mathrm{m}/\mu\mathrm{s}$, $3 \times 10^{-2}\mu\mathrm{m}/\mu\mathrm{s}$ and $4 \times 10^{-2}\mu\mathrm{m}/\mu\mathrm{s}$.

meshes ($N_{node} = 8,981$). However, for the low blood flow velocity case, this combination converges slower than $(\tau_k^I, h_{k,1})$ and $(\tau_k^{II}, h_{k,1})$ as the number of nodes increases.

In fig. 5.11, we plot the signal absolute errors with the three combinations $(\tau_k^I, h_{k,2})$, $(\tau_k^I, h_{k,1})$ and $(\tau_k^{II}, h_{k,1})$, with $\|\mathbf{g}\| = 200\,\mathrm{mT/m}$. We note that on the coarsest meshes ($N_{node} = 4,593$), only $(\tau_k^I, h_{k,2})$ can stabilize the equation. And the other two combinations need a denser mesh ($N_{node} \geq 10,379$). The directional diameter of elements yields a better solution on the coarse meshes. However, an advantage of the undirectional diameter of elements is that when velocity is time-dependent, we do not need to re-compute the stabilization at each step, which may save computational time.

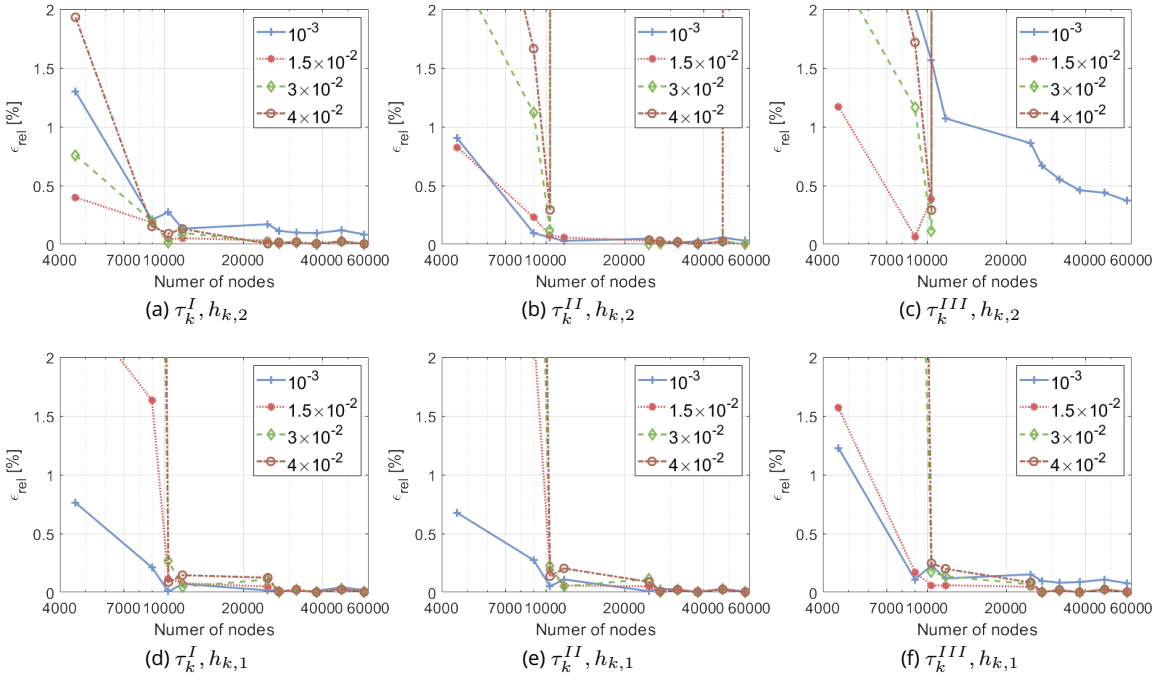

(a) $\tau_k^I, h_{k,2}$ (b) $\tau_k^{II}, h_{k,2}$ (c) $\tau_k^{III}, h_{k,2}$

(d) $\tau_k^I, h_{k,1}$ (e) $\tau_k^{II}, h_{k,1}$ (f) $\tau_k^{III}, h_{k,1}$

Figure 5.10: Relative errors of the signals by the SUPG method with six different combinations of stabilization parameters τ and diameter of element h_k, with $\|\mathbf{g}\| = 0\,\mathrm{mT/m}$. The solid, dotted, dashed, and dash-dot lines represent the velocity values of $10^{-3}\mu\mathrm{m}/\mu\mathrm{s}$, $1.5 \times 10^{-2}\mu\mathrm{m}/\mu\mathrm{s}$, $3 \times 10^{-2}\mu\mathrm{m}/\mu\mathrm{s}$ and $4 \times 10^{-2}\mu\mathrm{m}/\mu\mathrm{s}$.

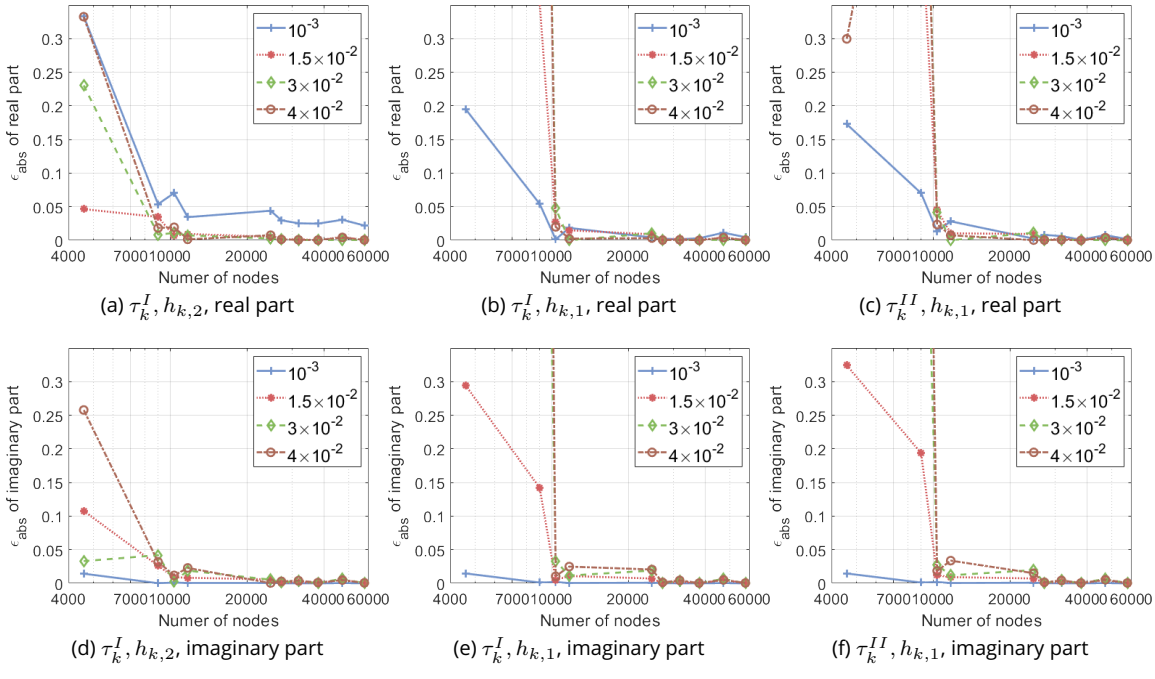

(a) $\tau_k^I, h_{k,2}$, real part (b) $\tau_k^I, h_{k,1}$, real part (c) $\tau_k^{II}, h_{k,1}$, real part

(d) $\tau_k^I, h_{k,2}$, imaginary part (e) $\tau_k^I, h_{k,1}$, imaginary part (f) $\tau_k^{II}, h_{k,1}$, imaginary part

Figure 5.11: Absolute errors of the signals by the SUPG method with three different combinations of stabilization parameters τ and diameter of element h_k, with $\|\mathbf{g}\| = 200\,\mathrm{mT/m}$. The solid, dotted, dashed, and dash-dot lines represent the velocity values of $10^{-3}\mu\mathrm{m}/\mu\mathrm{s}$, $1.5 \times 10^{-2}\mu\mathrm{m}/\mu\mathrm{s}$, $3 \times 10^{-2}\mu\mathrm{m}/\mu\mathrm{s}$ and $4 \times 10^{-2}\mu\mathrm{m}/\mu\mathrm{s}$.

5.5 Discussion

In this chapter, we extend our diffusion MRI simulator for blood flow imaging. Introducing the convection term can lead to stability issues in the convection-dominated region. To stabilize the equation, we employ the Streamline Upwind Petrov-Galerkin method to the generalized form of the Bloch-Torrey equation. Numerical simulations demonstrate its superiority over the standard Galerkin method, achieving stable results on coarser meshes.

In the implementation of the SUPG method, the selection of stabilization parameters τ_k and diameter of elements h_k is crucial. Our numerical simulations indicate that not all (τ_k, h_k) pairings are effective in stabilizing the equation. Of the pairings that do stabilize, $(\tau_k^I, h_{k,2})$ performs well on coarse meshes, yet it converges slower at low blood flow velocity, compared to $(\tau_k^I, h_{k,1})$ and $(\tau_k^{II}, h_{k,1})$.

Chapter 6

Conclusions and perspectives

The ultimate objective of this thesis is to offer robust numerical tools for studying diffusion MRI signals and ADC behaviors in a more complex and realistic context, evaluating the existing microstructure estimation techniques, such as diffusion MRI compartment signal models, designing appropriate diffusion MRI experimental setups, and developing new microstructure estimation models.

We develop a new formulation of Matrix Formalism, which computes the diffusion MRI signals of permeable medium using the impermeable Laplace eigenfunctions. This new formulation decomposes permeable magnetization into impermeable Laplace eigenfunctions and treats the permeability as a perturbation term $\boldsymbol{Q}_{proj}$ during the signal computation process. Thus, it saves computational resources for simulations when adjusting the permeability values, since the eigen-decomposition is only needed to be performed once. A promising application of this new formulation is to study the impact of permeability values on the signals or ADC patterns and evaluating diffusion MRI compartment signal models that account for permeability. $\boldsymbol{Q}_{proj}$ can be further split into two components: the permeability value and the interface shapes, which relate to the surface-to-volume ratio. Moreover, the numerical analysis on diffusion MRI signals illustrates that the signals can be approximated by an exponential relationship $S^{\text{APPROX}} = e^{-\beta \cdot \kappa} \cdot \left(S_{\text{imp}} - S_{\text{free}}\right) + S_{\text{free}}$, where β is related to interface shapes, providing the possibility to probe individually the surface-to-volume ratio of porous medium and permeability in the future.

Asymptotic model accounting for geometrical deformations is another powerful numerical analysis tool. By expanding the transformed diffusion MRI signal and ADC defined on canonical domain as a power series of deformation parameters, one can explicitly link the structure and signals. In the small deformation regime, a second-order correction is sufficient to yield good approximations. Minor corrections values imply that the deformations have minimal influence on the signals. This insight can guide the design of experimental settings to minimize the shape imperfections. In this thesis, we focus on the asymptotic expansions for bending and twisting deformations. Theoretically, this method can also be adapted to other types of deformations with analytical forms, such as undulation, beading, or orientation dispersion in the future.

Following the research in[3, 5], we conduct a numerical analysis on the relationship between inflection point-derived biomarkers and the soma size and volume fractions in the brain gray matter using the Numerical Matrix Formalism method. This analysis directly relates specific signal patterns to certain microstructures. Based on this investigation, we propose an IP-derived biomarkers exhaustive search method for volume fractions and soma size estimation. We validate this IP-derived biomarker-based estimation on both the Synthetic Voxels Set and the *in vivo* dataset, showing similar results compared to signals-based estimations. Potential performance improvements of this IP-derived biomarker-based method include:

1. Combining IP-derived biomarkers from various diffusion MRI sequences. Given that each sequence is particularly sensitive to a specific range of soma sizes, their combinations can potentially broaden the estimation range and enhance estimation reliability;

2. Introducing additional biomarkers. In this work, we focus on three IP-derived biomarkers. Incorporating other biomarkers, derived from the inflection point, like the error in the power-law approximation, or kurtosis tensor, may improve the method's robustness;

3. Using manifold learning to approximate the mappings. The mappings from biomarkers to soma size are effectively low dimensional manifolds. Some advanced machine learning techniques may help make a better estimation.

Diffusion MRI simulation with Streamline Upwind Petrov-Galerkin scheme addresses the instability issues in blood flow imaging. Numerical validation shows that the proposed scheme yields stable solutions on coarse meshes at large velocities. However, this method has been tested only on a simple case, further analysis of realistic velocity field and other inlet/outlet boundary conditions is essential before the practical applications. To be able to make an appropriate choice, a comprehensive study on velocity limits[234] and potentially integrating the imaginary reaction term with stabilization parameters is necessary for future research. In addition, to mitigate or even eliminate spurious oscillations in layers from SUPG solutions, a potential work in the future is to integrate the SOLD method into the formulation[229, 235].

To conclude, this thesis contributes to numerical simulation methods in diffusion MRI and microstructural imaging.

Appendix A

Appendix of Chapter 3

A.1 Alternative formula of HADC model

The ADC of compartment Ω_i by the HADC model in the original paper[151] is

$$\text{HADC}^i = \mathcal{D}^i - \frac{\mathcal{D}^i}{\int_0^{TE} F(t)^2 dt} \int_0^{TE} F(t)\ h^i(t)\ dt, \tag{A.1}$$

where

$$h^i(t) = \frac{1}{|\Omega_i|} \int_{\partial\Omega_i} \omega^i(\mathbf{r}, t)\ (\mathbf{u_g} \cdot \boldsymbol{n}(\mathbf{r}))\ ds_{\mathbf{r}} \tag{A.2}$$

is a quantity related to the directional gradient of a function ω^i that is the solution of the homogeneous diffusion equation with Neumann boundary condition and zero initial condition:

$$\frac{\partial}{\partial t}\omega^i(\mathbf{r}, t) = \nabla\mathcal{D}^i\nabla\omega^i(\mathbf{r}, t), \quad \mathbf{r} \in \Omega_i \tag{A.3}$$

$$\mathcal{D}^i\nabla\omega^i(\mathbf{r}, t) \cdot \boldsymbol{n}(\mathbf{r}) = \mathcal{D}^i F(t)\mathbf{u_g} \cdot \boldsymbol{n}(\mathbf{r}), \mathbf{r} \in \partial\Omega_i \tag{A.4}$$

$$\omega^i(\mathbf{r}, 0) = 0, \quad \mathbf{r} \in \Omega_i, \tag{A.5}$$

$\boldsymbol{n}$ being the outward normal and $t \in [0, TE]$.
We define a new function

$$\tilde{\omega}(\mathbf{r}, t) = \omega(\mathbf{r}, t) - F(t)\mathbf{u_g} \cdot \mathbf{r}. \tag{A.6}$$

Replacing eq. (A.6) into eqs. (A.3) to (A.5), we obtain the following non-homogeneous diffusion equation:

$$\frac{\partial}{\partial t}\tilde{\omega}^i(\mathbf{r}, t) = \nabla\mathcal{D}^i\nabla\tilde{\omega}^i(\mathbf{r}, t) - f(t)\mathbf{u_g} \cdot \mathbf{r}, \mathbf{r} \in \Omega_i \tag{3.2 revisited}$$

$$\mathcal{D}^i\nabla\tilde{\omega}^i(\mathbf{r}, t) \cdot \boldsymbol{n}(\mathbf{r}) = 0, \quad \mathbf{r} \in \partial\Omega_i \tag{3.3 revisited}$$

$$\tilde{\omega}^i(\mathbf{r}, 0) = 0, \quad \mathbf{r} \in \Omega_i, \tag{3.4 revisited}$$

Using the divergence theorem to the second term of the new function $F(t)\mathbf{u_g} \cdot \mathbf{r}$, we have

$$\int_{\partial\Omega_i} F(t)\mathbf{u_g} \cdot \mathbf{r}\ (\mathbf{u_g} \cdot \boldsymbol{n}(\mathbf{r}))\ ds_{\mathbf{r}} = F(t) \int_{\Omega_i} \nabla \cdot (\mathbf{u_g} \cdot \mathbf{r})\ \mathbf{u_g} d\mathbf{r} = |\Omega_i| F(t). \tag{A.7}$$

Therefore, eq. (A.2) becomes

$$\tilde{h}^i(t) = \frac{1}{|\Omega_i|} \int_{\partial\Omega_i} \tilde{\omega}^i(\mathbf{r}, t)\ (\mathbf{u_g} \cdot \boldsymbol{n}(\mathbf{r}))\ ds_{\mathbf{r}} - F(t). \tag{A.8}$$

And at echo time, the second term equals to $\mathcal{D}^i$ and the ADC is

$$\begin{aligned} \text{HADC}^i &= \mathcal{D}^i - \frac{-\mathcal{D}^i}{\int_0^{TE} F(t)^2 dt} \int_0^{TE} F(t)\tilde{h}^i(t) dt \\ &= \frac{\mathcal{D}^i}{\int_0^{TE} F(t)^2 dt} \int_0^{TE} F(t) \frac{1}{|\Omega_i|} \int_{\partial\Omega_i} \tilde{\omega}^i(\mathbf{r}, t)\ (\mathbf{u_g} \cdot \boldsymbol{n}(\mathbf{r}))\ ds_{\mathbf{r}} dt. \end{aligned} \tag{A.9}$$

A.2 Asymptotic expansion in Matrix Formalism representation

By decomposing each order of the asymptotic expansion of the transformed HADC model into the Laplace eigenfunctions, multiplying the eigenfunction $\phi(\mathbf{x})$, and integrating over the whole domain, we have

$$\frac{d\boldsymbol{\zeta}_0}{dt} = -\boldsymbol{L}\boldsymbol{\zeta}_0 - f(t)\mathbf{J}_0\mathbf{1}_{N_{eig},1}, \tag{A.10}$$

$$\frac{d\boldsymbol{\zeta}_{0,1}}{dt} = -\boldsymbol{L}\boldsymbol{\zeta}_{0,1} - \mathbf{C}_{b,1}\boldsymbol{\zeta}_0 - f(t)\mathbf{J}_{b,1}\mathbf{1}_{N_{eig},1}, \tag{A.11}$$

$$\frac{d\boldsymbol{\zeta}_{1,0}}{dt} = -\boldsymbol{L}\boldsymbol{\zeta}_{1,0} - \mathbf{C}_{t,1}\boldsymbol{\zeta}_0 - f(t)\mathbf{J}_{t,1}\mathbf{1}_{N_{eig},1}, \tag{A.12}$$

$$\frac{d\boldsymbol{\zeta}_{0,2}}{dt} = -\boldsymbol{L}\boldsymbol{\zeta}_{0,2} - \mathbf{C}_{b,1}\boldsymbol{\zeta}_{0,1} - \mathbf{C}_{b,2}\boldsymbol{\zeta}_0 - f(t)\mathbf{J}_{b,2}\mathbf{1}_{N_{eig},1}, \tag{A.13}$$

$$\frac{d\boldsymbol{\zeta}_{2,0}}{dt} = -\boldsymbol{L}\boldsymbol{\zeta}_{2,0} - \mathbf{C}_{t,1}\boldsymbol{\zeta}_{1,0} - \mathbf{C}_{t,2}\boldsymbol{\zeta}_0 - f(t)\mathbf{J}_{t,2}\mathbf{1}_{N_{eig},1}, \tag{A.14}$$

$$\frac{d\boldsymbol{\zeta}_{1,1}}{dt} = -\boldsymbol{L}\boldsymbol{\zeta}_{1,1} - \mathbf{C}_{tb,1}\boldsymbol{\zeta}_0 - \mathbf{C}_{b,1}\boldsymbol{\zeta}_{1,0} - \mathbf{C}_{t,1}\boldsymbol{\zeta}_{0,1} - f(t)\mathbf{J}_{tb,1,1}\mathbf{1}_{N_{eig},1}, \tag{A.15}$$

where $\mathbf{C}$ are correction matrices and $\mathbf{J}$ are matrices of transformation,

$$[\mathbf{C}_{b,1}]_{nm} = 2\mathcal{D}^i \int_\Omega z(\partial_z\phi_n\partial_x\phi_m + \partial_x\phi_n\partial_z\phi_m)d\mathbf{x}, \tag{A.16}$$

$$[\mathbf{C}_{b,2}]_{nm} = 4\mathcal{D}^i \int_\Omega z^2\partial_x\phi_n\partial_x\phi_m d\mathbf{x}, \tag{A.17}$$

$$[\mathbf{C}_{t,1}]_{nm} = \mathcal{D}^i \int_\Omega x(\partial_z\phi_n\partial_y\phi_m + \partial_y\phi_n\partial_z\phi_m) - y_n(\partial_z\phi_n\partial_x\phi_m + \partial_x\phi_n\partial_z\phi_m)d\mathbf{x}, \tag{A.18}$$

$$[\mathbf{C}_{t,2}]_{nm} = \mathcal{D}^i \int_\Omega xy(\partial_x\phi_n\partial_y\phi_m + \partial_y\phi_n\partial_x\phi_m) - x^2(\partial_y\phi_n\partial_y\phi_m) - y^2(\partial_x\phi_n\partial_x\phi_m)d\mathbf{x}, \tag{A.19}$$

$$[\mathbf{C}_{tb,1,1}]_{nm} = 2\mathcal{D}^i \int_\Omega z(\partial_x\phi_n\partial_y\phi_m + \partial_y\phi_n\partial_x\phi_m) - 2y\partial_x\phi_n\partial_x\phi_m d\mathbf{x}. \tag{A.20}$$

$$[\mathbf{J}_0]_{nm} = \int_\Omega \mathbf{u_g}\cdot\mathbf{x}\phi_n\phi_m d\mathbf{x}, \tag{A.21}$$

$$[\mathbf{J}_{b,1}]_{nm} = \int_\Omega \mathbf{u_g}_z z^2\phi_n\phi_m d\mathbf{x}, \tag{A.22}$$

$$[\mathbf{J}_{b,2}]_{nm} = 0, \tag{A.23}$$

$$[\mathbf{J}_{t,1}]_{nm} = \int_\Omega -yz\mathbf{u_g}_x + xz\mathbf{u_g}_y\phi_n\phi_m d\mathbf{x}, \tag{A.24}$$

$$[\mathbf{J}_{t,2}]_{nm} = \int_\Omega -xz^2\mathbf{u_g}_x - yz^2\mathbf{u_g}_y\phi_n\phi_m d\mathbf{x}, \tag{A.25}$$

$$[\mathbf{J}_{tb,1,1}]_{nm} = \int_\Omega \mathbf{u_g}_y z^3\phi_n\phi_m d\mathbf{x}. \tag{A.26}$$

We concatenate the solutions of each order as one new time-dependent variable

$$\boldsymbol{\zeta}^{\text{all}} = [\boldsymbol{\zeta}_0, \boldsymbol{\zeta}_{0,1}, \boldsymbol{\zeta}_{1,0}, \boldsymbol{\zeta}_{0,2}, \boldsymbol{\zeta}_{1,1}, \boldsymbol{\zeta}_{2,0}]^T \in \mathbb{R}^{6N_{eig},1},$$

and denote one new matrix and one vector

$$\boldsymbol{C}^{\text{all}} = \begin{bmatrix} \mathbf{L} & \mathbf{0} & \mathbf{0} & \mathbf{0} & \mathbf{0} & \mathbf{0} \\ \mathbf{C}_{b,1} & \mathbf{L} & \mathbf{0} & \mathbf{0} & \mathbf{0} & \mathbf{0} \\ \mathbf{C}_{t,1} & \mathbf{0} & \mathbf{L} & \mathbf{0} & \mathbf{0} & \mathbf{0} \\ \mathbf{C}_{b,2} & \mathbf{C}_{b,1} & \mathbf{0} & \mathbf{L} & \mathbf{0} & \mathbf{0} \\ \mathbf{C}_{t,2} & \mathbf{0} & \mathbf{C}_{t,1} & \mathbf{0} & \mathbf{L} & \mathbf{0} \\ \mathbf{C}_{tb,1,1} & \mathbf{C}_{t,1} & \mathbf{C}_{b,1} & \mathbf{0} & \mathbf{0} & \mathbf{L} \end{bmatrix} \tag{A.27}$$

$$\boldsymbol{J}_{vec}^{\text{all}} = \begin{bmatrix} \mathbf{J}_0 \\ \mathbf{J}_{b,1} \\ \mathbf{J}_{t,1} \\ \mathbf{J}_{b,2} \\ \mathbf{J}_{t,2} \\ \mathbf{J}_{tb,1,1} \end{bmatrix} \cdot \mathbf{1}_{N_{eig},1}. \tag{A.28}$$

The solution $\boldsymbol{\zeta}^{\text{all}}$ can be calculated by solving the following system of ODEs

$$\frac{d\boldsymbol{\zeta}^{\text{all}}}{dt} = -\boldsymbol{C}^{\text{all}}\boldsymbol{\zeta}^{\text{all}} - f(t)\boldsymbol{J}_{vec}^{\text{all}}. \tag{A.29}$$

and it can be expressed as

$$\boldsymbol{\zeta}^{\text{all}}(t) = -\int_0^t f(s)e^{-(t-s)\boldsymbol{C}^{\text{all}}}\boldsymbol{J}_{vec}^{\text{all}}ds. \tag{A.30}$$

The HADC is computed by

$$\text{HADC}^i = \frac{-\mathcal{D}^i}{|\Omega_i|\int_0^{TE} F(t)^2 dt}\int_{\partial\Omega_i}\int_0^{TE} F(t)\int_0^t f(s)e^{-(t-s)\boldsymbol{C}^{\text{all}}}\boldsymbol{J}_{vec}^{\text{all}}dsdt\left(\mathbf{u}_{\mathbf{g}}\cdot\boldsymbol{n}(\mathbf{r})\right)ds_{\mathbf{r}}. \tag{A.31}$$

Compared to the original HADC model, this alternative form needs to compute a double integral on $f(s)\cdot F(t)$ instead of $F(s)\cdot F(t)$, which requires less finer time steps to maintain a good accuracy.

Similarly, for the asymptotic expansion of transformed Bloch-Torrey PDE, we have

$$\frac{d\mathbf{T}_0}{dt} = -\boldsymbol{L}\mathbf{T}_0 - f(t)\mathbf{J}_0\mathbf{T}_0, \tag{A.32}$$

$$\frac{d\mathbf{T}_{0,1}}{dt} = -\left(\boldsymbol{L} + f(t)\mathbf{J}_0\right)\mathbf{T}_{0,1} - \left(\mathbf{C}_{b,1} + \mathbf{Q}_{b,1} + f(t)\mathbf{J}_{b,1}\right)\mathbf{T}_0, \tag{A.33}$$

$$\frac{d\mathbf{T}_{1,0}}{dt} = -\left(\boldsymbol{L} + f(t)\mathbf{J}_0\right)\mathbf{T}_{1,0} - \left(\mathbf{C}_{t,1} + \mathbf{Q}_{t,1} + f(t)\mathbf{J}_{t,1}\right)\mathbf{T}_0, \tag{A.34}$$

$$\frac{d\mathbf{T}_{0,2}}{dt} = -\left(\boldsymbol{L} + f(t)\mathbf{J}_0\right)\mathbf{T}_{0,2} - \left(\mathbf{C}_{b,1} + \mathbf{Q}_{b,1} + f(t)\mathbf{J}_{b,1}\right)\mathbf{T}_{0,1} - \left(\mathbf{C}_{b,2} + \mathbf{Q}_{b,2} + f(t)\mathbf{J}_{b,2}\right)\mathbf{T}_0, \tag{A.35}$$

$$\frac{d\mathbf{T}_{2,0}}{dt} = -\left(\boldsymbol{L} + f(t)\mathbf{J}_0\right)\mathbf{T}_{2,0} - \left(\mathbf{C}_{t,1} + \mathbf{Q}_{t,1} + f(t)\mathbf{J}_{t,1}\right)\mathbf{T}_{1,0} - \left(\mathbf{C}_{t,2} + \mathbf{Q}_{t,2} + f(t)\mathbf{J}_{t,2}\right)\mathbf{T}_0, \tag{A.36}$$

$$\begin{aligned}\frac{d\mathbf{T}_{1,1}}{dt} = &-\left(\boldsymbol{L} + f(t)\mathbf{J}_0\right)\mathbf{T}_{1,1} - \left(\mathbf{C}_{tb,1} + \mathbf{Q}_{tb,1} + f(t)\mathbf{J}_{tb,1,1}\right)\mathbf{T}_0 \\ &- \left(\mathbf{C}_{b,1} + \mathbf{Q}_{b,1} + f(t)\mathbf{J}_{b,1}\right)\mathbf{T}_{1,0} - \left(\mathbf{C}_{t,1} + \mathbf{Q}_{t,1} + f(t)\mathbf{J}_{t,1}\right)\mathbf{T}_{0,1},\end{aligned} \tag{A.37}$$

where the correction matrices for the flux term are

$$\left[\mathbf{Q}_{b,1}\right]_{nm} = -4\kappa^{ij}\int_{\partial\Omega} z\boldsymbol{n}_{\boldsymbol{x}}{}^i\boldsymbol{n}_{\boldsymbol{z}}{}^i\phi_n\phi_m ds_{\mathbf{x}}, \tag{A.38}$$

$$\left[\mathbf{Q}_{b,2}\right]_{nm} = 4\kappa^{ij}\int_{\partial\Omega} z^2\boldsymbol{n}_{\boldsymbol{x}}{}^i\boldsymbol{n}_{\boldsymbol{x}}{}^i\phi_n\phi_m ds_{\mathbf{x}}, \tag{A.39}$$

$$\left[\mathbf{Q}_{t,1}\right]_{nm} = 2\kappa^{ij}\int_{\partial\Omega} (y\boldsymbol{n}_{\boldsymbol{x}}{}^i\boldsymbol{n}_{\boldsymbol{z}}{}^i - x\boldsymbol{n}_{\boldsymbol{y}}{}^i\boldsymbol{n}_{\boldsymbol{z}}{}^i)\phi_n\phi_m ds_{\mathbf{x}}, \tag{A.40}$$

$$\left[\mathbf{Q}_{t,2}\right]_{nm} = \kappa^{ij}\int_{\partial\Omega} (y^2\boldsymbol{n}_{\boldsymbol{x}}{}^i\boldsymbol{n}_{\boldsymbol{x}}{}^i - 2xy\boldsymbol{n}_{\boldsymbol{x}}{}^i\boldsymbol{n}_{\boldsymbol{y}}{}^i + x^2\boldsymbol{n}_{\boldsymbol{y}}{}^i\boldsymbol{n}_{\boldsymbol{y}}{}^i)\phi_n\phi_m ds_{\mathbf{x}}, \tag{A.41}$$

$$\left[\mathbf{Q}_{tb,1,1}\right]_{nm} = 4\kappa^{ij}\int_{\partial\Omega} (-yz\boldsymbol{n}_{\boldsymbol{x}}{}^i\boldsymbol{n}_{\boldsymbol{x}}{}^i + xz\boldsymbol{n}_{\boldsymbol{x}}{}^i\boldsymbol{n}_{\boldsymbol{y}}{}^i)\phi_n\phi_m ds_{\mathbf{x}}. \tag{A.42}$$

Denoted the combining time-dependent variable as

$$\boldsymbol{T}^{\text{all}} = \left[\mathbf{T}_0, \mathbf{T}_{0,1}, \mathbf{T}_{1,0}, \mathbf{T}_{0,2}, \mathbf{T}_{1,1}, \mathbf{T}_{2,0}\right]^T \in \mathbb{R}^{6N_{eig},1},$$

and two new matrices

$$\boldsymbol{Q}^{\text{all}} = \begin{bmatrix} \mathbf{0} & \mathbf{0} & \mathbf{0} & \mathbf{0} & \mathbf{0} & \mathbf{0} \\ \mathbf{Q}_{b,1} & \mathbf{0} & \mathbf{0} & \mathbf{0} & \mathbf{0} & \mathbf{0} \\ \mathbf{Q}_{t,1} & \mathbf{0} & \mathbf{0} & \mathbf{0} & \mathbf{0} & \mathbf{0} \\ \mathbf{Q}_{b,2} & \mathbf{Q}_{b,1} & \mathbf{0} & \mathbf{0} & \mathbf{0} & \mathbf{0} \\ \mathbf{Q}_{t,2} & \mathbf{0} & \mathbf{Q}_{t,1} & \mathbf{0} & \mathbf{0} & \mathbf{0} \\ \mathbf{Q}_{tb,1,1} & \mathbf{Q}_{t,1} & \mathbf{Q}_{b,1} & \mathbf{0} & \mathbf{0} & \mathbf{0} \end{bmatrix}, \tag{A.43}$$

$$\boldsymbol{J}^{\text{all}} = \begin{bmatrix} \mathbf{J}_0 & \mathbf{0} & \mathbf{0} & \mathbf{0} & \mathbf{0} & \mathbf{0} \\ \mathbf{J}_{b,1} & \mathbf{J}_0 & \mathbf{0} & \mathbf{0} & \mathbf{0} & \mathbf{0} \\ \mathbf{J}_{t,1} & \mathbf{0} & \mathbf{J}_0 & \mathbf{0} & \mathbf{0} & \mathbf{0} \\ \mathbf{J}_{b,2} & \mathbf{J}_{b,1} & \mathbf{0} & \mathbf{J}_0 & \mathbf{0} & \mathbf{0} \\ \mathbf{J}_{t,2} & \mathbf{0} & \mathbf{J}_{t,1} & \mathbf{0} & \mathbf{J}_0 & \mathbf{0} \\ \mathbf{J}_{tb,1,1} & \mathbf{J}_{t,1} & \mathbf{J}_{b,1} & \mathbf{0} & \mathbf{0} & \mathbf{J}_0 \end{bmatrix}. \tag{A.44}$$

We obtain a new system of ODEs

$$\frac{d\boldsymbol{T}^{\text{all}}}{dt} = -\left(\boldsymbol{C}^{\text{all}} + \imath\gamma\|\mathbf{g}\|f(t)\boldsymbol{J}^{\text{all}} + \boldsymbol{Q}^{\text{all}}\right)\boldsymbol{T}^{\text{all}}. \tag{A.45}$$

At echo time, we have

$$\boldsymbol{T}^{\text{all}}(T_E) = e^{-\delta\left(\boldsymbol{C}^{\text{all}} - \imath\gamma\|\mathbf{g}\|\boldsymbol{J}^{\text{all}} + \boldsymbol{Q}^{\text{all}}\right)} \cdot e^{-(\Delta-\delta)\left(\boldsymbol{C}^{\text{all}} + \boldsymbol{Q}^{\text{all}}\right)} \cdot e^{-\delta\left(\boldsymbol{C}^{\text{all}} + \imath\gamma\|\mathbf{g}\|\boldsymbol{J}^{\text{all}} + \boldsymbol{Q}^{\text{all}}\right)} \cdot \boldsymbol{v}, \tag{A.46}$$

where $\boldsymbol{v}$ is a vector of size $6N_{eig}$, with all entries being zero except for the first item, which is ρ.

Appendix B

Appendix of Chapter 4

B.1 Numerical implementation of the first and second-order derivatives of signals

The computation of the first and second-order derivatives involves the integral of matrix exponentials. To be able to calculate them efficiently, we construct an upper triangular matrix, denoted as $\boldsymbol{C}$:

$$\boldsymbol{C} = \begin{bmatrix} -\delta(\boldsymbol{L} + \imath q \boldsymbol{W}) & -\imath\delta\boldsymbol{W} \\ 0_{N_{eig},N_{eig}} & -\delta(\boldsymbol{L} + \imath q \boldsymbol{W}) \end{bmatrix}, \tag{B.1}$$

where N_{eig} is the number of eigens. The exponential of $\boldsymbol{C}$ is expressed as[236]

$$e^{\boldsymbol{C}} = \begin{bmatrix} e^{-\delta(\boldsymbol{L}+\imath q\boldsymbol{W})} & \int_0^1 e^{-\alpha\delta(\boldsymbol{L}+\imath q\boldsymbol{W})}(-\imath\delta\boldsymbol{W})e^{-(1-\alpha)\delta(\boldsymbol{L}+\imath q\boldsymbol{W})}d\alpha \\ 0_{N_{eig},N_{eig}} & e^{-\delta(\boldsymbol{L}+\imath q\boldsymbol{W})} \end{bmatrix}. \tag{B.2}$$

Define two vectors:

$$\mathbf{v}_1 = [I_{N_{eig},N_{eig}}, 0_{N_{eig},N_{eig}}]^T \in \mathbb{R}^{2N_{eig},N_{eig}}, \tag{B.3}$$

$$\mathbf{v}_2 = [0_{N_{eig},N_{eig}}, I_{N_{eig},N_{eig}}]^T \in \mathbb{R}^{2N_{eig},N_{eig}}. \tag{B.4}$$

We have

$$\frac{\partial \boldsymbol{G}}{\partial q} = e^{-0.5(\Delta-\delta)\boldsymbol{L}} \left(\mathbf{v}_1^T \cdot e^{\boldsymbol{C}} \cdot \mathbf{v}_2\right). \tag{B.5}$$

Thus, by construction, we can calculate the first-order derivative by the action of the matrix exponential on one vector without explicitly computing the integral, using 'expmv'[126].

Analogously, to compute the second-order derivative, we construct a new matrix $\boldsymbol{D}$:

$$\boldsymbol{D} = \begin{bmatrix} \boldsymbol{C} & \begin{bmatrix} 0_{N_{eig},N_{eig}} & 0_{N_{eig},N_{eig}} \\ 0_{N_{eig},N_{eig}} & -\imath\delta\boldsymbol{W} \end{bmatrix} \\ 0_{2N_{eig},2N_{eig}} & \begin{bmatrix} 0_{N_{eig},N_{eig}} & 0_{N_{eig},N_{eig}} \\ 0_{N_{eig},N_{eig}} & -\delta(\boldsymbol{L} + \imath q \boldsymbol{W}) \end{bmatrix} \end{bmatrix}. \tag{B.6}$$

The second-order derivative is expressed as

$$\frac{\partial^2 \boldsymbol{G}}{\partial q^2} = 2e^{-0.5(\Delta-\delta)\boldsymbol{L}} \left(\mathbf{v}_3^T \cdot e^{\boldsymbol{D}} \cdot \mathbf{v}_4\right), \tag{B.7}$$

where

$$\mathbf{v}_3 = [I_{N_{eig},N_{eig}}, 0_{N_{eig},N_{eig}}, 0_{N_{eig},N_{eig}}, 0_{N_{eig},N_{eig}}]^T \in \mathbb{R}^{4N_{eig},N_{eig}}, \tag{B.8}$$

$$\mathbf{v}_4 = [0_{N_{eig},N_{eig}}, 0_{N_{eig},N_{eig}}, 0_{N_{eig},N_{eig}}, I_{N_{eig},N_{eig}}]^T \in \mathbb{R}^{4N_{eig},N_{eig}}. \tag{B.9}$$

Therefore, the expressions of a,b and c are

$$a = \int_0^{\pi}\int_0^{2\pi} \Re\left(T_{1,N_{eig}}^T e^{-\delta(\boldsymbol{L}-\imath q\boldsymbol{W})} e^{-(\Delta-\delta)\boldsymbol{L}} \left(\mathbf{v}_1^T e^{\boldsymbol{C}} \mathbf{v}_2\right) T_{1,N_{eig}}\right) d\theta d\phi, \tag{B.10}$$

$$b = \int_0^{\pi}\int_0^{2\pi} \Re\left(T_{1,N_{eig}}^T \left(\mathbf{v}_2^T (e^{\boldsymbol{C}})^* \mathbf{v}_1\right) e^{-(\Delta-\delta)\boldsymbol{L}} \left(\mathbf{v}_1^T e^{\boldsymbol{C}} \mathbf{v}_2\right) T_{1,N_{eig}}\right) d\theta d\phi, \tag{B.11}$$

$$c = \int_0^{\pi}\int_0^{2\pi} 2\Re(T_{1,N_{eig}}^T e^{-\delta(\boldsymbol{L}-\imath q\boldsymbol{W})} e^{-(\Delta-\delta)\boldsymbol{L}} \left(\mathbf{v}_3^T e^{\boldsymbol{D}} \mathbf{v}_4\right) T_{1,N_{eig}}) d\theta d\phi. \tag{B.12}$$

The inflection point is

$$\frac{2a}{q} + b + c = 0. \tag{B.13}$$

B.2 MLPs training

In the thesis of Fang[3], he proposed to using MLPs to learn the mappings from IP-derived biomarkers plus ADC to the microstructure parameters of interest, f_{soma} $\overline{R}_{\text{soma}}$ and f_{free}.

Consider a set of tuples that is extracted from the Synthetic voxels set, $\mathcal{T} = \{(\boldsymbol{X}_i, \boldsymbol{Y}_i), i \in \{1, \ldots, N_{\text{sample}}\}\}$ where N_{sample} (= 1.45 million for Synthetic voxels set) is the number of samples.

Refer to a tuple $(\boldsymbol{X}, \boldsymbol{Y})$ as a data point. The input of an IP-derived biomarker-based MLP is denoted by $\boldsymbol{X}_1$, which is the four IP-derived biomarkers x_0, c_0, c_1 and y_0 arising from an artificial brain voxel, plus the ADC. The input of a signal-based MLP is denoted by $\boldsymbol{X}_2$, which is the 64 dierction-averaged signals. The desired output (f_{soma}, $\overline{R}_{\text{soma}}$ or f_{free}) is denoted by $\boldsymbol{Y}$. To reduce the learning difficulty, two individual MLPs are trained, for the volume fractions and the volume-averaged soma radius, instead of combining them as one. The four MLPs are

1. $\boldsymbol{X}_1 \in \mathbb{R}^5$ is the four IP-derived biomarkers plus ADC with Δ being 19 or $49\,ms$, $\boldsymbol{Y}_1 = [f_{\text{soma}}, f_{\text{neurite}}, f_{\text{free}}]^T \in [0,1]^3$ represents the volume fractions, and the sum (the L^1-norm of output $\|\boldsymbol{Y}\|_1$) should be one;
2. $\boldsymbol{X}_1 \in \mathbb{R}^5$ is same as above, $\boldsymbol{Y}_2 = \overline{R}_{\text{soma}}$ represents the volume averaged soma radius.
3. $\boldsymbol{X}_2 \in [0,1]^{64}$ is the 64 direction-averaged signals linearly spaced between 0 and $290\,\text{mT/m}$, with Δ being 19 or $49\,ms$, $\boldsymbol{Y}_1 = [f_{\text{soma}}, f_{\text{neurite}}, f_{\text{free}}]^T \in [0,1]^3$ represents the volume fractions, and the sum (the L^1-norm of output $\|\boldsymbol{Y}\|_1$) should be one;
4. $\boldsymbol{X}_2 \in [0,1]^{64}$ is same as above, $\boldsymbol{Y}_2 = \overline{R}_{\text{soma}}$ represents the volume averaged soma radius.

It is worth noting that the measurements at two diffusion times are analyzed separately. According to[237], combining diverse input data or incorporating multi-modal data can enhance the robustness of the estimation.

We randomly select one million samples from the Synthetic voxels set to form the the training set $\mathcal{T}_{\text{train}}$; the rest (0.45 million samples) makes up the test set $\mathcal{T}_{\text{test}}$ which is held out and not used for model training. The test set allows us to assess the generalization of a trained MLP[238].

An MLP is a nonlinear function h parameterized by its weights $\boldsymbol{\theta}$[238]. The model training is to find optimal weights $\boldsymbol{\theta}^*$ that minimize the loss function defined by the distance between the MLP's output and the desired output

$$\boldsymbol{\theta}^* = \arg\min_{\boldsymbol{\theta}} \frac{1}{\#\mathcal{T}_{\text{train}}} \sum_{i=1}^{\#\mathcal{T}_{\text{train}}} \|\boldsymbol{Y}_i - h(\boldsymbol{X}_i; \boldsymbol{\theta})\|_2^2. \tag{B.14}$$

Here, the mean squared error (MSE) is chosen as the loss function. The minimization is possible if an underlying function ζ mapping $\boldsymbol{X}_i$ to $\boldsymbol{Y}_i$ exists. Once the optimization converged, the trained MLPs could be a good approximation of the underlying function, i.e., $h(\cdot; \boldsymbol{\theta}^*) \simeq \zeta$ in the sense of minimizing L^2-norm in the training set.

The function ζ varies with the choice of the microstructure parameters of interest, and the MR physics determines its existence. One must be careful about the initial normalization, activation

function, initial weights, and optimization algorithm to reach the convergence[239]. Here, the Gaussian error linear unit (GELU)[240] is employed, a ReLU-like activation function that incorporates the properties of stochastic regularizers such as dropout[241]. The weights $\boldsymbol{\theta}$ are initialized using Kaiming initialization[242] because of the ReLU-like activation functions. The optimization is performed with a variant of the Adam optimizer that has a long-term memory of past gradients to enhance the convergence[243, 244]. The initial learning rate is 0.01, the batch size is 10,000, and the maximum number of epochs is 500. The two parameters (betas) of the Adam optimizer for computing running averages of gradient and its square are 0.9 and 0.999.

The architecture of an artificial MLP can also significantly affect its performance. Finding a suitable network architecture for brain microstructure estimation is a subject worth investigating in the future. Here a four-layer MLP structure are chosen. Even though it is simple, it can effectively "learn" a wide range of mappings or functions if there are enough nodes[245]. For MLPs using IP-derived biomarkers plus ADC as inputs, the selected size of each layer is set to $(5, 30, 30, 3)$ for the volume fractions estimation and $(5, 30, 30, 1)$ for the effective soma radius estimation. For MLPs using signals as inputs, the selected size of each layer is set to $(64, 128, 64, 3)$ for the volume fractions estimation and $(64, 128, 64, 1)$ for the effective soma radius estimation. For the volume fractions estimation MLP, to guarantee the outputs are all positive and sum to unity, a softmax function[246] is used as the output layer. The implementation and training of MLPs are performed with PyTorch[247].

In total, eight MLPs (2 kinds of inputs, 2 kinds of outputs, and 2 different sequences) are trained to find optimal hyper-parameters.

Bibliography

[1] Z. Yang, C. Fang, and J.-R. Li, "Incorporating interface permeability into the diffusion MRI signal representation while using impermeable Laplace eigenfunctions," *Phys. Med. Biol.*, vol. 68, no. 17, p. 175 036, Sep. 2023.

[2] Z. Yang, I. Mekkaoui, J. Hesthaven, and J.-R. Li, "Asymptotic models of the diffusion MRI signal accounting for geometrical deformations," *MathematicS In Action*, vol. 12, no. 1, pp. 65–85, Sep. 2023.

[3] C. Fang, "Neuron modeling, Bloch-Torrey equation, and their application to brain microstructure estimation using diffusion MRI," Ph.D. dissertation, 2023.

[4] C. Fang, Z. Yang, D. Wassermann, and J.-R. Li, "A simulation-driven supervised learning framework to estimate brain microstructure using diffusion MRI," *Medical Image Analysis*, vol. 90, p. 102 979, Dec. 2023.

[5] C. Fang, V.-D. Nguyen, D. Wassermann, and J.-R. Li, "Diffusion MRI simulation of realistic neurons with SpinDoctor and the Neuron Module," *NeuroImage*, vol. 222, p. 117 198, Nov. 2020.

[6] R. Damadian, "Tumor Detection by Nuclear Magnetic Resonance," *Science*, vol. 171, no. 3976, pp. 1151–1153, Mar. 1971.

[7] W. Oldendorf and W. Oldendorf, "Advantages and Disadvantages of MRI," in *Basics of Magnetic Resonance Imaging*. Boston, MA: Springer US, 1988, pp. 125–138.

[8] B. M. Dale, M. A. Brown, and R. C. Semelka, *MRI Basic Principles and Applications*, 1st ed. Wiley, Oct. 2015.

[9] P. A. Bottomley, "NMR imaging techniques and applications: A review," *Review of Scientific Instruments*, vol. 53, no. 9, pp. 1319–1337, Sep. 1982.

[10] A. D. A. Maidment, "An Introduction to MRI for Medical Physicists and Engineers. Anthony-Wolbarst and NathanYanasak, Authors. Medical Physics Publishing, Madison, WI, 2019. Hardcover 318pp. Price: $120.00. ISBN: 9781930524200.," *Med. Phys.*, vol. 48, no. 1, pp. 535–535, Jan. 2021.

[11] M. H. Levitt, *Spin Dynamics: Basics of Nuclear Magnetic Resonance*. John Wiley & Sons, 2013.

[12] C. J. Lote, "The body fluids," in *Principles of Renal Physiology*. Dordrecht: Springer Netherlands, 1994, pp. 1–20.

[13] H. Mitchell, T. Hamilton, F. Steggerda, and H. Bean, "THE CHEMICAL COMPOSITION OF THE ADULT HUMAN BODY AND ITS BEARING ON THE BIOCHEMISTRY OF GROWTH," *Journal of Biological Chemistry*, vol. 158, no. 3, pp. 625–637, May 1945.

[14] M. H. Levitt, *Spin Dynamics: Basics of Nuclear Magnetic Resonance*, 2nd ed. Chichester, England ; Hoboken, NJ: John Wiley & Sons, 2008.

[15] L. C. Balling and F. M. Pipkin, "Gyromagnetic Ratios of Hydrogen, Tritium, Free Electrons, and Rb 85," *Phys. Rev.*, vol. 139, no. 1A, A19–A26, Jul. 1965.

[16] P. T. Callaghan, *Principles of Nuclear Magnetic Resonance Microscopy* (Oxford Science Publications), Repr. Oxford: Clarendon Press, 2011.

[17] R. Brown, E. Haacke, Y. Cheng, M. Thompson, and R. Venkatesan, *Magnetic Resonance Imaging: Physical Principles and Sequence Design*. Wiley, 2014.

[18] H. Johansen-Berg, Ed., *Diffusion MRI: From Quantitative Measurement to in-Vivo Neuroanatomy*. Amsterdam: Academic Pr, 2009.

[19] F. Bloch, "Nuclear induction," *Phys. Rev.*, vol. 70, no. 7-8, pp. 460–474, Oct. 1946.

[20] H. Johansen-Berg and T. E. Behrens, *Diffusion MRI: From Quantitative Measurement to in Vivo Neuroanatomy*. Elsevier Science, 2013.

[21] E. L. Hahn, "Spin echoes," *Phys. Rev.*, vol. 80, no. 4, pp. 580–594, Nov. 1950.

[22] F. Liu, M. Hernandez-Cabronero, V. Sanchez, M. Marcellin, and A. Bilgin, "The Current Role of Image Compression Standards in Medical Imaging," *Information*, vol. 8, no. 4, p. 131, Oct. 2017.

[23] I. Mekkaoui, "Analyse numérique des équations de Bloch-Torrey," Ph.D. dissertation, 2018.

[24] R Mezrich, "A perspective on K-space.," *Radiology*, vol. 195, no. 2, pp. 297–315, May 1995.

[25] R. Brown, "XXVII. *A brief account of microscopical observations made in the months of June, July and August* 1827, *on the particles contained in the pollen of plants; and on the general existence of active molecules in organic and inorganic bodies*," *The Philosophical Magazine*, vol. 4, no. 21, pp. 161–173, Sep. 1828.

[26] A. Einstein, "Über die von der molekularkinetischen Theorie der Wärme geforderte Bewegung von in ruhenden Flüssigkeiten suspendierten Teilchen," *Ann. Phys.*, vol. 322, no. 8, pp. 549–560, 1905.

[27] D. Romascano, M. Barakovic, J. Rafael-Patino, T. B. Dyrby, J.-P. Thiran, and A. Daducci, "ActiveAx $_{\text{ADD}}$: Toward non-parametric and orientationally invariant axon diameter distribution mapping using PGSE," *Magn Reson Med*, vol. 83, no. 6, pp. 2322–2330, Jun. 2020.

[28] M. Palombo *et al.*, "SANDI: A compartment-based model for non-invasive apparent soma and neurite imaging by diffusion MRI," *NeuroImage*, vol. 215, p. 116 835, Jul. 2020.

[29] H. C. Torrey, "Bloch Equations with Diffusion Terms," *Phys. Rev.*, vol. 104, no. 3, pp. 563–565, Nov. 1956.

[30] S. Herculano-Houzel, "The remarkable, yet not extraordinary, human brain as a scaled-up primate brain and its associated cost," *Proceedings of the National Academy of Sciences*, vol. 109, no. supplement_1, pp. 10 661–10 668, 2012.

[31] D. Debanne, E. Campanac, A. Bialowas, E. Carlier, and G. Alcaraz, "Axon physiology," *Physiological reviews*, vol. 91, no. 2, pp. 555–602, 2011.

[32] S. G. Waxman, "Determinants of conduction velocity in myelinated nerve fibers," *Muscle Nerve*, vol. 3, no. 2, pp. 141–150, 1980.

[33] B. S. Brown, *Biological Membranes*. London: Biochemical Society, 1996.

[34] W. A. Banks, "From blood–brain barrier to blood–brain interface: New opportunities for CNS drug delivery," *Nat Rev Drug Discov*, vol. 15, no. 4, pp. 275–292, Apr. 2016.

[35] A. L. Hodgkin and A. F. Huxley, "A quantitative description of membrane current and its application to conduction and excitation in nerve," *The Journal of Physiology*, vol. 117, no. 4, pp. 500–544, Aug. 1952.

[36] S. G. Waxman and J. M. Ritchie, "Molecular dissection of the myelinated axon," *Ann Neurol.*, vol. 33, no. 2, pp. 121–136, Feb. 1993.

[37] C.-L. Chin, F. W. Wehrli, S. N. Hwang, M. Takahashi, and D. B. Hackney, "Biexponential diffusion attenuation in the rat spinal cord: Computer simulations based on anatomic images of axonal architecture," *Magnetic Resonance in Medicine*, vol. 47, no. 3, pp. 455–460, 2002.

[38] E. A. Disalvo and S. A. Simon, *Permeability and Stability of Lipid Bilayers*, First edition. Boca Raton, FL: CRC Press, 2017.

[39] A. Peters, S. L. Palay, and H. deF Webster, *The Fine Structure of the Nervous System: Neurons and Their Supporting Cells*, 3rd ed. New York: Oxford University Press, 1991.

[40] "Medical gallery of Blausen Medical 2014," *Wiki J Med*, vol. 1, no. 2, 2014.

[41] C. Henley, *Foundations of Neuroscience* (Open Textbook Library). Michigan State University, 2021.

[42] W. G. Webb, "4 - neuronal function in the nervous system," in *Neurology for the Speech-Language Pathologist (Sixth Edition)*, W. G. Webb, Ed., Sixth Edition, Mosby, 2017, pp. 74–92.

[43] P. J. Basser, S. Pajevic, C. Pierpaoli, J. Duda, and A. Aldroubi, "In vivo fiber tractography using DT-MRI data," *Magnetic Resonance in Medicine*, vol. 44, no. 4, pp. 625–632, 2000.

[44] M. S. Chow, S. L. Wu, S. E. Webb, K. Gluskin, and D. Yew, "Functional magnetic resonance imaging and the brain: A brief review," *WJR*, vol. 9, no. 1, p. 5, 2017.

[45] P. Stys, S. Waxman, and B. Ransom, "Ionic mechanisms of anoxic injury in mammalian CNS white matter: Role of Na+ channels and Na(+)-Ca2+ exchanger," *J. Neurosci.*, vol. 12, no. 2, pp. 430–439, Feb. 1992.

[46] B. V. Zlokovic, "Neurovascular pathways to neurodegeneration in Alzheimer's disease and other disorders," *Nat Rev Neurosci*, vol. 12, no. 12, pp. 723–738, Dec. 2011.

[47] R. Kortekaas *et al.*, "Blood-brain barrier dysfunction in parkinsonian midbrain in vivo," *Ann Neurol.*, vol. 57, no. 2, pp. 176–179, Feb. 2005.

[48] M. J. Craner, J. Newcombe, J. A. Black, C. Hartle, M. L. Cuzner, and S. G. Waxman, "Molecular changes in neurons in multiple sclerosis: Altered axonal expression of Na_v 1.2 and Na_v 1.6 sodium channels and Na^+ /Ca^{2+} exchanger," *Proc. Natl. Acad. Sci. U.S.A.*, vol. 101, no. 21, pp. 8168–8173, May 2004.

[49] S. Minosse *et al.*, "Compartmental models for diffusion weighted MRI reveal widespread brain changes in HIV-infected patients," in *2021 43rd Annual International Conference of the IEEE Engineering in Medicine & Biology Society (EMBC)*, Mexico: IEEE, Nov. 2021, pp. 3834–3837.

[50] V.-D. Nguyen *et al.*, "Portable simulation framework for diffusion MRI," *Journal of Magnetic Resonance*, vol. 309, p. 106 611, Dec. 2019.

[51] V. D. Nguyen, "A finite elements method to solve the Bloch-Torrey equation applied to diffusion magnetic resonance imaging of biological tissues," Ph.D. dissertation, Ecole polytechnique, 2014, 1 vol. (117 p.)

[52] E. O. Stejskal and J. E. Tanner, "Spin diffusion measurements: Spin echoes in the presence of a time-dependent field gradient," *The Journal of Chemical Physics*, vol. 42, no. 1, pp. 288–292, 1965.

[53] P. T. Callaghan and J. Stepišnik, "Frequency-domain analysis of spin motion using modulated-gradient NMR," *Journal of Magnetic Resonance, Series A*, vol. 117, no. 1, pp. 118–122, Nov. 1995.

[54] M. D. Does, E. C. Parsons, and J. C. Gore, "Oscillating gradient measurements of water diffusion in normal and globally ischemic rat brain," *Magn. Reson. Med.*, vol. 49, no. 2, pp. 206–215, 2003.

[55] A. A. Khrapitchev and P. T. Callaghan, "Double PGSE NMR with stimulated echoes: Phase cycles for the selection of desired encoding," *Journal of Magnetic Resonance*, vol. 152, no. 2, pp. 259–268, 2001.

[56] S. Schiavi, "Homogenized and analytical models for the diffusion MRI signal," Ph.D. dissertation, 2017.

[57] D. L. Bihan, E Breton, D Lallemand, P Grenier, E Cabanis, and M Laval-Jeantet, "MR imaging of intravoxel incoherent motions: Application to diffusion and perfusion in neurologic disorders.," *Radiology*, vol. 161, no. 2, pp. 401–407, November 1, 1986, 1986.

[58] R. G. González, "Clinical MRI of acute ischemic stroke," *Journal of Magnetic Resonance Imaging*, vol. 36, no. 2, pp. 259–271, 2012.

[59] R. Bai, Z. Li, C. Sun, Y.-C. Hsu, H. Liang, and P. Basser, "Feasibility of filter-exchange imaging (FEXI) in measuring different exchange processes in human brain," *NeuroImage*, vol. 219, p. 117 039, 2020.

[60] C. A. Baron and C. Beaulieu, "Oscillating gradient spin-echo (OGSE) diffusion tensor imaging of the human brain," *Magnetic Resonance in Med*, vol. 72, no. 3, pp. 726–736, Sep. 2014.

[61] V Kenkre, "Simple solutions of the Torrey-Bloch equations in the NMR study of molecular diffusion," *Journal of Magnetic Resonance*, vol. 128, no. 1, pp. 62–69, Sep. 1997.

[62] J.-R. Li, H. T. Nguyen, D. Van Nguyen, H. Haddar, J. Coatléven, and D. Le Bihan, "Numerical study of a macroscopic finite pulse model of the diffusion MRI signal," *Journal of Magnetic Resonance*, vol. 248, no. 0, pp. 54–65, Nov. 2014.

[63] H. Haddar, J.-R. Li, and S. Schiavi, "Understanding the Time-Dependent Effective Diffusion Coefficient Measured by Diffusion MRI: The IntraCellular Case," *SIAM J. Appl. Math.*, vol. 78, no. 2, pp. 774–800, Jan. 2018.

[64] J. Veraart, E. Fieremans, and D. S. Novikov, "On the scaling behavior of water diffusion in human brain white matter," *NeuroImage*, vol. 185, pp. 379–387, Jan. 2019.

[65] J. Veraart, E. Fieremans, and D. S. Novikov, "Universal power-law scaling of water diffusion in human brain defines what we see with MRI," *arXiv preprint arXiv:1609.09145*, 2016. arXiv: 1609.09145.

[66] J. Veraart *et al.*, "Noninvasive quantification of axon radii using diffusion MRI," *eLife*, vol. 9, e49855, Feb. 2020.

[67] D. S. Tuch, "Q-ball imaging," *Magnetic Resonance in Medicine*, vol. 52, no. 6, pp. 1358–1372, 2004. eprint: https://onlinelibrary.wiley.com/doi/pdf/10.1002/mrm.20279.

[68] P. T. Callaghan, A. Coy, D. MacGowan, K. J. Packer, and F. O. Zelaya, "Diffraction-like effects in NMR diffusion studies of fluids in porous solids," *Nature*, vol. 351, no. 6326, pp. 467–469, Jun. 1991.

[69] JE Tanner and E. O. Stejskal, "Restricted self-diffusion of protons in colloidal systems by the pulsed-gradient, spin-echo method," *The Journal of Chemical Physics*, vol. 49, pp. 1768–1777, Aug. 1968.

[70] D. S. Grebenkov, "NMR survey of reflected Brownian motion," *Rev. Mod. Phys.*, vol. 79, no. 3, pp. 1077–1137, Aug. 2007.

[71] B. Robertson, "Spin-echo decay of spins diffusing in a bounded region," *Physical Review*, vol. 151, no. 1, p. 273, 1966.

[72] C. H. Neuman, "Spin echo of spins diffusing in a bounded medium," *The Journal of Chemical Physics*, vol. 60, no. 11, pp. 4508–4511, Jun. 1974.

[73] J. Karger, "Principles and application of self-diffusion measurements by nuclear magnetic resonance," *Adv Magn Reson*, vol. 12, pp. 1–89, 1988.

[74] J. Coatléven, H. Haddar, and J.-R. Li, "A Macroscopic Model Including Membrane Exchange for Diffusion MRI," *SIAM J. Appl. Math.*, vol. 74, no. 2, pp. 516–546, Jan. 2014. eprint: http://epubs.siam.org/doi/pdf/10.1137/130914255.

[75] P. A. Cook, Y. Bai, M. G. Hall, S. Nedjati-Gilani, K. K. Seunarine, and D. C. Alexander, "Camino: Diffusion MRI reconstruction and processing," 2005.

[76] G. T. Balls and L. R. Frank, "A simulation environment for diffusion weighted MR experiments in complex media," *Magn. Reson. Med.*, vol. 62, no. 3, pp. 771–778, 2009.

[77] D. S. Grebenkov, H. T. Nguyen, and J.-R. Li, "A fast random walk algorithm for computing diffusion-weighted NMR signals in multi-scale porous media: A feasibility study for a Menger sponge," *Microporous and Mesoporous Materials*, vol. 178, pp. 56–59, Sep. 2013.

[78] C.-H. Yeh, B. Schmitt, D. Le Bihan, J.-R. Li-Schlittgen, C.-P. Lin, and C. Poupon, "Diffusion Microscopist Simulator: A General Monte Carlo Simulation System for Diffusion Magnetic Resonance Imaging," *PLoS ONE*, vol. 8, no. 10, W. Zhan, Ed., e76626, Oct. 2013.

[79] K.-V. Nguyen, E. Hernández-Garzón, and J. Valette, "Efficient GPU-based Monte-Carlo simulation of diffusion in real astrocytes reconstructed from confocal microscopy," *Journal of Magnetic Resonance*, vol. 296, pp. 188–199, Nov. 2018.

[80] C. A. Waudby and J. Christodoulou, "GPU accelerated Monte Carlo simulation of pulsed-field gradient NMR experiments," *Journal of Magnetic Resonance*, vol. 211, no. 1, pp. 67–73, Jul. 2011.

[81] M. Hall and D. Alexander, "Convergence and Parameter Choice for Monte-Carlo Simulations of Diffusion MRI," *IEEE Trans. Med. Imaging*, vol. 28, no. 9, pp. 1354–1364, Sep. 2009.

[82] H. Hagslatt, B. Jonsson, M. Nyden, and O. Soderman, "Predictions of pulsed field gradient NMR echo-decays for molecules diffusing in various restrictive geometries. Simulations of diffusion propagators based on a finite element method," *Journal of Magnetic Resonance*, vol. 161, no. 2, pp. 138–147, Apr. 2003.

[83] N. Loren, H. Hagslatt, M. Nyden, and A.-M. Hermansson, "Water mobility in heterogeneous emulsions determined by a new combination of confocal laser scanning microscopy, image analysis, nuclear magnetic resonance diffusometry, and finite element method simulation," *The Journal of Chemical Physics*, vol. 122, no. 2, 024716, pp. –, 2005.

[84] B. F. Moroney, T. Stait-Gardner, B. Ghadirian, N. N. Yadav, and W. S. Price, "Numerical analysis of NMR diffusion measurements in the short gradient pulse limit," *Journal of Magnetic Resonance*, vol. 234, no. 0, pp. 165–175, Sep. 2013.

[85] J Xu, MD Does, and JC Gore, "Numerical study of water diffusion in biological tissues using an improved finite difference method," *Physics in medicine and biology*, vol. 52, no. 7, Apr. 2007.

[86] G. Russell, K. D. Harkins, T. W. Secomb, J.-P. Galons, and T. P. Trouard, "A finite difference method with periodic boundary conditions for simulations of diffusion-weighted magnetic resonance experiments in tissue," *Phys. Med. Biol.*, vol. 57, no. 4, N35–N46, Feb. 2012.

[87] J.-R. Li *et al.*, "SpinDoctor: A MATLAB toolbox for diffusion MRI simulation," *NeuroImage*, vol. 202, p. 116 120, Nov. 2019.

[88] P. T. Callaghan, "A simple matrix formalism for spin echo analysis of restricted diffusion under generalized gradient waveforms," *Journal of Magnetic Resonance*, vol. 129, no. 1, pp. 74–84, Nov. 1997.

[89] I. Drobnjak, H. Zhang, M. G. Hall, and D. C. Alexander, "The matrix formalism for generalised gradients with time-varying orientation in diffusion NMR," *Journal of Magnetic Resonance*, vol. 210, no. 1, pp. 151–157, May 2011.

[90] A. V. Barzykin, "Theory of spin echo in restricted geometries under a step-wise gradient pulse sequence," *Journal of Magnetic Resonance*, vol. 139, no. 2, pp. 342–353, 1999.

[91] J.-R. Li, T. N. Tran, and V.-D. Nguyen, "Practical computation of the diffusion MRI signal of realistic neurons based on Laplace eigenfunctions," *NMR in Biomedicine*, vol. 33, no. 10, e4353, Oct. 2020.

[92] S. D. Agdestein, T. N. Tran, and J.-R. Li, "Practical computation of the diffusion MRI signal based on Laplace eigenfunctions: Permeable interfaces," *NMR in Biomedicine*, vol. 35, no. 3, e4646, Nov. 2021.

[93] N. M. Naughton, C. G. Tennyson, and J. G. Georgiadis, "Lattice Boltzmann method for simulation of diffusion magnetic resonance imaging physics in multiphase tissue models," *Phys. Rev. E*, vol. 102, no. 4, p. 043 305, Oct. 2020.

[94] C. Fang, D. Wassermann, and J.-R. Li, "Fourier Representation of the Diffusion MRI Signal Using Layer Potentials," *SIAM J. Appl. Math.*, vol. 83, no. 1, pp. 99–121, Feb. 2023.

[95] D. V. Nguyen, J.-R. Li, D. Grebenkov, and D. Le Bihan, "A finite elements method to solve the Bloch–Torrey equation applied to diffusion magnetic resonance imaging," *Journal of Computational Physics*, vol. 263, no. 0, pp. 283–302, Apr. 2014.

[96] M. G. Larson and F. Bengzon, *The Finite Element Method: Theory, Implementation, and Applications*. Springer Science & Business Media, 2013, vol. 10.

[97] D. S. Grebenkov, "Laplacian eigenfunctions in NMR. I. A numerical tool," *Concepts Magn. Reson.*, vol. 32A, no. 4, pp. 277–301, Jul. 2008.

[98] H. Zhang, T. Schneider, C. A. Wheeler-Kingshott, and D. C. Alexander, "NODDI: Practical in vivo neurite orientation dispersion and density imaging of the human brain," *NeuroImage*, vol. 61, no. 4, pp. 1000–1016, Jul. 2012.

[99] D. C. Alexander *et al.*, "Orientationally invariant indices of axon diameter and density from diffusion MRI," *NeuroImage*, vol. 52, no. 4, pp. 1374–1389, Oct. 2010.

[100] I. O. Jelescu, A. de Skowronski, F. Geffroy, M. Palombo, and D. S. Novikov, "Neurite Exchange Imaging (NEXI): A minimal model of diffusion in gray matter with inter-compartment water exchange," *NeuroImage*, vol. 256, p. 119 277, Aug. 2022.

[101] M. Andersson *et al.*, "Axon morphology is modulated by the local environment and impacts the noninvasive investigation of its structure–function relationship," *Proc. Natl. Acad. Sci. U.S.A.*, vol. 117, no. 52, pp. 33 649–33 659, Dec. 2020.

[102] H. Zhang, P. L. Hubbard, G. J. Parker, and D. C. Alexander, "Axon diameter mapping in the presence of orientation dispersion with diffusion MRI," *NeuroImage*, vol. 56, no. 3, pp. 1301–1315, Jun. 2011.

[103] A. Szafer, J. Zhong, and J. C. Gore, "Theoretical Model for Water Diffusion in Tissues," *Magn. Reson. Med.*, vol. 33, no. 5, pp. 697–712, May 1995.

[104] D. Barazany, P. J. Basser, and Y. Assaf, "In vivo measurement of axon diameter distribution in the corpus callosum of rat brain," *Brain*, vol. 132, no. 5, pp. 1210–1220, May 2009.

[105] P. Vangelderen, D. Despres, P. Vanzijl, and C. Moonen, "Evaluation of Restricted Diffusion in Cylinders. Phosphocreatine in Rabbit Leg Muscle," *Journal of Magnetic Resonance, Series B*, vol. 103, no. 3, pp. 255–260, Mar. 1994.

[106] B. Balinov, B Jonsson, P. Linse, and O Soderman, "The NMR self-diffusion method applied to restricted diffusion. Simulation of echo attenuation from molecules in spheres and between planes," *Journal of Magnetic Resonance, Series A*, vol. 104, no. 1, pp. 17–25, 1993.

[107] I. Aslund, A. Nowacka, M. Nilsson, and D. Topgaard, "Filter-exchange PGSE NMR determination of cell membrane permeability," *Journal of Magnetic Resonance*, vol. 200, no. 2, pp. 291–295, 2009.

[108] M. Nilsson *et al.*, "Noninvasive mapping of water diffusional exchange in the human brain using filter-exchange imaging: Filtered-Exchange Imaging in the Human Brain," *Magn Reson Med*, vol. 69, no. 6, pp. 1572–1580, Jun. 2013.

[109] H. T. Nguyen, D. Grebenkov, D. Van Nguyen, C. Poupon, D. Le Bihan, and J.-R. Li, "Parameter estimation using macroscopic diffusion MRI signal models," *Phys. Med. Biol.*, vol. 60, no. 8, pp. 3389–3413, Apr. 2015.

[110] J. L. Olesen, L. Østergaard, N. Shemesh, and S. N. Jespersen, "Diffusion time dependence, power-law scaling, and exchange in gray matter," *NeuroImage*, vol. 251, p. 118 976, May 2022.

[111] N. Moutal and D. Grebenkov, "Diffusion Across Semi-permeable Barriers: Spectral Properties, Efficient Computation, and Applications," *J Sci Comput*, vol. 81, no. 3, pp. 1630–1654, Dec. 2019.

[112] G. L. Nedjati-Gilani *et al.*, "Machine learning based compartment models with permeability for white matter microstructure imaging," *NeuroImage*, vol. 150, pp. 119–135, Apr. 2017.

[113] D. S. Grebenkov, "A fast random walk algorithm for computing the pulsed-gradient spin-echo signal in multiscale porous media," *Journal of Magnetic Resonance*, vol. 208, no. 2, pp. 243–255, 2011.

[114] D. Grebenkov, "Efficient Monte Carlo Methods for Simulating Diffusion-Reaction Processes in Complex Systems," in *First-Passage Phenomena and Their Applications*. WORLD SCIENTIFIC, May 2014, pp. 571–595.

[115] L. Beltrachini, Z. A. Taylor, and A. F. Frangi, "A parametric finite element solution of the generalised Bloch–Torrey equation for arbitrary domains," *Journal of Magnetic Resonance*, vol. 259, pp. 126–134, Oct. 2015.

[116] E. Fieremans, D. S. Novikov, J. H. Jensen, and J. A. Helpern, "Monte Carlo study of a two-compartment exchange model of diffusion," *NMR in Biomedicine*, vol. 23, no. 7, pp. 711–724, 2010.

[117] I. Alemany, J. N. Rose, J. Garnier-Brun, A. D. Scott, and D. J. Doorly, "Random walk diffusion simulations in semi-permeable layered media with varying diffusivity," *Sci Rep*, vol. 12, no. 1, p. 10 759, Jun. 2022.

[118] H.-H. Lee, E. Fieremans, and D. S. Novikov, "Realistic Microstructure Simulator (RMS): Monte Carlo simulations of diffusion in three-dimensional cell segmentations of microscopy images," *Journal of Neuroscience Methods*, vol. 350, p. 109 018, Feb. 2021.

[119] H.-H. Lee, A. Papaioannou, D. S. Novikov, and E. Fieremans, "In vivo observation and biophysical interpretation of time-dependent diffusion in human cortical gray matter," *NeuroImage*, vol. 222, p. 117 054, Nov. 2020.

[120] D. V. Nguyen, J.-R. Li, D. Grebenkov, and D. Le Bihan, "A finite elements method to solve the Bloch-Torrey equation applied to diffusion magnetic resonance imaging," *Journal of Computational Physics*, vol. 263, no. 0, pp. 283–302, Apr. 2014.

[121] H. Si, "TetGen, a delaunay-based quality tetrahedral mesh generator," *ACM Trans. Math. Softw.*, vol. 41, no. 2, 11:1–11:36, Feb. 2015.

[122] D. S. Grebenkov, D. Van Nguyen, and J.-R. Li, "Exploring diffusion across permeable barriers at high gradients. I. Narrow pulse approximation," *Journal of Magnetic Resonance*, vol. 248, pp. 153–163, Nov. 2014.

[123] S. Y. Huang *et al.*, "Connectome 2.0: Developing the next-generation ultra-high gradient strength human MRI scanner for bridging studies of the micro-, meso- and macro-connectome," *NeuroImage*, p. 118 530, Aug. 2021.

[124] D. Coppersmith and S. Winograd, "Matrix multiplication via arithmetic progressions," *Journal of Symbolic Computation*, vol. 9, no. 3, pp. 251–280, 1990.

[125] J. Lee, V. Balakrishnan, C.-K. Koh, and D. Jiao, "From O(k2N) to O(N): A fast complex-valued eigenvalue solver for large-scale on-chip interconnect analysis," in *2009 IEEE MTT-S International Microwave Symposium Digest*, 2009, pp. 181–184.

[126] A. H. Al-Mohy and N. J. Higham, "Computing the action of the matrix exponential, with an application to exponential integrators," *SIAM Journal on Scientific Computing*, vol. 33, no. 2, pp. 488–511, 2011. eprint: `https://doi.org/10.1137/100788860`.

[127] E. M. Haacke and G. W. Lenz, "Improving MR image quality in the presence of motion by using rephasing gradients," *American journal of roentgenology*, vol. 148, no. 6, pp. 1251–1258, 1987.

[128] F. B. Laun, T. A. Kuder, W. Semmler, and B. Stieltjes, "Determination of the Defining Boundary in Nuclear Magnetic Resonance Diffusion Experiments," *Phys. Rev. Lett.*, vol. 107, no. 4, p. 048 102, Jul. 2011.

[129] F. B. Laun and T. A. Kuder, "Diffusion pore imaging with generalized temporal gradient profiles," *Magnetic Resonance Imaging*, vol. 31, no. 7, pp. 1236–1244, Sep. 2013.

[130] J. Haus and K. Kehr, "Diffusion in regular and disordered lattices," *Physics Reports*, vol. 150, no. 5-6, pp. 263–406, Jun. 1987.

[131] L. L. Latour, P. P. Mitra, R. L. Kleinberg, and C. H. Sotak, "Time-dependent diffusion coefficient of fluids in porous media as a probe of surface-to-volume ratio," *Journal of Magnetic Resonance, Series A*, vol. 101, no. 3, pp. 342–346, 1993.

[132] P. N. Sen, "Time-dependent diffusion coefficient as a probe of the permeability of the pore wall," *The Journal of Chemical Physics*, vol. 119, no. 18, pp. 9871–9876, Nov. 2003.

[133] F. Crick, "Diffusion in Embryogenesis," *Nature*, vol. 225, no. 5231, pp. 420–422, Jan. 1970.

[134] I. Mekkaoui, K. Moulin, P. Croisille, J. Pousin, and M. Viallon, "Quantifying the effect of tissue deformation on diffusion-weighted MRI: A mathematical model and an efficient simulation framework applied to cardiac diffusion imaging," *Phys. Med. Biol.*, vol. 61, no. 15, pp. 5662–5686, Aug. 2016.

[135] I. Mekkaoui, J. Pousin, J. Hesthaven, and J.-R. Li, "Apparent diffusion coefficient measured by diffusion MRI of moving and deforming domains," *Journal of Magnetic Resonance*, vol. 318, p. 106 809, Sep. 2020.

[136] Y. Assaf, T. Blumenfeld-Katzir, Y. Yovel, and P. J. Basser, "Axcaliber: A method for measuring axon diameter distribution from diffusion MRI," *Magn. Reson. Med.*, vol. 59, no. 6, pp. 1347–1354, Jun. 2008.

[137] L. M. Burcaw, E. Fieremans, and D. S. Novikov, "Mesoscopic structure of neuronal tracts from time-dependent diffusion," *NeuroImage*, vol. 114, pp. 18–37, Jul. 2015.

[138] E. Fieremans, J. H. Jensen, and J. A. Helpern, "White matter characterization with diffusional kurtosis imaging," *NeuroImage*, vol. 58, no. 1, pp. 177–188, 2011.

[139] E. Panagiotaki, T. Schneider, B. Siow, M. G. Hall, M. F. Lythgoe, and D. C. Alexander, "Compartment models of the diffusion MR signal in brain white matter: A taxonomy and comparison," *NeuroImage*, vol. 59, no. 3, pp. 2241–2254, Feb. 2012.

[140] S. N. Jespersen, C. D. Kroenke, L. Østergaard, J. J. Ackerman, and D. A. Yablonskiy, "Modeling dendrite density from magnetic resonance diffusion measurements," *NeuroImage*, vol. 34, no. 4, pp. 1473–1486, 2007.

[141] M. Palombo, C. Ligneul, and J. Valette, "Modeling diffusion of intracellular metabolites in the mouse brain up to very high diffusion-weighting: Diffusion in long fibers (almost) accounts for non-monoexponential attenuation," *Magnetic Resonance in Medicine*, vol. 77, no. 1, pp. 343–350, 2017.

[142] S. Minosse *et al.*, "Multishell diffusion MRI reveals whole-brain white matter changes in HIV," *Human Brain Mapping*, vol. 44, no. 15, pp. 5113–5124, Oct. 2023.

[143] M. D. Budde and J. A. Frank, "Neurite beading is sufficient to decrease the apparent diffusion coefficient after ischemic stroke," *Proc. Natl. Acad. Sci. U.S.A.*, vol. 107, no. 32, pp. 14 472–14 477, Aug. 2010.

[144] M. M. Greenberg, C. Leitao, J. Trogadis, and J. K. Stevens, "Irregular geometries in normal unmyelinated axons: A 3D serial EM analysis," *J Neurocytol*, vol. 19, no. 6, pp. 978–988, Dec. 1990.

[145] M. Nilsson, J. Lätt, F. Ståhlberg, D. Van Westen, and H. Hagslätt, "The importance of axonal undulation in diffusion MR measurements: A Monte Carlo simulation study: THE IMPORTANCE OF AXONAL UNDULATION IN DIFFUSION MR MEASUREMENTS," *NMR Biomed.*, vol. 25, no. 5, pp. 795–805, May 2012.

[146] M. D. Budde and J. Annese, "Quantification of anisotropy and fiber orientation in human brain histological sections," *Front. Integr. Neurosci.*, vol. 7, 2013.

[147] S. N. Jespersen *et al.*, "Neurite density from magnetic resonance diffusion measurements at ultrahigh field: Comparison with light microscopy and electron microscopy," *NeuroImage*, vol. 49, no. 1, pp. 205–216, Jan. 2010.

[148] K. Schilling, V. Janve, Y. Gao, I. Stepniewska, B. A. Landman, and A. W. Anderson, "Comparison of 3D orientation distribution functions measured with confocal microscopy and diffusion MRI," *NeuroImage*, vol. 129, pp. 185–197, 2016.

[149] H.-H. Lee, S. N. Jespersen, E. Fieremans, and D. S. Novikov, "The impact of realistic axonal shape on axon diameter estimation using diffusion MRI," *NeuroImage*, vol. 223, p. 117 228, Dec. 2020.

[150] J. P. Elie Bretin Imen Mekkaoui, "Assessment of the effect of tissue motion in diffusion MRI: Derivation of new apparent diffusion coefficient formula," *Inverse Problems and Imaging*, vol. 12, no. 1, pp. 125–152, 2018.

[151] H. Haddar, J.-R. Li, and S. Schiavi, "A Macroscopic Model for the Diffusion MRI Signal Accounting for Time-Dependent Diffusivity," *SIAM J. Appl. Math.*, vol. 76, no. 3, pp. 930–949, Jan. 2016.

[152] M. Pharr, W. Jakob, and G. Humphreys, *Physically Based Rendering: From Theory to Implementation*, Third edition. Cambridge, MA: Morgan Kaufmann Publishers/Elsevier, 2017.

[153] T. Rahman and J. Valdman, "Fast MATLAB assembly of FEM matrices in 2D and 3D: Nodal elements," *Applied Mathematics and Computation*, vol. 219, no. 13, pp. 7151–7158, 2013.

[154] F. Sepehrband, D. C. Alexander, K. A. Clark, N. D. Kurniawan, Z. Yang, and D. C. Reutens, "Parametric Probability Distribution Functions for Axon Diameters of Corpus Callosum," *Front. Neuroanat.*, vol. 10, p. 59, May 2016.

[155] D. Liewald, R. Miller, N. Logothetis, H.-J. Wagner, and A. Schüz, "Distribution of axon diameters in cortical white matter: An electron-microscopic study on three human brains and a macaque," *Biol Cybern*, vol. 108, no. 5, pp. 541–557, Oct. 2014.

[156] Q. Tian *et al.*, "Comprehensive diffusion MRI dataset for in vivo human brain microstructure mapping using 300 mT/m gradients," *Sci Data*, vol. 9, no. 1, pp. 1–11, Dec. 2022.

[157] M. Andersson, M. Pizzolato, H. M. Kjer, K. F. Skodborg, H. Lundell, and T. B. Dyrby, "Does powder averaging remove dispersion bias in diffusion MRI diameter estimates within real 3D axonal architectures?" *NeuroImage*, vol. 248, p. 118 718, Mar. 2022.

[158] E. Özarslan, C. Yolcu, M. Herberthson, H. Knutsson, and C.-F. Westin, "Influence of the Size and Curvedness of Neural Projections on the Orientationally Averaged Diffusion MR Signal," *Front. Phys.*, vol. 6, p. 17, Mar. 2018.

[159] G. A. Ascoli, D. E. Donohue, and M. Halavi, "NeuroMorpho.Org: A central resource for neuronal morphologies," *Journal of Neuroscience*, vol. 27, no. 35, pp. 9247–9251, 2007. eprint: `http://www.jneurosci.org/content/27/35/9247.full.pdf`.

[160] A. F. Howard *et al.*, "Estimating axial diffusivity in the NODDI model," *bioRxiv*, pp. 2020–10, 2022.

[161] K. K. Watson, T. K. Jones, and J. M. Allman, "Dendritic architecture of the von Economo neurons," *Neuroscience*, vol. 141, no. 3, pp. 1107–1112, 2006.

[162] L. Madisen *et al.*, "Transgenic mice for intersectional targeting of neural sensors and effectors with high specificity and performance," *Neuron*, vol. 85, no. 5, pp. 942–958, 2015.

[163] J. Berg *et al.*, "Human cortical expansion involves diversification and specialization of supragranular intratelencephalic-projecting neurons," *BioRxiv*, 2020.

[164] C. Koch and A. Jones, "Big science, team science, and open science for neuroscience," *Neuron*, vol. 92, no. 3, pp. 612–616, 2016.

[165] T. L. Hayes and D. A. Lewis, "Magnopyramidal neurons in the anterior motor speech region: Dendritic features and interhemispheric comparisons," *Archives of neurology*, vol. 53, no. 12, pp. 1277–1283, 1996.

[166] B. Jacobs, L. Driscoll, and M. Schall, "Life-span dendritic and spine changes in areas 10 and 18 of human cortex: A quantitative Golgi study," *Journal of comparative neurology*, vol. 386, no. 4, pp. 661–680, 1997.

[167] R. Benavides-Piccione, J. I. Arellano, and J. DeFelipe, "Catecholaminergic innervation of pyramidal neurons in the human temporal cortex," *Cerebral Cortex*, vol. 15, no. 10, pp. 1584–1591, 2005.

[168] B. Hrvoj-Mihic *et al.*, "Basal dendritic morphology of cortical pyramidal neurons in Williams syndrome: Prefrontal cortex and beyond," *Frontiers in neuroscience*, vol. 11, p. 419, 2017.

[169] C. Falcone *et al.*, "Cortical interlaminar astrocytes across the therian mammal radiation," *Journal of Comparative Neurology*, vol. 527, no. 10, pp. 1654–1674, 2019.

[170] R. Benavides-Piccione *et al.*, "Differential structure of hippocampal CA1 pyramidal neurons in the human and mouse," *Cerebral Cortex*, vol. 30, no. 2, pp. 730–752, 2020.

[171] C. Falcone *et al.*, "Cortical interlaminar astrocytes are generated prenatally, mature postnatally, and express unique markers in human and nonhuman primates," *Cerebral Cortex*, vol. 31, no. 1, pp. 379–395, 2021.

[172] B. Jacobs *et al.*, "Comparative morphology of gigantopyramidal neurons in primary motor cortex across mammals," *Journal of Comparative Neurology*, vol. 526, no. 3, pp. 496–536, 2018.

[173] A. Warling *et al.*, "Putative dendritic correlates of chronic traumatic encephalopathy: A preliminary quantitative Golgi exploration," *Journal of Comparative Neurology*, vol. 529, no. 7, pp. 1308–1326, 2021.

[174] K. Anderson, E. Yamamoto, J. Kaplan, M. Hannan, and B. Jacobs, "Neurolucida Lucivid versus Neurolucida camera: A quantitative and qualitative comparison of three-dimensional neuronal reconstructions," *Journal of neuroscience methods*, vol. 186, no. 2, pp. 209–214, 2010.

[175] B. Jacobs *et al.*, "Regional dendritic and spine variation in human cerebral cortex: A quantitative golgi study," *Cerebral cortex*, vol. 11, no. 6, pp. 558–571, 2001.

[176] K. Anderson *et al.*, "The morphology of supragranular pyramidal neurons in the human insular cortex: A quantitative Golgi study," *Cerebral Cortex*, vol. 19, no. 9, pp. 2131–2144, 2009.

[177] K. Travis, K. Ford, and B. Jacobs, "Regional dendritic variation in neonatal human cortex: A quantitative Golgi study," *Developmental neuroscience*, vol. 27, no. 5, pp. 277–287, 2005.

[178] B. Jacobs *et al.*, "Comparative neuronal morphology of the cerebellar cortex in afrotherians, carnivores, cetartiodactyls, and primates," *Frontiers in neuroanatomy*, vol. 8, p. 24, 2014.

[179] D. Linaro *et al.*, "Xenotransplanted human cortical neurons reveal species-specific development and functional integration into mouse visual circuits," *Neuron*, vol. 104, no. 5, pp. 972–986, 2019.

[180] G. Eyal *et al.*, "Unique membrane properties and enhanced signal processing in human neocortical neurons," *Elife*, vol. 5, e16553, 2016.

[181] T. Chailangkarn *et al.*, "A human neurodevelopmental model for Williams syndrome," *Nature*, vol. 536, no. 7616, pp. 338–343, 2016.

[182] M. Vukšić, Z. Petanjek, M. R. Rašin, and I. Kostović, "Perinatal growth of prefrontal layer III pyramids in Down syndrome," *Pediatric neurology*, vol. 27, no. 1, pp. 36–38, 2002.

[183] M. Waskom, "Seaborn: Statistical data visualization," *JOSS*, vol. 6, no. 60, p. 3021, Apr. 2021.

[184] P. Virtanen *et al.*, "SciPy 1.0: Fundamental algorithms for scientific computing in Python," *Nature methods*, vol. 17, no. 3, pp. 261–272, 2020.

[185] C. De Boor and C. De Boor, *A Practical Guide to Splines*. springer-verlag New York, 1978, vol. 27.

[186] R. M. Wilcox, "Exponential Operators and Parameter Differentiation in Quantum Physics," *Journal of Mathematical Physics*, vol. 8, no. 4, pp. 962–982, Apr. 1967.

[187] R. P. Brent, *Algorithms for Minimization without Derivatives* (Prentice-Hall Series in Automatic Computation). Englewood Cliffs, N.J: Prentice-Hall, 1973.

[188] A. Ianus, D. Alexander, H. Zhang, and M. Palombo, "Mapping complex cell morphology in the grey matter with double diffusion encoding MR: A simulation study," *NeuroImage*, vol. 241, p. 118 424, Nov. 2021.

[189] A. Daducci, E. J. Canales-Rodríguez, H. Zhang, T. B. Dyrby, D. C. Alexander, and J.-P. Thiran, "Accelerated Microstructure Imaging via Convex Optimization (AMICO) from diffusion MRI data," *NeuroImage*, vol. 105, pp. 32–44, Jan. 2015.

[190] U. Ferizi *et al.*, "Diffusion MRI microstructure models with in vivo human brain Connectome data: Results from a multi-group comparison," *NMR in Biomedicine*, vol. 30, no. 9, e3734, 2017.

[191] A. De Luca *et al.*, "On the generalizability of diffusion MRI signal representations across acquisition parameters, sequences and tissue types: Chronicles of the MEMENTO challenge," *NeuroImage*, vol. 240, p. 118 367, 2021.

[192] S. Coelho *et al.*, "Reproducibility of the Standard Model of diffusion in white matter on clinical MRI systems," *NeuroImage*, vol. 257, no. 2022, p. 119 290, Aug. 2022.

[193] C. Mekkaoui, T. G. Reese, M. P. Jackowski, H. Bhat, and D. E. Sosnovik, "Diffusion MRI in the heart," *NMR in Biomedicine*, vol. 30, no. 3, e3426, Mar. 2017.

[194] S. Haller, G. Zaharchuk, D. L. Thomas, K.-O. Lovblad, F. Barkhof, and X. Golay, "Arterial Spin Labeling Perfusion of the Brain: Emerging Clinical Applications," *Radiology*, vol. 281, no. 2, pp. 337–356, Nov. 2016.

[195] M. M. Bissell *et al.*, "4D Flow cardiovascular magnetic resonance consensus statement: 2023 update," *J Cardiovasc Magn Reson*, vol. 25, no. 1, p. 40, Jul. 2023.

[196] A. Z. Lau, J. J. Miller, M. D. Robson, and D. J. Tyler, "Cardiac perfusion imaging using hyperpolarized ^{13} c urea using flow sensitizing gradients," *Magnetic Resonance in Med*, vol. 75, no. 4, pp. 1474–1483, Apr. 2016.

[197] D. Le Bihan, "What can we see with IVIM MRI?" *NeuroImage*, vol. 187, pp. 56–67, Feb. 2019.

[198] A. Andreou *et al.*, "Measurement reproducibility of perfusion fraction and pseudodiffusion coefficient derived by intravoxel incoherent motion diffusion-weighted MR imaging in normal liver and metastases," *Eur Radiol*, vol. 23, no. 2, pp. 428–434, Feb. 2013.

[199] H. J. Park *et al.*, "Intravoxel incoherent motion diffusion-weighted MRI of the abdomen: The effect of fitting algorithms on the accuracy and reliability of the parameters," *Magnetic Resonance Imaging*, vol. 45, no. 6, pp. 1637–1647, Jun. 2017.

[200] S.-E. Lee *et al.*, "Recent Advances in Cardiac Magnetic Resonance Imaging," *Korean Circ J*, vol. 49, no. 2, p. 146, 2019.

[201] Z. Khalique, P. F. Ferreira, A. D. Scott, S. Nielles-Vallespin, D. N. Firmin, and D. J. Pennell, "Diffusion Tensor Cardiovascular Magnetic Resonance Imaging," *JACC: Cardiovascular Imaging*, vol. 13, no. 5, pp. 1235–1255, May 2020.

[202] G. Zhu *et al.*, "Comparison of MRI IVIM and MR perfusion imaging in acute ischemic stroke due to large vessel occlusion," *International Journal of Stroke*, vol. 15, no. 3, pp. 332–342, Apr. 2020.

[203] C. Federau, "Intravoxel incoherent motion MRI as a means to measure *in vivo* perfusion: A review of the evidence," *NMR in Biomedicine*, vol. 30, no. 11, e3780, Nov. 2017.

[204] M. Lashgari *et al.*, "Three-dimensional micro-structurally informed in silico myocardium—Towards virtual imaging trials in cardiac diffusion weighted MRI," *Medical Image Analysis*, vol. 82, p. 102 592, Nov. 2022.

[205] J. Jeener, "Macroscopic molecular diffusion in liquid NMR, revisited," *Concepts Magn. Reson.*, vol. 14, no. 2, pp. 79–88, 2002.

[206] A. N. Brooks and T. J. Hughes, "Streamline upwind/Petrov-Galerkin formulations for convection dominated flows with particular emphasis on the incompressible Navier-Stokes equations," *Computer Methods in Applied Mechanics and Engineering*, vol. 32, no. 1-3, pp. 199–259, Sep. 1982.

[207] R. W. Lewis, P. Nithiarasu, and K. N. Seetharamu, *Fundamentals of the Finite Element Method for Heat and Fluid Flow*, 1st ed. Wiley, Apr. 2004.

[208] Q. Zhang, H. Johansen, and P. Colella, "A Fourth-Order Accurate Finite-Volume Method with Structured Adaptive Mesh Refinement for Solving the Advection-Diffusion Equation," *SIAM J. Sci. Comput.*, vol. 34, no. 2, B179–B201, Jan. 2012.

[209] M. Augustin *et al.*, "An assessment of discretizations for convection-dominated convection–diffusion equations," *Computer Methods in Applied Mechanics and Engineering*, vol. 200, no. 47-48, pp. 3395–3409, Nov. 2011.

[210] V. John and E. Schmeyer, "Finite element methods for time-dependent convection–diffusion–reaction equations with small diffusion," *Computer Methods in Applied Mechanics and Engineering*, vol. 198, no. 3-4, pp. 475–494, Dec. 2008.

[211] T. J. Hughes, L. P. Franca, and M. Mallet, "A new finite element formulation for computational fluid dynamics: VI. Convergence analysis of the generalized SUPG formulation for linear time-dependent multidimensional advective-diffusive systems," *Computer Methods in Applied Mechanics and Engineering*, vol. 63, no. 1, pp. 97–112, Jul. 1987.

[212] V. John and J. Novo, "Error Analysis of the SUPG Finite Element Discretization of Evolutionary Convection-Diffusion-Reaction Equations," *SIAM J. Numer. Anal.*, vol. 49, no. 3, pp. 1149–1176, Jan. 2011.

[213] T. Tezduyar, "Stabilized Finite Element Formulations for Incompressible Flow Computations," in *Advances in Applied Mechanics*, vol. 28, Elsevier, 1991, pp. 1–44.

[214] J.-L. Guermond, "Subgrid stabilization of Galerkin approximations of linear monotone operators," *IMA Journal of Numerical Analysis*, vol. 21, no. 1, pp. 165–197, Jan. 2001.

[215] R. Codina and J. Blasco, "Analysis of a stabilized finite element approximation of the transient convection-diffusion-reaction equation using orthogonal subscales," *Comput Visual Sci*, vol. 4, no. 3, pp. 167–174, Feb. 2002.

[216] T. J. Hughes, L. P. Franca, and G. M. Hulbert, "A new finite element formulation for computational fluid dynamics: VIII. The galerkin/least-squares method for advective-diffusive equations," *Computer Methods in Applied Mechanics and Engineering*, vol. 73, no. 2, pp. 173–189, May 1989.

[217] P. T. Callaghan, *Translational Dynamics and Magnetic Resonance: Principles of Pulsed Gradient Spin Echo NMR*. Oxford ; New York: Oxford University Press, 2011.

[218] I. Seroussi, D. S. Grebenkov, O. Pasternak, and N. Sochen, "Microscopic interpretation and generalization of the Bloch-Torrey equation for diffusion magnetic resonance," *Journal of Magnetic Resonance*, vol. 277, pp. 95–103, Apr. 2017.

[219] Q. Long, X. Xu, M. Bourne, and T. Griffith, "Numerical study of blood flow in an anatomically realistic aorto-iliac bifurcation generated from MRI data," *Magn. Reson. Med.*, vol. 43, no. 4, pp. 565–576, Apr. 2000.

[220] F. Schmid, P. S. Tsai, D. Kleinfeld, P. Jenny, and B. Weber, "Depth-dependent flow and pressure characteristics in cortical microvascular networks," *PLoS Comput Biol*, vol. 13, no. 2, J. J. Saucerman, Ed., e1005392, Feb. 2017.

[221] É. Guyon, J.-P. Hulin, and L. Petit, *Hydrodynamique physique* (Savoirs actuels), Nouv. éd. rev. et augm. Les Ulis Paris: EDP sciences CNRS éd, 2001.

[222] S. V. Patankar, *Numerical Heat Transfer and Fluid Flow* (Series in Computational Methods in Mechanics and Thermal Sciences). Boca Raton: CRC Press, 2009.

[223] P. B. Bochev, M. D. Gunzburger, and J. N. Shadid, "Stability of the SUPG finite element method for transient advection–diffusion problems," *Computer Methods in Applied Mechanics and Engineering*, vol. 193, no. 23-26, pp. 2301–2323, Jun. 2004.

[224] R. Codina, "On stabilized finite element methods for linear systems of convection–diffusion-reaction equations," *Computer Methods in Applied Mechanics and Engineering*, vol. 188, no. 1-3, pp. 61–82, Jul. 2000.

[225] L. P. Franca, S. L. Frey, and T. J. Hughes, "Stabilized finite element methods: I. Application to the advective-diffusive model," *Computer Methods in Applied Mechanics and Engineering*, vol. 95, no. 2, pp. 253–276, Mar. 1992.

[226] T Knopp, G Lube, and G Rapin, "Stabilized finite element methods with shock capturing for advection–diffusion problems," *Computer Methods in Applied Mechanics and Engineering*, vol. 191, no. 27-28, pp. 2997–3013, Apr. 2002.

[227] G. Lube and G. Rapin, "Residual-based stabilized higher-order FEM for advection-dominated problems," *Computer Methods in Applied Mechanics and Engineering*, vol. 195, no. 33-36, pp. 4124–4138, Jul. 2006.

[228] L. Franca and F. Valentin, "On an improved unusual stabilized finite element method for the advective–reactive–diffusive equation," *Computer Methods in Applied Mechanics and Engineering*, vol. 190, no. 13-14, pp. 1785–1800, Dec. 2000.

[229] V. John and P. Knobloch, "On spurious oscillations at layers diminishing (SOLD) methods for convection–diffusion equations: Part I – A review," *Computer Methods in Applied Mechanics and Engineering*, vol. 196, no. 17-20, pp. 2197–2215, Mar. 2007.

[230] V. P. Van, F. Schmid, G. Spinner, S. Kozerke, and C. Federau, "Simulation of intravoxel incoherent perfusion signal using a realistic capillary network of a mouse brain," *NMR in Biomedicine*, vol. 34, no. 7, e4528, Jul. 2021.

[231] M. Intaglietta, N. Silverman, and W. Tompkins, "Capillary flow velocity measurements in vivo and in situ by television methods," *Microvascular Research*, vol. 10, no. 2, pp. 165–179, Sep. 1975.

[232] M. Klarhöfer, B. Csapo, Cs. Balassy, J. Szeles, and E. Moser, "High-resolution blood flow velocity measurements in the human finger: Blood Flow Velocities in the Human Finger," *Magn. Reson. Med.*, vol. 45, no. 4, pp. 716–719, Apr. 2001.

[233] J. Crank and P. Nicolson, "A practical method for numerical evaluation of solutions of partial differential equations of the heat-conduction type," *Math. Proc. Camb. Phil. Soc.*, vol. 43, no. 1, pp. 50–67, Jan. 1947.

[234] J. Akin and T. E. Tezduyar, "Calculation of the advective limit of the SUPG stabilization parameter for linear and higher-order elements," *Computer Methods in Applied Mechanics and Engineering*, vol. 193, no. 21-22, pp. 1909–1922, May 2004.

[235] V. John and P. Knobloch, "On spurious oscillations at layers diminishing (SOLD) methods for convection–diffusion equations: Part II – Analysis for and finite elements," *Computer Methods in Applied Mechanics and Engineering*, vol. 197, no. 21-24, pp. 1997–2014, Apr. 2008.

[236] R. Bhatia, *Matrix Analysis* (Graduate Texts in Mathematics). New York, NY: Springer New York, 1997, vol. 169.

[237] H.-I. Suk, S.-W. Lee, and D. Shen, "Hierarchical feature representation and multimodal fusion with deep learning for AD/MCI diagnosis," *NeuroImage*, vol. 101, pp. 569–582, Nov. 2014.

[238] I. Goodfellow, Y. Bengio, and A. Courville, *Deep Learning*. MIT press, 2016.

[239] X. Glorot and Y. Bengio, "Understanding the difficulty of training deep feedforward neural networks," in *Proceedings of the Thirteenth International Conference on Artificial Intelligence and Statistics*, JMLR Workshop and Conference Proceedings, 2010, pp. 249–256.

[240] D. Hendrycks and K. Gimpel, "Gaussian error linear units (gelus)," *arXiv preprint arXiv:1606.08415*, 2016. arXiv: 1606.08415.

[241] N. Srivastava, G. Hinton, A. Krizhevsky, I. Sutskever, and R. Salakhutdinov, "Dropout: A simple way to prevent neural networks from overfitting," *The journal of machine learning research*, vol. 15, no. 1, pp. 1929–1958, 2014.

[242] K. He, X. Zhang, S. Ren, and J. Sun, "Delving deep into rectifiers: Surpassing human-level performance on imagenet classification," in *Proceedings of the IEEE International Conference on Computer Vision*, 2015, pp. 1026–1034.

[243] D. P. Kingma and J. Ba, "Adam: A method for stochastic optimization," *arXiv preprint arXiv:1412.6980*, 2014. arXiv: 1412.6980.

[244] S. J. Reddi, S. Kale, and S. Kumar, "On the convergence of adam and beyond," *arXiv preprint arXiv:1904.09237*, 2019. arXiv: 1904.09237.

[245] K. Hornik, M. Stinchcombe, and H. White, "Multilayer feedforward networks are universal approximators," *Neural networks*, vol. 2, no. 5, pp. 359–366, 1989.

[246] J. Bridle, "Training stochastic model recognition algorithms as networks can lead to maximum mutual information estimation of parameters," *Advances in neural information processing systems*, vol. 2, 1989.

[247] A. Paszke *et al.*, "Pytorch: An imperative style, high-performance deep learning library," *Advances in neural information processing systems*, vol. 32, 2019.

ECOLE
DOCTORALE
DE MATHEMATIQUES
HADAMARD

Titre: Méthodes numériques pour l'estimation de la microstructure du cerveau à partir de données d'IRM de diffusion

Mots clés: EDP de Bloch-Torrey,IRM de diffusion, estimation des microstructures, simulation numérique

Résumé: Les objectifs de cette thèse sont (1) de présenter de nouvelles méthodes de simulation basées sur l'EDP de Bloch-Torrey, facilitant les études numériques sur les paramètres liés à la géométrie, et (2) d'employer ces méthodes proposées pour évaluer les modèles de signal de compartiment en IRM de diffusion et pour analyser le signal d'IRM de diffusion ou le coefficient de diffusion apparent (CDA).
Tout d'abord, nous présentons une nouvelle représentation sous forme de Formalisme Matriciel, qui réutilise les fonctions propres de Laplace imperméables pour calculer les signaux perméables. Grâce à cette formulation, nous illustrons que (1) les signaux d'IRM de diffusion ont un taux exponentiel vers la perméabilité; (2) le CDA montre un taux de dépendance différent à faibles et hautes perméabilités; (3) il existe une corrélation entre la perméabilité et le modèle NEXI.
Ensuite, nous développons une expansion asymptotique du second ordre sur deux déformations géométriques analytiques. À travers une investigation numérique, nous montrons que (1) le pliage réduit la diffusion dans la direction de diffusion maximale; (2) la déformation par torsion change la direction de diffusion maximale.
Troisièmement, nous identifions des biomarqueurs dérivés du point d'inflexion (PI) de la déviation de la loi de puissance $1/\sqrt{b}$ dans la matière grise du cerveau. Nous effectuons une analyse numérique de la relation entre les biomarqueurs dérivés du PI, les fractions de volume, la taille du soma, et proposons une estimation basée sur la recherche exhaustive efficace en utilisant ces biomarqueurs.
Enfin, pour résoudre l'instabilité dans la simulation d'écoulement sanguin en IRM de diffusion, nous appliquons le schéma Streamline Upwind Petrov Galerkin. La validation numérique montre que cette nouvelle méthode est capable de fournir une solution stable pour une vitesse d'écoulement sanguin relativement élevée sur un maillage creux.

Title: Numerical methods to estimate brain micro-structure from diffusion MRI data

Keywords: Bloch-Torrey PDE, diffusion MRI, microstructural imaging, numerical simulation

Abstract: The objectives of this thesis are (1) to introduce novel simulation methods based on the Bloch-Torrey PDE, facilitating numerical studies on geometry-related parameters and (2) to employ the proposed methods, to evaluate the existing diffusion MRI compartment signal models, and to analyze diffusion MRI signal or apparent diffusion coefficient (ADC).
First, we present a novel Matrix Formalism representation, which can re-use the impermeable Laplace eigenfunctions to compute the permeable signals. Using this formulation, we illustrate that (1) diffusion MRI signal shows an exponential rate towards permeability; (2) Long-time limit ADC shows different rates of dependence at low and high permeabilities; (3) there is a correlation between permeability and the NEXI model.
Second, we develop a second-order asymptotic expansion towards two analytical geometrical deformations. By numerical studies, we illustrate that (1) bending will decrease the signal value in the maximum diffusion direction; (2) twisting will change the maximum diffusion direction.
Third, we identify inflection point (IP) derived biomarkers from the deviation of the $1/\sqrt{b}$ power-law scaling in the brain gray matter. We conduct numerical analysis on the relationship between the IP-derived biomarkers and volume fractions and soma size and propose an efficient exhaustive search based on these biomarkers.
Finally, to address the instability issues in diffusion MRI blood flow imaging simulation, we apply the Streamline Upwind Petrov Galerkin scheme. Numerical validation illustrates that this new method is able to yield a stable solution for a quite high blood flow velocity on a coarse mesh.

Institut Polytechnique de Paris
91120 Palaiseau, France